Politecnico di Milano

Department of Energy

Doctoral Programme in Energy and Nuclear Science and Technology

1D thermo-fluid dynamic modelling of IC engines
and system integration on electrified vehicles

Doctoral dissertation of

Andrea Massimo Marinoni

Supervisors

Prof. Angelo Onorati and Prof. Gianluca Montenegro

Tutor

Prof. Angelo Onorati

The Chair of the Doctoral Programme

Prof. Vincenzo Dossena

July 2023 – Cycle XXXV

Abstract

In this Ph.D. thesis, the development and application of advanced predictive 1D/0D methodologies to simulate Real Driving Emission (RDE) cycles are described. The goal is to obtain an integrated co-simulation model of a modern Plug-in Hybrid Vehicle (PHEV). In the first chapter, a general introduction to the Internal Combustion Engine (ICE) simulation topic is presented. With chapter 2 the mathematical model of an ICE is described together with the innovative numerical method used to speed up the simulation time in this work. Then in chapter 3 the two real engine test cases investigated are presented and their respective 1D models are obtained. In chapter 4 the steady state validation against experimental data of the two 1D models is carried out and in chapter 5 the same is achieved for the Fast Simulation Method (FSM) models. With chapter 6 the focus shifts towards the prediction of performance and emissions during real-world driving cycles, with a comparison with respect to measured cycles. In chapter 7 it is introduced the coupling methodology developed to allow the co-simulation of the 1D engine model with external sub-models. With chapters 7 and 8 the integrated simulation framework achieved is exploited to simulate a complete Plug-in Hybrid Electric Vehicle performing a general driving cycle. This work is strongly coupled with the activities of the European project "VISION-xEV", see Figure 1.1, which aimed at the development of an integrated co-simulation framework for the prediction of performance and emissions of a modern hybrid vehicle [1].

Figure 1.1 – Logo of the European project.

Table of Contents

1. Introduction

Nowadays the urgent environmental concern has led to the adoption of stringent policies to reduce the impact of human activities on the overall balance of CO2 and the emission of pollutant chemicals such as CO (Carbon Monoxide) and NO_x (Nitrogen Oxides). In the automotive field the main consequence has been the introduction of the recent Euro6D emission regulation, and the upcoming Euro7, which now have more realistic testing procedures, such as Real Drive Emission (RDE) cycles [2,3] along with a reduction of the emitted pollutants. A typical RDE cycle is presented in Figure 1.2. From a technical point of view, the challenge will be to comply with the emission regulation during real-world cycles, where the engine may be turned off most of the time in the case of Plug-in Hybrid Electric Vehicles (PHEV), emphasizing the need of reducing the impact of multiple cold starts. Recently the development of new powertrains has moved from a steady state towards a transient kind of characterization, to ensure real-world compliance with emission targets [4,5].
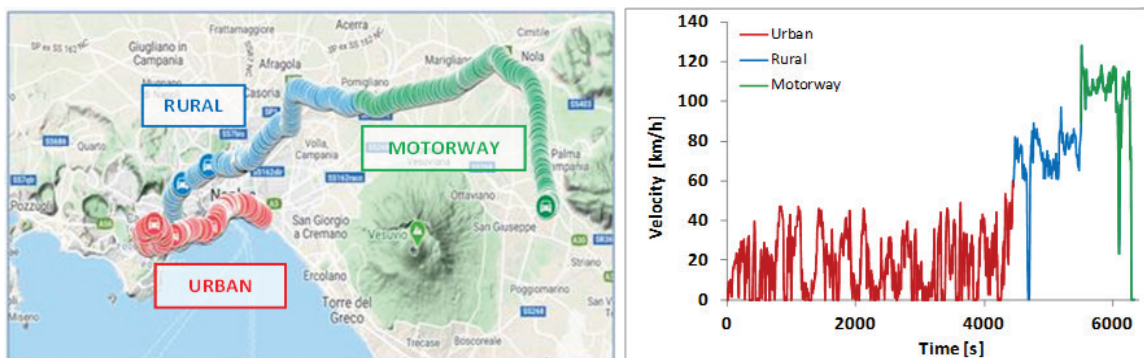
Figure 1.2 – Example of Real Driving Cycle from the VISION-xEV project.

Despite the tightening trend of regulation, internal combustion engines will still play a crucial role in the mobility of the next decades and their design must be based on a careful tuning of all the engine parameters, to achieve the best thermodynamic efficiency of the power unit along with constantly effective after-treatment system activity. The cost of engine calibration and testing is raising its impact on the production cost and time because the test cycles are repeated continuously to achieve compliance with the regulation limits [6]. The usage of advanced simulation tools, accompanied by a focused experimental campaign, can significantly reduce costs and time. In this scenario, the application of advanced 1D/0D modelling tools becomes a fundamental step to quickly test new virtual engine configurations and calibrations [7]. Hence, the reduction of computational effort is crucial to achieve a fast evaluation of different engine parametrizations and ECU strategies. Fast simulation tools are also beneficial for the integration of 1D crank angle resolved engine models with other vehicle simulation tools, to evaluate different powertrain architectures with a more detailed methodology.

Modern vehicle architecture is becoming more and more complex. Nowadays Plug-in Hybrid Electric Vehicles, which feature both an IC engine and an electric motor powered by a battery, are widespread. The development and simulation of these vehicle involves many different sub-systems which impact on the design of each other. In this framework, a fully integrated predictive model of a complete hybrid vehicle (see Figure 1.3) would be beneficial for the development and optimization of new configurations. Being able to quickly simulate driving cycles with real time interaction among all sub-components of the engine allows to reduce development costs, since less iterative calibration loops are required for each component.
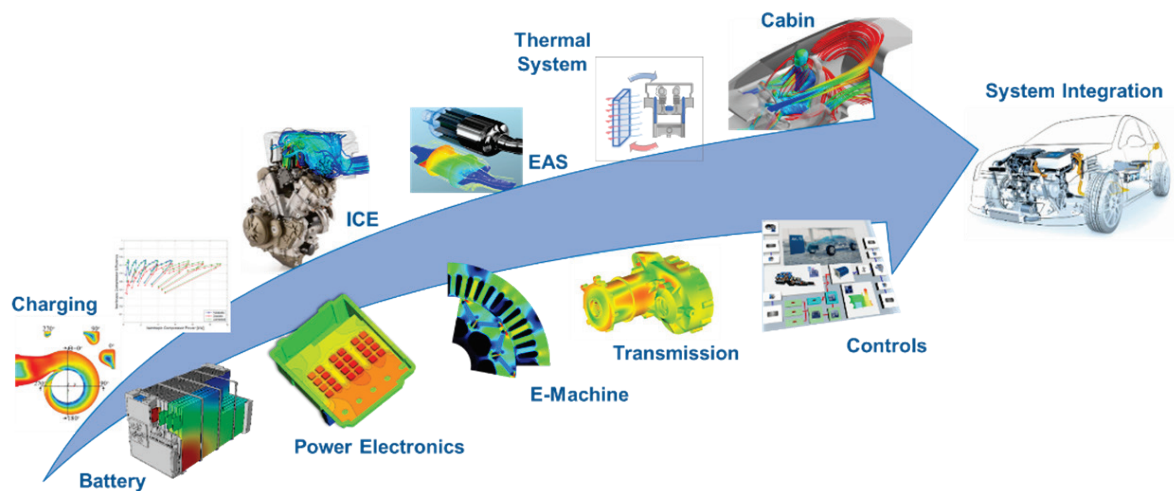
Figure 1.3 – Modern Plug-in Hybrid Electric Vehicle (PHEV) components and system integration.

In this scenario, state-of-the-art 0D/1D simulation codes allow the prediction of the steady state engine map of operating points at various speeds and loads (providing the calculated values of air mass flow rate, torque, power, fuel consumption, cylinder pressure and emissions), starting from a set of experimental data for the initial calibration and model characterization. These steady state maps can be used to represent the engine operating conditions during transients, such as in the case of homologation (RDE and WHTC) driving cycles [8]. This map-based method shown in [9] is certainly a fast solution which, however, completely neglects the dynamic behaviour of the IC engine, dictated by the unsteady flows in the pipes and the fluid dynamic inertia of the main components (intake and exhaust manifolds, turbocharger, injection system, etc.). Hence, the possible use of a crank-angle resolved 0D/1D engine model is crucial to obtain more realistic results during transients. However, the use of a 1D model for a driving cycle simulation, as performed in [8], requires a high simulation time, which prevents the systematic application of the 1D model to assess the influence of many engine parameters. In this work this weakness is solved by means of the Fast Simulation Method developed, allowing to simulate a driving cycle with a CPU time close to the real time.

More specifically, mathematical 1D modelling of internal combustion engines is employed by more than 25 years to assist the design and development of any ICE powered transportation system [10,11]. In previous works as [12,13] the engine has been usually represented by a 0D map. This so-called map-based approach allows to simulate a generic driving cycle performed by a vehicle with a low computational effort. The fast simulation benefit comes with the cost of a less detailed IC engine model, since this look-up table approach neglects the unsteadiness of the IC engine phenomena. Most importantly, in a map-based engine the torque request is potentially immediately available, while this is not the case in a real engine. This approach also introduces an inevitable inaccuracy when estimating pollutant emissions. For this reason, the focus of some works in this field has shifted towards the simulation of engines in transient conditions. The results described in [14] were promising but the high computational effort required for the 1D simulation restricted the applicability of the approach to few and short driving cycles. Hence, several authors have searched for methods to reduce the computational effort of a 1D model, while maintaining the accuracy. For example, in the work presented by [15] it is proposed to simplify the 1D model itself. It was suggested to modify the engine schematic removing 1D pipes and replacing them with 0D volumes to represent the intake and exhaust system. This allowed to reach the target goals and the accuracy, even if the procedure required a minimal recalibration of the model, well compensated by the fast simulation times achieved. In this framework, the present work aims at achieving the same goal with a different strategy: the 1D elements are maintained, while their discretization is coarsened. Hence, it is not needed to carry out a recalibration of the model parameters, to obtain a satisfactory fluid dynamic solution, very similar to that provided by the accurate, refined 1D model.

2. Governing equations for 1D, compressible, unsteady flows

The simulation of the phenomena occurring in an IC engine starts from the formulation of a physical model of the gas flow in the duct systems [16,17,18]. The following assumptions are made:

- The flow is unsteady.
- The gas is compressible.
- The viscosity of the fluid is not negligible.
- The fluid is subject to non-adiabatic and non-isentropic transformations.
- The flow is three dimensional.

These assumptions, and especially the last one, would require a fully three-dimensional approach to the problem. However, in order to simulate the whole engine, the following assumption is made to simplify the physical model, considering the large scale of the domain usually encountered, which consists of the entire intake and exhaust system of the IC engine: the flow is hence assumed to be one-dimensional. It is important to highlight that the unsteady characteristic of the flow has not been simplified, nor the compressibility or the non-adiabaticity of the transformations. The one-dimensional hypothesis is based on the assumptions that in most of the domain the ratio between transversal dimension and the length of the domain is small. This is true for example for straight pipes and becomes less valid with strong area variations.

To build the mathematical model for the unsteady, compressible, 1D flow, we can consider the following generic infinitesimal slice of fluid contained in the one-dimensional domain represented in Figure 2.1, where ρ is the density, u the velocity, p the pressure and F the cross section [19]. The infinitesimal length of the slice is dx.
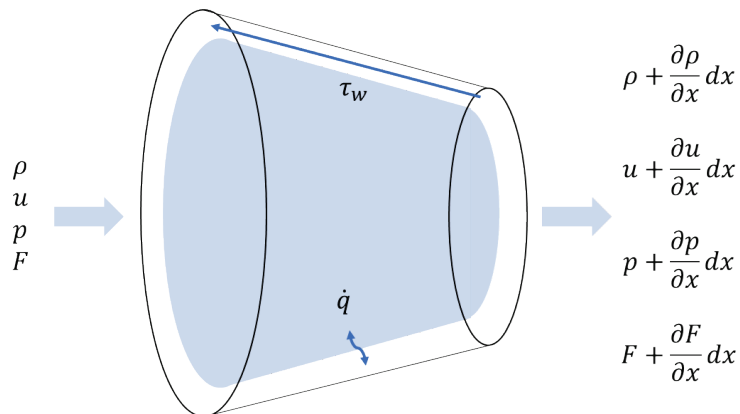
Figure 2.1 – 1D infinitesimal volume of working fluid.

Hence, at a fixed time, the right properties will differ from the left properties by an infinitesimal quantity. The governing equation for this control volume highlighted in blue can be written, namely the mass, momentum, and energy conservation equation. As highlighted by the picture, the gas properties are only defined along the space coordinate x and they change time-step after timestep.

2.1 Mass conservation

This equation expresses the principle which states that the mass is conserved or that the net flux of fluid mass must be equal to the change of the fluid mass in time contained in the control volume.

$$\dot{m}_{out} - \dot{m}_{in} = -\frac{\partial(\rho F dx)}{\partial t} \qquad (2.1)$$

The entering and exiting mass flow rates are:

$$\dot{m}_{in} = \rho u F \qquad \dot{m}_{out} = \left(\rho + \frac{\partial \rho}{\partial x}dx\right)\left(u + \frac{\partial u}{\partial x}dx\right)\left(F + \frac{\partial F}{\partial x}dx\right) \tag{2.2}$$

So, the starting equation becomes:

$$\left(\rho + \frac{\partial \rho}{\partial x}dx\right)\left(u + \frac{\partial u}{\partial x}dx\right)\left(F + \frac{\partial F}{\partial x}dx\right) - \rho u F = -\frac{\partial(\rho F dx)}{\partial t} \tag{2.3}$$

and rearranging the terms it finally becomes:

$$\frac{\partial \rho}{\partial t} + \frac{\partial(\rho u)}{\partial x} + \frac{\rho u}{F}\frac{dF}{dx} = 0 \tag{2.4}$$

2.2 Momentum conservation

This equation, which is also Newton's second law, states that the rate of change of momentum of the fluid is equal to the sum of the forces on the fluid. Hence the sum of pressure forces and shear forces acting on the surface of the control volume is equal to the sum of the net flux of momentum through the control volume and the rate of change of momentum within the control volume. The sum of forces on the fluid, hence the resultant force, is due to two different contributions: one is due to the difference in pressure between the end faces and another is due to the component, on the x direction, of the pressure acting on the side of the control volume. The first contribution, f_{p1}, is given by the product between the gradient of the force along the x direction and the length of the pipe section dx. In the equation the minus sign states that the force is in the opposite direction of the gradient. While the second contribution, the force f_{p2}, is due to the pressure acting on the side of the control volume in the x direction and can be expressed as depicted below. The friction force f_{att} is due to the presence of shear stress τ_w, due to friction f related to viscosity and the interaction between the fluid and the pipe walls on the boundaries. The force is directed in the opposite direction of x.

$$f_{p1} = -\frac{\partial(pF)}{\partial x}dx \qquad f_{p2} = p\frac{dF}{dx}dx \qquad \tau_w = \frac{1}{2}\rho u^2 f \qquad f_{att} = -\tau_w \pi D dx \tag{2.5}$$

The variation of momentum of the control volume in time and the net flux of momentum through inlet and outlet surfaces are:

$$\text{Variation in time} = \frac{\partial(\rho u F dx)}{\partial t} \qquad\qquad \text{Net flux} = \frac{\partial(\rho F u^2)}{\partial x}dx \tag{2.6}$$

Summing up all the terms and rearranging we obtain:

$$\frac{\partial(\rho u F)}{\partial t} + \frac{\partial(\rho u^2 + p)F}{\partial x} - p\frac{dF}{dx} + \frac{1}{2}\rho u^2 f \pi D = 0 \tag{2.7}$$

2.3 Energy conservation

This equation expresses the conservation of energy and can be derived from the first law of thermodynamic which states that the rate of change of internal energy of the fluid is equal to the rate of heat addition to the fluid plus the rate of work done on the fluid:

$$\dot{Q} + \dot{W} = \frac{\partial E_0}{\partial t} + \frac{\partial H_0}{\partial x}dx \tag{2.8}$$

Where E_0 is the stagnation internal energy, H_0 is the stagnation enthalpy, $\dot{W}$ is the rate of work done on the fluid, which is zero, and $\dot{Q}$ is the net rate of heat to the fluid. These quantities are defined according to the following relations, where e_0 and h_0 are respectively the specific stagnation internal energy and specific stagnation enthalpy, and are defined as:

$$\dot{Q} = \dot{q}\rho F dx \qquad E_0 = e_0 \rho F dx \qquad H_0 = h_0 \rho F u \qquad e_0 = e + \frac{1}{2}u^2 \qquad h_0 = e_0 + \frac{p}{\rho} \tag{2.9}$$

Then, the final form of the energy equation can be written as:

12

$$\dot{q}\rho F dx = \frac{\partial(e_0 \rho F dx)}{\partial t} + \frac{\partial(h_0 \rho F u)}{\partial x} dx \tag{2.10}$$

2.4 The system of equations

The three conservation equations can be then grouped and rearranged into a system of equations:

$$\begin{cases} \dfrac{\partial(\rho F)}{\partial t} + \dfrac{\partial(\rho u F)}{\partial x} = 0 \\ \dfrac{\partial(\rho u F)}{\partial t} + \dfrac{\partial(\rho u^2 + p)F}{\partial x} - p\dfrac{dF}{dx} + \rho FG = 0 \qquad \text{where: } G = \frac{1}{2}u|u|f\frac{4}{D} \\ \dfrac{\partial(\rho e_0 F)}{\partial t} + \dfrac{\partial(\rho h_0 u F)}{\partial x} - \dot{q}\rho F = 0 \end{cases} \tag{2.11}$$

However, the number of unknowns is four (ρ, u, p, e), greater than the number of equations that are three. To mathematically close the problem, so that the number of unknowns matches the number of independent equations, a last relationship between the unknowns must be introduced. This is the equation describing the fluid, which is also called the Equation of State (EOS). If the fluid is modelled as a gas, the ideal gas equation can be used:

$$pv = RT \qquad \text{where } R = R_u/M_g = 287.1\frac{J}{Kg*K} \text{ and } R_u = 8.134\frac{J}{mol*K} \tag{2.12}$$

With this additional equation we have introduced a new unknown, T, the gas temperature, which we are now going to link by thermodynamic relationships to the internal energy e. For an ideal gas the following hypothesis holds:

$$e_0 = e + \frac{1}{2}u^2 \qquad e = c_v T \qquad h_0 = h + \frac{1}{2}u^2 \qquad h = e + RT = c_p T \tag{2.13}$$

The terms c_v and c_p are the specific heat capacities respectively at constant volume and pressure which can be expressed as a function of their ratios k and the gas constant R, and for a perfect gas they are constants:

$$c_p = c_v + R \qquad k = c_p/c_v \qquad c_v = R/(k-1) \qquad c_p = kR/(k-1) \tag{2.14}$$

It is useful to highlight that the perfect gas model does not allow to consider variation of specific gas properties due to temperature, pressure, and chemical composition.

2.5 Transporting the chemical composition

It is possible to transport additional variables representing the specie concentration in the gas. Each specie is transported as a scalar, hence not influencing the gas properties.

$$\frac{\partial(\rho Y_i F)}{\partial t} + \frac{\partial(\rho u Y_i F)}{\partial x} = \rho \dot{Y}_i F \qquad\qquad Y_N = 1 - \sum_{1}^{N-1} Y_i \tag{2.15}$$

Since every specie is transported with one equation, the system of equations contains one additional equation for every specie, hence the number of unknowns still matches the number of equations. Now that the system of equations is mathematically closed, the system of equations can be written in matrix form, so that it is more suitable for the numerical implementation:

Conserved variables   Flux of the conserved variables   Source terms

$$W = \begin{bmatrix} \rho F \\ \rho u F \\ \rho e_0 F \\ \rho Y F \end{bmatrix} \qquad F(W) = F = \begin{bmatrix} \rho u F \\ (\rho u^2 + p)F \\ \rho u h_0 F \\ \rho u Y F \end{bmatrix} \qquad C = \begin{bmatrix} 0 \\ -p\dfrac{dF}{dx} + \rho GF \\ -\rho \dot{q} F \\ -\rho \dot{Y} F \end{bmatrix} \tag{2.16}$$

So that the whole system can be written as a single equation as follows:

$$\frac{\partial W}{\partial t} + \frac{\partial F(W)}{\partial x} + C = 0 \qquad (2.17)$$

Unfortunately, the system of equations does not have a general analytical solution, hence numerical methods have been proposed to obtain an approximate solution.

2.7 Discretizing the domain

As mentioned before, it is not possible to obtain an analytical and continuous solution as function of time t and space coordinate x. It is necessary to introduce some approximations. The first approximation is to accept that we will only get a numerical solution, which will satisfy, with a certain accuracy, our system of equations in the domain. However, we cannot solve the equations in all the infinite points of a continuum. Hence the second approximation is the discretization of the domain, accepting that the numerical solution will be available only in a finite number of points. As represented in Figure 2.2, depending on the level of refinement requested when dividing the domain, the number of computational nodes changes. Of course, the more refined the discretization is, the more accurate the solution [20]. Both because a smaller numerical error is introduced and because a refined mesh reduces, by definition, the global "approximation".
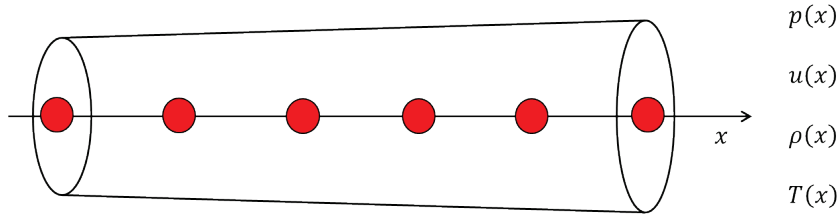

Figure 2.2 - Discretization of the 1D domain.

2.8 From the solution to the state variables

Let's assume for a moment that we have our solution at a given time step. Here it is shown how the actual solution in terms of the fundamental variables is obtained. The technique consists of the combination of the element of the solution array which contains the unknown and the use of the equation of state. Of course, other combinations which exploit the components of the solutions array are possible.

$$\frac{W[1]}{F} = \frac{\rho F}{F} = \rho \qquad \frac{W[2]}{W[1]} = \frac{\rho u F}{\rho F} = u \qquad \frac{W[4]}{W[1]} = \frac{\rho Y F}{\rho F} = Y$$

$$\left(F(W)[2] - \frac{W[2] * W[2]}{W[1]}\right)/F = \left((\rho u^2 + p)F - \frac{\rho u F * \rho u F}{\rho F}\right)/F = p \qquad \frac{p}{\rho R} = T$$

For completeness, the last thermodynamic useful variables, the speed of sound a, is obtained as:

$$\sqrt{k\left(F(W)[2] - \frac{W[2] * W[2]}{W[1]}\right)/W[1]} = \sqrt{k\left((\rho u^2 + p)F - \frac{\rho u F * \rho u F}{\rho F}\right)/\rho F} = \sqrt{k\frac{pF}{\rho F}} = \sqrt{k\frac{p}{\rho}} = \sqrt{kRT} = a$$

2.9 Numerical methods

Now are described the numerical methods used to solve the system of equations. The first, also historical, approach is the so called the "Method of Characteristics" (MOC) extensively described in [21,22,23]. It was proposed before the exponential growth in computational capabilities, so it was a simple and graphical method which could be also graphically implemented. The MOC is only first order accurate due to the underlying linearization, hence more accurate methods based on the finite difference technique have been developed, mainly the Lax-Wendroff or MacCormack schemes. However, the MOC allows to resolve the boundary conditions and accurately transmit the pressure wave information between 1D domains, while the finite difference methods cannot be easily applied on the boundary conditions. Recently the numerical

developments have been focused on increasing the conservation capabilities and on the ability of capturing sharp solutions such as shock waves. In this chapter we will focus on these modern methods which are currently used in the Gasdyn program, mainly the Corberán-Gascon (CG) and the "1D Cell" methods [24] which will be presented in the next paragraphs. These new methods have also tackled the challenge of using larger meshes and tried to limit the unstable behaviour typical of 2nd order accurate methods.

2.9.1 The Method of Characteristics

This method is based on the transformation of the hyperbolic system of conservation equations from partial derivatives to total derivatives along lines traceable in the flow field, of x and t coordinates, called characteristic lines [25,26]. The method starts rearranging the original system of equation to express each equation in this form:

$$\begin{cases} \dfrac{\partial \rho}{\partial t} + \dfrac{\partial (\rho u)}{\partial x} + \dfrac{\rho u}{F}\dfrac{dF}{dx} = 0 \\[2mm] \dfrac{\partial u}{\partial t} + u\dfrac{\partial u}{\partial x} + \dfrac{1}{\rho}\dfrac{\partial \rho}{\partial x} + G = 0 \qquad\qquad + pv = RT \\[2mm] \left(\dfrac{\partial p}{\partial t} + u\dfrac{\partial p}{\partial x}\right) - a^2\left(\dfrac{\partial \rho}{\partial t} + u\dfrac{\partial \rho}{\partial x}\right) - (k-1)\rho(\dot q + uG) = 0 \end{cases} \qquad (2.18)$$

By a linear combination of these equations, it is possible to rewrite the equations isolating the following structures: $(u + a)$, $(u - a)$ and (u).

$$\begin{cases} \left[\dfrac{\partial p}{\partial t} + (u+a)\dfrac{\partial p}{\partial x}\right] + \rho a\left[\dfrac{\partial u}{\partial t} + (u+a)\dfrac{\partial u}{\partial x}\right] + \Delta_1 + \Delta_2 + \Delta_3 = 0 \\[2mm] \left[\dfrac{\partial p}{\partial t} + (u-a)\dfrac{\partial p}{\partial x}\right] - \rho a\left[\dfrac{\partial u}{\partial t} + (u-a)\dfrac{\partial u}{\partial x}\right] + \Delta_1 + \Delta_2 - \Delta_3 = 0 \\[2mm] \left[\dfrac{\partial p}{\partial t} + u\dfrac{\partial p}{\partial x}\right] - a^2\left[\dfrac{\partial \rho}{\partial t} + u\dfrac{\partial \rho}{\partial x}\right] + \Delta_1 = 0 \end{cases} \qquad (2.19)$$

where Δ_1, Δ_2 e Δ_3 are respectively:

$$\Delta_1 = -(k-1)\rho(\dot q + uG) \qquad \Delta_2 = \frac{\rho u a^2}{F}\frac{dF}{dx} \qquad \Delta_3 = \rho a G \qquad (2.20)$$

If no friction and heat transfer is present, the flow is isentropic and the term Δ_1 is zero. The term Δ_2 instead is zero if no area variation is present while Δ_3 is zero only if no friction is present. The three equations can be rewritten by considering the following three space-time equations, which correspond to the two velocities of propagation of a pressure wave and of a mass impulse:

$$\frac{dx}{dt} = u + a \qquad\qquad \frac{dx}{dt} = u - a \qquad\qquad \frac{dx}{dt} = u \qquad (2.21)$$

Along these lines it is possible to apply the "compatibility" conditions and, only along these lines, to perform the substitution and obtain the following equations only in terms of their total derivatives:

$$\begin{cases} \dfrac{dp}{dt} + \rho a\dfrac{du}{dt} + \Delta_1 + \Delta_2 + \Delta_3 = 0 \\[2mm] \dfrac{dp}{dt} - \rho a\dfrac{du}{dt} + \Delta_1 + \Delta_2 - \Delta_3 = 0 \\[2mm] \dfrac{dp}{dt} - a^2\dfrac{d\rho}{dt} + \Delta_1 = 0 \end{cases} \qquad (2.22)$$

To better understand the MOC method, the hypothesis of homentropic flow is added, i.e., the absence of friction on the walls, heat exchange and section variation; in this way, since the three terms Δ_1, Δ_2 and Δ_3 are null, the three equations can be simplified and rewritten as follows:

$$dp + \rho a\, du = 0 \qquad\qquad dp - \rho a\, du = 0 \qquad\qquad p - a^2 d\rho = 0 \qquad (2.23)$$

If the fluid is a perfect gas and isentropic (as just mentioned), the isentropic transformation, combined with the speed of sound relationship give us:

$$\frac{p}{\rho^k} = const \qquad \text{and} \qquad a^2 = \frac{kp}{\rho} \qquad \rightarrow \qquad \frac{p}{p_0} = \left(\frac{a}{a_0}\right)^{2k/k-1} \qquad (2.24)$$

So that differentiating:

$$\frac{p}{p_0} = \left(\frac{a}{a_0}\right)^{2k/k-1} \qquad \text{Differentiating} \qquad \frac{dp}{p} = \frac{2k}{k-1}\frac{da}{a} \qquad (2.25)$$

which substituted in previous simplified equations gives the expression of the *Riemann* invariants (J_+ and J_-). For an isentropic flow, along the respective characteristic line, this quantity is constant.

$$du + \frac{2}{k-1}da = 0 \quad \rightarrow \quad d\left(u + \frac{2}{k-1}a\right) = dJ_+ = 0 \quad \rightarrow \quad J_+ = const$$

$$du - \frac{2}{k-1}da = 0 \quad \rightarrow \quad d\left(u - \frac{2}{k-1}a\right) = dJ_- = 0 \quad \rightarrow \quad J_- = const$$

$$(2.26)$$

Until now no approximation has been performed on the equations, they have been simply rewritten. Considering the complete form of the compatibility equations for the non-homentropic flow, the *Riemann* variables are no longer constant and are called *Riemann* variables:

$$dJ_+ = \frac{(k-1)}{2}\frac{T}{a}ds - \frac{(k-1)}{2\rho a}[\Delta_1 + \Delta_2 + \Delta_3]dt \neq 0 \qquad \rightarrow \qquad \begin{array}{l} J_{+,new} = J_{+,old} + dJ_+ \\ J_{-,new} = J_{-,old} + dJ_- \end{array} \qquad (2.28)$$

$$dJ_- = \frac{(k-1)}{2}\frac{T}{a}ds - \frac{(k-1)}{2\rho a}[\Delta_1 + \Delta_2 - \Delta_3]dt \neq 0$$

Since dJ_+ and dJ_- are not equal to zero, the *Riemann* variables, along the characteristic lines in the space-time domain, change by this infinitesimal quantity. Hence the new value of the *Riemann* variable along the characteristic line at the next time step can be evaluated.

We can observe that the three characteristic equations contain four variables: p, a, u, ρ. It is very useful to introduce an additional equation, in order to express the three equations as function of only three variables a, u and a_A, where the last one is the sound speed obtained with an isentropic expansion or compression to a reference pressure p_{ref}, as presented in Figure 2.3 below.
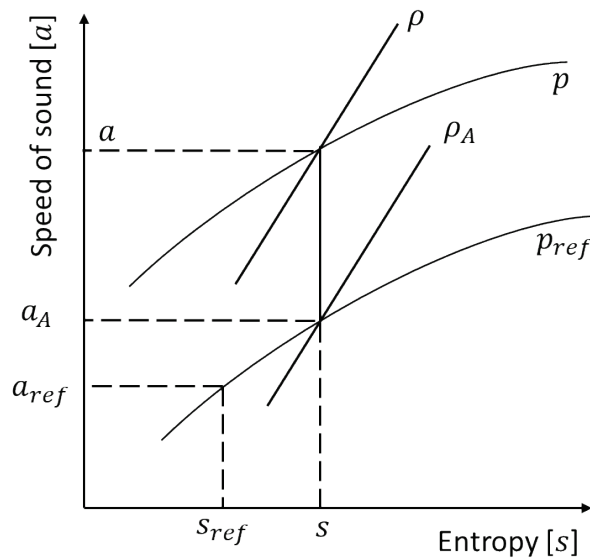

Figure 2.3 - Figure highlighting an isentropic expansion on the entropy-speed of sound diagram.

The reference values of each quantity ($p_{ref}, a_{ref}, u_{ref}, x_{ref}$) are introduced to work with non-dimensional variables and can be arbitrarily fixed. The relationship between λ, β, a and u still holds, the dimensional *Riemann* invariants are replaced by their non-dimensional value.

$$p_{ref}, a_{ref}, u_{ref}, x_{ref} \qquad A = \frac{a}{a_{ref}} \quad U = \frac{u}{a_{ref}} \quad A_A = \frac{a_A}{a_{ref}} \quad Z = \frac{a_{ref} * t}{x_{ref}} \quad X = \frac{x}{x_{ref}}$$

In non-dimensional form, the *Riemann* invariants can be obtained and are called λ and β. A useful relationship allows to evaluate the state variables from the *Riemann* variables:

$$\int_1^2 da \pm \frac{k-1}{2} \int_1^2 du = 0 \quad \rightarrow \quad \begin{aligned} \lambda &= A + \frac{k-1}{2} U \\ \beta &= A - \frac{k-1}{2} U \end{aligned} \quad \rightarrow \quad \begin{aligned} A &= \frac{\lambda + \beta}{2} \\ U &= \frac{\lambda - \beta}{k-1} \end{aligned} \qquad (2.27)$$

Considering a perfect gas, the following isentropic relationship is valid:

$$\frac{p}{\rho^k} = cost \quad \rightarrow \quad \frac{\rho}{\rho_A} = \left(\frac{p}{p_{ref}}\right)^{1/k} \quad \rightarrow \quad \frac{p}{p_{ref}} = \left(\frac{a}{a_A}\right)^{2k/(k-1)}$$

Along the isobaric transformation:

$$ds|_p = \frac{dh}{T} = \frac{c_p dh}{h} \qquad h = c_p T = \frac{kRT}{k-1} = \frac{a^2}{k-1} \qquad \frac{dh}{h} = \frac{2da}{a} \quad \rightarrow \quad ds|_p = 2c_p \frac{da}{a} \qquad (2.29)$$

Integrating the $ds|_p$ and rearranging we obtain:

$$A_A = \frac{a_A}{a_{ref}} = e^{\frac{s - s_{ref}}{2c_p}}$$

Where A_A represents the so-called "entropy level", the non-dimensional equivalent of a_A. With the above relations, it is possible to express the complete compatibility equations for the two characteristic equations $dx/dt = u \pm a$ as:

$$d\lambda = A \frac{dA_A}{A_A} - \frac{(k-1)}{2} \frac{AU}{F} \frac{dF}{dX} dZ - (k-1) \frac{f}{D} x_{ref} U^2 \frac{U}{|U|} \left[1 - (k-1)\frac{U}{A}\right] dZ + \frac{(k-1)^2}{2} \dot{q} \frac{x_{ref}}{a_{ref}^3} \frac{1}{A} dZ$$

where $dX = dx/x_{ref}$ and $dZ = dt/z_{ref}$. In the equation above, the following terms can be identified, corresponding to a different source of irreversibility:

$$d\lambda = \delta\lambda_{entropy} + \delta\lambda_{area} + \delta\lambda_{friction} + \delta\lambda_{heat\ transfer}$$

Regarding the last compatibility equation for the characteristic line $dx/dt = u$, the resulting formula is:

$$dA_A = \frac{k-1}{2} \frac{A_A}{A^2} \left(\frac{\dot{q} x_{ref}}{a_{ref}^3} + \frac{2f x_{ref}}{D} |U^3|\right) dZ \qquad \text{or} \qquad dA_A = \delta A_{A,heat\ transfer} + \delta A_{A,friction}$$

The third compatibility equation allows to track the entropy level variation along its characteristic line $dx/dt = u$ and evaluate $A_A^{new} = A_A^{old} + dA_A$.

2.9.2 The mesh MOC

It is now introduced how the MOC is implemented on a general grid of discrete computational nodes. When this method is applied to a 1D grid mesh, it is often referred as the "mesh" MOC. When applying the method everything is known at the starting time step, the goal is to evaluate the unknowns λ, β and A_A at each node at the next time step. We will assume that the time step size is given (the time step size determination is discussed in the next paragraph). With the help of Figure 2.4 below it is possible to visualize the numerical method. The mesh size is usually around $1\ cm$.
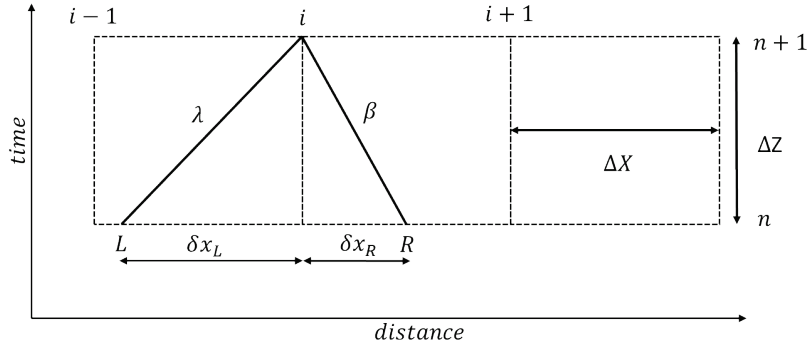
Figure 2.4 – Method of characteristics (MOC) numerical scheme reference.

The method is based on linear interpolation between mesh nodes to evaluate the gas-dynamic variables. Hence, the *Riemann* variables between the nodes can be interpolated to estimate the value of the *Riemann* variable that, traveling along its characteristic line backward in time (see Figure 2.4) from time t_{n+1}, will end on the node positions L and R at the previous time step t_n:

$$\lambda_L^n = \lambda_i^n - \frac{\delta X_L}{\Delta X}(\lambda_i^n - \lambda_{i-1}^n) \qquad \beta_R^n = \beta_i^n - \frac{\delta X}{\Delta X}(\beta_{i+1}^n - \beta_i^n) \qquad (2.30)$$

Hence, by definition of characteristic line:

$$\frac{\delta X_L}{\Delta X} = U_L^n + A_L^n \qquad\qquad \frac{\delta X_R}{\Delta X} = U_R^n - A_R^n \qquad (2.31)$$

it is demonstrated that it is possible to obtain the terms $\delta X / \Delta X$ as function of the *Riemann* variables at current time step:

$$\frac{\delta X_L}{\Delta X} = \frac{a\lambda_i^n - b\beta_i^n}{\frac{\Delta X}{\Delta Z} + a(\lambda_i^n - \lambda_{i-1}^n) - b(\beta_i^n - \beta_{i-1}^n)} \qquad \frac{\delta X_R}{\Delta X} = \frac{a\beta_i^n - b\lambda_i^n}{\frac{\Delta X}{\Delta Z} + a(\beta_i^n - \beta_{i-1}^n) - b(\lambda_i^n - \lambda_{i-1}^n)}$$

Where:

$$a = \frac{k+1}{2(k-1)} \qquad\qquad b = \frac{3-k}{2(k-1)}$$

Once determined λ_L^n and β_R^n, the corresponding compatibility equations are used to compute the new timestep value λ_L^{n+1} and β_R^{n+1}.

The entropy level is instead simply interpolated depending on the direction of the flow, as depicted by the Figure 2.5 below. To compute A_i^{n+1} and A_{i+1}^{n+1} (or A_{i-1}^{n+1} if the velocity is in the opposite direction) the corresponding compatibility equation is used.

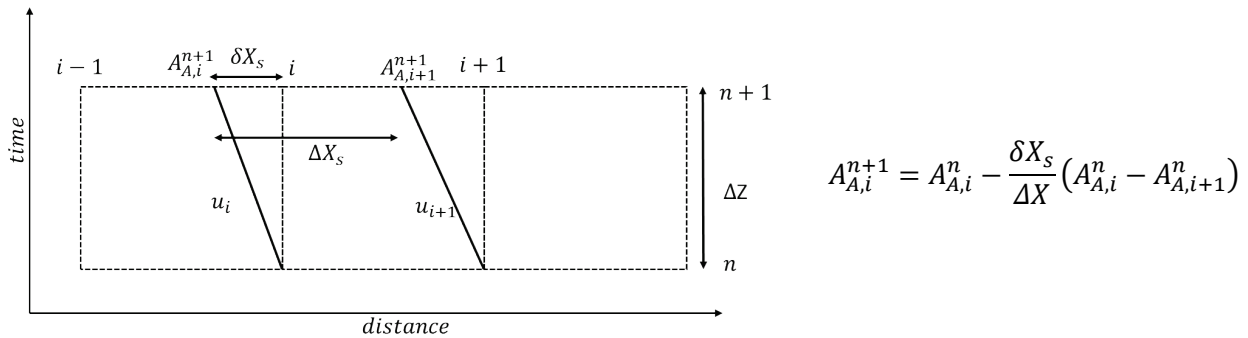$$A_{A,i}^{n+1} = A_{A,i}^n - \frac{\delta X_s}{\Delta X}(A_{A,i}^n - A_{A,i+1}^n)$$

Figure 2.5 - Method of characteristics (MOC) entropy level scheme.

The method is applied in the interior nodes of the pipe, where a left and right node always exist. Instead, on the boundaries the left or right nodes are missing by construction. Hence, on the boundaries the method can

be applied to determine only one of the two *Riemann* variables. In addition, a boundary condition is needed to achieve the solution, as described in the next paragraphs. Currently, the MOC is used to solve the boundary conditions, and is hence applied to the pipe boundaries. The internal part of the pipes is solved by the finite difference methods described in the following section.

2.9.3 Determining the appropriate timestep

As described above, the MOC is an explicit method. The determination of the time step is crucial to ensure stability of the explicit numerical method. The time step size is established by the *Courant-Friedrichs-Lewy* [27] condition: once defined the CFL, as:

$$CFL = \frac{\Delta t}{\left(\frac{\Delta x}{a + |u|}\right)} \leq 1$$

this condition must be true for all calculation nodes. This means that the maximum time step is determined by the most limiting node, hence the one with smallest mesh size and higher speed of sound a and speed of the gas u. To implicitly consider both the right and left pressure waves, the gas velocity is considered with its magnitude. This criterion guarantees that any characteristic line starting from one side of the mesh doesn't exit the other side of the mesh before being detected by the neighbour node. This condition requires that information, in the form of disturbances or waves, cannot travel more than one mesh length in one calculation time increment.

2.9.4 The finite difference method

It is now described the numerical method which is currently used to solve the 1D domain. In particular, the starting point is the same system of equation obtained for the MOC. We can start by integrating the general formulation presented in the previous chapter of the system of equations for the infinitesimal slice of 1D fluid, which now becomes a control volume centred on the node, hence its boundaries, across which the fluxes F occur, are at positions $i - 1/2$ and $i + 1/2$.

$$\int_x \int_t \left(\frac{\partial W}{\partial t} + \frac{\partial F(W)}{\partial x} + C\right) dx \, dt = 0 \tag{2.32}$$

To better understand the scheme the following Figure 2.6 is presented:
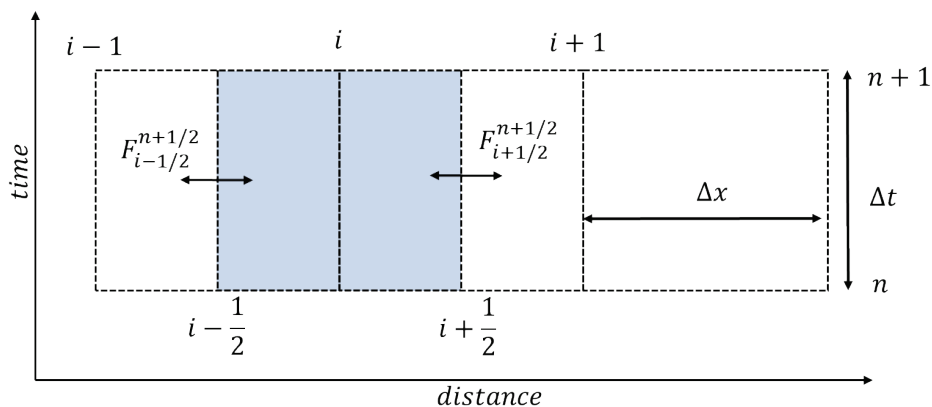

Figure 2.6 - Shifted control volume and numerical method discretization scheme.

The integration on the single control volume gives the following discretized equation:

$$\left(W_i^{n+1} - W_i^n\right)\Delta x + \left(F_{i+1/2}^n - F_{i-1/2}^n\right)\Delta t + C_i^n \Delta x \Delta t = 0 \tag{2.33}$$

19

Now the quantities represent their average value on the mesh: the W_i is the average value of the conserved variable in the domain between $i - 1/2$ and $i + 1/2$ and F now depicts the average fluxes on the cross-section. This control volume integration guarantees the conservation on each volume and on the whole domain, since the global conservation is ensured by the single volume's conservation. For simplicity the source terms C are assumed to be zero. The equation can be rewritten isolating the new time step solution:

$$W_i^{n+1} = W_i^n + \frac{\Delta t}{\Delta x}\left(F_{i+1/2}^n - F_{i-1/2}^n\right) \tag{2.34}$$

To find the new time step solution, we must estimate the fluxes. A simple strategy is to assume:

$$F_{i+1/2}^n = (F_i^n + F_{i+1}^n)/2 \qquad\qquad F_{i-1/2}^n = (F_i^n + F_{i-1}^n)/2 \tag{2.35}$$

In this way the equation becomes:

$$W_i^{n+1} = W_i^n + \frac{\Delta t}{\Delta x}\frac{(F_{i-1}^n - F_{i+1}^n)}{2} \tag{2.36}$$

Unfortunately, this makes the method very unstable, to smooth the method behaviour it was suggested to replace the previous time step value with the average:

$$W_i^{n+1} = \frac{(W_{i-1}^n + W_{i+1}^n)}{2} + \frac{\Delta t}{\Delta x}\frac{(F_{i-1}^n - F_{i+1}^n)}{2} \tag{2.37}$$

This simple method has also a first order accuracy since the method is still linearizing unknown quantities with neighbouring nodes information. However, this method is simple starting point to show the logic behind these finite difference methods. This method is also called "symmetric" since it is not biased by the flow direction, which instead an "upwind" method would do. It is now described the current and most recent method used in the solver of the Gasdyn code: the Gascon-Corberán (or CG) method.

2.9.5 The Gascon-Corberán numerical method

This method, which takes the name from the original authors, was proposed in [28,29,30,31]. It is an explicit, symmetric, finite difference method. It is possible to implement a first or second order accuracy method. The fundamental points are similar to the Lax-Wendroff method, the difference is mainly in the evaluation of fluxes F. The method is supposed to solve equation of the type:

$$w_t + f(w)_x = s(w, x) \tag{2.38}$$

This is the scalar version of the usual system of equations. First, like in the Lax-Wendroff the conserved quantities are evaluated at half of the time step and at a half of the distance between the nodes:

$$w_{i+\frac{1}{2}}^{n+\frac{1}{2}} = \frac{1}{2}[w_i^n + w_{i+1}^n - \lambda(f_{i+1}^n - f_i^n) + \frac{\Delta t}{2}(s_{i+1}^n - s_i^n)] \qquad \text{where} \qquad \lambda = \frac{\Delta t}{\Delta x} \tag{2.39}$$

Hence, the actual solution at the new time step is obtained as:

$$w_i^{n+1} = w_i^n - \lambda\left(f_{i+1/2}^{n+1/2} - f_{i-1/2}^{n+1/2}\right) + \frac{\Delta t}{2}(s_{i+1/2}^{n+1/2} + s_{i-1/2}^{n+1/2})]$$

Which is also similar to the Lax-Wendroff scheme, the difference is in the evaluation of the $f_{i\pm1/2}^{n+1/2}$ and $s_{i\pm1/2}^{n+1/2}$. The CG method introduces an additional equation to solve (2.38) as a homogeneous equation, hence:

$$w_t + f'(x, w)_x = 0 \tag{2.40}$$

This is achieved by introducing the following quantity $g(x, w)$ and $b_{i,j}(x, w)$ defined as:

$$g(x, w) = f(w) - \int_0^x s(y, w(y, t))dy \qquad b_{i,j}(x, w) = -\int_{x_i}^{x_j} s(y, w(y, t))dy \qquad g(x, w) = f(w) + b(x, w) \tag{2.41}$$

Replacing this into equation (2.40) we can obtain that:

20

$$w_i^{n+1} = w_i^n - \lambda \left(g_{i+1/2}^{n+1/2} - g_{i-1/2}^{n+1/2} \right) \tag{2.42}$$

Where the term $g_{i\pm1/2}^{n+1/2}$ is obtained as a Taylor expansion:

$$g_{i\pm1/2}^{n+1/2} = \frac{1}{2}(g_i^n + g_{i+1}^n - \lambda * \left.\frac{\partial g}{\partial w}\right|_{i+1/2}^n * (g_{i+1}^n - g_i^n)) \tag{2.43}$$

It is observed how this scheme is second order accurate, extending the Lax-Wendroff method and returning to it for $g = f$. Being second order accurate, the issue of spurious oscillations is present, and an artificial viscosity term is introduced to stabilize the method. For the homogeneous system:

$$w_t + f(w)_x = 0 \tag{2.44}$$

A Total Variation Diminishing (TVD) scheme of this type is used:

$$w_i^{n+1} = w_i^n - \lambda(\tilde{f}_{i+1/2} - \tilde{f}_{i-1/2}) \tag{2.45}$$

where these artificial fluxes $\tilde{f}_{i\pm1/2}$ are calculated as:

$$\tilde{f}_{i+1/2} = \frac{1}{2}[f_i^n + f_{i+1}^n - \frac{1}{\lambda}Q\alpha_{i+1/2}^n(w_{i+1}^n - w_i^n)] \quad \text{and} \quad \alpha_{i+1/2}^n = \lambda\left.\frac{\partial f}{\partial w}\right|_{i+1/2}^n = \begin{cases} \lambda\frac{(f_{i+1} - f_i)}{(w_{i+1} - w_i)} \\ \lambda\left.\frac{\partial f}{\partial w}\right|_i^n \quad if \; w_{i+1} - w_i = 0 \end{cases}$$

and $Q(x)$ is a function to tune the numerical viscosity. It has been shown that this scheme is TVD if:

$$|\alpha| \le Q \le 1$$

Parallelly, for this equation: $w_t + g(x, w)_x = 0$ this scheme is proposed: $w_i^{n+1} = w_i^n - \lambda(\tilde{g}_{i+1/2} - \tilde{g}_{i-1/2})$, Where the artificial fluxes $\tilde{g}_{i\pm1/2}$ are (similarly to the $\tilde{f}_{i\pm1/2}$) defined as:

$$\tilde{g}_{i+1/2} = \frac{1}{2}[g_i^n + g_{i+1}^n - h(\alpha_{i+1/2}^n + \beta_{i+1/2}^n)(g_{i+1}^n - g_i^n)] \quad \text{and} \quad \beta_{i+1/2}^n = \begin{cases} \lambda\frac{b_{i,j}}{(w_{i+1} - w_i)} \\ 0, if \; w_{i+1} - w_i = 0 \end{cases}$$

$h(x)$ is the equivalent of $Q(x)$. Harten [28], hence showed that the scheme can be written as:

$$w_i^{n+1} = w_i^n - C_{i+1/2}^+(w_{i+1}^n - w_i^n) - C_{i-1/2}^-(w_i^n + w_{i-1}^n)] \tag{2.46}$$

Where $C_{i+1/2}^+$ and $C_{i-1/2}^-$ are function of w_i^n and w_{i+1}^n, for which ensures the scheme is TVD:

$$C_{i+1/2}^+ \ge 0 \qquad\qquad C_{i-1/2}^- \ge 0 \qquad\qquad C_{i+1/2}^+ + C_{i-1/2}^- \le 1$$

The final step is to evaluate w_i^{n+1} combining the previous equations:

$$w_i^{n+1} = w_i^n - \frac{\lambda}{2}[(g_i^n + g_{i+1}^n) + (g_i^n + g_{i-1}^n) - h(\alpha_{i+1/2}^n + \beta_{i+1/2}^n)(g_{i+1}^n + g_i^n) + h(\alpha_{i-1/2}^n + \beta_{i-1/2}^n)(g_i^n + g_{i-1}^n)]$$

Which reduces to the (2.46) for:

$$C_{i+1/2}^+ = \frac{1}{2}[(\alpha_{i+1/2}^n + \beta_{i+1/2}^n)(h(\alpha_{i+1/2}^n - \beta_{i+1/2}^n) - 1] \qquad C_{i-1/2}^- = \frac{1}{2}[(\alpha_{i+1/2}^n + \beta_{i+1/2}^n)(h(\alpha_{i+1/2}^n - \beta_{i+1/2}^n) + 1]$$

The method is further extended by Harten [28] with a proper second order formulation, adding a series of terms containing the second derivatives:

$$w_t + f_x - s = \frac{1}{2}[(\alpha + \beta)(h - 1)](\Delta x)(f_{xx} - s_x) + O(\Delta x^2) \tag{2.47}$$

This is not directly applied but another scheme is developed:

$$w_t + (g + \varphi)_x = 0 \qquad\qquad \text{where} \qquad\qquad \varphi = \frac{1}{2}[(\alpha + \beta)(h - 1)](\Delta x)g_x \tag{2.48}$$

The authors [28] also propose to evaluate $\tilde{g}_{i+1/2}$ as:

$$\tilde{g}_{i+1/2} = \frac{1}{2}[g_i^n + g_{i+1}^n + \varphi_i^n + \varphi_{i+1}^n - h(\alpha_{i+1/2}^n + \beta_{i+1/2}^n + \gamma_{i+1/2}^n)(g_{i+1}^n - g_i^n + \varphi_{i+1}^n - \varphi_i^n)]$$

where:

$$\gamma_{i+1/2}^n = \begin{cases} \lambda \dfrac{\varphi_{i+1}^n - \varphi_i^n}{(w_{i+1} - w_i)} \\ 0, if\ w_{i+1} - w_i = 0 \end{cases} \qquad and \qquad \varphi_i^n = \begin{cases} s_{i+\frac{1}{2}} min(\varphi_{i+1/2}^n, \varphi_{i-1/2}^n) \\ 0, if\ s_{i+1/2} \neq s_{i-1/2} \end{cases} \qquad (2.49)$$

where:

$$s_{i+\frac{1}{2}} = sign(\varphi_{i+1/2}^n) \qquad and \qquad \varphi_{i+1/2}^n = \frac{1}{2}[(\alpha_{i+1/2}^n + \beta_{i+1/2}^n)(h-1)](g_{i+1}^n - g_i^n) \qquad (4.50)$$

This new scheme is TVD under this modified CFL criteria:

$$CFL = max((\alpha_{i+1/2}^n + \beta_{i+1/2}^n + \gamma_{i+1/2}^n) \leq 1$$

2.9.6 The vectorial formulation of the Gascon-Corberán method

The proposed numerical method can be applied to scalar equations, but when it must be applied to a system of equations, some adjustments are needed. So, this section deals with how the equations are solved in the solver. Let's recall the vectorial formulation of the system of equations in its non-homogeneous form:

$$W_t + F(W)_x = S(x, W) \qquad (2.51)$$

where W_t is the column array containing the conserved quantities, $F(W)$ is the column array containing the respective fluxes while in $S(x, W)$ are present the corresponding source terms. Parallelly to the scalar case, also in the vectorial case the equation is manipulated defining:

$$G(x, w) = F(W) - \int_{x_i}^{x_j} S(y, W(y, t))dy \qquad\qquad B_{i,j}(x, W) = -\int_{x_i}^{x_j} S(y, W(y, t))dy \qquad (2.52)$$

If $S(\dots)$ is sufficiently smooth, $B = S$, and equation (2.51) can be written in a homogenous form:

$$W_t + G(x, W)_x = 0$$

The first step is to consider a linear equation with constant coefficients:

$$W_t + JW_x = 0 \qquad\qquad with \qquad\qquad J_{i,j} = \frac{\partial f_{i,j}}{\partial w_{i,j}} \forall\ i,j$$

It has been demonstrated that the Jacobian matrix J of a hyperbolic problem has three eigenvalues α_k and, in addition, a complete set of linearly independent right eigen vectors can be found. Hence, we have that:

$$J = PDQ \qquad\qquad with \qquad\qquad Q = P^{-1} \qquad\qquad and \qquad\qquad D = diag(\alpha_k)$$

Then equation (2.51) is multiplied by Q and a new matrix U is introduced and after substitutions:

$$(QW)_t + QJP(QW)_x = QS \qquad U = QW \qquad QJP = D \qquad \rightarrow \qquad U_t + D(U)_x = QS \qquad (2.53)$$

Since the matrix D is diagonal, the vectorial system (2.53) compactly represents a system of three scalar equations, linearly independent, which can be solved one by one as scalar equations shown in previous paragraph. The scheme is hence inherited from the scalar equations, starting from:

$$U_i^{n+1} = U_i^n - \lambda(\bar{G}_{i+1/2}^U - \bar{G}_{i-1/2}^U) \qquad (2.54)$$

Where the flux G is:

$$\bar{G}_{i+1/2}^U = \frac{1}{2}[G_{i+1}^U - G_i^U + \varphi_i + \varphi_{i+1} - h(\lambda\bar{D})(G_{i+1}^U - G_{i+}^U + \varphi_{i+1} - \varphi_i)] \qquad (2.55)$$

with:

$$G^U = QG = Q\left(F - \int_{x_i}^{x_j} S\right) = DU + QB$$

We can observe that the product $P \times Q = 1$, and multiplying (2.54) and (2.55) we obtain an explicit expression of W:

$$W_i^{n+1} = W_i^n - \lambda\left(\bar{G}_{i+1/2} - \bar{G}_{i-1/2}\right)$$

With:

$$\bar{G}_{i+1/2} = \frac{1}{2}[G_i + G_{i+1} + P_{i+1/2}(\varphi_i + \varphi_{i+1}) - P_{i+1/2}h(\lambda\bar{D})(Q_{i+1/2}(G_{i+1} - G_i) + \varphi_{i+1} - \varphi_i)]$$

Like the scalar case, also in the vectorial case the column array φ_i is defined as:

$$\varphi_i^k = \begin{cases} s_{i+1/2}^k \min\left(|\varphi_{i+1/2}^k|, |\varphi_{i-1/2}^k|\right) \\ 0, if\ s_{i+1/2}^k \neq s_{i-1/2}^k \end{cases} \qquad \text{with} \qquad s_{i+1/2}^k = sign(\varphi_{i+1/2}^k)$$

And

$$\bar{\varphi}_{i+1/2}^k = \frac{1}{2}(h(\lambda\bar{D})_{i+\frac{1}{2}} - (\lambda\bar{D})_{i+\frac{1}{2}})Q_{i+\frac{1}{2}}(F_{i+1} - F_i + B_{i,i+1})$$

In conclusion, the matrixes are computed as:

$$(\lambda\bar{D})_{i+\frac{1}{2}} = diag(\alpha_{i+\frac{1}{2}}^k + \beta_{i+1/2}^k) \qquad h(\lambda\bar{D})_{i+\frac{1}{2}} = diag(sign(\alpha_{i+\frac{1}{2}}^k + \beta_{i+\frac{1}{2}}^k)) \qquad Q_{i+\frac{1}{2}} = diag(sign(\alpha_{i+\frac{1}{2}}^k + \beta_{i+\frac{1}{2}}^k + \gamma_{i+1/2}^k))$$

Where:

$$\alpha_{i+1/2}^k = \lambda\frac{\partial f_{i+1/2}^k}{\partial u_{i+1/2}^k} \qquad\qquad \beta_{i+1/2}^k = \lambda\frac{\partial \beta_{i+1/2}^k}{\partial u_{i+1/2}^k} \qquad\qquad \gamma_{i+1/2}^k = \begin{cases} \lambda\dfrac{\varphi_{i+1}^k - \varphi_i^k}{\partial u_{i+1/2}^k} \\ 0\ if\ \partial u_{i+1/2}^k = 0 \end{cases}$$

Like the scalar case the vectorial scheme is TVD, under a similar condition. Summing up, the scheme is:

$$\bar{G}_{i+\frac{1}{2}} = \frac{1}{2}[F_i + F_{i+1} + B_{i,i+\frac{1}{2}} + B_{i,i+\frac{1}{2}} + P_{i+\frac{1}{2}}(\varphi_{i+1} + \varphi_i) - P_{i+\frac{1}{2}}h(\lambda\bar{D})_{i+\frac{1}{2}}(Q_{i+\frac{1}{2}}(F_{i+1} - F_i + B_{i,i+1}) + \varphi_{i+1} - \varphi_i)]$$

2.9.7 The Gascon-Corberán method applied

It is described now the application of the method to the system of equation describing the 1D flow in ICE engines, discussed in previous chapter. The system, was written as:

$$W_t + F(W)_x = S(x, W)$$

and the corresponding quantities are now:

$$W = W_t = \begin{bmatrix} \rho F \\ \rho u F \\ \rho e_0 F \end{bmatrix} \qquad F = F(W)_x = \begin{bmatrix} \rho u F \\ (\rho u^2 + p)F \\ \rho u h_0 F \end{bmatrix} \qquad C = S(x, W) = \begin{bmatrix} 0 \\ -p\dfrac{dF}{dx} + \rho GF \\ -\rho \dot{q} F \end{bmatrix}$$

Together with the last closing equation of perfect gas $pv = Rt$. The Jacobian is then:

$$J = \begin{bmatrix} 0 & 1 & 0 \\ \dfrac{k-3}{2}u^2 & u(3-k) & k-1 \\ u\left(\dfrac{(k-1)}{2}u^2 - H\right) & H - (k-1)u^2 & ku \end{bmatrix} \qquad \text{with:} \qquad H = \frac{a^2}{(k-1)} + \frac{u^2}{2}$$

With these three real eigen values α_k and the corresponding eigen vectors $P_{1,2,3}$:

$$\alpha_k = \begin{bmatrix} u - a \\ u \\ u + a \end{bmatrix} \qquad\qquad P = \begin{bmatrix} 1 & 1 & 1 \\ u - 1 & u & u + a \\ uH - ua & \dfrac{u^2}{2} & H + ua \end{bmatrix}$$

As shown above, the P matrix diagonalizes J with the following expression:

$$JQP = diag(u - a, u, u + a) \qquad Q = P^{-1} = \begin{bmatrix} -\dfrac{u}{2a} + \dfrac{(k-1)}{4}\dfrac{u^2}{a^2} & -\dfrac{1}{2a} - \dfrac{(k-1)}{2}\dfrac{u}{a^2} & \dfrac{(k-1)}{2a^2} \\ 1 - \dfrac{(k-1)}{2}\dfrac{u^2}{a^2} & (k-1)\dfrac{u}{a^2} & -\dfrac{(k-1)}{a^2} \\ -\dfrac{u}{2a} - \dfrac{(k-1)}{4}\dfrac{u^2}{a^2} & \dfrac{1}{2a} - \dfrac{(k-1)}{2}\dfrac{u}{a^2} & \dfrac{(k-1)}{2a^2} \end{bmatrix}$$

The new time step quantity is evaluated as:

$$W_i^{n+1} = W_i^n - \lambda\left(G_{i+1/2}^{TVD} - G_{i-1/2}^{TVD}\right) - \lambda(B_{i-1/2,i} + B_{i,i+1/2})$$

with:

$$G_{i+1/2}^{TVD} = \frac{1}{2}(F_i + F_{i+1} - B_{i,i+\frac{1}{2}} + B_{i+\frac{1}{2},i+1} - P_{i+\frac{1}{2}}h\lambda\overline{D}_{i+\frac{1}{2}}Q_{i+\frac{1}{2}}(F_{i+1} - F_i + B_{i,i+1}) + P_{i+1/2}\varphi_{i+1/2})$$

where $\varphi_{i+1/2}$ has the components:

$$\varphi_{i+1/2} = s_{i+1/2}^k \max\left(0, \min\left(\left|\overline{\varphi}_{i+\frac{1}{2}}^k\right|, s_{i+\frac{1}{2}}^k\overline{\varphi}_{i-\frac{1}{2}}^k, s_{i+\frac{1}{2}}^k\overline{\varphi}_{i+\frac{3}{2}}^k\right)\right)$$

with:

$$\overline{\varphi}_{i+\frac{1}{2}}^k = \frac{1}{2}(h(\lambda\overline{D})_{i+\frac{1}{2}} - \lambda\overline{D}_{i+\frac{1}{2}})Q_{i+\frac{1}{2}}(F_{i+1} - F_i - B_{i,i+1})$$

Regarding the matrix h, it is calculated as:

$$h(\lambda\overline{D})_{i+\frac{1}{2}} = diag(sign(\lambda\alpha_{i+\frac{1}{2}}^k, \lambda\beta_{i+\frac{1}{2}}^k))$$

where $\alpha_{i+\frac{1}{2}}^k$ are the eigen values, $\beta_{i+\frac{1}{2}}^k$ and the source terms $B_{i,i+1}$ are:

$$\beta = \frac{\left(\dfrac{1}{2a} + \dfrac{k-1}{2}\dfrac{u}{a^2}\right)\left(p\dfrac{dF}{dx} - \rho GF\right)\left(-\dfrac{k-1}{2a^2}\rho\dot{q}F\right)}{-\dfrac{1}{2a}\rho F\dfrac{\partial u}{\partial x} + \dfrac{1}{2a^2}\dfrac{\partial(pF)}{\partial x}} \qquad B_{i,i+1} = \begin{bmatrix} 0 \\ -p_{i+\frac{1}{2}}(A_{i+1} - A_i) + \Delta x(\rho GF)_{i+1/2} \\ -\Delta x(\rho\dot{q}F)_{i+1/2} \end{bmatrix}$$

where for example, the term $p_{i+\frac{1}{2}}$ is a simple arithmetic average:

$$p_{i+\frac{1}{2}}(A_{i+1} - A_i) = \frac{(p_{i+1} + p_i)}{2}(A_{i+1} - A_i)$$

The final step is to define the physical quantities between the calculation nodes $(i + 1/2)$. It is proposed to use the following approximations:

$$X_{i+1/2} = \sqrt{\frac{\rho_{i+1}A_{i+1}}{\rho_i A_i}} \qquad u_{i+1/2} = \frac{X_{i+1/2}u_{i+1} + u_i}{X_{i+1/2} + 1} \qquad H_{i+1/2} = \frac{X_{i+1/2}H_{i+1} + H_i}{X_{i+1/2} + 1}$$

$$\rho_{i+1/2} = \sqrt{\rho_{i+1}\rho_i} \qquad\qquad \rho_{i+1/2}A_{i+1/2} = \sqrt{A_{i+1}\rho_{i+1}\rho_i A_i}$$

2.10 Boundary conditions

The previous chapters have illustrated the two families of numerical methods which can be applied to the interior part of the 1D domain to be solved, hence all the nodes except the ones on the boundaries. It is now described the numerical method used to solve the boundaries [21,22]. In particular, the boundary conditions are solved at every timestep, assuming steady state conditions at each timestep. This is because the role of the boundaries is not to advance the solution in time but to "merge" the incoming solutions where two 1D domains are matching and be sure that mass, momentum, and energy are transferred correctly from one domain to the other and determine the 'boundary' nodes. Hence the boundary conditions are essentially driving the physical solution toward what is imposed at the boundary node.

The numerical method on which the solution of the boundary conditions relies is the MOC, because it is very convenient to exploit the MOC variables to correctly transfer the wave motion between 1D domains. Generally, the steady state conservation equations are written considering the boundary element under examination and transforming those equations in terms of the MOC variables (λ_{in}, A_{An}).

As presented in Figure 2.7, the MOC is applied to the pipe ends before solving the boundaries, to provide the boundaries with the input MOC variables and then apply the steady state solution to determine the missing variable λ_{out}, finding the correct entropy level on the boundary node. This is because, as explained before, on the boundary nodes the λ_{out} cannot be determined since a mesh does not exist outside the 1D domain. The entropy level instead can be determined for exiting flows but cannot be determine by this procedure for entering flows. Additionally, the actual flow direction at the next time step might change with respect to he current time step, due to the matching between the two incoming pressure waves. Moreover, where the flow is entering the pipe, the entropy level depends on the incoming flow and the transformations occurring to the flow, i.e., an expansion due to a section enlargement.
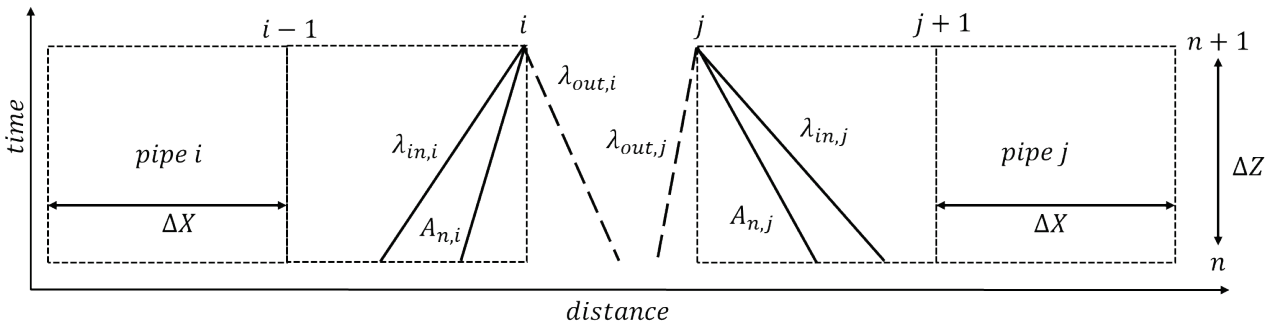

Figure 2.7 – Method of characteristic applied close to the boundary conditions.

2.10.1 Starred variables

When solving the boundary condition, the starred *Riemann* variables are used. A starred variable is defined by dividing the same variable by the corresponding entropy level A_A. Hence, the following definitions are obtained:

$$\lambda^* = \lambda/A_A \qquad\qquad A^* = A/A_A \qquad\qquad U^* = U/A_A$$

The non dimensional entropy level A_A can also be obtained as:

$$\frac{p}{p_{ref}} = \left(\frac{a}{a_A}\right)^{2k/(k-1)} = \left(\frac{a_{ref}}{a_A}\frac{a}{a_{ref}}\right)^{2k/(k-1)} = \left(\frac{1}{A_A}A\right)^{2k/(k-1)} \xrightarrow{yields} A_A = A \Big/ \left(\frac{p}{p_{ref}}\right)^{(k-1)/2k}$$

Hence, the definition of A^* becomes:

$$A^* = A/A_A = \left(\frac{p}{p_{ref}}\right)^{(k-1)/2k}$$

25

2.10.2 Junction boundary condition

As an example, the simple junction between pipes is presented. This boundary condition is very commonly used to model the connection between joining or leaving pipes when no preferential directionality of the flow is identified. The junction scheme is presented in Figure 2.8.
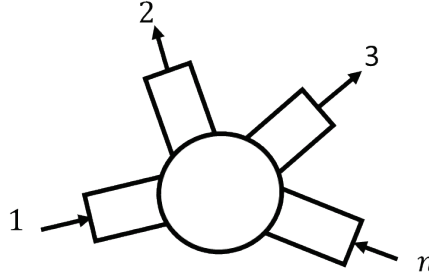

Figure 2.8 – Schematic model of a junction between n pipes.

The solution methodology has been proposed by Benson [21], where also reference about the other type of boundary conditions solution can be found. The following hypothesis are made regarding the junction: the pressure is constant where the pipes meet, the flow is steady state, and the fluid is a perfect gas. This means that:

$$p_1 = p_2 = p_n = \cdots = const \qquad \xrightarrow{yields} \qquad A_n^* = \left(\frac{p_n}{p_{ref}}\right)^{(k-1)/2k} = const$$

The mass conservation equation applied to the junction is:

$$\sum_1^n [\rho_n u_n F_n] = 0$$

Where F_n is the flow area, ρ_n is the density and u_n the flow velocity of each section facing the junction. The mass conservation equation can be rewritten in terms of the *Riemann* variables, isolating the A_n^* term:

$$A_n^* = \sum_1^n \left[\frac{F_n}{A_{A,n}} \lambda_{in,n}^*\right] \Big/ \sum_1^n \left[\frac{F_n}{A_{A,n}}\right]$$

It is now possible to evaluate the flow direction in each pipe calculating U_n^* from its definition:

$$U_n^* = \frac{2}{k_n - 1}\left(\lambda_{in,n}^* - A_n^*\right)$$

Once established the flow direction Benson proposes to calculate the entropy level of the exiting flows $A_{A,n,out}$ as a mass flow weighted average of the entering flows entropy levels, applying a sort of conservation of entropy, while the entering flow entropy level $A_{A,n,in}$ in not changed. The flow direction is established from the sign of U_n^*: positive entering the junction and vice versa. Hence $A_{A,n,out}$ is computed as:

$$A_{A,out} = \frac{\sum_1^{n,in} \dot{m}_n A_{A,n}}{\sum_1^{n,in} \dot{m}_n}$$

Where the mass flow of each section is computed as:

$$\dot{m}_n = \frac{A_n^{*\,2/(k_n-1)}}{A_{A,n}} U_n^* \left(\frac{k_n p_{ref}}{a_{ref}}\right) F_n$$

It is now possible to proceed, as indicated also by Winterbone [22], by correcting the incident *Riemann* variable, of the only pipes with exiting flow from the junction, as:

$$\lambda_{in,n,c}^* = A_n^* + \frac{A_{A,n}}{A_{A,out}}\left(\lambda_{in,n}^* - A_n^*\right)$$

The remaining missing variable can be computed from their definition:

$$\lambda_{in} = \lambda_{in,n,c}^* * A_{A,n} \qquad \lambda_{out,n} = A_{A,n}(2A_n^* - \lambda_{in,n,c}^*) \qquad A_{A,n,out} = A_{A,out}$$

The procedure is iterative, once the new value of λ_{in} is found, it is compared to the previous step calculation, and if the difference is within a certain tolerance (10^{-6}), the process is considered as solved. Otherwise, the calculation of A_n^* is repeated and the iterative cycle repeats. Starting from the current time step solution, typically a few iterations are usually needed, since the solution tend to change slowly time step after time step. However, in case of strong thermal discontinuities entering the junction, more iterations are usually needed, since the entropy levels of the flow are very different.

2.11 Timestep advancement

It is now described how the two numerical methods (CG-TVD and MOC) are used during the solution of a single timestep. The calculation loop is graphically presented in Figure 2.9. First the time step size is computed according to the gas properties in the whole domain and each cell dimension. Then the MOC is used on each pipe end, to determine the incoming λ_{in} and A_A reaching the boundary nodes at the next time step. Then the boundary conditions are solved and λ_{out} is computed on each pipe end, allowing to determine the solution W, F, C at the new time step in the boundary nodes. Then the numerical method is called to compute the solution in the internal nodes at the new timestep and the process is repeated. It is important to highlight that the boundary solution is considered by the numerical method at the following time step, because it will be part of the computational stencil when the next time advancement is considered.
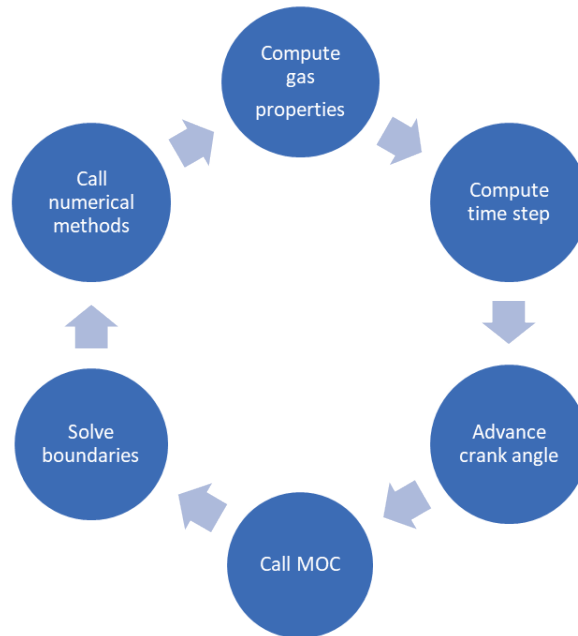

Figure 2.9 - Solver time step advancement chain of events.

2.12 Turbocharger modeling

It is here described how the turbocharger is modelled in the 1D engine simulations. The fluid dynamic boundary condition solution [21,22] relies on the steady state characteristic maps of the fluid machine, mainly its expansion or compression ratio characteristic map as function of the mass flow rate and rotational speed. The same maps for the efficiency are needed. The approach is the same for both the turbine and the

compressor. This approach allows to propagate the pressure waves through the boundary condition considering their respective reflection on the boundary. The maps are usually not well populated to be used on the whole range of instantaneous mass flow rates; hence the curves are extended with techniques proposed by literature [32,33] as shown in Figure 2.10. Moreover, usually manufacturer data have limited number of speed lines, hence the same technique are used to get additional speed lines.
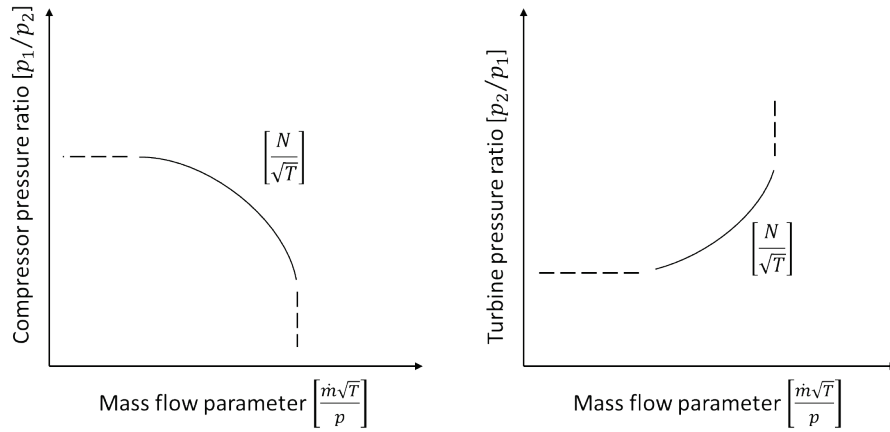

Figure 2.10 – Compressor and turbine maps extension.

The boundary condition solution algorithm used is the one presented in [22,23] and once the fluid dynamic solution is found it is possible to compute the power and torque at the turbocharger shaft. The turbocharger shaft speed is not fixed but depend on the instantaneous balance of torque at the shaft and on the inertia of the rotating ensemble. The turbocharger group inertia allows to compute the shaft acceleration. This occurs every time step since the boundary is solved at each time step. It is possible to do a cyclic approach, but it has been found that negligible difference in computational cost is obtained while having a nor realistic trend of shaft speed as function of time (cyclic steps). The turbocharger speed evolution is computed by the following equation:

$$N_{new} = N_{old} + \frac{(T_{torque} - C_{torque})}{2\pi J_{shaft}} dt$$

where J_{shaft} is the axial inertia of the turbocharger, which depends on the dimension of the turbocharger rotors. It is usually around $10^{-5} kgm^2$ for cars and light duty turbocharged engines. T_{torque} and C_{torque} are respectively the turbine and compressor torque.

Twin entry turbines are modelled as two half-sized turbines in parallel. Instead, Variable Geometry Turbines (VGT) are modelled as a different Fixed Geometry Turbine (FGT) for each opening percentage of the VGT. The characteristic maps are interpolated when operating at non defined opening percentage.

The control of FGT turbochargers is mainly performed by means of wastegate valves, which are modelled as valves connecting the upstream and downstream duct of the turbine boundary condition, controlling the mass flow bypass ratio and hence varying the expansion ratio through the turbine.

2.13 In-cylinder phenomena models

Combustion in ICE is a very complex phenomenon to describe as it involves both physical and chemical processes that have a stochastic and chaotic nature. In this chapter are described the main modelling approaches used in the 1D simulation field for the evaluation of the in-cylinder phenomena [34]. In this field the "phenomenological" models are used (also called Quasi-dimensional) and are based on the observation of the real world. These models subdivide the combustion chamber into different zones, each characterized

by different thermodynamic conditions such as temperature, pressure and composition. The cylinder is also modelled as a 0D volume with time-varying volume according to the kinematics of the piston, as function of the crank angle. The cylinder is fluid-dynamically coupled to the ducts external fluid dynamics only when any of the poppet valve is open. In this period the cylinder pressure and temperature depend on the exchange of mass and energy through the open valves. The heat exchange occurring with the walls of the cylinder is always present and the model proposed by Woschni is considered [35]. When the valves are closed combustion can take place.

In the SI combustion model the in-cylinder mixture is first divided into two zones, burned and unburned gas, separated by the flame front, which is assumed to be spherical and infinitesimally thin. The solution of mass and energy equations applied to the burned and unburned zone allows the computation of the pressure and temperature of the two zones. The burnt zone can be further divided into an arbitrary number of zones of equal mass, created during the combustion process. Each zone is spherical with its centre located on the spark plug position and exchanges heat with the cylinder walls, according to the respective wetted area. The chemical composition is computed in each zone, assuming uniform pressure in all the combustion chamber. A schematic of the multi-zone is illustrated in the following Figure 2.11.
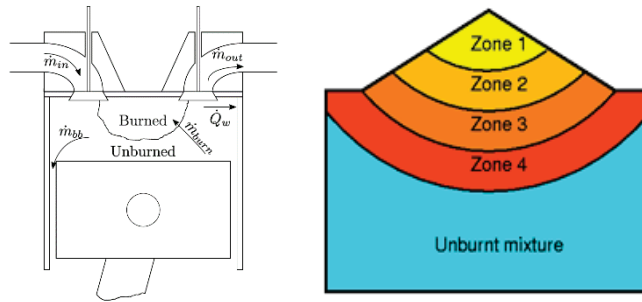
Figure 2.11 – 0D-quasiD schematic of the combustion chamber (left),
and sub-division into zones (right) by the thermodynamic SI combustion model.

For each zone, the mass and energy balance are written resulting in having the following system of partial differential equations:

$$\frac{dm}{dt} = \dot{m}_{in} - \dot{m}_{out} \mp \dot{m}_{burn} - \dot{m}_{bb} \qquad \frac{d(mu)}{dt} = -p\frac{dV}{dt} + \dot{Q} \mp \sum_i \dot{m}_i h_i \mp \dot{m}_{burn} h_u - \dot{m}_{bb} h_{bb}$$

$\dot{m}_{burn}$ is the mass of mixture burned in the unit of time by the flame which acts as coupling term, and $\dot{m}_{bb}$ is a term introduced to include the mass lost due to blow-by process in each zone. The values $\dot{m}_{in}$ and $\dot{m}_{out}$ represent the fresh mass entering in the cylinder during Intake Valve Opening (IVO) and the burned mass exiting from Exhaust Valve Opening (EVO). The variable h represents the enthalpy of a given zone. Moreover, the sum of the volumes of both zones must be equal to the instantaneous value of the cylinder volume.

The burning rate can be assigned by Wiebe combustion model functions [36] or computed by a predictive approach considering the in-cylinder conditions: pressure and temperature, thermodynamic and chemical properties of the gas, intensity of turbulence ($K - k$ turbulence model), chamber design and heat flux through the boundaries [37,38]. To simulate the combustion and the heat released by an air-fuel mixture, it is necessary to compute the burning rate of the mixture, starting from the laminar one. A_l is the surface of the laminar unstretched flame and u_l is the unstrained laminar velocity. Instead, by considering the wrinkling of the surface due to turbulence, the burning rate of the turbulent flame is similarly defined, and they are coupled:

$$\left(\frac{dm_b}{dt}\right)_l = \rho_u A_l u_l \qquad \left(\frac{dm_b}{dt}\right)_t = \rho_u A_t u_t \qquad \left(\frac{dm_b}{dt}\right)_t = \left(\frac{dm_b}{dt}\right)_l \frac{A_t}{A_l} \qquad \frac{A_t}{A_l} = \frac{S_t}{S_l}$$

The phenomenological models have the objective to estimate the additional contribution of turbulence to the laminar speed. It is assumed that the area ratio is equal to the respective flame speed ratio. The laminar flame speed S_l is calculated by means of correlations influenced by the mixture properties (temperature, pressure, residuals). The turbulent flame speed is instead computed by correlation depending on turbulent velocity u', mixture diffusivity k_u and integral length scale L_i and the laminar flame speed itself:

$$S_t = u'^{3/4} * L_i^{1/4} * S_l^{1/2} * k_u^{-1/4}$$

The turbulent velocity u' is evaluated with the two-equation model $K - k$ evaluating the turbulent kinetic energy k and the mean flow kinetic energy K [39]. Tabulated chemistry can also be exploited to compute look-up pre-calculated reaction rates and laminar flame speed from more complex 3D CFD simulations [40] in conditions where correlations are not applicable.

Regarding the CI engine combustion, a model has been developed to handle current multi-pulse injection systems, ensuring fast run-times [41,42]. Basically, the thermodynamic combustion model subdivides the chamber into three zones represented in Figure 2.12: fresh charge, fuel (vaporized) and burned gas, applying the first energy conservation law to compute the pressure and temperature variations.
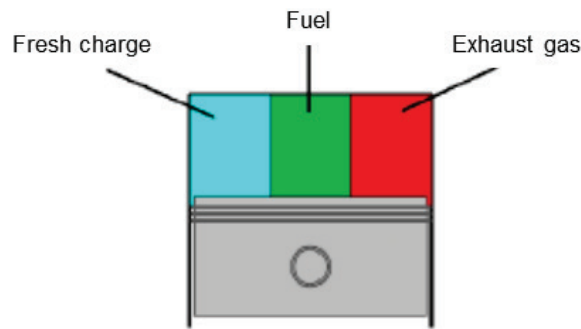
Figure 2.12 – 0D schematic of the mass in the combustion chamber,
split into three zones by the thermodynamic CI combustion model.

For what concerns the injection process, each discrete injection event is defined as a pulse. In this case the combustion rate is computed by means of multiple double-Wiebe laws. All the Wiebe law parameters are fixed as a function of the injection strategy, depending on the number of pulses and on the duration of the single pulse. Each pulse injected during the compression/combustion phases burns with a rate defined by the following expression (double Wiebe):

$$x_b = p\left\{1 - e^{\left[-\frac{(\theta-\theta_0)}{\alpha_1}\right]^{\beta_1}}\right\} + (1-p)\left\{1 - e^{\left[-\frac{(\theta-\theta_0)}{\alpha_2}\right]^{\beta_2}}\right\}$$

The first term into the brackets (1st Wiebe function) describes the premixed combustion phase, whereas the second term (2nd Wiebe function) describes the diffusive combustion phase. This non-predictive description application is represented in Figure 2.13, which points out how this equation can describe, with a rather good result, the computed burning rate, when compared to the experimental one.
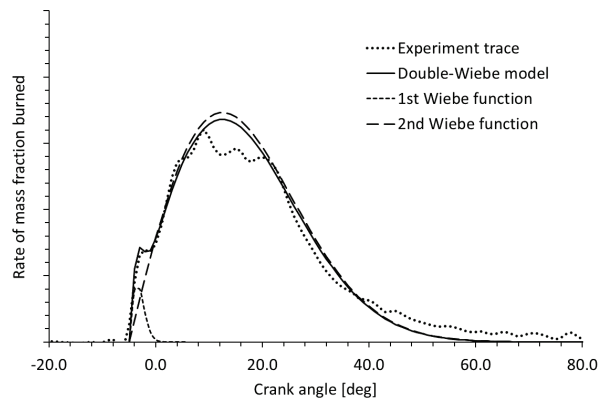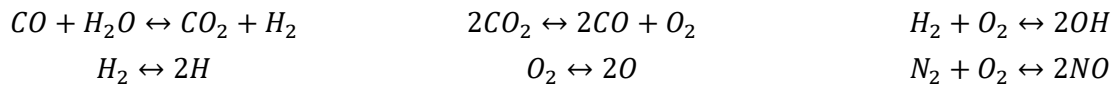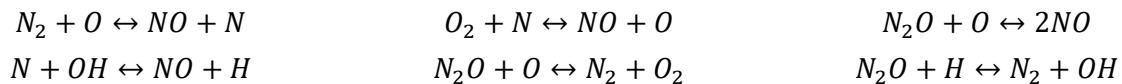
Figure 2.13 – Rate of burned mass fraction computed by means of the double-Wiebe function.

2.13.1 Pollutant formation and emissions

In this paragraph it is described how the different species of pollutants are computed to give the chemical composition at exhaust valve opening, hence the so-called cylinder-out emissions [43]. The Gasdyn code can predict the concentration of the main chemical species such as NO, CO, CO2, HC, O2, etc, during the combustion process and their concentration in the exhaust gases discharged by cylinders at EVO. In particular, the combustion model adopts an equilibrium approach to evaluate the concentrations of the major species (H2O, H, H2, CO, CO2, O, O2, OH, N2, NO) undergoing the following reactions:

$$CO + H_2O \leftrightarrow CO_2 + H_2 \qquad 2CO_2 \leftrightarrow 2CO + O_2 \qquad H_2 + O_2 \leftrightarrow 2OH$$
$$H_2 \leftrightarrow 2H \qquad O_2 \leftrightarrow 2O \qquad N_2 + O_2 \leftrightarrow 2NO$$

The resulting chemical equilibrium is correct for some species while other sub-models are used for the prediction of CO, NO and unburnt hydrocarbons (HC). The NO is evaluated resorting to the 6-reaction model proposed by Zeldovich [44,45] to predict the kinetically controlled formation of NOx which involves the following reactions:

$$N_2 + O \leftrightarrow NO + N \qquad O_2 + N \leftrightarrow NO + O \qquad N_2O + O \leftrightarrow 2NO$$
$$N + OH \leftrightarrow NO + H \qquad N_2O + O \leftrightarrow N_2 + O_2 \qquad N_2O + H \leftrightarrow N_2 + OH$$

This model, coupled to the discretization of the burnt charge mass gives a reliable and accurate prediction of the global NO_x emission. In this work, the CO concentration is evaluated by the model proposed by Baruah [43]. The CO is related to the actual equilibrium value CO_{eq}, the maximum CO_{max}, achieved in the combustion chamber. This simple model states:

$$CO = CO_{eq} + f_{CO}(CO_{max} - CO_{eq})$$

Where f_{CO} is a calibration coefficient between 0 and 1. However this method is not predictive and can be calibrated for a single operating point. The sub-model for unburned HC is based on the approach described in [46,47], the specific sub-model considers the storage and release of fresh mixture from the piston top land crevice and the absorption and desorption of hydrocarbons in the oil film layer, as presented in Figure 2.14. Another source of unburnt hydrocarbons, which may be relevant during cold start, is due to the flame quenching, and is considered by the combustion model when the model detects the flame extinguishes.
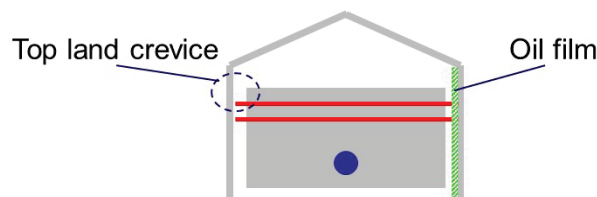

Figure 2.14 – Unburnt hydrocarbons (HC) sources.

3. 1D Internal Combustion Engine modelling

This chapter describes the modelling approach exploited to simulate an internal combustion engine. The simulation effort is focused on the fluid dynamic phenomena occurring along the intake and exhaust ducts and into the cylinder. In order to simulate the complete engine, the one-dimensional model is selected as the best compromise between zero-dimensional and 3D approaches.

3.1 1D ICE simulation procedure overview

The 1D model simulation assumes the gas state to be initialized at zero speed, constant pressure and temperature. The simulation starts from the EVO (Exhaust Valve Opening) of the cylinder number one; hence the zero crank angle is the top dead centre of cylinder number one. The engine speed is always fixed (steady operating point). Then the simulation starts computing the initial time step and at each time step the crank shaft is moved forward by an angle corresponding to the time step size at the current engine speed. Just to have a feeling of the order of magnitude of the time step and consequent time evolution of the simulation, it is reported below an example of time step calculation and corresponding crank angle advancing:

$$dt = \frac{dx}{a + |u|} \approx \frac{10^{-2}[m]}{(10^2 + 0)\left[\frac{m}{s}\right]} = 10^{-4} = 0.0001\,[s]$$

$$d\alpha = \frac{dt * N * 360}{60} = \frac{10^{-4}[s] * 10^3 \left[\frac{rev}{min}\right] * 360 \left[\frac{deg}{rev}\right]}{60\left[\frac{s}{min}\right]} \approx 0.6\,[deg]$$

Where dt is the time step, a is the gas speed of sound, u is the gas flow speed, N is the engine speed. The resulting advancement of crank angle is $d\alpha$.

It is evident why this class of 1D models is also referred to as "crank angle resolved", since often the time step duration corresponds to a fraction of the crank angle. Of course, the actual simulation time depends on the physical time simulated and how fast the solution at each time step is computed. However, it is important to highlight the order of magnitude of the model time steps and what are the quantities controlling the size of the time step. The mesh size is determined by the discretization of the domain, and its magnitude strongly influences the time step size. Instead, the gas speed of sound is typically due to the hot gas on the exhaust side, which cannot be chosen. Once the time step size is calculated, the engine speed determines how much the crank angle is advanced. It is important to highlight that the time step continuously varies during the simulation, as well as the engine speed (for different operating points).

As presented by Figure 3.1 the solution then proceeds invoking the numerical solution at the current time step, as described in the dedicated chapter about the numerical methods used to solve the 1D conservation equations. The data needed by the boundary conditions are obtained applying the method of characteristics on each pipe end. Then all the boundaries are solved to provide the pipe end conditions for the numerical method, which can solve the interior part of the ducts. At each time step all the boundaries are solved, this requires also to identify if the valves of the cylinders are open or closed and eventually start the combustion calculation.

With the crank shaft movement, the pistons are also moved and the volume in the combustion chamber is updated considering the actual cinematic mechanism. It is important to highlight that, when all the valves of a cylinder are closed, the in-cylinder solution is decoupled from the fluid dynamic solutions in the pipes: the code essentially performs the combustion arriving until the conditions at EVO, then when the fluid dynamic calculation reaches the EVO angle, the combustion result is transferred into the fluid dynamic simulation, with the dedicated valve boundary conditions at any time step, when the valves are open. During the engine cycle the data needed for output is tracked.

The start of a new cycle is identified when the actual crank angle is lower than the advancement angle and the output quantities are printed or calculated, and the next cycle starts. This repeats until convergence is reached. In an unsteady simulation convergence is trivial, since the time-step convergence loses its meaning. The fluid dynamic solution is by nature 'unsteady', hence a true constant solution between time steps cannot be achieved.

However, in the case of IC engines, the cyclic and periodic nature of the volumetric machine simulated helps identifying the engine cycle, as a period in which the solution should repeat itself cycle after cycle. In this case, convergence is reached, and the simulation can switch to the next operating point to be simulated. The solution continues from the previous fluid dynamic solution, only the engine speed is instantly modified.
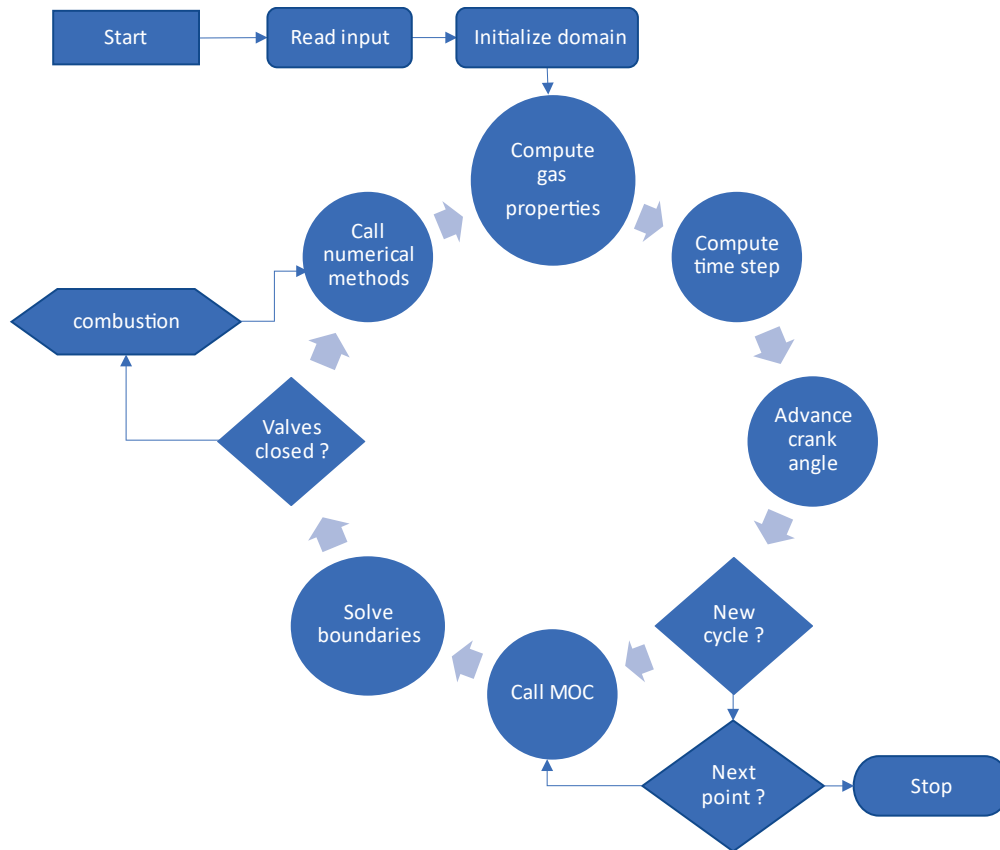
Figure 3.1 - High level computational procedure for the simulation of the 1D ICE model.

The only difference occurring when a driving cycle is simulated is that convergence is never reached and each cycle is, in principle, the first cycle of a new operating point which stops after one engine cycle.

3.2 1D modelling tool

The informatic tools used to model IC engines and to simulate them is GASDYN. The software has been developed at Politecnico di Milano, within the Internal Combustion Engine research group (see Figure 3.2), in the last 25 years and consists of a pre-processor and a numerical solver. The pre-processor allows to build the engine model with its architecture and geometrical dimension, connecting the 1D and 0D elements. During the pre-processing phase, the combustion model must also be chosen and set up. Moreover, at this stage, it is necessary to configure the desired operating conditions of the engine and the simulation which is requested. Once everything is set, the pre-processor generates input files which are used by the numerical solver. The solver, ones executed, reads the input file and starts the simulation procedure described in the previous chapter. The solver also writes the simulation output files from which the performance, emission and fluid dynamic solutions can be analysed. Within this complex framework, the main contribution described

in this thesis is related to the improvements of the numerical solvers, boundary conditions models and interconnectivity features, as explained in the following chapters.

Figure 3.2 - Logo of the research group within the Politecnico di Milano and logo of the software.

3.3 1D models of the use case engines

In this chapter it is described how the actual 1D models of the two engines presented in this thesis have been obtained. The goal was to reproduce as well as possible the real engine they represent. The two engines have been developed separately since they are completely different. The most important aspect for a satisfactory modelling is to ensure that the engine architecture is correctly reproduced, hence the main components of the engine should be considered. The process of building the 1D model of an engine starts from gathering the data needed by the modelling tool, mainly geometrical data, asking the manufacturer the dimensions or photos of the components used on the engine. It is also important to gather the widest range of experimental data available, to choose the most suitable sub-model to be configured in the model and then perform an extended validation.

As presented in the next paragraph, the two engines modelled are very different in size, application and working principles, covering a wide, but not complete, range of the ICE family. However, the methodology developed can be applied to any IC engine, provided that the underlying mathematical models are developed. For both engines the refined discretization consists in a uniform 1 cm mesh. The models have also been constructed according to the data gathered during the experimental instrumentation, which also provided the data for the validation of the models. For example, the spark advance data was measured at fixed operating conditions and used by the 1D model as an input parameter. This is why the information in the model reflect the same operating points investigated experimentally.

3.3.1 3-cylinder passenger car spark ignition engine

This is a 1liter, GDI, three-cylinder turbocharged, SI engine. The engine is a modern and consolidated kind of powertrain for currently produced passenger cars, often coupled to a mild hybrid configuration. This engine has been proposed for the project activity by the "VISION-xEV" project partner Renault SAS. The engine is equipped with an EU6d compliant aftertreatment system. However, the engine has been instrumented by the project partner colleagues in Valencia (UPV-CMT), which provided the engine data and experimental values for the validation activity. The engine features a single-entry fixed geometry turbocharger, with an electronically controlled wastegate valve. The throttle body is placed between the compressor and the cylinders before the intake manifold splitting. It was very helpful to have some photos, like the ones reported here in Figure 3.3, of the actual engine parts for modelling the geometry of the exhaust ducts. Regarding the valve lift profile and their timing, the engine manufacturer has shared the data needed, together with the flow coefficients of the poppet valves.
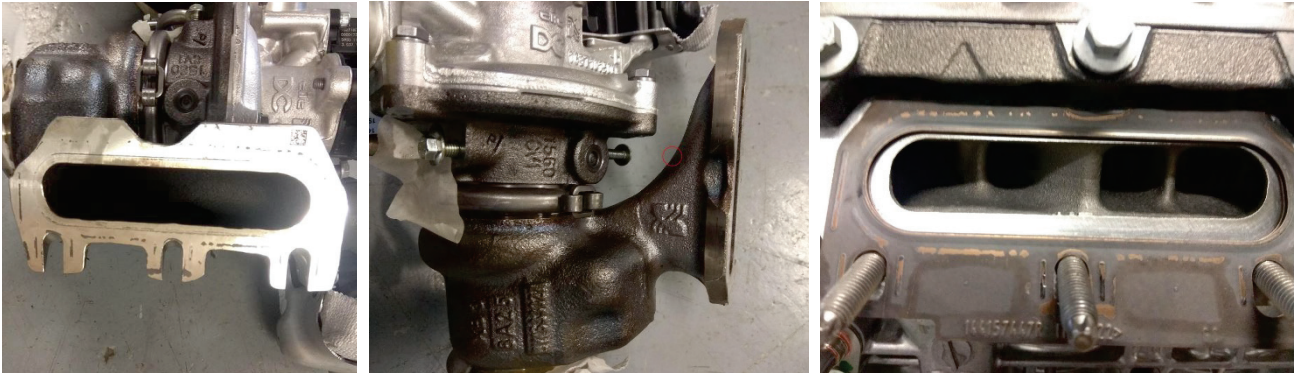
Figure 3.3 - Photos of the engine configuration, exhaust manifolds and turbine, courtesy of UPV-CMT.

The final 1D engine model obtained is reported in Figure 3.4 below. In the model can be immediately spotted the intake and exhaust side, the turbocharger with the by-pass wastegate valve, the intercooler, and the throttle body. The injectors are connected to the cylinders indicating the fuel is injected directly in the combustion chamber, as GDI engines. The spark ignition engine requires a lambda value to be assigned for each operating point simulated, this was available from the measurements. The same applied for the spark advance value, which must be set. The combustion chamber is a classical 165° pent-roof shape. The blue dots in the scheme are PID controllers used to control the engine during the simulation.

Three PIDs are present: one controls the throttle plate position, to adjust the brake torque of the engine; one controls the wastegate opening, to adapt the boost pressure and another one controls the intercooler wall temperature, to act on the charge cooling. Each PID is connected to a sensor and an actuator, to sense the target parameter and actuate the control variable. The control is cyclic.

The main data of the engine are reported in the Table 3.1:

Quantity	Value	Unit of measure
Bore x Stroke	72.2 x 81.3	mm x mm
Rod Length	132.5	mm
Number of Cylinders	3 in line	-
Firing order	1 - 2 - 3 (0 - 240 – 480)	# (Crank angle degree)
Displacement	999	cm^3
Compression Ratio	11.0	-
Valves per Cylinder	4	-
EVO - EVC	93° - 402°	Degrees (after TDC)
IVO - IVC	334° - 624°	Degrees (after TDC)
Maximum Brake Torque	180 @ 2250 rpm	Nm
Maximum Brake Power	85 @ 5250 rpm	kW
Rotational Speed Range	750 ÷ 6250	rpm
Fuel	Gasoline SP95 – E10	-

Table 3.1 - Main data regarding the 3-cylinder 1 Litre spark ignition engine.

In the model, the catalyst is modelled as several parallel ducts representing the channels. Only one of these ducts is simulated and the boundary conditions takes care of merging the solution to the neighbour pipes, by multiplying the single duct contribution by the input number of channels.

The engine friction, or friction mean effective pressure (FMEP), imposed to the 1D model has been computed as the difference between experimental values of IMEP and BMEP, where the IMEP has been derived integrating the indicated cycle measured experimentally for each operating point.
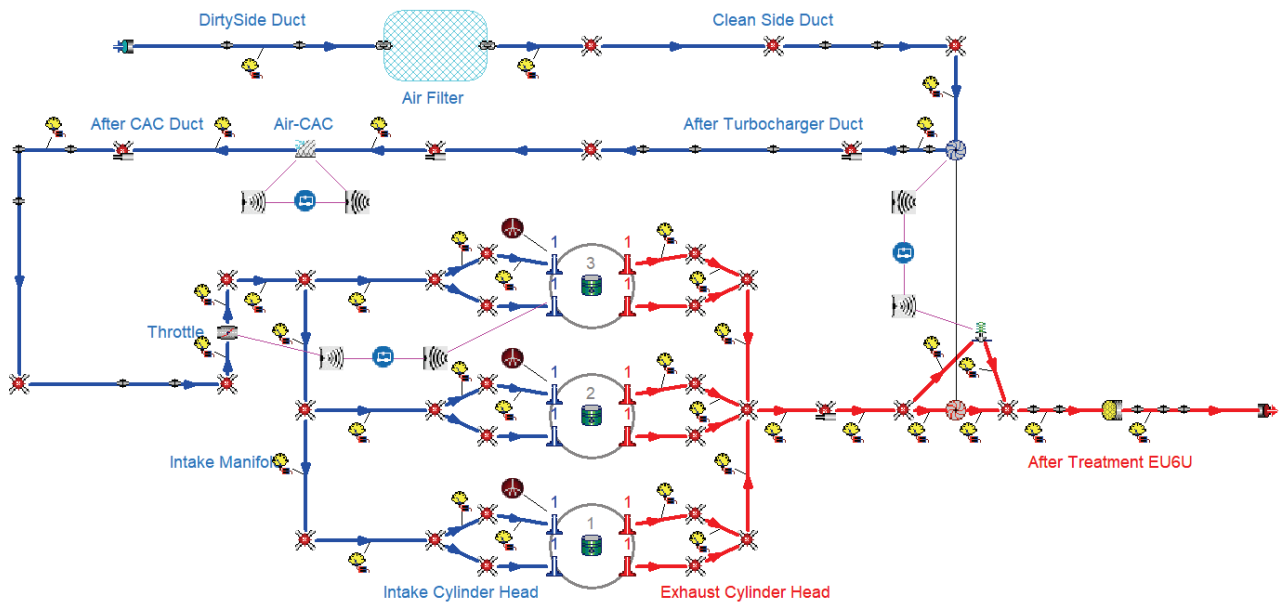
Figure 3.4 – Gasdyn 1D ICE model of the 3-cylinder spark ignition engine.

The correct modelling of the exhaust manifold was very important, to capture the shape of the exhaust pulses transmitted to the turbine. Thanks to an STL file of the part reported in Figure 3.5, it was possible to take measurements and obtain a 1D model of this very complicated geometry. The GT-Power schematic of the same engine was also available and was used to have a starting schematic of the final model.

Figure 3.5 - Exhaust manifolds Standard Tessellation Language object (STL) of the engine under examination.

The turbocharger is another very important component which requires a careful modelling, to guarantee a good simulation of the boosted operating points. First, the data regarding the boost pressure has been obtained from the experimental measurements and is shown in Figure 3.8. Then the compressor and turbine maps have been obtained from the manufacturer data sheet. These manufacturer's maps are typically very limited, since the machines are characterized over a limited range of operating conditions and for very few points. Hence, it was needed to interpolate between known speed lines and to extrapolate the curves to achieve the maps of Figure 3.6 and 3.7.
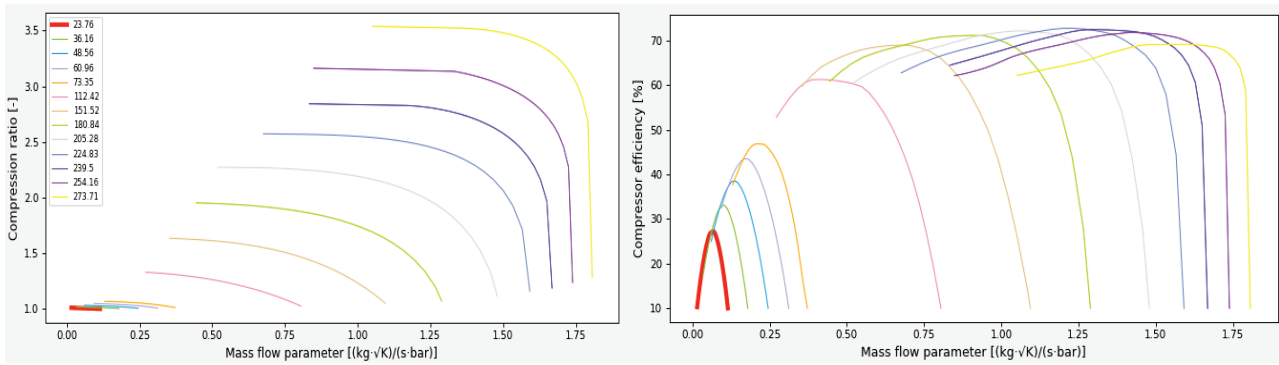
Figure 3.6 - Compressor maps for use in the 1D model: compression ratio (left) and efficiency (right).
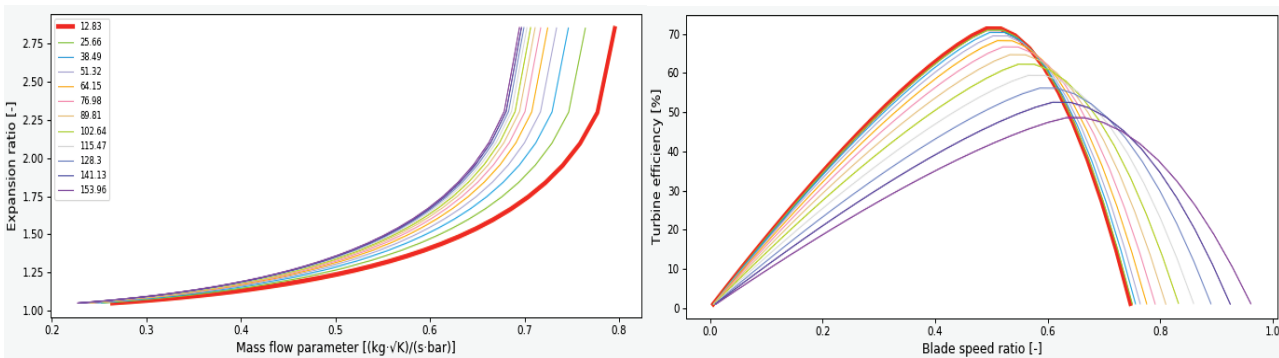
Figure 3.7 - Turbine maps for use in the 1D model: expansion ratio (left) and efficiency (right).
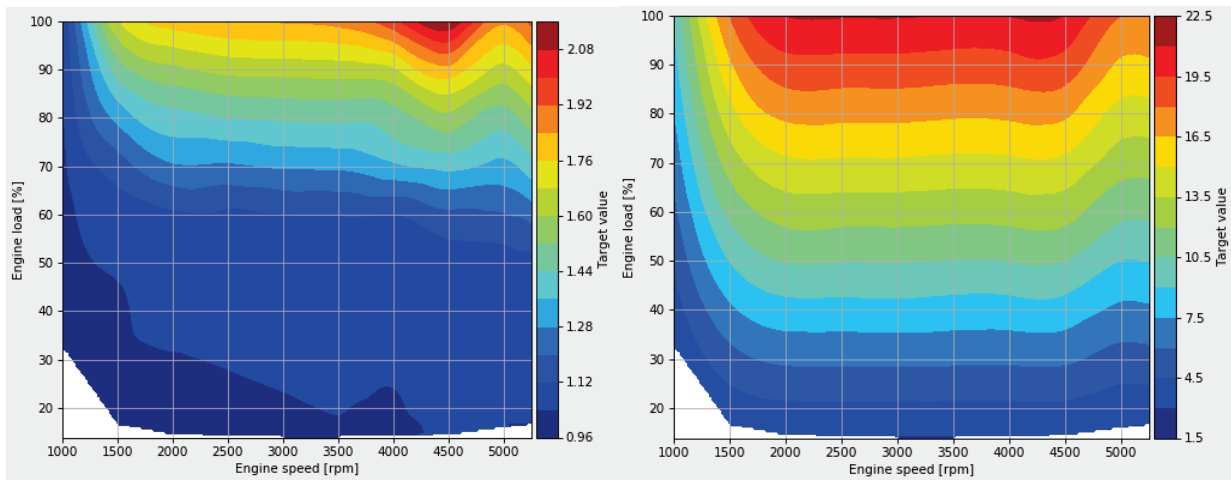
Figure 3.8 – Target boost pressure [bar] (left) and target BMEP [bar] (right).

With regard to the valve timings and lift profiles, the manufacturer data has been exploited and is reported in Figure 3.9. The intake and exhaust lifts are equal, with a small effective overlap. The engine is also equipped with a variable valve timing (VVT) system which allows to change both the intake and exhaust camshaft phase with respect to the crankshaft. The map of the setting of the VVT system is presented in Figure 3.10.
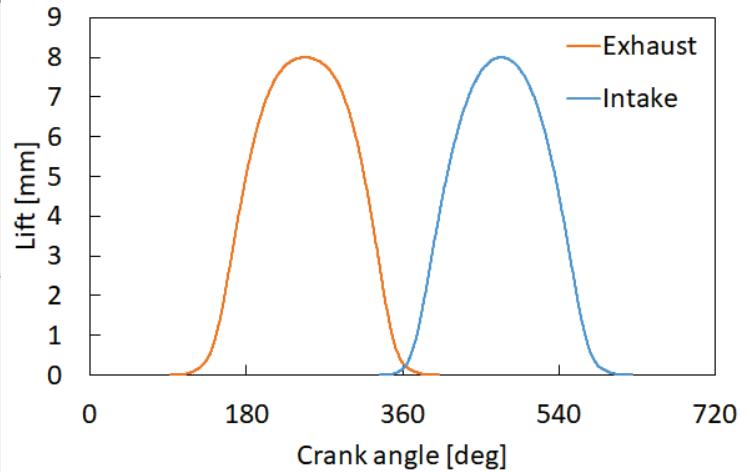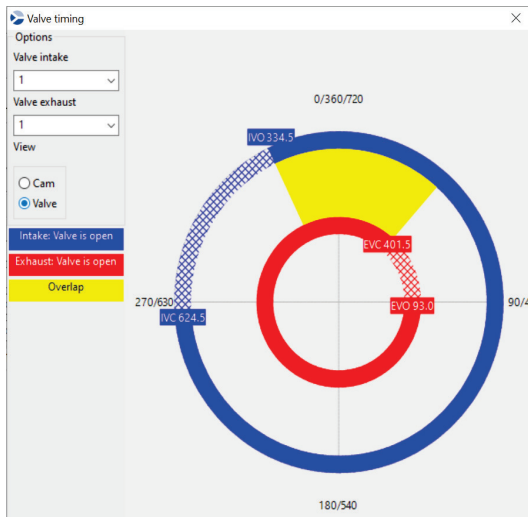
Figure 3.9 - Valve timing (left) and lift profiles (right) of the 3-cyclinder spark ignition engine.
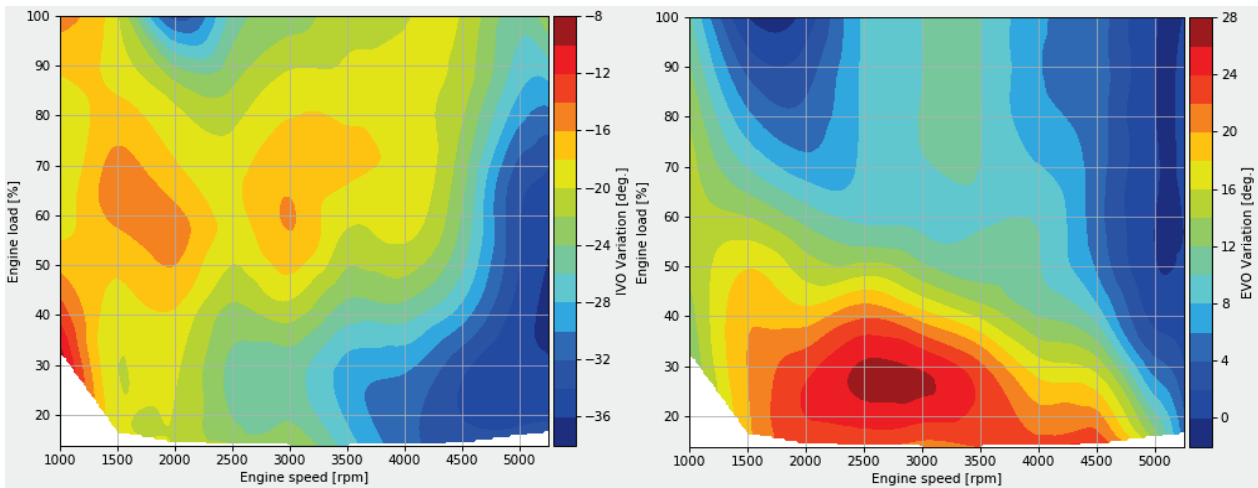
Figure 3.10 - Variable valve timing configuration, IVO variation (left) and EVO variation (right).

Lastly, the very important information regarding the mixture preparation in the combustion chamber. The required data to set up the combustion model are the lambda and the spark advance value. The data on the whole engine map was shared by the manufacturer and is presented in Figure 3.11. As expected the spark advance increases as the engine speed increases and load reduces. The lambda values, measured by UPV and sused for the modle set up, instead show an engine running mostly in rich conditions with slightly lean mixture only at low load. This is probably to limit the production NO_x emission at the expense of higher fuel consumptions. However it is acknowledged that this calibration could make the engine non-compliant with EU6d limit.
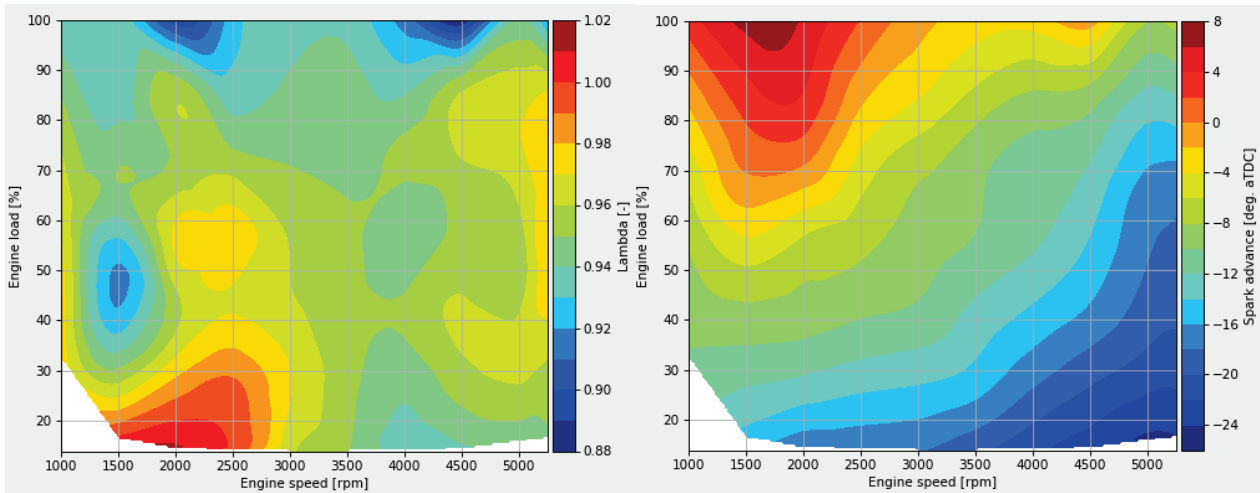
Figure 3.11 - Combustion data: lambda (left) and spark advance (right).

3.3.2 6-cylinder heavy duty compression ignition engine

This is an in-line 6-cyclinder, turbocharged, CI engine for heavy duty application, i.e., a passenger bus. The engine features a twin entry, fixed geometry turbine; Table 3.2 below reports the main engine characteristics used to build the 1D engine schematic. Once again, the manufacturer (FPT) provided all the requested data regarding the engine and turbocharger to set-up a predictive 1D model.

Quantity	Value	Unit of measure
Bore x Stroke	104 x 132	mm x mm
Rod Length	195	mm
Number of Cylinders	6 in line	-
Firing order	1-5-3-6-2-4 (0-120-240-360-480-600)	# (Crank angle degree)
Displacement	6728	cm^3
Compression Ratio	17	-
Valves per Cylinder	4	-
EVO - EVC	129° - 373°	Degrees (after TDC)
IVO - IVC	339° - 593 °	Degrees (after TDC)
Maximum Brake Torque	1010 @ 1250 rpm	Nm
Maximum Brake Power	210 @ 2200 rpm	kW
Rotational Speed Range	600 ÷ 2600	rpm
Fuel	Diesel B0	-

Table 3.2 - Main data of the 6-cylinder Diesel engine.

In Figure 3.12 below is reported the 1D model developed in the Gasdyn Graphical User Interface (GUI), like the previous engine. The engine does not feature a variable valve timing. It can be noticed how the wastegate by-pass is modelled. Like in the real engine, the mass flow rate from the engine is discharged only from one of the exhaust manifolds leading to the turbine. The fuel injectors are connected to the engine cylinders since the diesel fuel is injected directly in the combustion chamber. The combustion chamber is a classical cylindrical shape.

A very important data for the combustion model is the injection pressure, which determines the fuel injection characteristics. The rail injection pressure and the start/end of the pilot and main injections were provided from the manufacturer. Being a CI engine, no throttle valve element is present in the engine.
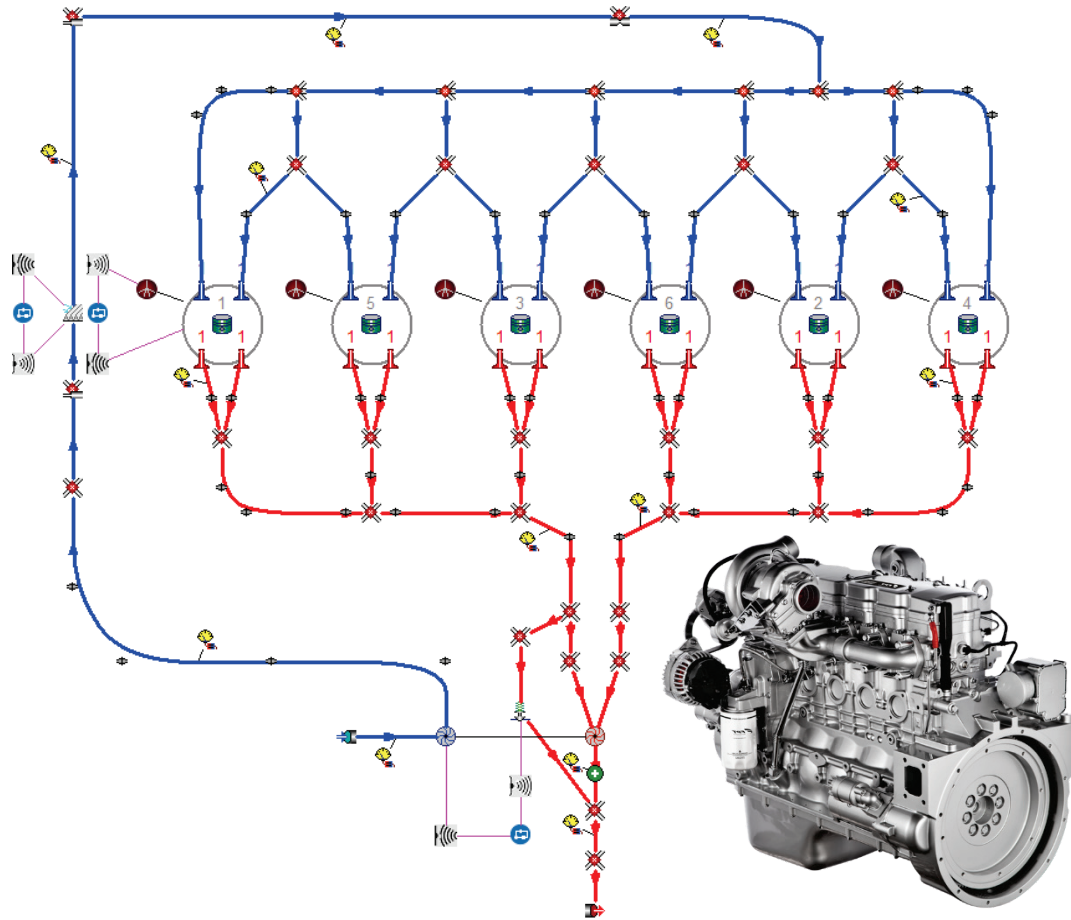
Figure 3.12 - 1D model developed in Gasdyn of the 6-cylinder compression ignition engine.

The blue dots in the schematic, like the previous schematic, represent the PID controllers used to control the engine during the simulation. Like in the previous engine model, three PIDs are adopted. One controlling the boost pressure by changing the wastegate opening, one controlling the gas temperature after the intercooler and one controlling the injected fuel per cylinder per cycle.

The peculiarity of this engine is the twin-entry fixed geometry turbine. The turbine boundary is solved as if two half-sized turbines were in place. Each turbine has its own distinct inlet and outlet. On the exhaust side, there are two pipes connected to the turbine. The compressor and turbine characteristics map, after the elaboration started from the manufacturer data are presented in Figure 3.13 and 3.14. It can be noticed the larger size of the turbocharger comparing these maps with the corresponding maps of the much smaller 3-cylinder spark ignition engine previously presented.
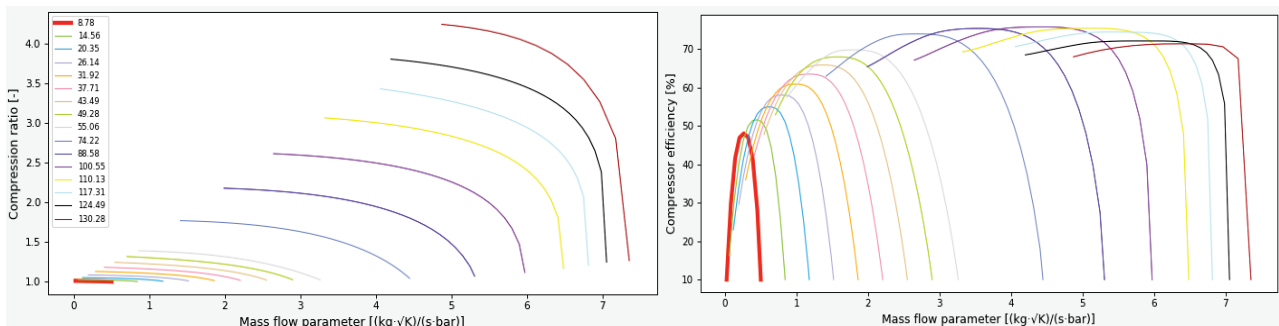
Figure 3.13 - Compressor maps for use in the 1D model: compression ratio (left) and efficiency (right).
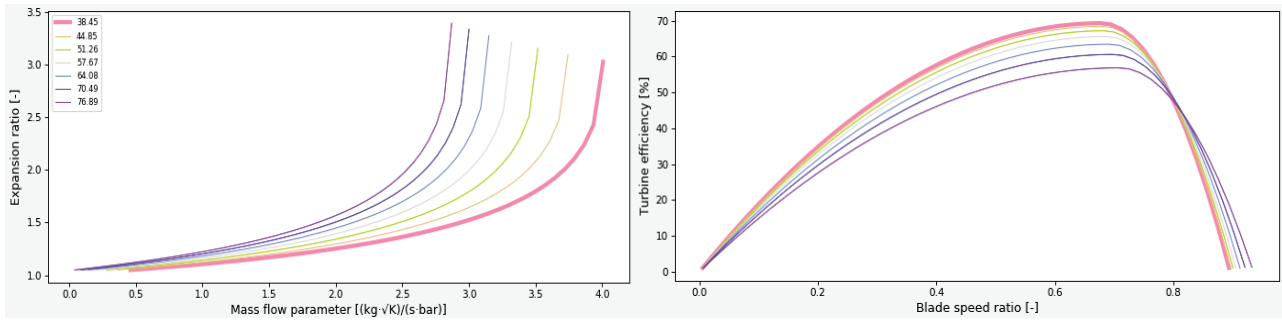
Figure 3.14 - Turbine maps for use in the 1D model: expansion ratio (left) and efficiency (right).

In the model an intercooler is present, like in the 3-cylinder SI engine. The intercooler is modelled like the catalyst in the 3-cylinder model. The intercooler is considered as a system of very small parallel ducts. Again, only one of these parallel ducts is simulated, leaving to the boundary the task of multiplying the solution and transmit the information to the adjacent pipes. In this way the wave motion is transferred while considering the heat and friction occurring in the small pipes.

In Figure 3.15 below the valve timing is reported, which is constant across the operating points, since this engine does not feature any variable valve timing technology. It can be noticed the higher effective compression, as expected for a CI engine with respect to the SI engine previously presented, since the IVC is more advanced. The exhaust lift is very different from the intake lift, both in its maximum value and shape (initial and final part of the profile).
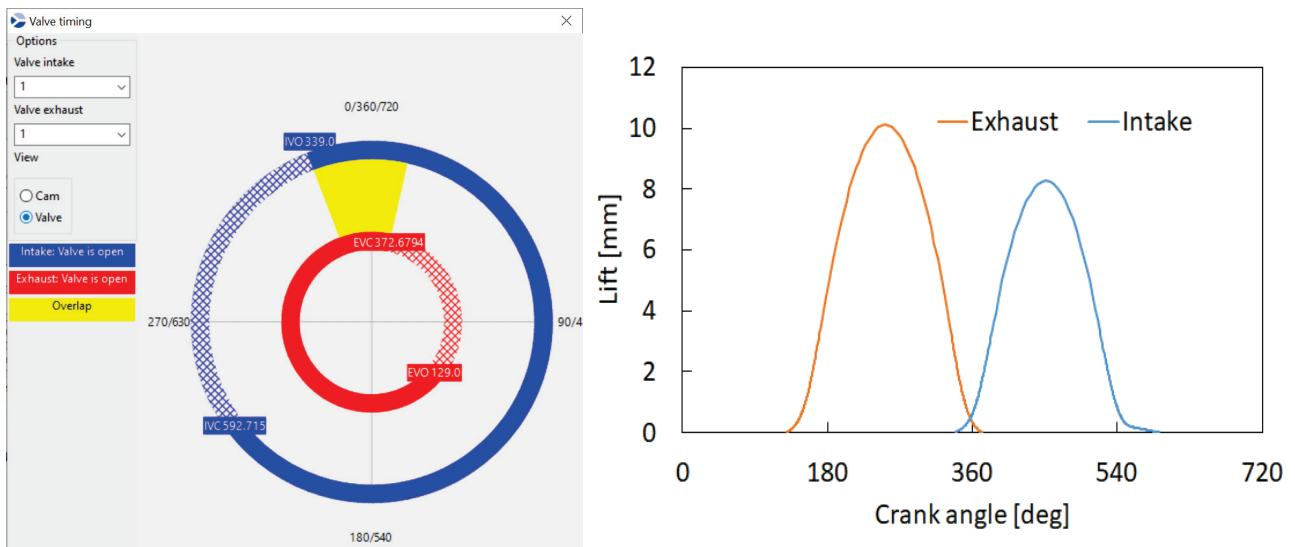
Figure 3.15 - Valve timing (left) and lift profile (right) of the 6-cyclinder Diesel engine.

Moreover, Figure 3.16 below highlights the map of target boost pressure (bar) and target BMEP. As expected, the boost pressure increases with the engine load and engine speed since more mass flow is available to drive the turbine.
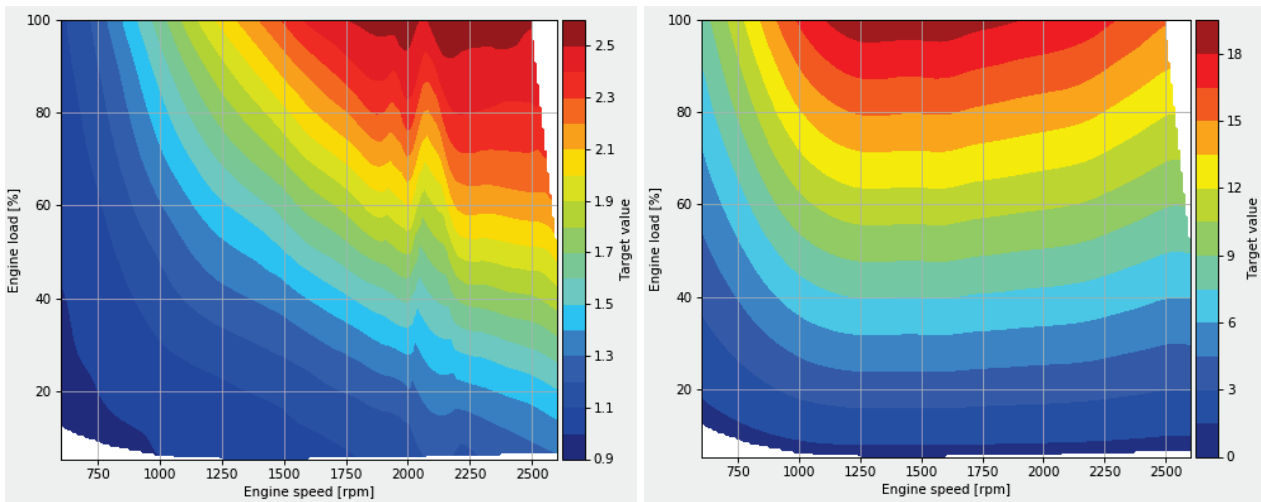
Figure 3.16 - Boost pressure target [bar] (left) and BMEP target [bar] (right).

Also in this case the engine friction has been derived as the difference between IMEP and BMEP, where the IMEP has been derived from the indicated cycle.

3.4 Considerations on the 1D modelling activity

This modelling phase, during which the model data are selected, reviewed, verified and inserted, is crucial for the simulation of transient cycles, in which the engine speeds and loads are continuously changed, and the operating parameters are determined correspondingly by interpolating the available grid data using the current engine speed and load. Hence a well populated map of data allows to have a better model predictivity during RDE driving cycle simulations.

4. 1D engine model steady state validation

In this chapter the validations of the two engines at steady state conditions are presented. Both engine simulations are compared with the experimental data at same engine speed and identical engine load (BMEP). The simulations have been performed ensuring that the fluid dynamic solutions reach convergency, this means that the target are met and that, calculation cycles after calculation cycle, the solution doesn't change. The operating points are simulated one after the other to reduce the computational effort.

4.1 Steady state validation of the 3-cylinder spark ignition engine

Within the activities and work-packages carried out during the EU H2020 project "VISION-xEV", the experimental campaign conducted on the 3-cylinder engine by Universitat Politècnica de Valencia (UPV) has been exploited for an extensive validation of the 1D engine model. UPV provided an experimental database with a total of 83 operating points, evaluated at steady state conditions as shown in Figure 4.1. As requested, engine torque, engine speed, air and fuel consumption, pressures and temperatures, gas mas flow rates at different locations along the engine have been measured together with instantaneous in-cylinder pressure curves. The engine speed range spanned from 1000 to 5250 rpm in this campaign, with engine BMEP varying between full load and motoring conditions.

The engine was instrumented with in-cylinder pressure sensor so that a verification point-by-point of the prediction of the combustion model could be performed. The engine on the test bench at UPV-CMT is presented in Figure 4.1 (right). Sensor to measure gas mass flow rates, pressures, fuel consumption and turbocharger speed together with engine brake power and speed, have been fitted to the engine.
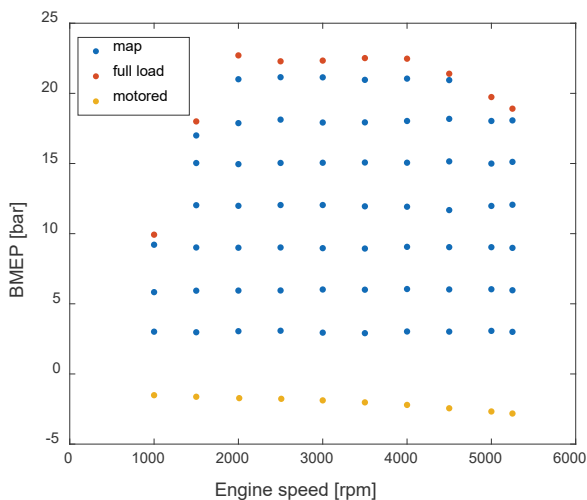
Figure 4.1 - Experimental operating points (left) and instrumented engine on the test bench (right), courtesy of UPV-CMT.

A detailed comparison between experimental data and predicted results has been carried out, to check the predictiveness and the robustness of the simulation model. To ensure a fair comparison, the comparison is done matching the engine speed and load of the engine (brake torque). The measured brake mean effective pressure (BMEP) was matched in all operating points with a PID controller acting on the opening of the throttle valve. Two further PID controllers guarantee the matching with the experimental values of boost pressure downstream of the compressor, acting on the waste-gate valve, and the air temperature after the intercooler, acting on the heat transfer in the intercooler. The information about the spark advance in each operating point was available, so that it was possible to apply an advanced, predictive combustion model, to evaluate the propagation of the flame front by a quasi-D approach. Additionally, since the engine was instrumented with an in-cylinder pressure sensor, a point-by-point verification of the combustion model prediction was performed. The cylinder-out emissions were also measured and compared while the tailpipe pollutants were not measured.

After the simulation of the whole set of operating points present in the map, it is possible to evaluate if the compressor is operating too close to the surge or chocking limit (see Figure 4.2), or even evlauate if the size of the machine is correct for the engine.
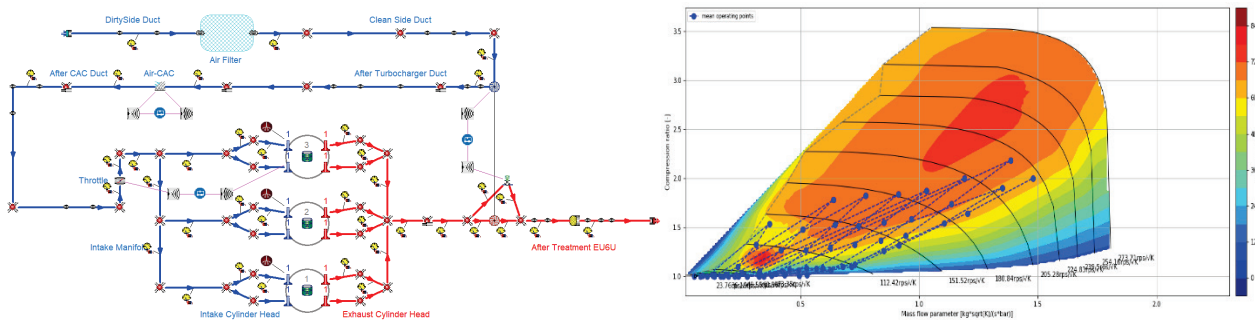

Figure 4.2 – 1D engine model scheme (left) and calculated compressor operating points on the map (rigth).

To simulate the different operating condition, the 1D model has been configured to target the same operating conditions of the experimental data. Hence PID controller have been used to target the desired experimental BMEP, boost pressure and gas temperature after the intercooler. The three PIDs regulate the throttle position, the wastegate opening and the wall temperature of the intercooler ducts. The set of operating points is represented in the picture below (Figure 4.3).

In Figure 4.3 the typical convergency of the turbocharger and throttle during the simulation of one operating point is reported. The throttle is controlled to reach the BMEP, which is proportional to the torque, while the wastegate is controlled to target the boost pressure. The two controllers do not interact with each other, even if the controlled quantity is influenced by the result of the other controller. For example, the increase of boost, at constant throttle position would anyway determine an increase of torque. It is currently in development a more advanced controller, called MIMO (Multi-Input and Multi-Output) to improve the control. However, for this case, where the goal is the simulation of the steady state operating conditions, this simple PID is enough.
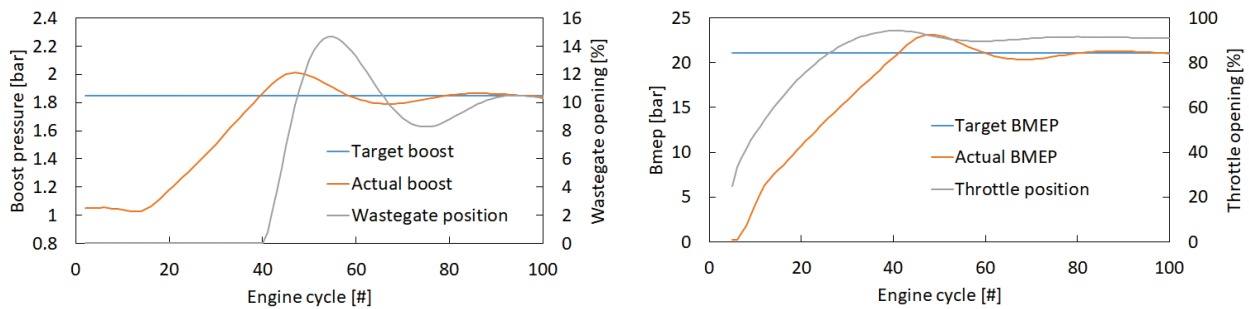
Figure 4.3 - Simulation convergence toward boost preessure (left) and BMEP (right) targets. Operating point: 3000 rpm - 21 BMEP.

It is also reported the calculated turbine and compressor power which determines the reported turbocharged speed evolution (Figure 4.4). It can be seen how the final speed of the turbocharger depends on the final value of power being produced and consumed at the turbocharger shaft, while the decelerations and accelerations depend on the unbalanced torque.
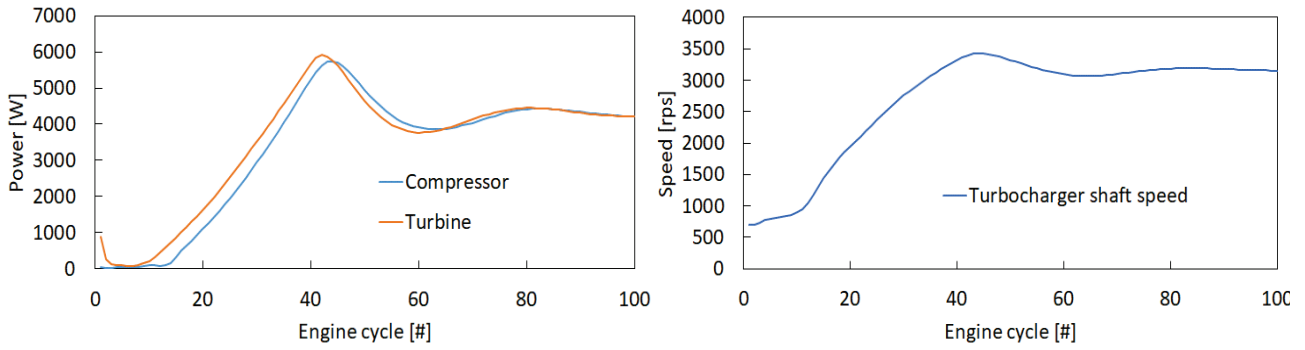
Figure 4.4 – Compressor and turbine (left) power and turbocharger shaft speed (right). Operating point: 3000 rpm - 21 BMEP.

Figure 4.5 shows where the operating points of the turbine and of compressor have worked, on their respective maps used for the calculations, during the simulation. This allows to see the transient points swept when reaching the turbo matching.
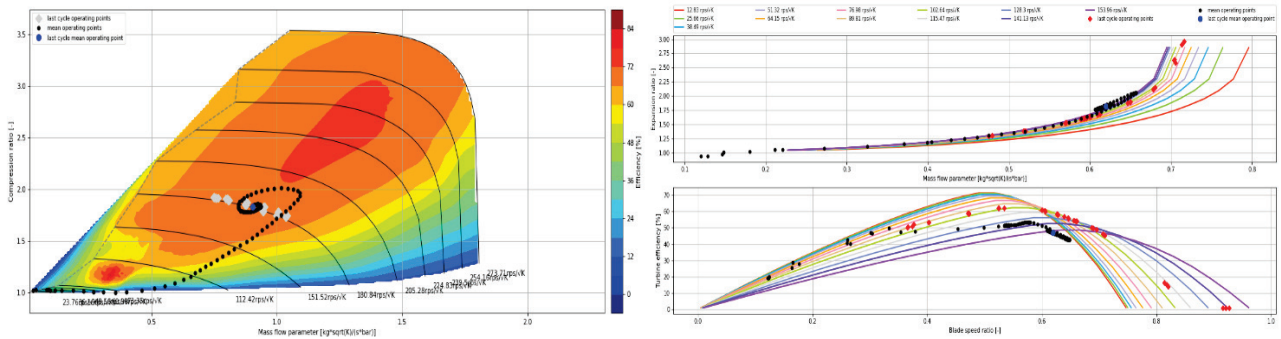

Figure 4.5 – Compressor (left) and turbine (right) operating point on their respective maps. Operating point: 3000 rpm - 21 Bmep.

The mass flow rates and pressure in some key locations along the intake and exhaust systems of the engine are reported in Figure 4.6. It is evident the transient behaviour of the simulation, which reaches convergency once the PID controllers and the turbocharger are in at equilibrium condition. It can be appreciated the dynamic occurring between the mass flow rates and the pressure at the corresponding locations. Just for reference, at the examined operating point (3000 rpm) the engine cycle (4 strokes = 2 revolutions) has a duration of 0.04 seconds; hence 100 cycles correspond to a physical time of 4 seconds.
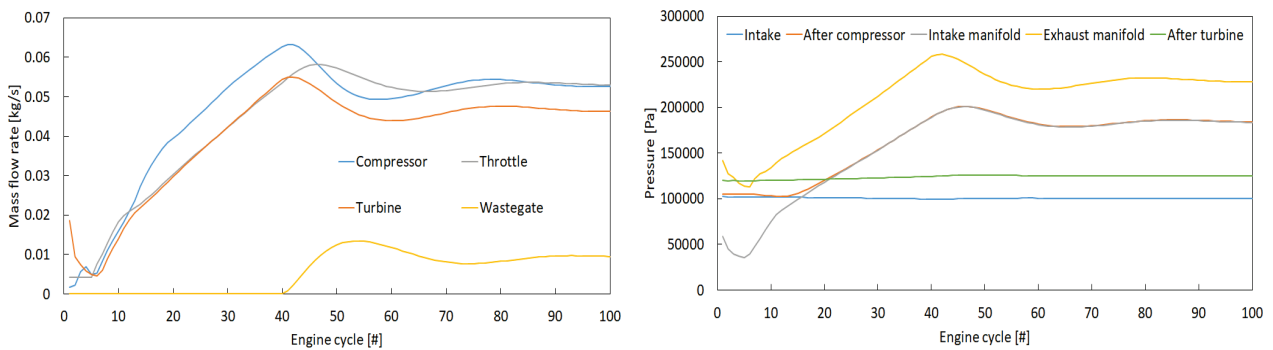
Figure 4.6 - Average mass flow rates (left) and pressure (right) along the engine. Operating point: 3000 rpm - 21 Bmep.
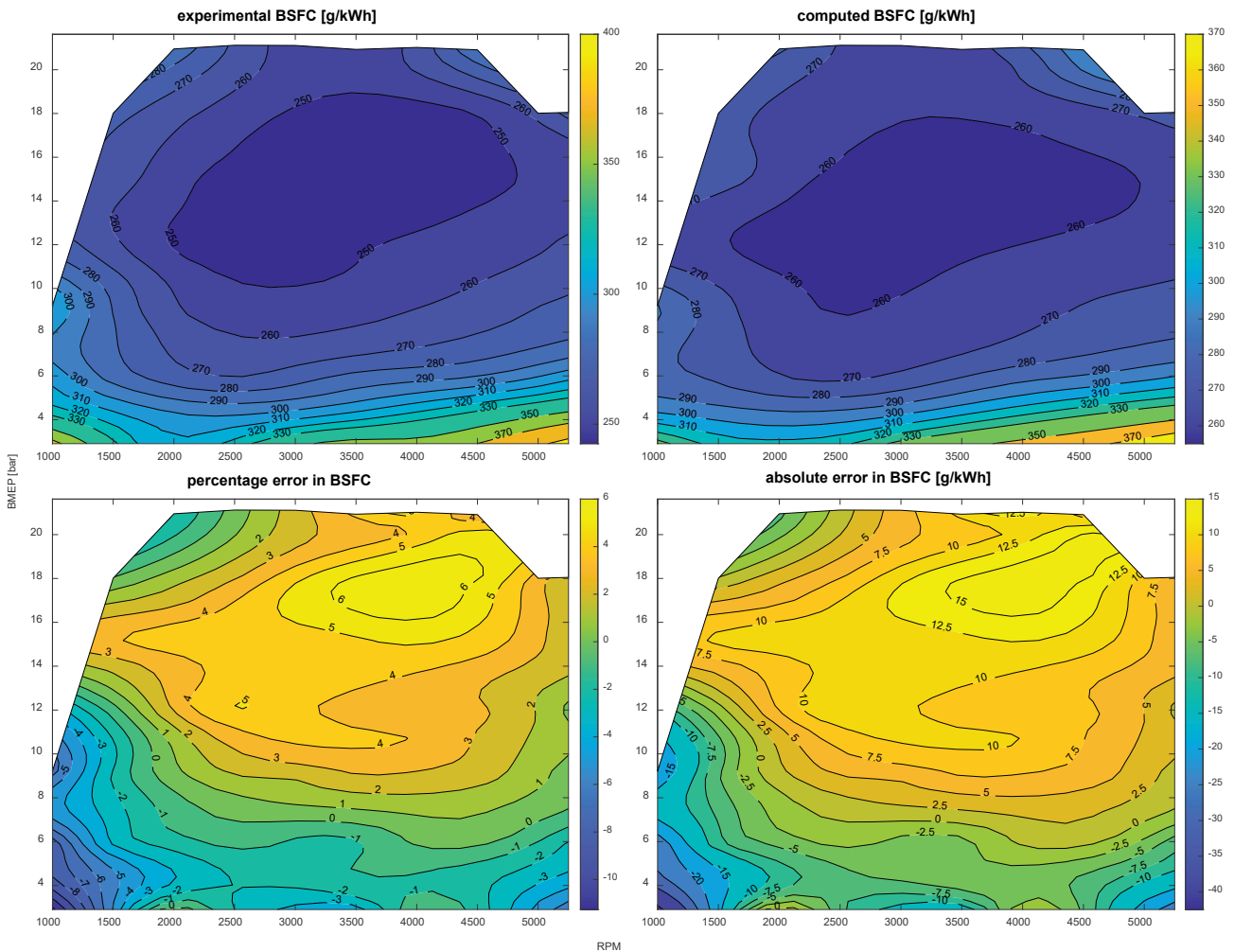
Figure 4.7 shows the contour plots of the measured and computed brake specific fuel consumption (BSFC) and the corresponding relative and absolute errors over the entire steady state engine map. Overall, a rather good agreement is shown, with a good identification of the regions of lower fuel consumption and a relative error which, apart from a few areas, is around 5% with a good quantitative and qualitative prediction level. This accurate result is important to allow the use of the 1D engine model for the evaluation of possible modifications of the baseline engine configuration, as well for the simulation of transient operating conditions based on the 1D model virtual engine, instead of a simple, static engine map.

Figure 4.7 - Contour plots of the measured and computed Brake Specific Fuel Consumption (BSFC in g/kWh), with relative and absolute errors in the entire steady state engine map.

Since a PID controller is active on the throttle body, it is important to verify the accuracy achieved in terms of volumetric efficiency. Figure 4.8 shows the comparison between the predicted and the experimental volumetric efficiency, confirming the accuracy of the fluid dynamic model, but also that some further investigation of the observed differences in mid-load range is required.

48
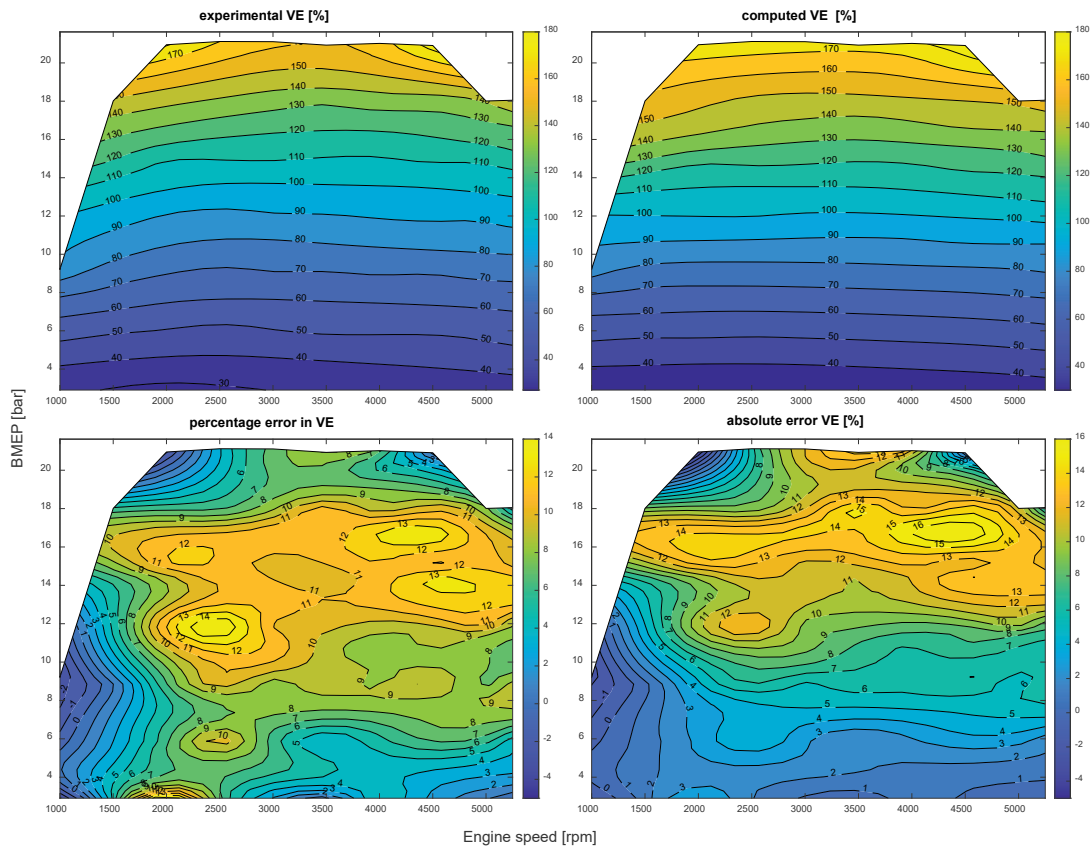
Figure 4.8 - Contour plots of the measured and computed volumetric efficiency,
with relative and absolute errors in the entire steady state engine map.
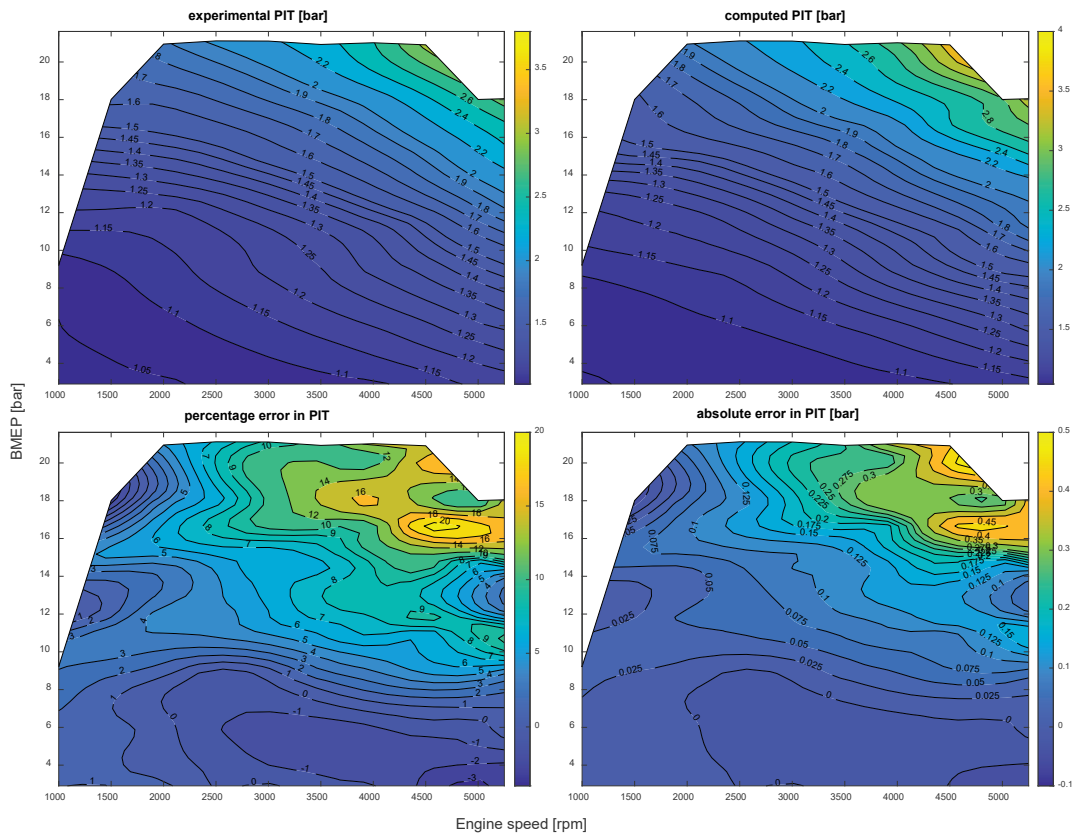
Figure 4.9 - Contour plots of the measured and computed pressure upstream of the turbine,
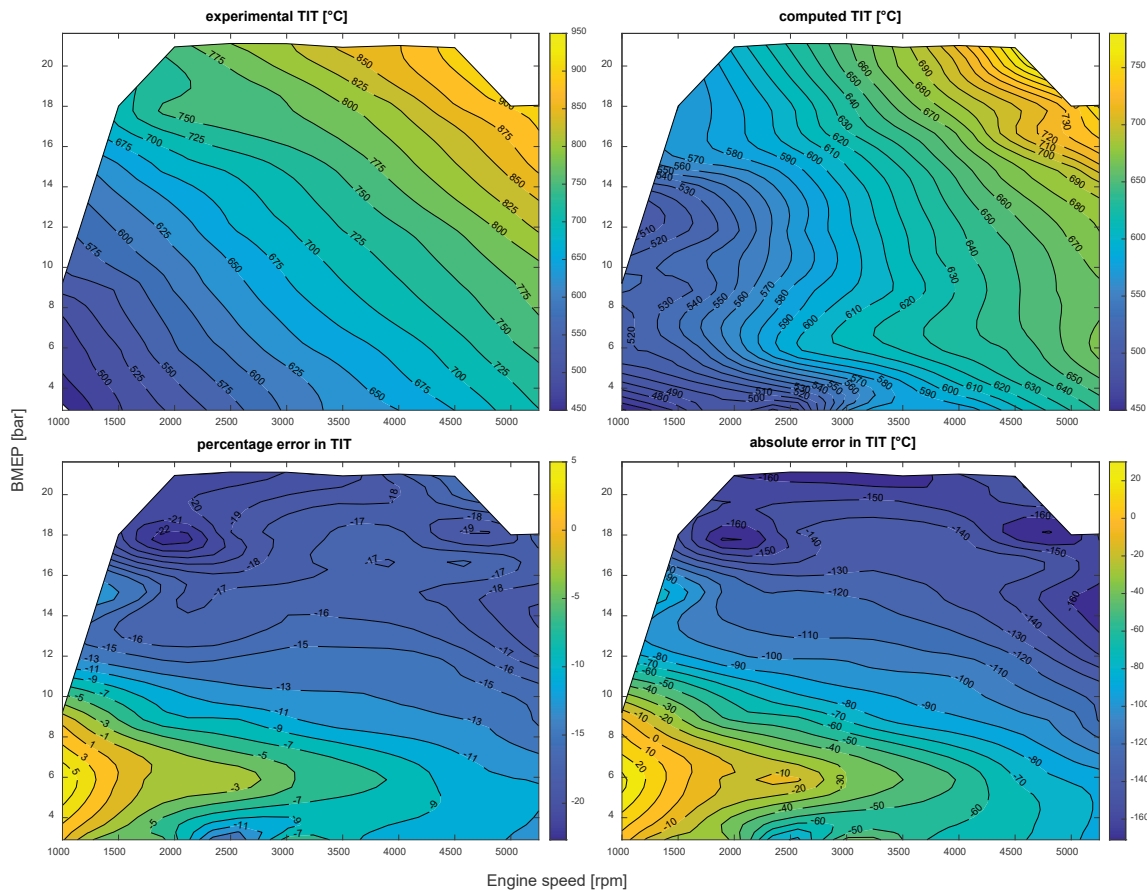with relative and absolute errors in the entire steady engine map.

Figure 4.10 - Contour plots of the measured and computed temperature upstream of the turbine, with relative and absolute errors in the entire steady engine map.

Figure 4.9 shows the agreement achieved in terms of average backpressure upstream of the turbine (PIT), with the highest errors occurring in the high load/high speed range and a rather good prediction elsewhere. Moreover, Figure 4.10 describes the gas temperature upstream the turbine (TIT), showing a good agreement with the largest errors occurring the high load/high-speed range and a rather good prediction at lower loads and speeds. Regarding the comparison of gas temperature, the calculated value is the true gas temperature while the experimental value is the temperature sensed by the thermocouple, that typically differs from the actual gas temperature.

Finally, the following Figures 4.11 and 4.12 focus on the comparison between predicted and measured pollutant emissions, namely CO and NO_x. Figure 4.11 represents the map of CO concentration, CO production mainly depends on the equivalence ratio and fuel composition, as a function of load and engine speed. It can be seen that the model can predict the shape of the contour map, even if the percentage error is not negligible.

Figures 4.12 highlights the comparison for NO_x concentration, showing a good agreement over a large range of operating conditions. NO_x concentrations depend on multiple factors (equivalence ratio, cylinder pressure and temperature, heat fluxes, dilution by burnt gases), however a good qualitative agreement is achieved, apart from an overestimation of absolute values in specific regions of the operating map. The resulting average error is around 15%-20% for both the CO and NO_x concentrations.

It is important to highlight that the pollutant emission model calibration coefficients have been chosen to achieve an average agreement with experimental data. A point-by-point calibration has not been performed to not distort the predictiveness of the model.
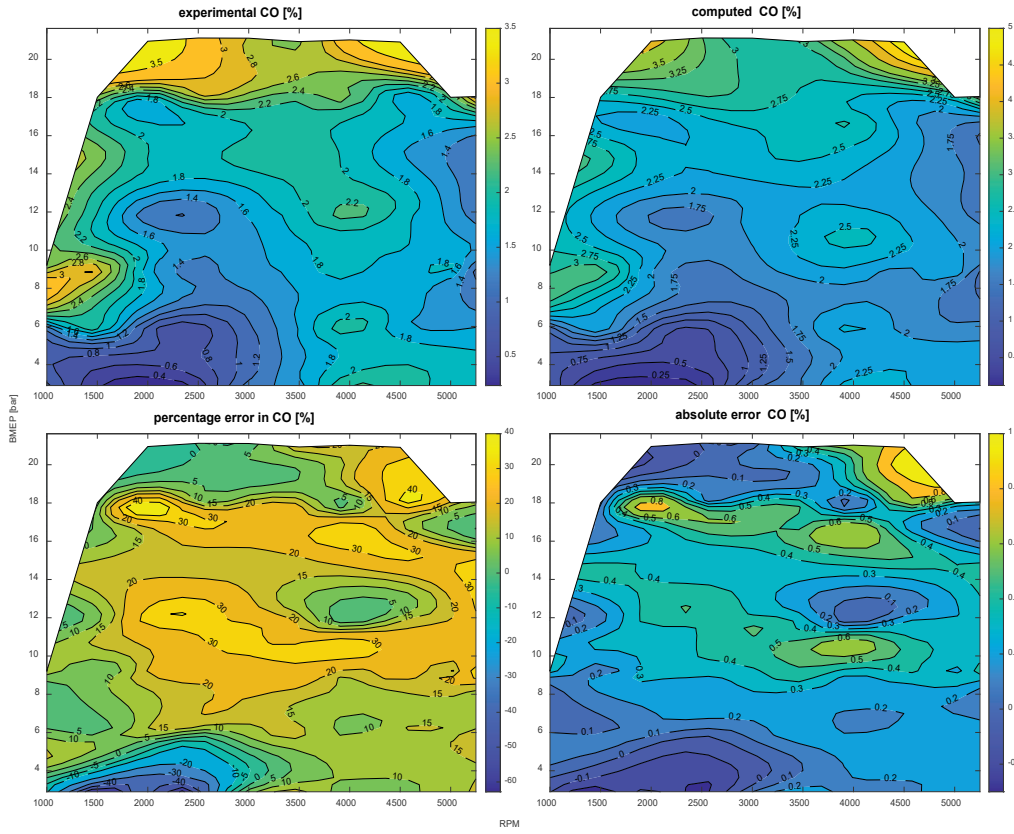
Figure 4.11 - Contour plots of the measured and computed cylinder-out CO,
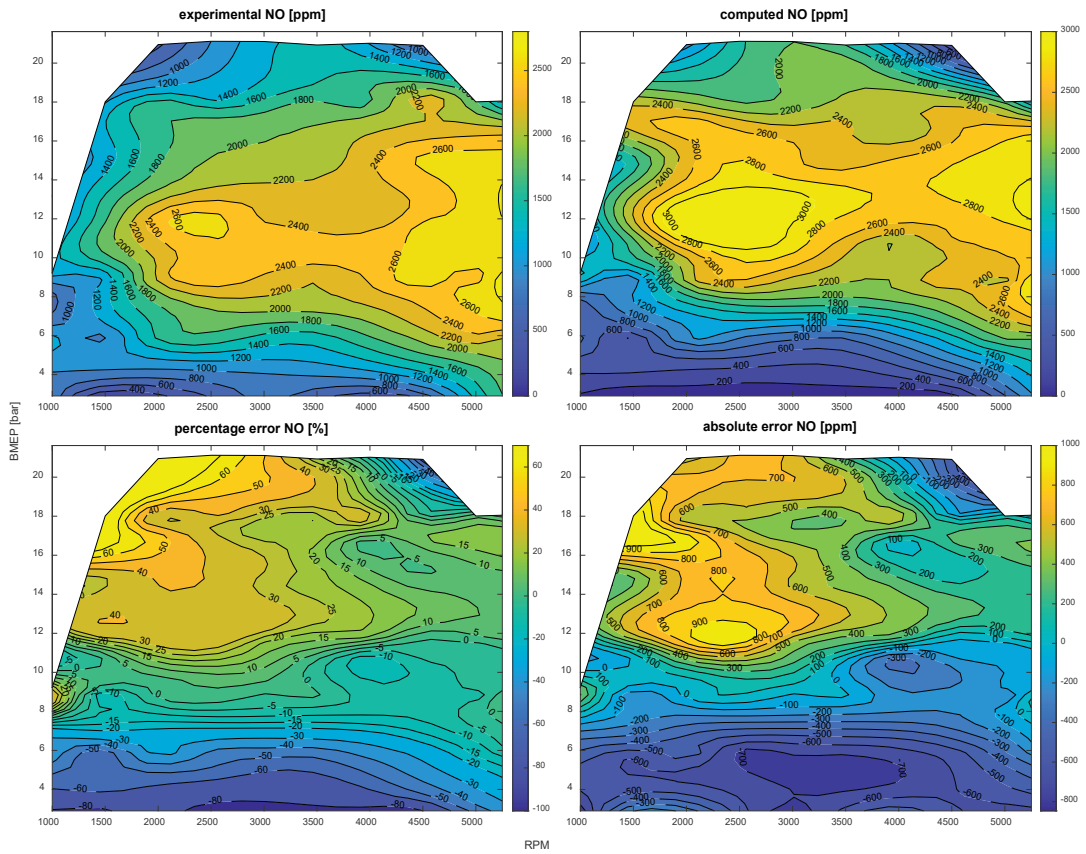with relative and absolute errors in the entire steady state engine map.

Figure 4.12 - Contour plots of the measured and computed cylinder-out NOₓ,
with relative and absolute errors in the entire steady state engine map.

The availability of measured instantaneous pressures traces allowed the detailed validation of the 1D engine model under different aspects. Figure 4.13 shows the measured and computed in-cylinder pressures curves at three different regimes (1000, 3000, 5250 rpm) and same load (BMEP=3 bar), where it can be seen that the peak pressure is captured with fair agreement both in terms of value and of crank angle at with it is reached. Moreover, Figure 4.14 shows the same comparison, at different load (BMEP=6), between the computed in-cylinder pressure trace and the measured one in logarithmic scale, showing that a disagreement is present especially during the expansion stroke. These results prove the predictiveness of the advanced SI model, as well as the accuracy in the modelling of the in-cylinder thermo-fluid dynamic processes. Doubling the load from 3 to 6 bar (BMEP), results are still in reasonable agreement, with differences in the maximum values of in-cylinder pressure in the range of 1-2 % instantaneously.
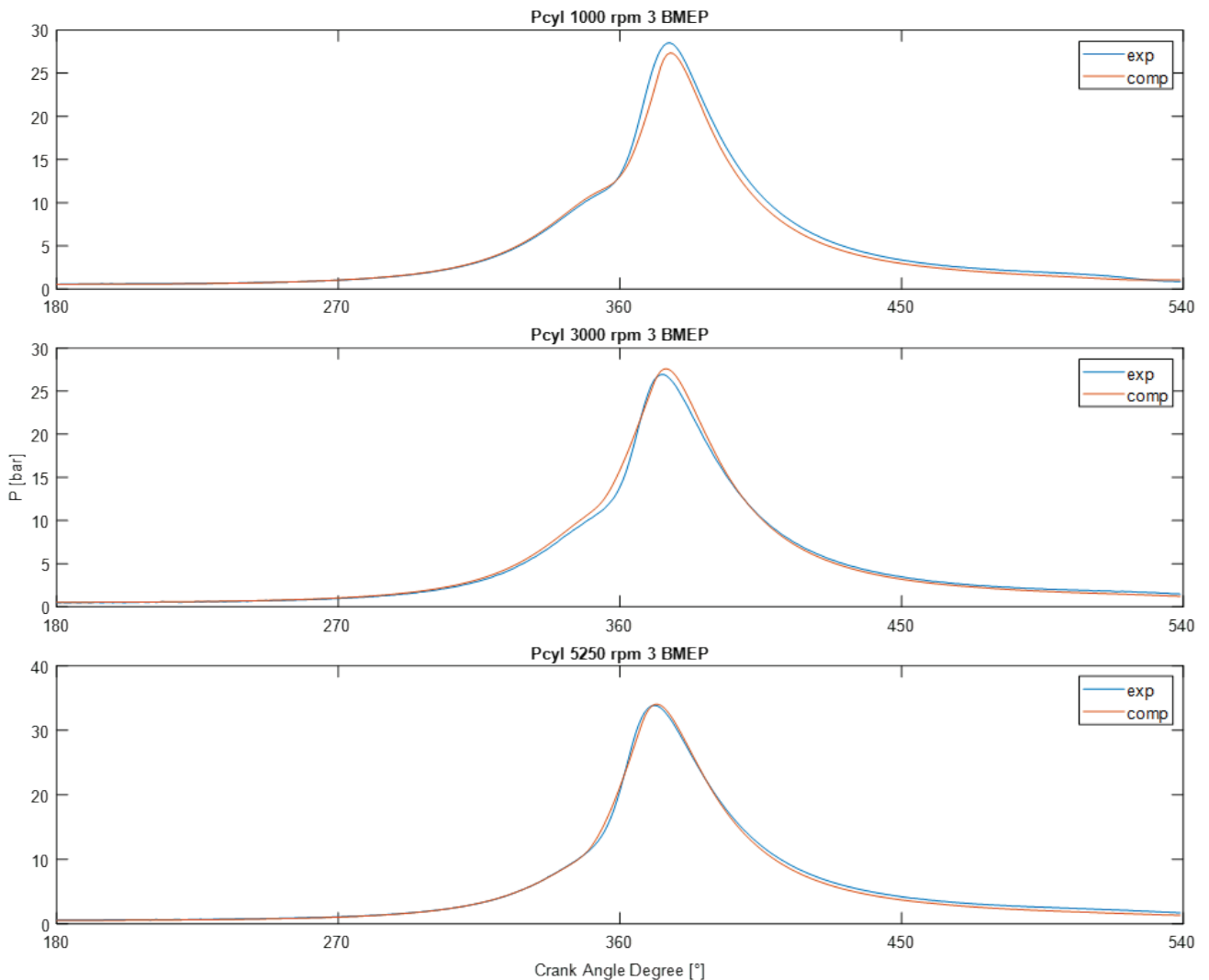
Figure 4.13 - In-cylinder pressure at 1000, 3000 and 5250 rpm, same engine load (BMEP = 3 bar).
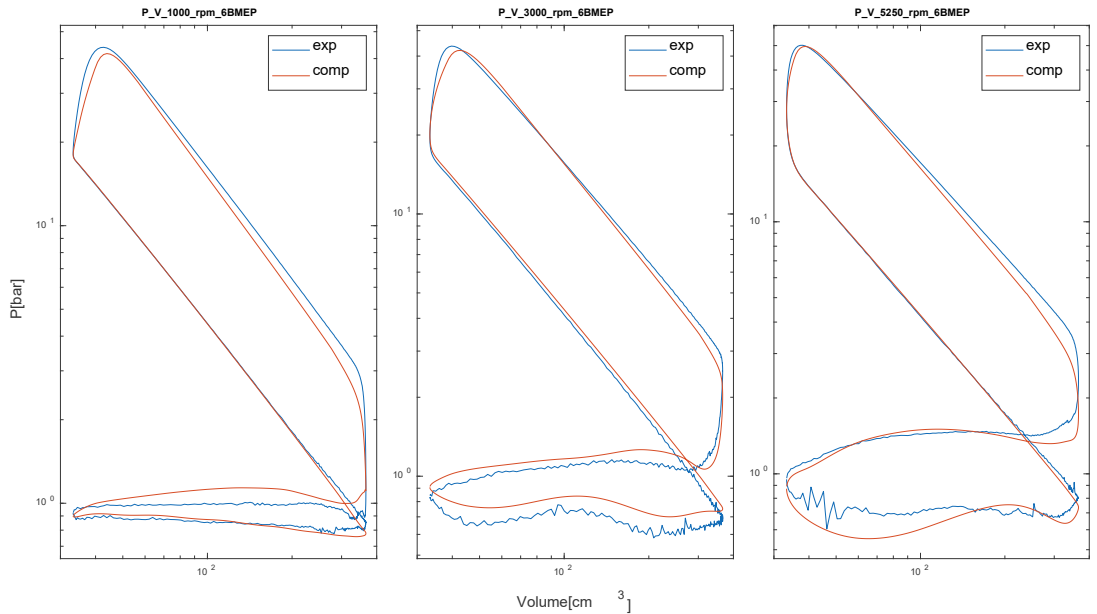
Figure 4.14 - In-cylinder pressure-volume diagram at 1000, 3000 and 5250 rpm, same engine load (BMEP = 6 bar).

Furthermore, the analysis of the unsteady flows in the intake and exhaust system was also carried out for several steady state operating points. As an example, the pre-turbine and intake manifold comparison results are shown in Figure 4.15, where the computed pressure waves look in good agreement with the measured data, showing the typical three-cylinder engine pulsations.
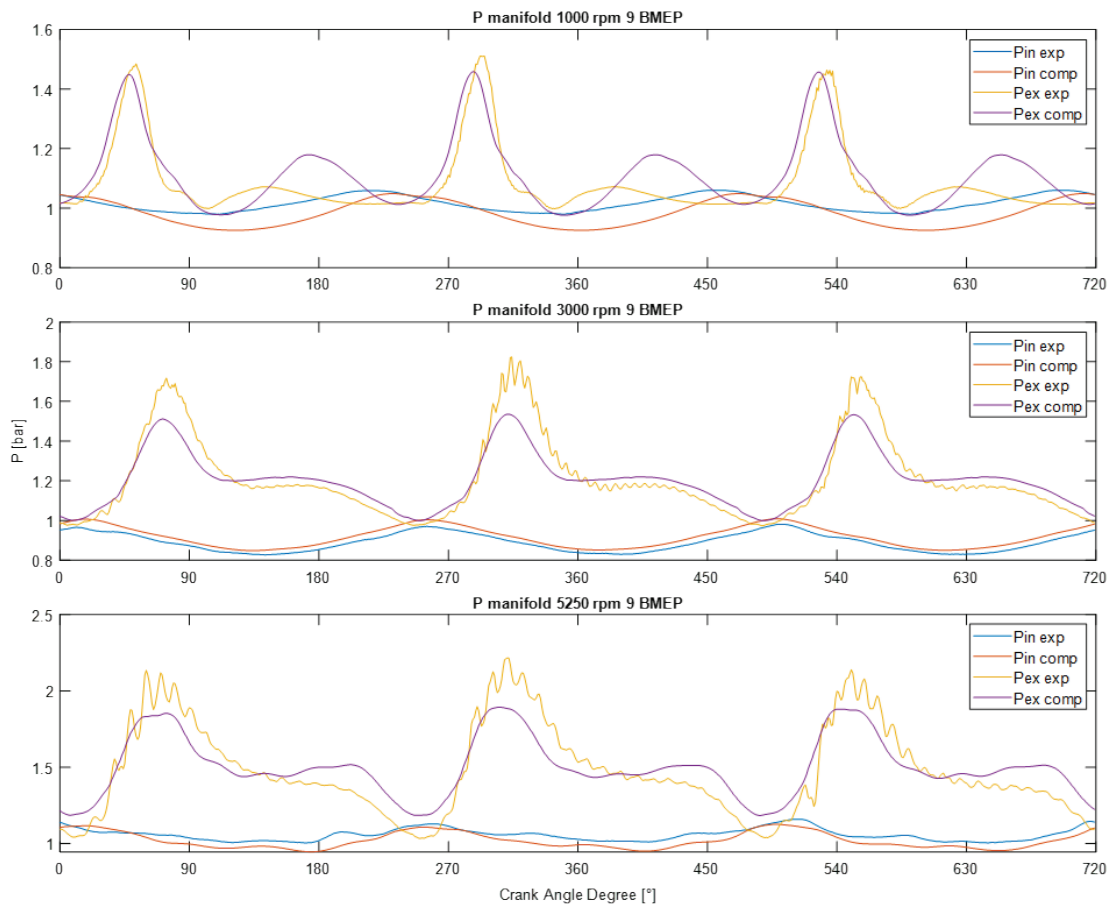

Figure 4.15 - Instantaneous pressures in the intake and exhaust manifold for 1000, 3000 and 5250 rpm, same engine load (BMEP = 9).

4.2 Steady state validation of the 6-cylinder compression ignition engine

In the framework of the European project "VISION-xEV", the other engine under investigation has been instrumented to carry out an extensive measurement campaign finalized to the validation of the developed code. The experimental campaign was conducted by the manufacturer FPT. The set of operating points consists of 187 steady state operating points, from a low to full load and across the whole engine speed range. Like before, the points are defined by the engine speed and BMEP of the engine. The operating map of the 210-kW engine is represented by the red points in Figure 4.16.
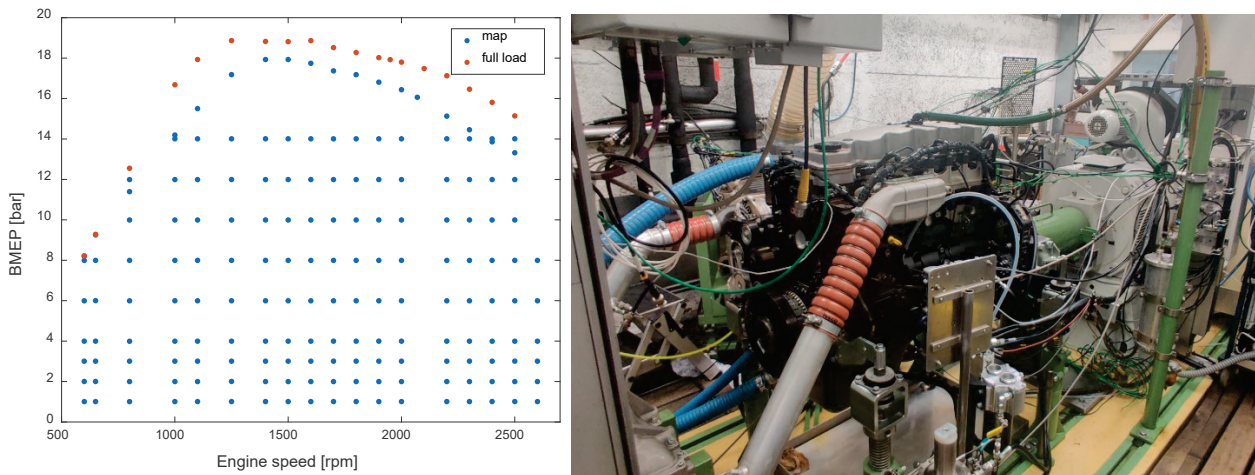
Figure 4.16 – The 187 operating points investigated on the 6-cylinder CI engine (left),
and the instrumented engine on the test bench (courtesy of FPT - right).

Similarly to the model built for the SI engine, three PIDs controllers were used: this time the one controlling the engine load, hence targeting the BMEP, acts on the injected mass of fuel per cylinder per cycle. The other two PID are instead similar to the 3-cylinder engine: the target compressor boost pressure is achieved acting on the wastegate opening, and the cooling of the fresh charge temperature is achieved with the actuation of the intercooler wall temperature. Once the whole engine map is simulated, it is possible to see where the compressor is working at the end of each operating condition (see Figure 4.17), to verify normal operating conditions of the turbomachine, avoiding to operate the compressor too close to surge or chocking limits.
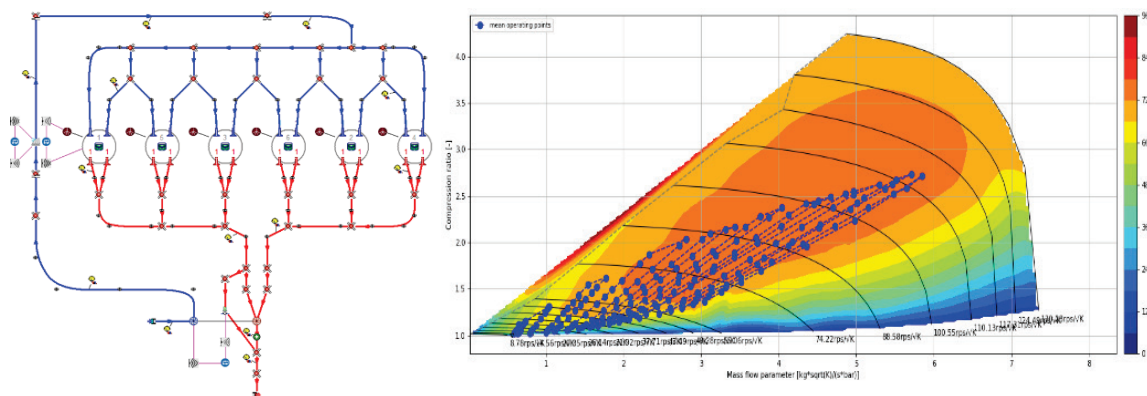

Figure 4.17 – 1D engine model (left) and the 187 operating point resulting operating points of the compressor represented on the compressor characteristic map (right).

Like the previous engine, it is reported as example of the simulation convergency of the turbocharger and fuel injection during the simulation of the operating point at 800 rpm and 12.5 BMEP (see Figure 4.18). In this case the load of the engine, being a compression ignition engine, is mainly controlled by the injected fuel quantity while the wastegate is controlled to reach the boost pressure, as done in the three cylinder spark ignition engine.
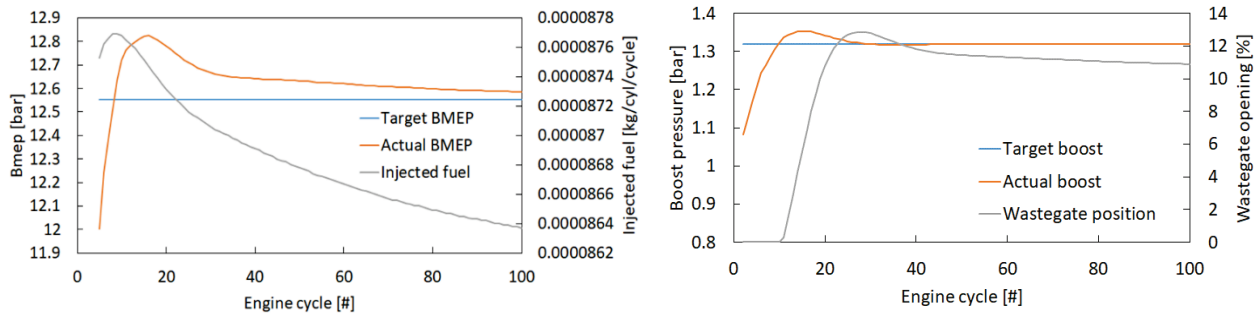
Figure 4.18 - Simulation convergence toward targets. Operating point: 800 rpm – 12.5 BMEP.

It is also reported, for the same operating point, the turbine and compressor power. Also in this case the turbocharger reaches convergence when the power produced by the turbine equals the one consumed by the compressor. This happens in around 50 cycles, corresponding to around 7.5 seconds of real time from a completely still state (see Figure 4.19).
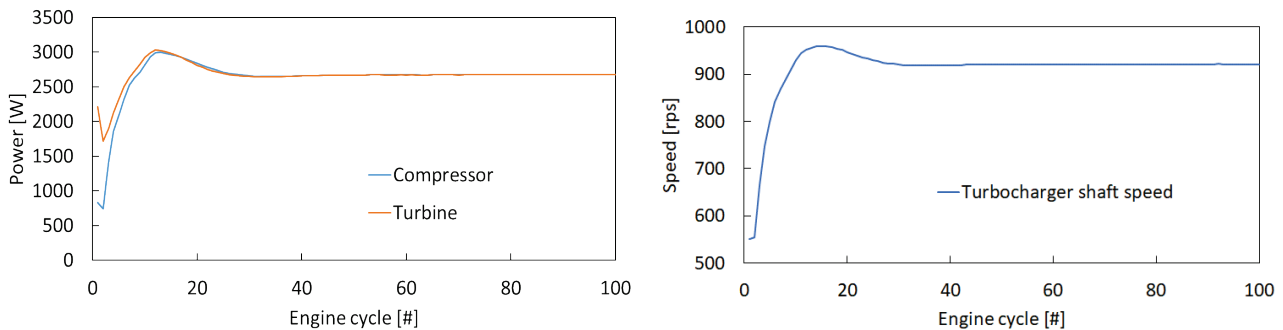

Figure 4.19 – Compressor and turbine power and turbocharger shaft speed. Operating point: 800 rpm – 12.5 BMEP.

In Figure 4.20 are reported the mass flow rates and pressure in some key locations along the intake and exhaust system of the engine. It can be noted that this time the mass flow thorugh the turbine comes from the two sides of the exhaust, the total gives the same mass flow rate thorugh the compressor. Still some mass flow is discarded by the wastegate as reflected by the loweer prssure on the left side of the exhaust manifold.
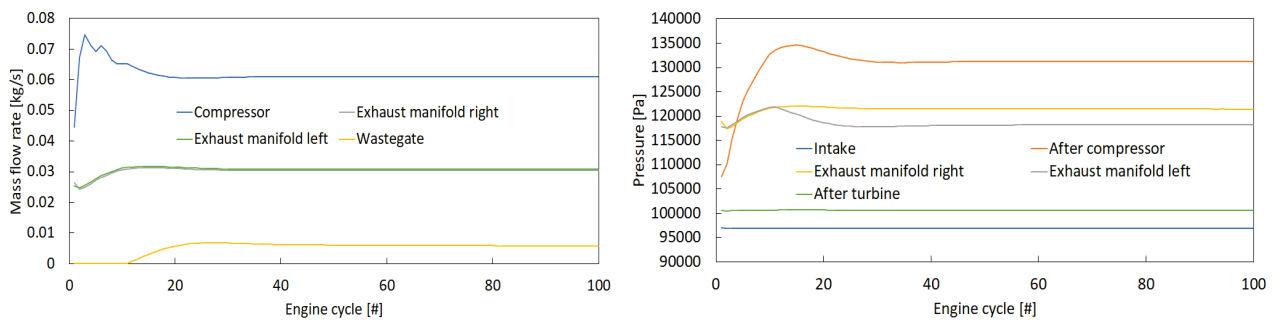

Figure 4.20 - Average mass flow rates (left) and pressure (right) along the engine. Operating point: 800 rpm – 12.5 BMEP.

The measured in-cylinder pressure data received (courtesy of FPT) were used to improve the calibration of the combustion model and the prediction of NO_x. Such measurements were available for a 235kW version of the engine, so the double Wiebe combustion model was calibrated for this version and then applied to the 210kW version that is actually modelled.

Due to confidentiality requisites, the experimental and calculated value shown have been normalized with respect to the maximum value, allowing to compare the trends without disclosing absolute values, except for the BSFC, where the minimum experimental value has been used.

The prediction of specific fuel consumption by means of the 0D/1D code is very accurate at high-medium engine speeds, as reported in Figure 4.21, whereas a larger discrepancy can be found at lower regimes. However, considering the typical applications of the engine investigated, that part of the engine map is not frequently exploited, so that a reliable evaluation of fuel consumption is expected during an RDE test cycle. A maximum difference below 4% would have been better.
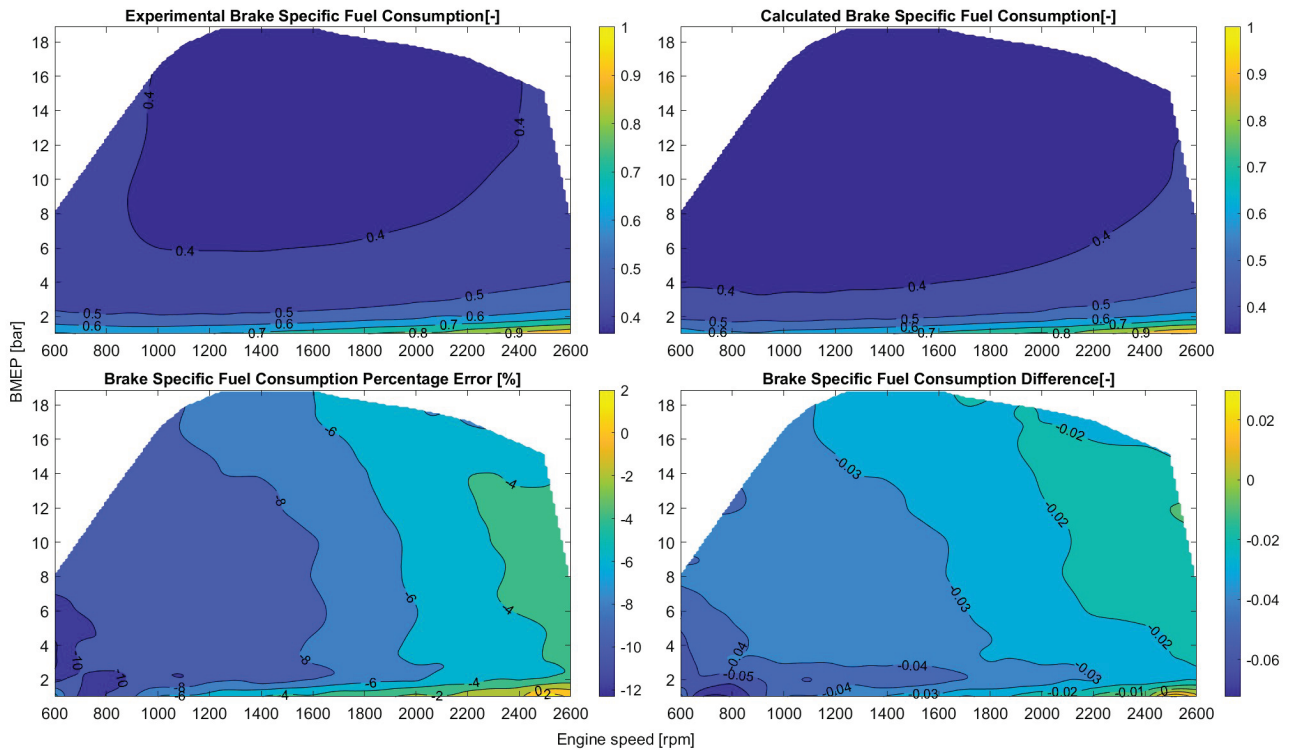
Figure 4.21 - Contour plots of the measured and computed Brake Specific Fuel Consumption (BSFC in g/kWh), with relative and absolute errors in the entire steady state engine map.

Considering further important engine parameters Figures 4.22 and 4.23 describe the calculated equivalence ratio and the air mass flow rate, showing a good agreement with measured data over a wide range of BMEP and engine revolution speed, with limited discrepancies.

Similarly, Figure 4.24 and Figure 4.25 report the predicted gas temperature and pressure at the turbine inlet, showing a rather small percentage error if compared to measured values.
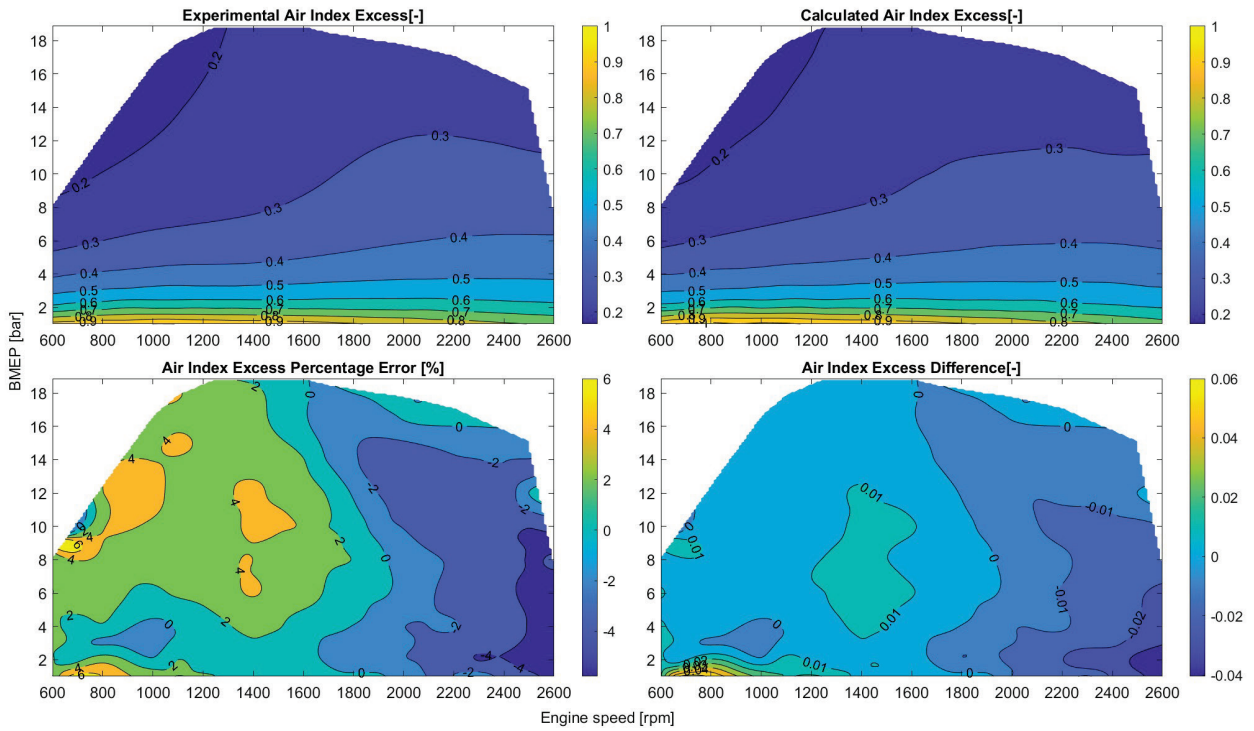
Figure 4.22 - Contour plots of the measured and computed air index excess,
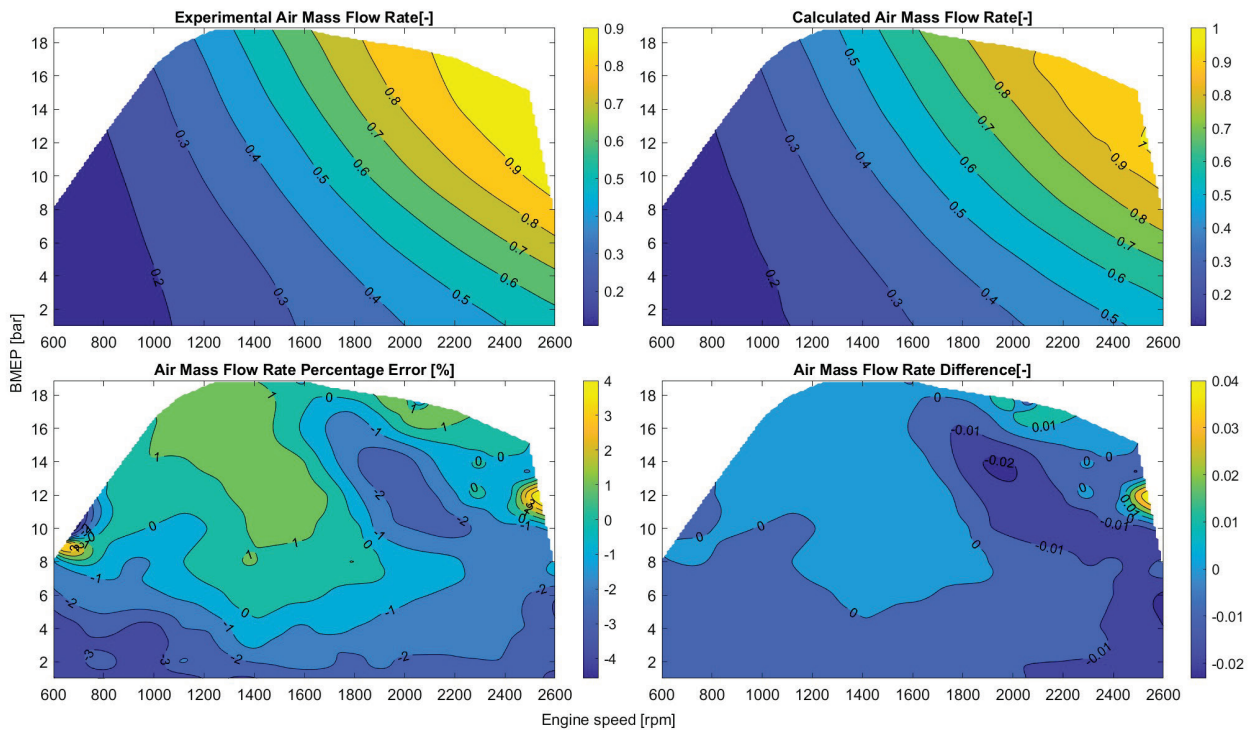with relative and absolute errors on the entire steady state engine map.

Figure 4.23 - Contour plots of the measured and computed air mass flow rate,
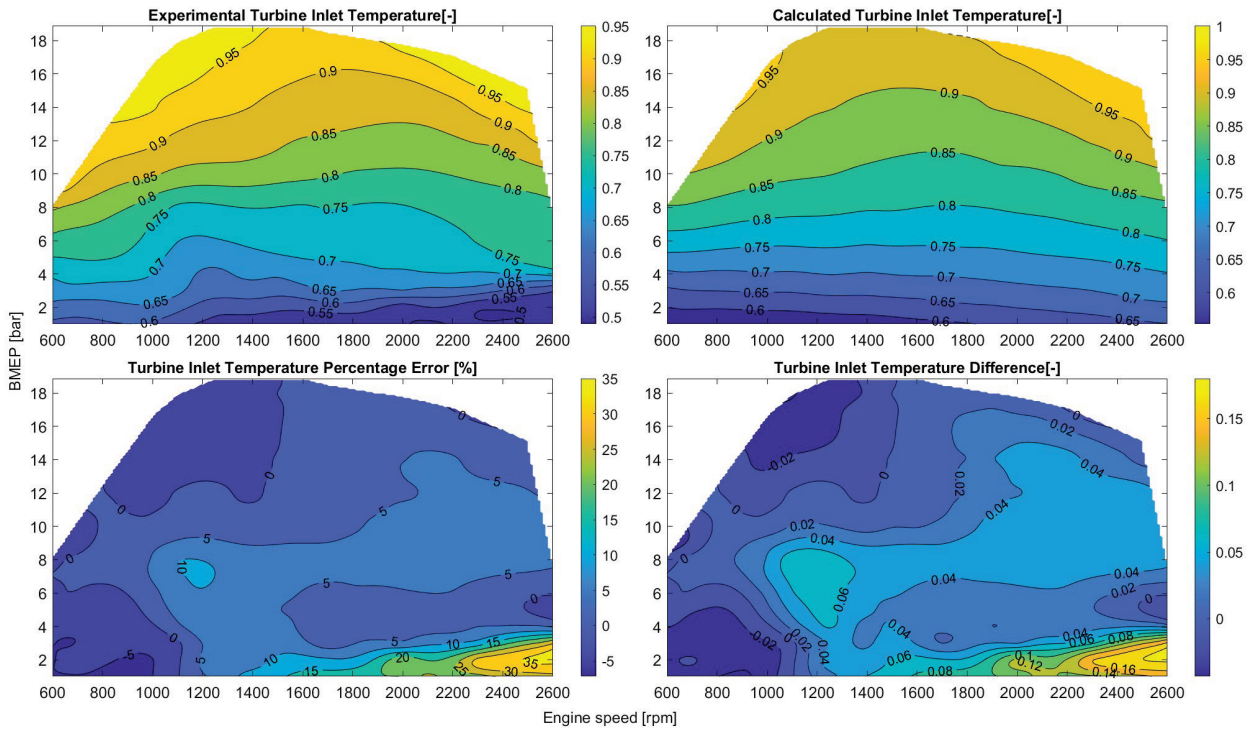with relative and absolute errors on the entire steady state engine map.

Figure 4.24 - Contour plots of the measured and computed temperature upstream of the turbine, with relative and absolute errors on the entire steady state engine map.
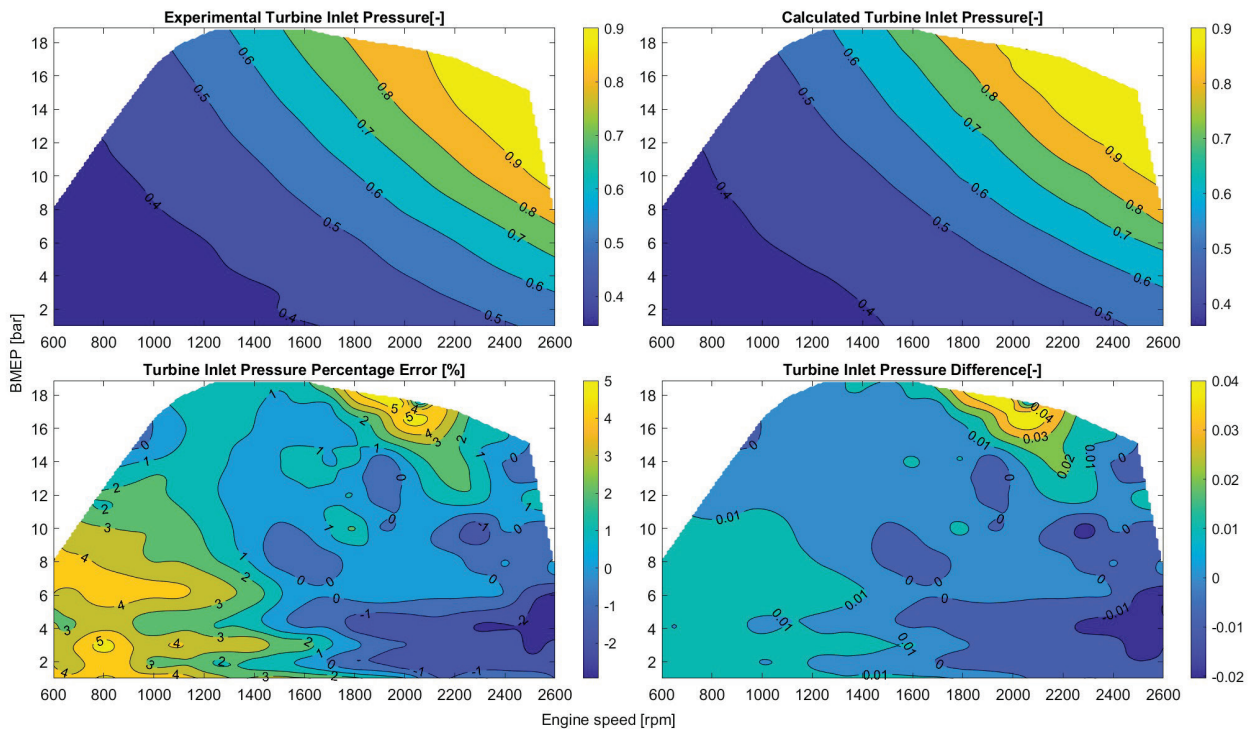

Figure 4.25 - Contour plots of the measured and computed pressure upstream of the turbine, with relative and absolute errors on the entire steady state engine map.

The virtual engine model demonstrated fairly high accuracy in predicting both the in-cylinder peak pressure (Figure 4.26) and the turbocharger rotational speed (Figure 4.27), reporting a small percentage error with respect to experimental measurements. This is a key aspect since it implies a correct matching between the engine model and the turbocharger model.
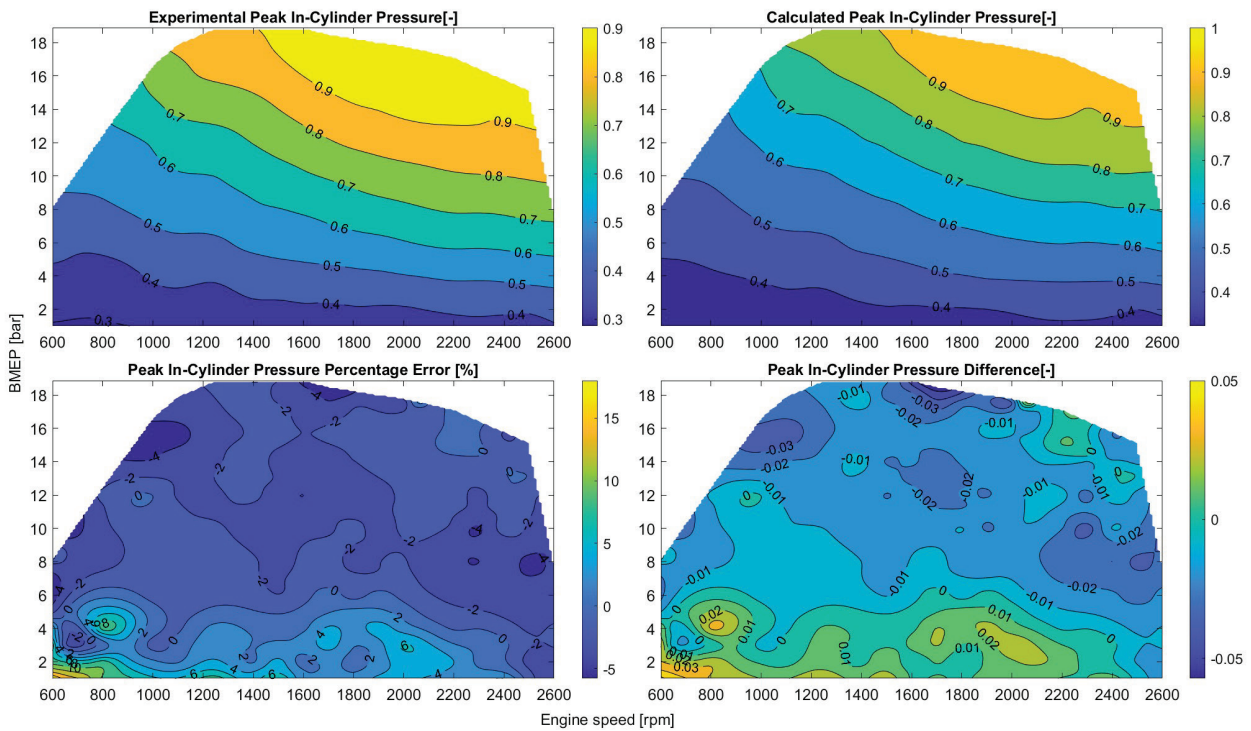
Figure 4.26 - Contour plots of the measured and computed maximum in-cylinder pressure,
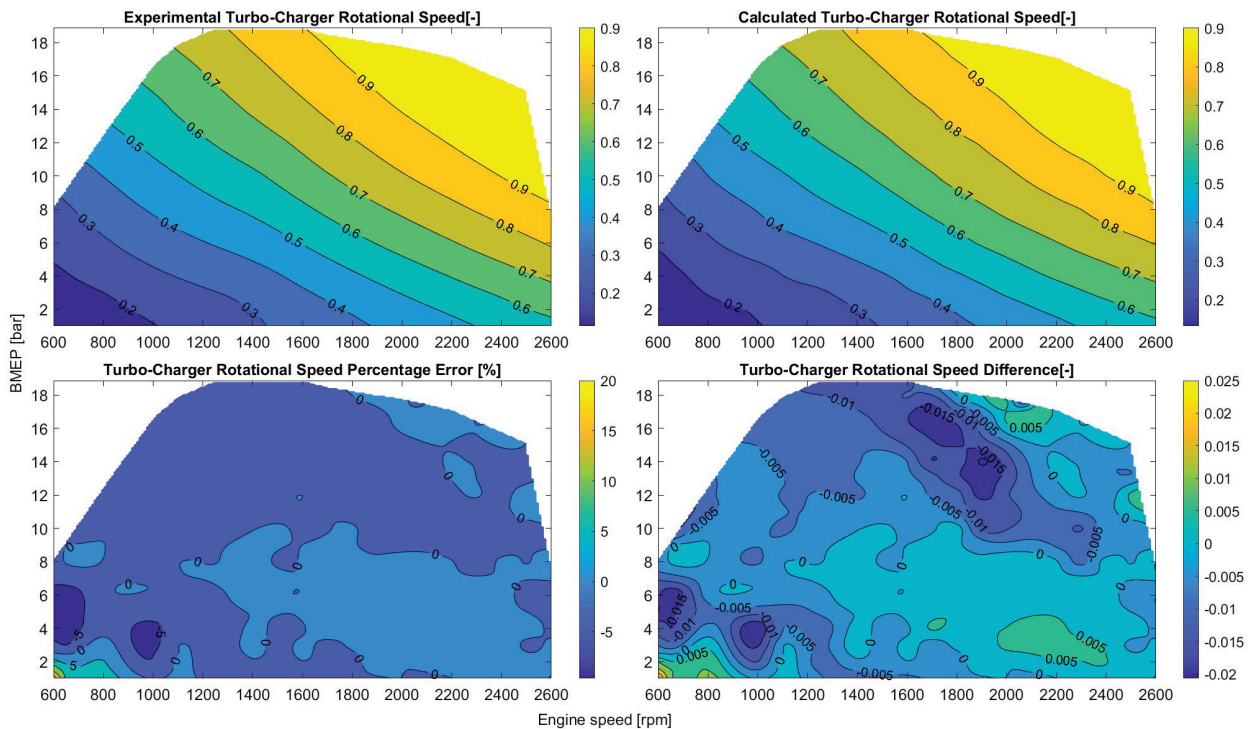with relative and absolute errors in the entire steady engine map.

Figure 4.27 - Contour plots of the measured and computed turbocharger shaft rotational speed,
with relative and absolute errors in the entire steady engine map.

Finally, the calculated cylinder-out concentrations of CO_2 and NO_x pollutant emissions have been compared to the measured data on the whole engine map. Figures 4.28 and 4.29 show the contour maps and the percentage errors; CO_2 is very well captured as a consequence of the accurate agreement in lambda. Instead, the CO concentration exhibit a lager error which is due to the low level of CO produced (close to zero), typical for the CI engine. Therefore, even a small amount of predicted CO ends up in a high percentage error.

Conversely, the NO$_x$ prediction is rather good considering the difficult prediction of this pollutant, with an average error around 10-20%. The satisfactory comparison confirms the good set-up of the combustion model, being NO$_x$ formation dependent on the correct prediction of in-cylinder temperature and local air-to-fuel ratio.
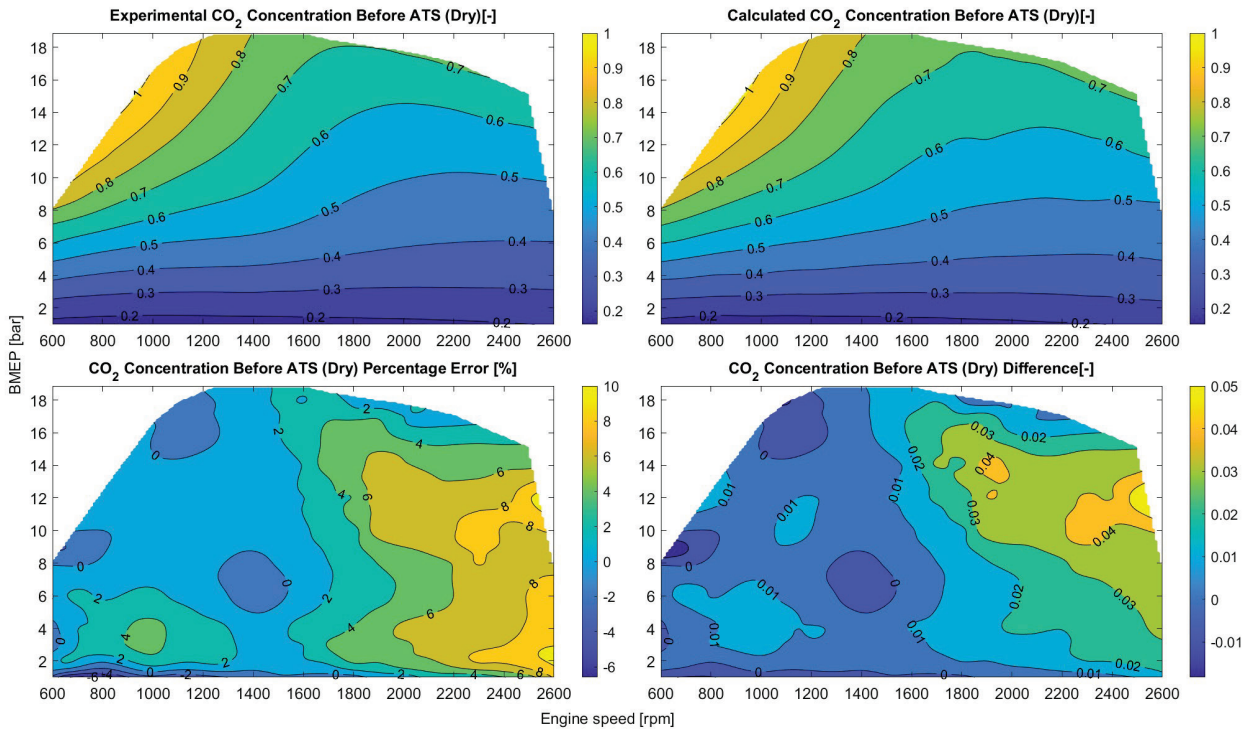

Figure 4.28 - Contour plots of the measured and computed CO$_2$ concentration upstream of the ATS, with relative and absolute errors in the entire steady engine map.
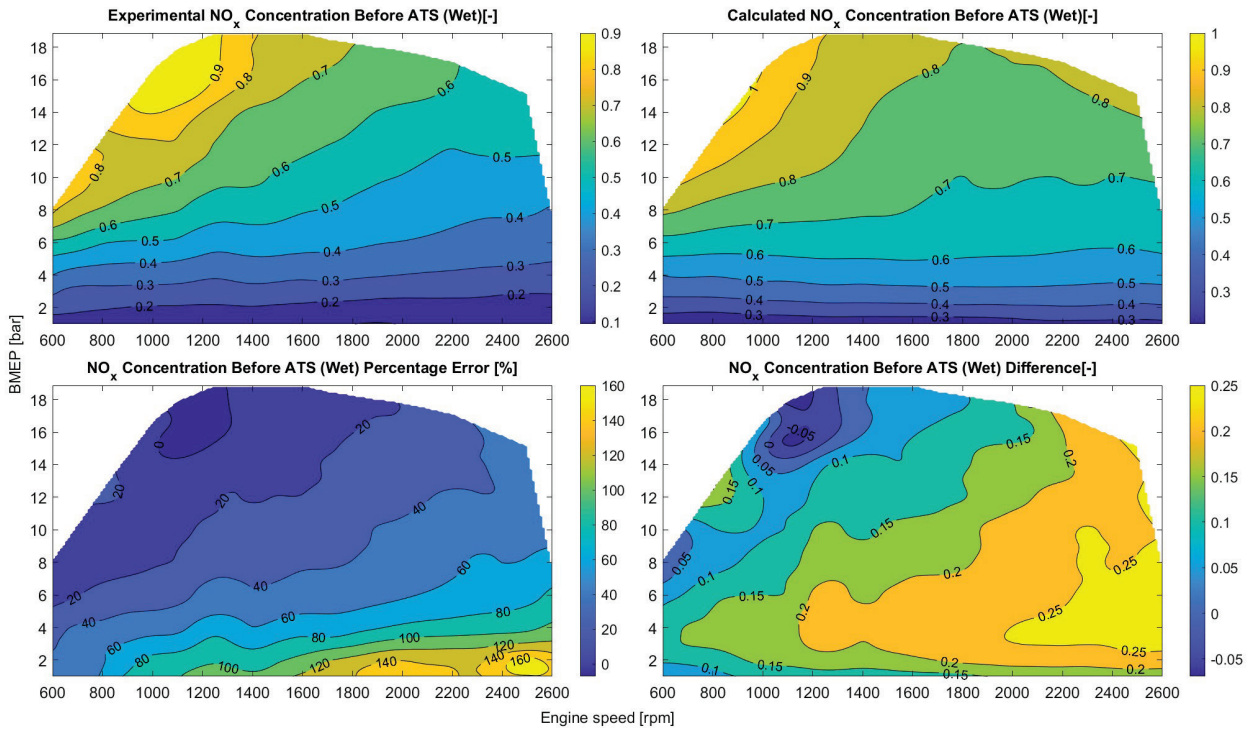

Figure 4.29 - Contour plots of the measured and computed NO$_x$ concentration upstream of the ATS, with relative and absolute errors in the entire steady engine map.

Thanks to the availability of in cylinder measurements, also in this case a comparison of the in-cylinder pressure traces has been carried out, highlighting a good agreement with experimental data as shown in Figure 4.30. The in-cylinder pressure is correctly predicted according to injection timing and the correctly predicted heat release rate due to the combustion of the injected fuel.
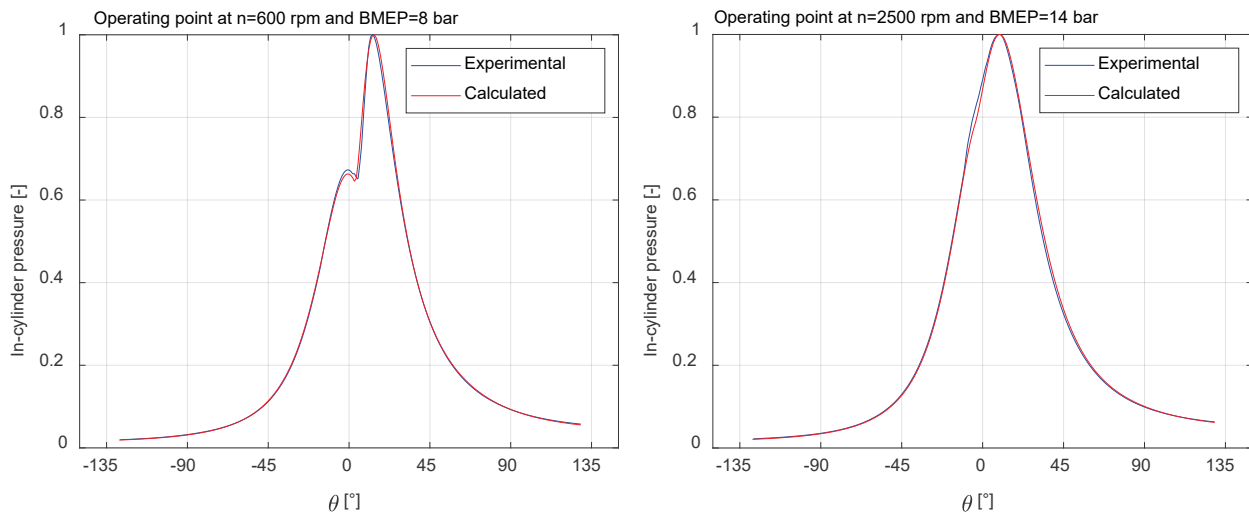

Figure 4.30 – Comparison of experimental and computed normalized in-cylinder pressure traces.

4.3 Final considerations on the steady state validation

Finally, an important remark about this steady state validation performed on the two engines just presented. The goal is to have a predictive 1D model so that during the simulation of driving cycle, the engine will run across non-mapped conditions reflecting the behaviour of the real engine. When the model runs in transient, interpolations are performed to set up the engine model exploiting the known values of the nearest mapped operating conditions parameters.

5. The Fast Simulation Method (FSM)

An important goal of this work is to reduce the computational effort of the 1D fluid dynamic simulations by means of a suitable numerical solver, based on a Fast Simulation Method (FSM). This would allow to perform the simulation of driving cycles in few hours, in order to run the cycles during the night and analyse the result the morning after.

As explained in the previous chapters, when discussing the time step size, the mesh size is the limiting factor to the time step size, while the gas temperature and speed of sound depend on the actual solution. However, the mesh size is defined during the discretization phase of the domain. Hence, the proposed idea is to speed up the simulation by increasing the mesh size so that, at equal fluid dynamics conditions, the time step can be larger, hence reducing the simulation time for the physical time considered. The goal is to reduce the simulation time by one order of magnitude, while preserving the accuracy. It is reported again a simplified calculation of time step and crank angle advancement at some typical conditions but for an FSM model.

$$dt = \frac{dx}{a + |u|} \approx \frac{10^{-1}[m]}{(10^2 + 0)\left[\frac{m}{s}\right]} = 10^{-3} = 0.001\ [s]$$

$$d\alpha = \frac{dt * N * 360}{60} = \frac{10^{-3}[s] * 10^3\left[\frac{rev}{min}\right] * 360\left[\frac{deg}{rev}\right]}{60\left[\frac{s}{min}\right]} \approx 6\ [deg]$$

This simple calculation shows that, thanks to an order of magnitude increase of mesh size (from 1 cm to 10 cm), the time step and the crank angle advancement increase by one order of magnitude (from 0.6 deg to 6 deg). It is expected a similar decrease of the simulation time needed for the same real time simulated.

Of course, with a coarser mesh some information is lost, since it is possible to know the solution in fewer points of the domain, however the wave motion is still captured, since the solution methodology is preserved. The typical mesh size which is often referred to as "refined" is a uniform mesh of 1 cm, while the larger mesh, referred to as "FSM" or "coarse", is a uniform or hybrid mesh of 5 and 10 cm. The authors who developed the state-of-the-art numerical methods for refined meshes, such as the Corberán-Gascon method [29,30], recognized that these methods could not suit well the larger mesh stencils. Hence in this work a new method which showed better conservation properties on large meshes, developed recently at Politecnico di Milano, has been applied. The method is called "1D Cell", referring to its relationship with the corresponding three-dimensional method "3D Cell" from which it has been derived [48,49]. As an example of the change of discretization, the pipe presented in Figure 5.1 below shows the different mesh size discretization.
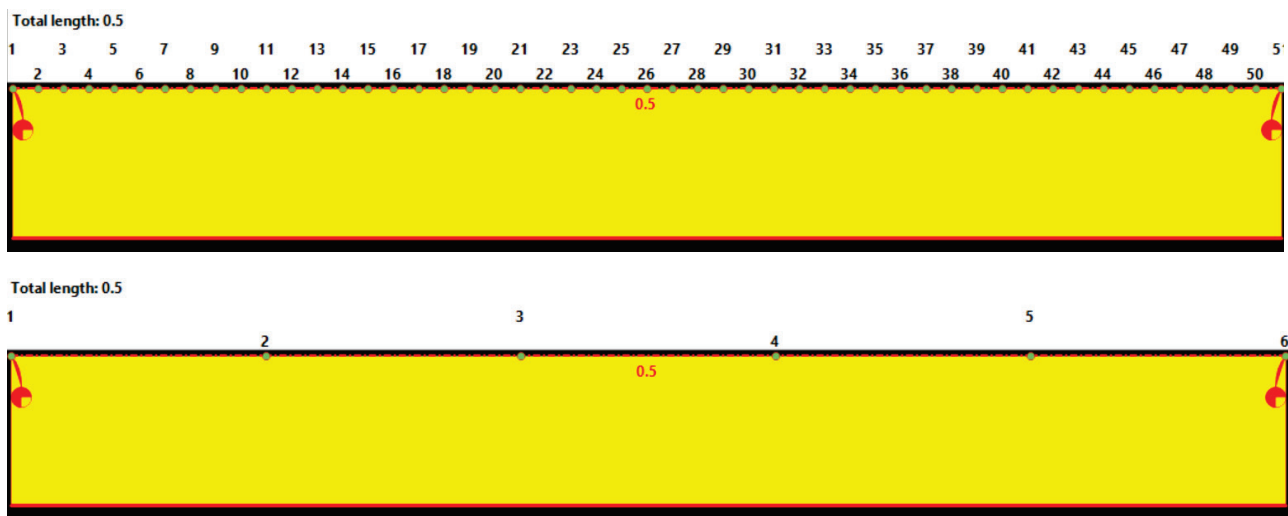

Figure 5.1 – 1D pipe discretization, original and with the increased mesh size, for the same total length.

5.1 The 1D Cell method

This chapter describes the 1D cell numerical method used with coarser meshes, to achieve fast simulations. This method is the 1D derivation of the same method originally developed for 3D modelling described by A. Della Torre and G. Montenegro in [50,51,52,53]. The main difference with respect to the CG (Corberán-Gascon) method illustrated before is that the 1D cell is a finite volume method instead of a finite difference method, like the CG-TVD. This allows the method to be more conservative. The computational stencil differs from the usual one used for the CG-TVD method. This poses the challenge of transferring the solution from the 1D cell domain to the actual computational nodes, where the W and F arrays are defined. The 1D cell method works on cells (c) and ports (p). The ports coincide with the nodes of the discretized domain, while the cells are located between the ports, hence the cells centres do not coincide with the computational nodes. Each cell is geometrically defined by its volume, to represent the actual 1D domain shape, while the ports are defined according to the flow area in between cells boundaries. It is reported the spatial discretization of the original 3D cell method, on a 2D grid in Figure 5.2.
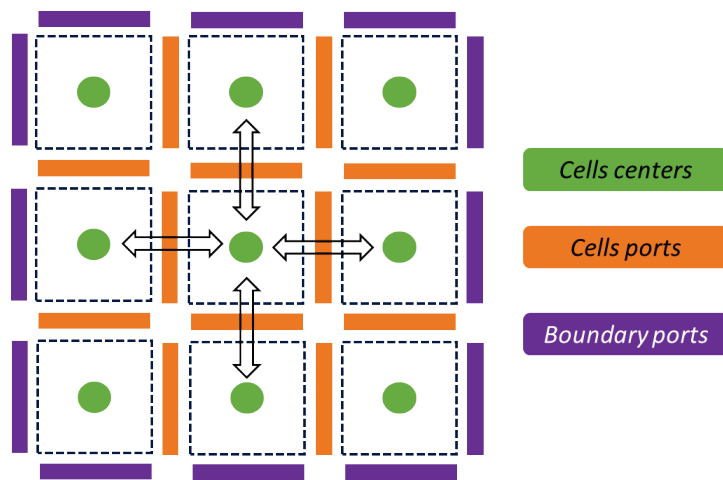

Figure 5.2 – The 3D cell arrangement of cells and connecting ports on a 2D space framework.

The conserved quantities are defined only in the cell centres and the fluxes of the conserved quantities are defined at the ports. The method exploits an explicit, staggered, leapfrog method to advance in time: for each time step $\Delta t = t^{n+1} - t^n$, also an intermediate time $n + 1/2$ is considered. This intermediate step is needed because the fluxes through the ports are defined at this intermediate time in the calculation node positions. The staggered scheme is reported below in Figure 5.3:
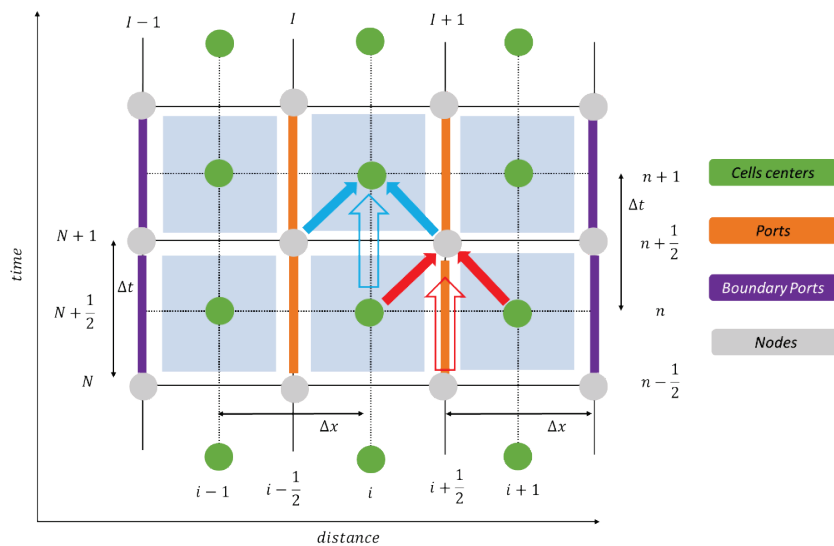

Figure 5.3 – Staggered calculation stencil of the 1D cell method.

Therefore, the ducts are divided into N cells and $N + 1$ ports (equal to the number of conventional nodes) as presented in Figure 5.4. It is now described the solution of the conservation equations by the 1D cell numerical scheme. First, the fluxes through the ports are evaluated and then the cells properties are found as described below.
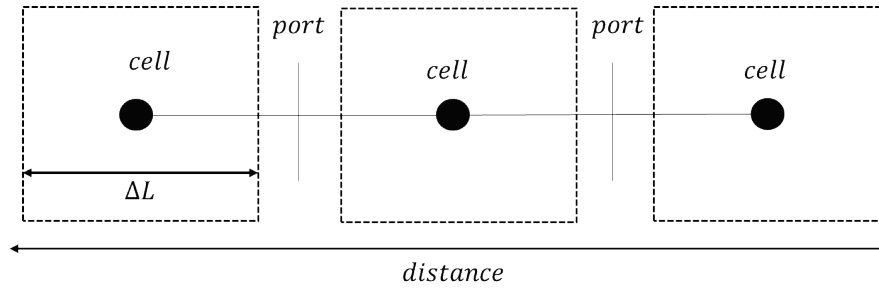

Figure 5.4 – 1D scheme of the 1D cell highlighting cells and ports position.

5.1.1 Mass conservation equation

The mass in the cell at the next time step is equal to the previous mass in the cell plus the net flux of entering and exiting mass flows at the ports, connected to the cell. The area in the ports is the geometrical one in the nodes; the same equation, multiplied by each specie y_i, gives the specie transport equation. Eventually a specie mass source term can be added to the right term of the equation, to include specie reactions. FM_p is the mass flow rate of the port:

$$M_{c,i}^{n+1} = M_c^n + \left(FM_{p,i}^{n+\frac{1}{2}} - FM_{p,i+1}^{n+\frac{1}{2}} \right) \Delta t$$

V_c is the cell volume and F_c is the required cell area as function of the left and right port area, defined as:

$$F_c = \frac{1}{4} (\sqrt{F_{p,i}} + \sqrt{F_{p,i+1}})^2 \qquad\qquad V_c = F_c \Delta x$$

Where the subscript p indicates the port.

5.1.2 Energy conservation equation

Following the same approach, and including a source term for heat transfer, the cell energy balance is:

$$E_{c,i}^{n+1} = E_{c,i}^n + \left(FH_{p,i}^{n+\frac{1}{2}} - FH_{p,i+1}^{n+\frac{1}{2}} + E_{s,i} \right) \Delta t \quad \text{where} \quad FH_p = (\rho u F h)_p \quad \text{and} \quad E_s = \pi D_c \Delta x h_{conv} (T_c - T_{wall})$$

The enthalpy of the cell is evaluated by an upwind logic.

5.1.3 Momentum conservation equation

This equation is applied at the ports considering the neighbouring cells momentum.

$$FM_{p,i}^{n+1/2} = FM_{p,i}^{n-1/2} + \frac{\Delta t}{\Delta x} \left((\rho u^2 + p)_{c,i-1}^n - (\rho u^2 + p)_{c,i}^n \right) F_p + M_{s,i} * \Delta t + DTM_{p,i} * \Delta t$$

The term $M_{s,i}$ represents the friction forces and is evaluated as:

$$M_{s,i} = -FM_{p,i} \frac{|FM_{p,i}|}{\frac{1}{2} (\rho_{c,i-1} + \rho_{c,i}) F_{p,i}} f_{p,i} \frac{2}{D_{p,i}}$$

Both the heat transfer coefficient h_{conv} and friction coefficient $f_{p,i}$ are calculated by dedicated correlations like in the CG numerical method. The term DTM is called "Diffusion Term Momentum" since it is a fictious numerical term introduced to stabilize the 2nd order method and avoid spurious oscillations: it is calculated as a quantity proportional to the divergence of the mass flux, which discretized becomes:

$$DTM_{p,i} = (DF_{p,i} - DF_{p,i-1})/\Delta x_{p,i} \qquad\qquad \text{where} \qquad\qquad DF_{p,i} = \varepsilon_{p,i}(FM_{p,i+1} - FM_{p,i-1})/\Delta x_{c,i}$$

The value of the coefficient $\varepsilon_{p,i}$ is calculated depending on the flow field. The proposed formulation is:

$$\varepsilon_{p,i} = \frac{1}{4}\left| \Delta x_{c,i} \left| \frac{FM_{p,i}}{\rho_{p,i}F_{p,i}} \right| - \Delta t \left(\frac{FM_{p,i}}{\rho_{p,i}F_{p,i}} \right)^2 \right| + \frac{1}{4}\left| \Delta x_{c,i} \left| \frac{FM_{p,i+1}}{\rho_{p,i+1}F_{p,i+1}} \right| - \Delta t \left(\frac{FM_{p,i+1}}{\rho_{p,i+1}F_{p,i+1}} \right)^2 \right|$$

Finally, one last equation is necessary to evaluate the cell momentum, which is necessary to calculate the cell velocity and then the cell pressure and density. This is calculated as an arithmetic average of the neighbouring ports:

$$Q_{c,i}^{n+1} = \frac{1}{2}\left(FM_{p,i}^{n+\frac{1}{2}} - FM_{p,i+1}^{n+\frac{1}{2}} \right)\Delta x_{c,i}$$

It is noted here that the cell momentum is evaluated at each time step, it is not updated from the previous time. The method evaluates the cell properties as:

$$e_{0,c} = E_{0,c}/M_c \qquad\qquad e_{0,c} = Q_c/M_c \qquad\qquad \rho_c = M_c/V_c \qquad\qquad p_c = \rho_c RT_c/MM_c$$

and:

$$h_{0,c} = e_{0,c} + p_c/\rho_c \qquad\qquad T_c = (e_{0,c} - u^2/2)/c_v \qquad\qquad a_c = \sqrt{R/MM_c}k_v T_v$$

In this way, the solution is found in the cells and ports but the actual solution, which must be found to allow the boundary condition resolution, is requested in the usual grid of calculation nodes where the W is evaluated:

$$W(1)_i = M_{c,i}/\Delta x_{c,i} \qquad\qquad W(2)_i = FM_{p,i} \qquad\qquad W(3)_i = E_{c,i}/\Delta x_{c,i}$$

5.2 FSM (Fast Simulation Method) models

In this chapter are described the fast simulation models of the two engines described before. As required by the fast simulation methodology, the only modification apported to the 1D models consists of the mesh size. However due to the physical limitations on the length of the 1D elements, some adjustments have been required to exploit the large mesh while not distorting the actual geometry and main length of the ducts. For example:

- Replace gradual area variations along the pipes with the sudden area variation boundary condition.
- Merge adjacent ducts: some pipes have been merged with the following or previous duct to obtain 1D elements long at least 10, 15 or 20 cm so that a large mesh would not be longer than the pipe.
- When possible, it is preferred to obtain 1D pipes with at least one middle calculation node, especially close to the cylinder valves.
- Merging pipes also usually leads to removing intermediate boundary conditions.

All the other set-up of the model remains unchanged, and a comparison of results has been performed to compare simulation times and accuracy. In principle no change in the diameter of the pipes is required, but occasionally, due to simplifications such as replacing a gradual area variation with a sudden boundary, there might be some diameter changes.

5.3 FSM model and validation of the 3-cylinder spark ignition engine

The FSM has been applied for the simulation of the engine map, to compare the accuracy and the reduction of computational effort achieved. First, the 1D model of the 3-cylinder spark ignition engine has been modified, applying the criteria mentioned previously, to achieve a model with a larger mesh size. The same map has been simulated, also fixing the same number of calculated engine cycles. Then the overall physical time is computed as reported below, while the CPU time is printed in the simulation output, which exploits

an internal intrinsic clock function which gives the total time of CPU used from the start to the end of the simulation.

$$Real\ time[s] = \sum_{i=1}^{Number\ of\ operating\ points} \frac{60\left[\frac{s}{min}\right] * 2\left[\frac{rev}{cycle}\right]}{N_i\left[\frac{rev}{min}\right]} * ncycles_i[number\ of\ cycles]$$

The CPU/real time ratio is then computed as:

$$CPU/Real[-] = \frac{CPU\ time\ [s]}{Real\ time[s]}$$

This quantity gives the indication of how many simulation seconds have been necessary for the calculation of 1 second of real time. If equal to one, it means that the simulation proceeds as fast as the physical time.

The CPU/real time ratio comparison show a terrific reduction of computational effort with a reduction by 85%. This allowed to perform the map simulation in less than 20 minutes, with respect to the 2 hours and 15 minutes required by the refined model. As reported in Figure 5.5, the CPU/Real time ratio is around 2.5 for the FSM approach, whereas it is around 28 with the refined mesh, conventional approach.
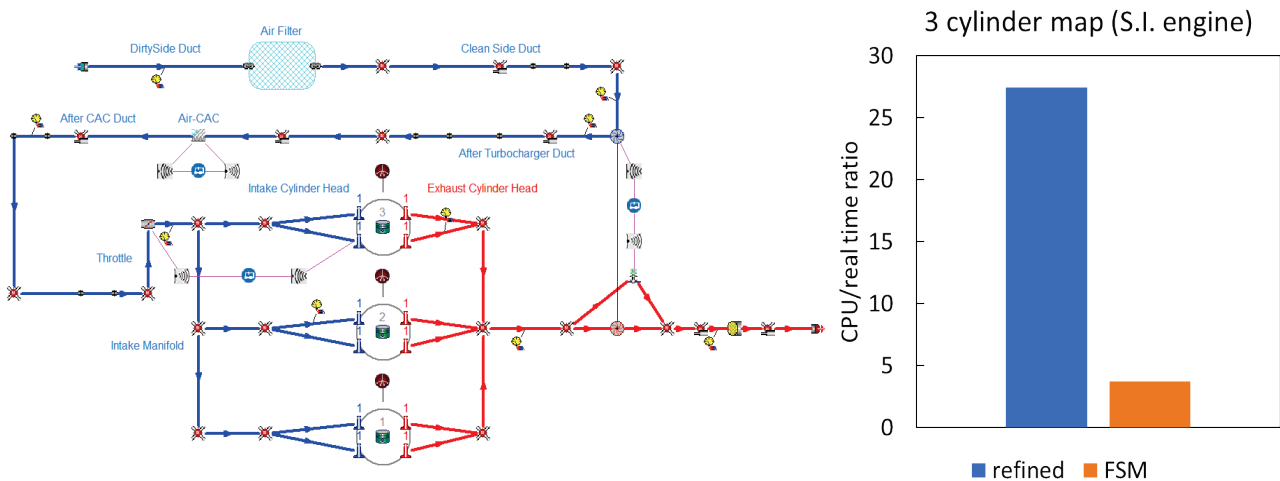

Figure 5.5 – 1D FSM model (left) of the 3-cylinder engine and CPU/real time ratio (right) comparison, for of the simulation of the same map of steady state operating points of the Spark Ignition engine.

In what follows It is presented an analysis regarding the reduction of elements which helps reducing the simulation effort. Figure 5.6 below shows that the simplification process has reduced the number of computational nodes considerably. Also, the number boundaries and pipes has been reduced by merging ducts and simplifying the model. However, the main features of the engine have been preserved.
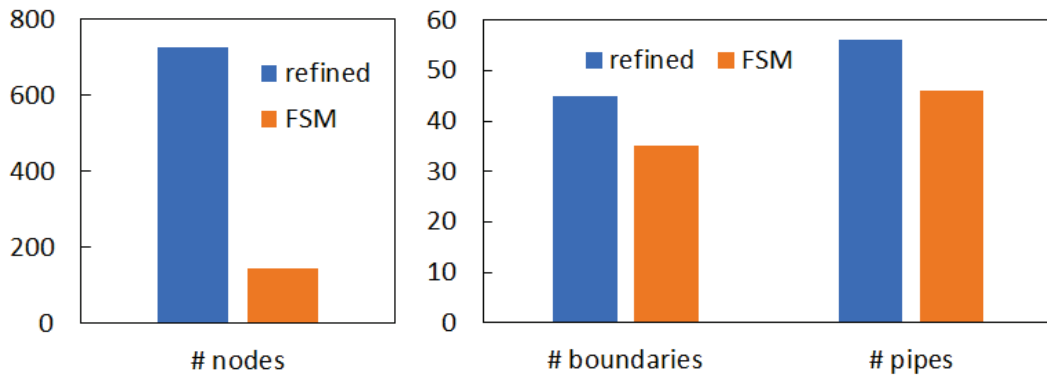
Figure 5.6 – Number of elements (nodes - left, pipes and boundaries - right) in the 1D scheme
of the 3-cylinder refined and FSM model.

The goal of reducing the computational effort has been achieved. It is now analysed the difference in results between the refined and FSM model, as reported in the following Figures 5.7 and 5.8. The predicted BSFC of both models is very similar for most of the operating points with higher discrepancies, still contained within less than 5%, at full load, 1500 rpm engine speed. It is also reported the comparison of the CO concentrations at cylinder-out emissions, which shows lower differences. In both comparisons the predictivity of the FSM model is confirmed, showing its ability to capture the trends of the refined model.
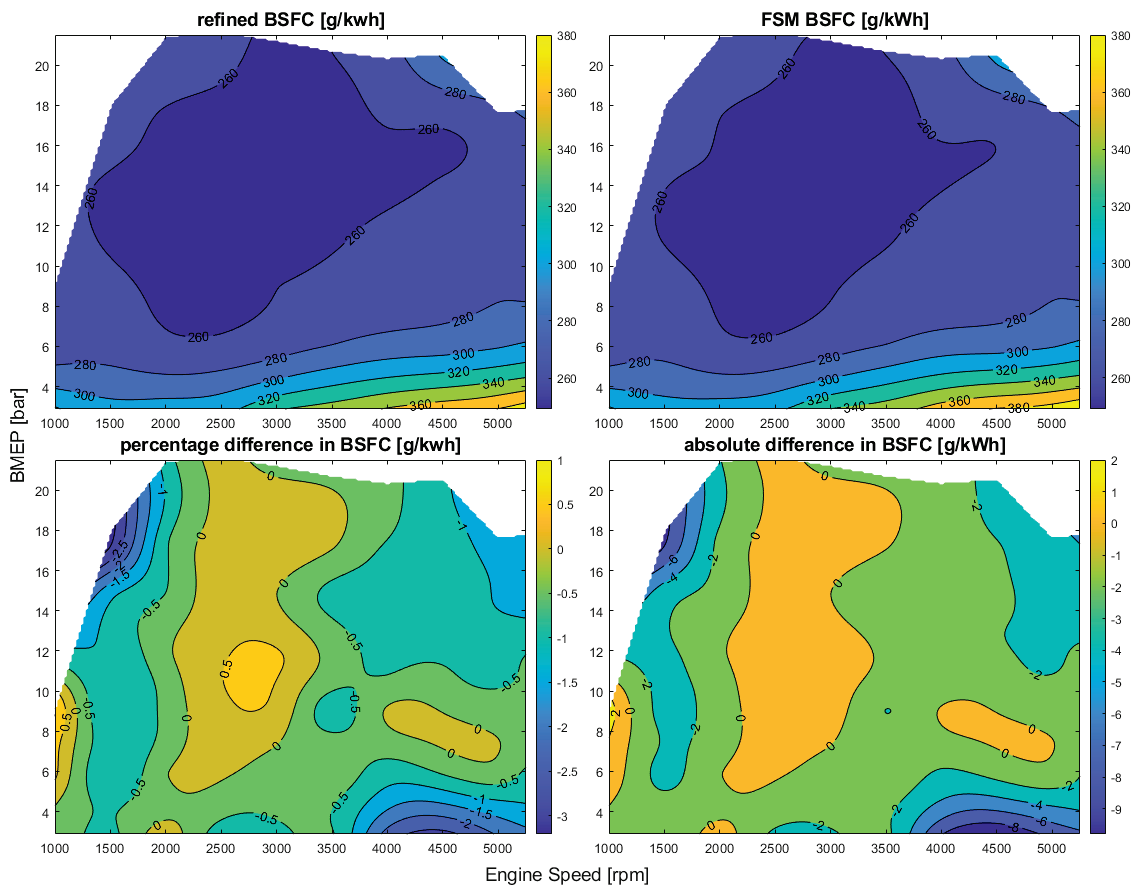

Figure 5.7 – Comparison of BSFC between refined and FSM 1D models with percentage error and absolute difference.
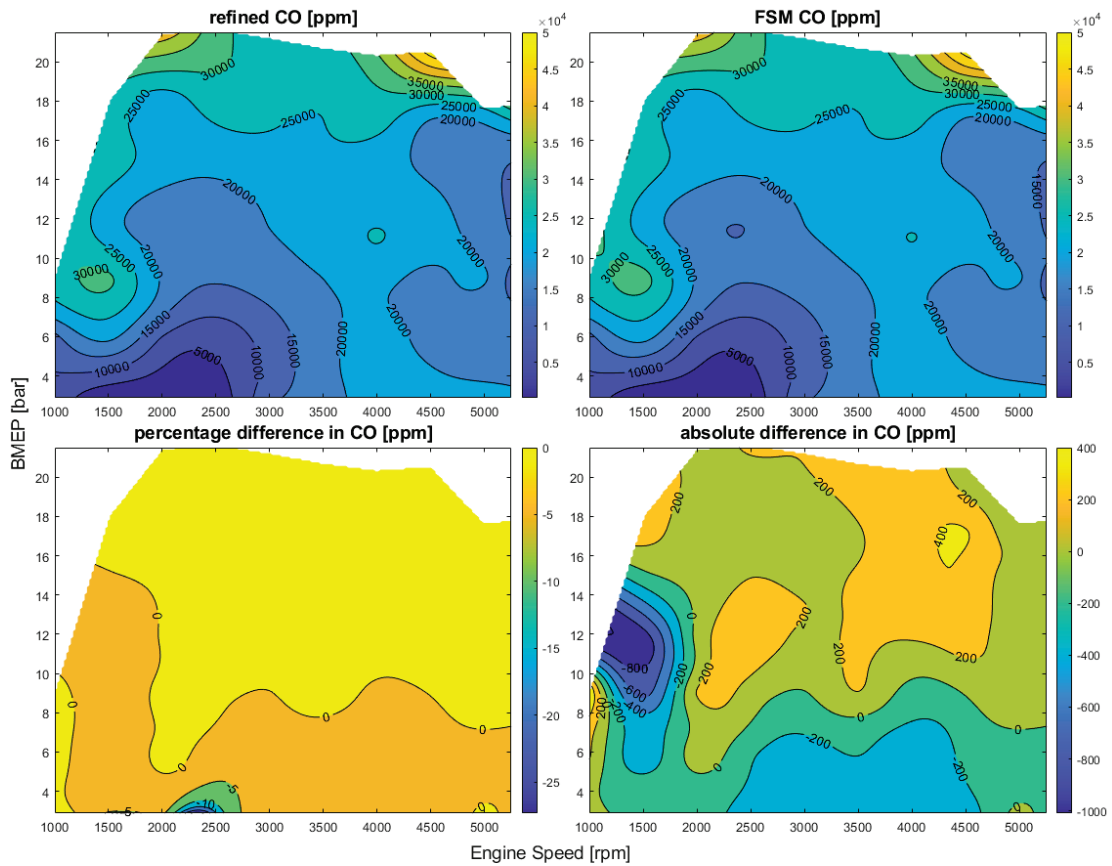
Figure 5.8 – Comparison of CO between refined and FSM 1D models with percentage error and absolute difference.

In Figure 5.9 below it is reported a comparison of the instantaneous pressure traces in different locations along the engine pipe systems, at some operating conditions. The refined (1cm mesh) and the FSM model (10 cm mesh) achieved very similar results, very similarly capturing the wave motion.
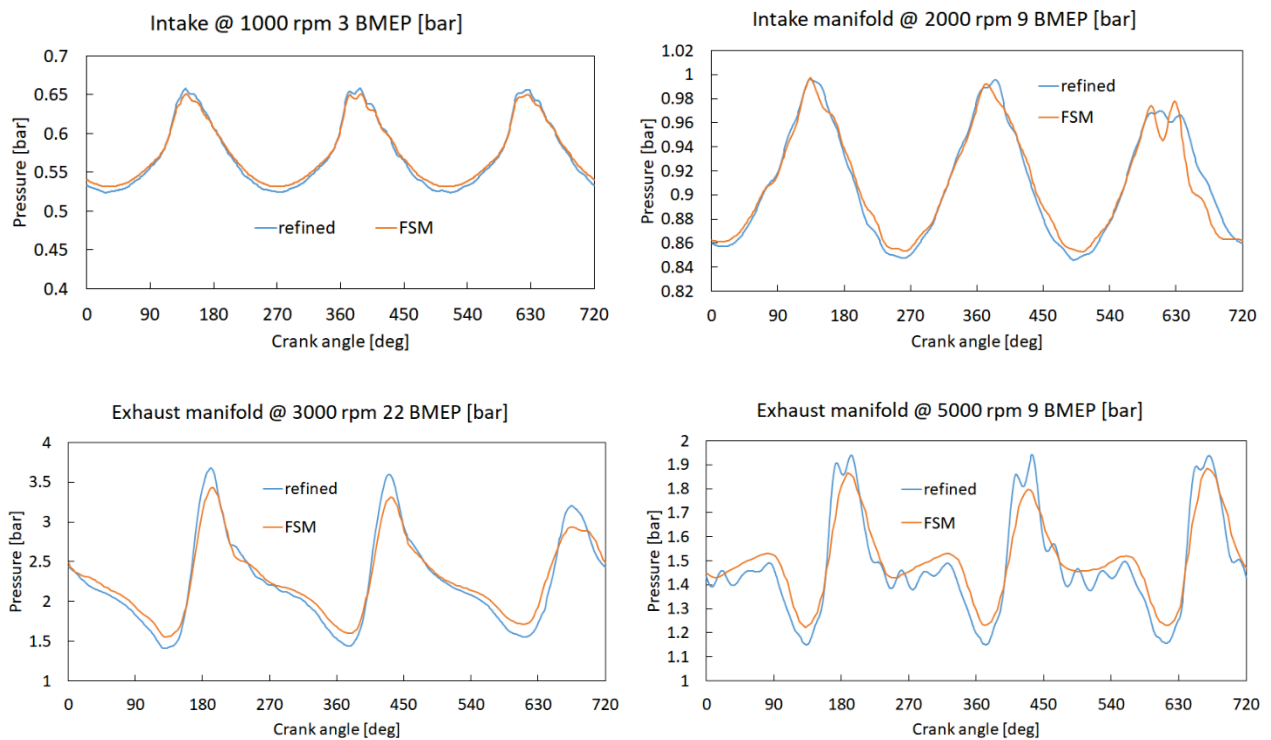

Figure 5.9 – Instantaneous pressure in the ducts, comparison of refined and FSM models of the 3-cylinder SI engine.

5.4 FSM model and validation of the 6-cylinder Diesel engine

In Figure 5.10 below it is reported the FSM 1D schematic of the 6-cylinder Diesel engine. It can be noticed how the layout is still the same and the architecture of the engine has been preserved. The CPU/real time ratio to simulate the whole engine map has decreased to just 5 from around 55. This means that the engine map simulation, which took 15 hours, now requires just over an hour.
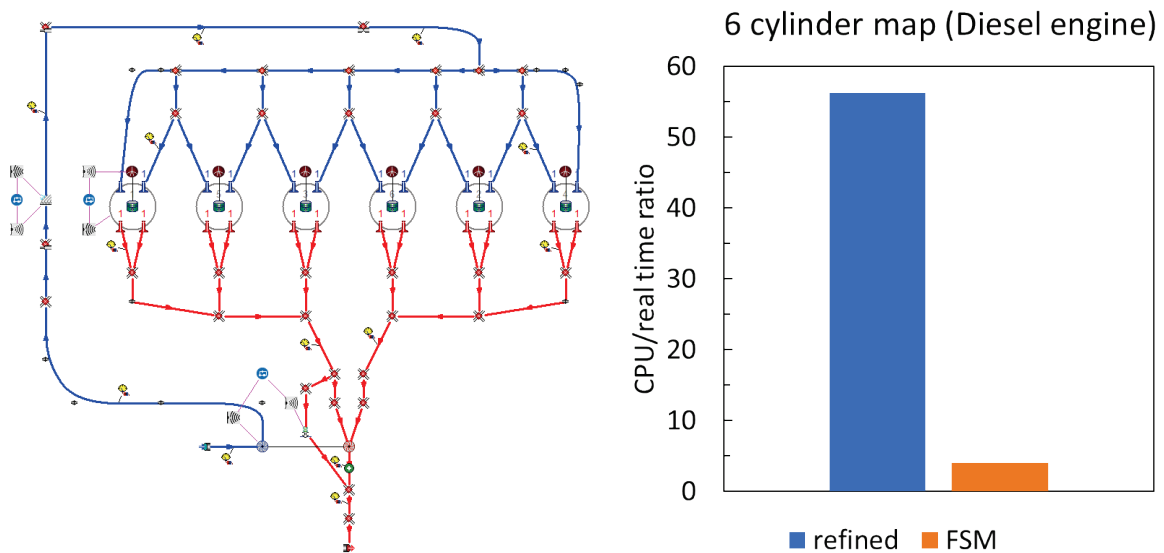

Figure 5.10 – 1D FSM model of the 6-cylinder engine (left) and CPU/real time ratio (right);
Comparison of the simulation time for the steady state operating points of the Diesel engine map.

In Figure 5.11 below it is reported a numeric comparison of the number of boundary conditions, pipes and nodes with respect to the refined mesh. As forecasted, keeping the total length on the intake and exhaust manifold systems and subsystems equal to the refined mesh configuration, the larger mesh has reduced the overall number of computational nodes, while the number of boundaries and pipes has remained constant.
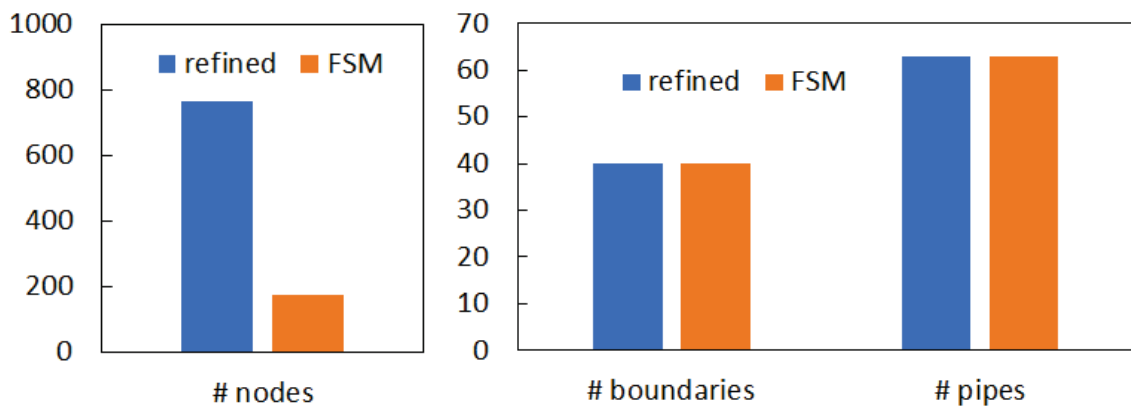

Figure 5.11 – Number of elements (nodes - left, pipes and boundaries - right) in the 1D scheme.

It is also important to check if the results of the FSM model depart from the refined approach. Figure 5.12 below reports the comparison of BSFC between the refined and FSM simulation. The two simulations show very close results, allowing the use of the FSM model for faster simulations, while maintaining a satisfactory accuracy.
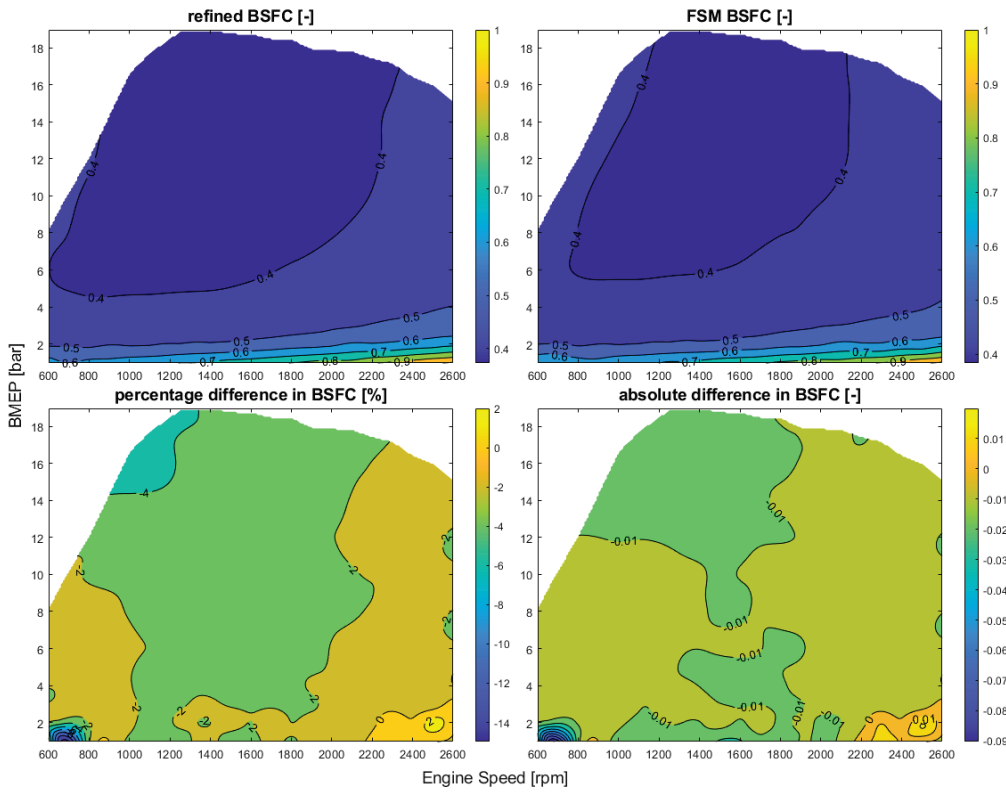
Figure 5.12 – Comparison of BSFC between refined and FSM 1D models with percentage error and absolute difference.

In Figure 5.13 it is also reported the same analysis focusing on the cylinder-out NO_x emissions. The comparison shows higher differences, still limited. However, the NO_x prediction is very sensitive to maximum pressure and temperature in the cylinder that, even within a very similar engine load, can vary enough to result in a detectable NO_x difference prediction.
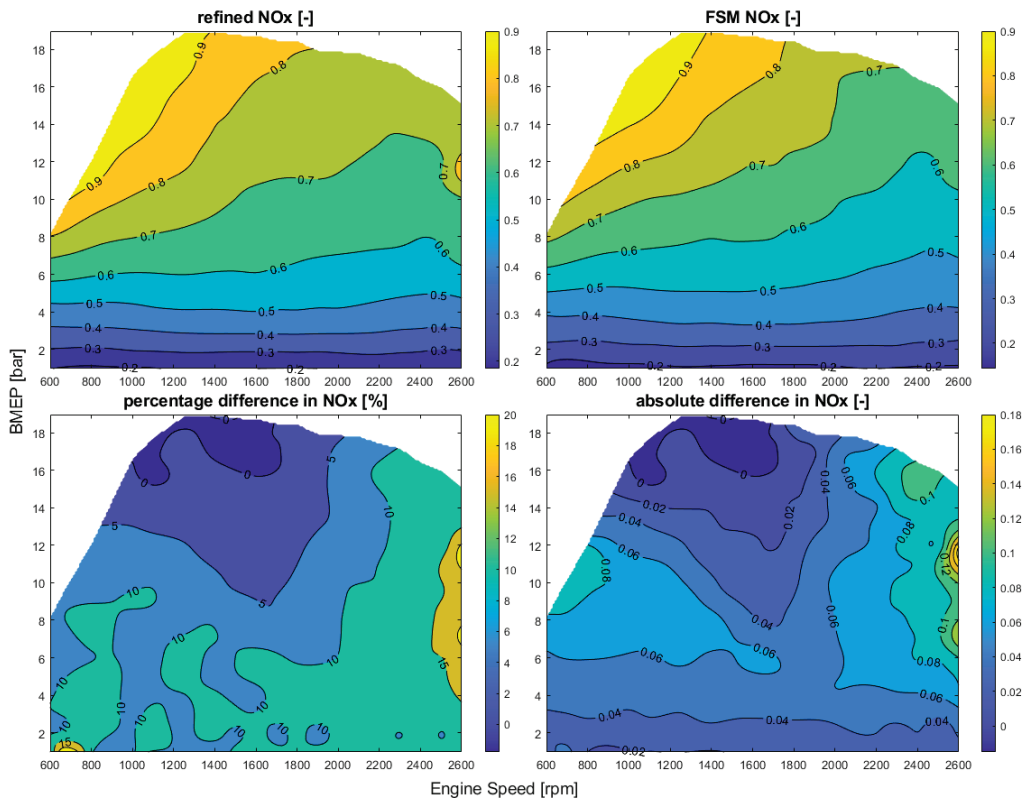

Figure 5.13 – Comparison of NO_x between refined and FSM 1D models with percentage error and absolute difference.

A comparison of the instantaneous pressure waves along the engine pipe systems is shown in Figure 5.14. The pressure pulses show some differences, still limited and due to the different discretization and simplifications made in the 1D model. Both the intake and exhaust wave motions are well captured at low and high load and different engine speeds.
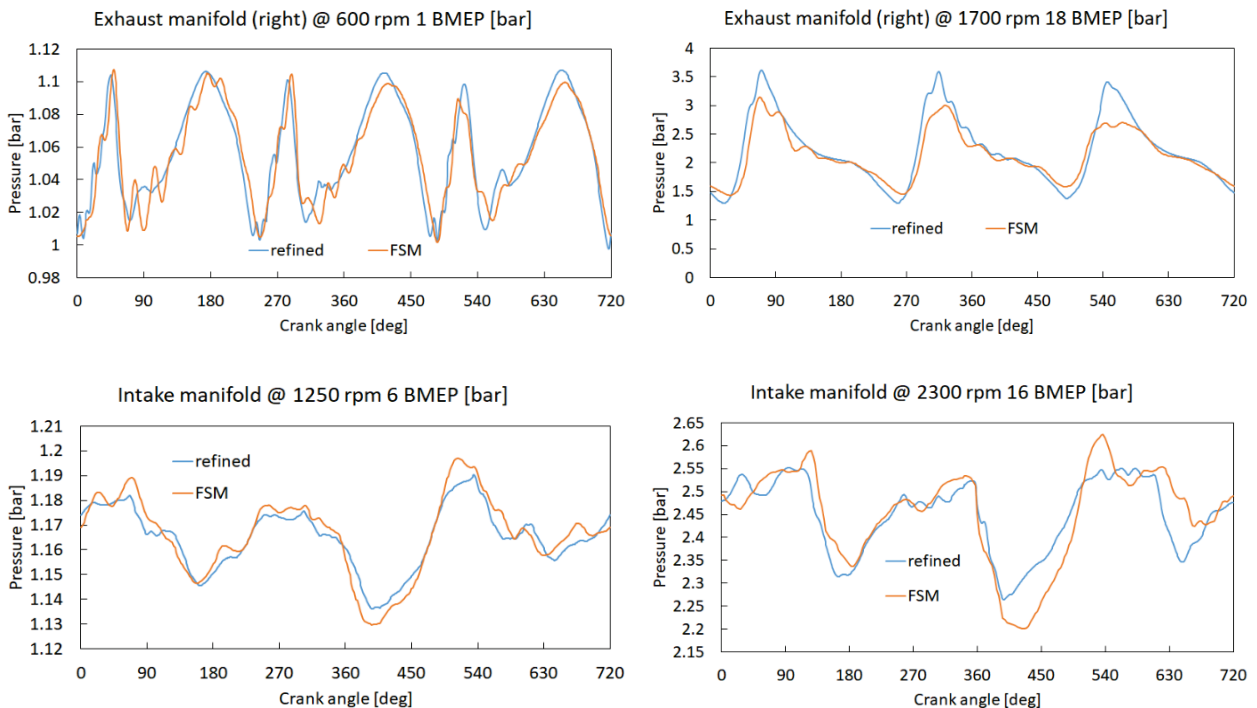

Figure 5.14 – Instantaneous pressure trace in the intake and exhaust ducts, at convergency, of some operating conditions; Comparison of refined and FSM models of the 6-cylinder CI engine.

5.5 Other techniques to speed up the simulations

Different simulation techniques to speed up the calculation, without compromising the accuracy of the 1D solution, have been proposed by other authors. In the work of [26] it is proposed to exploit the fact that usually, with a uniform mesh, the limiting cell which determines the time step is on the exhaust side, due to the higher speed of sound in the hot gases. This means that the calculation at the intake side, at equal mesh size is advancing with a low CFL. If the simulation solver could advance the intake and exhaust domains by different time steps, it would be possible to reduce the simulation time, since the intake system would be solved with larger time steps. However, this poses significant challenges to the solver organization, to manage the asynchronous solution of the boundaries. Nevertheless, this approach gives great opportunity for the reduction of the simulation time, without interfering with the mesh discretization process.

On the other hand, a different technique could be exploited to speed up the simulation. Since it is not necessary to solve each pipe after the other, it would be faster to solve all pipes in parallel, by exploiting to the maximum the CPU capability instead of exploiting only a CPU's single core capacity. This 'parallelization' consists in assigning to each CPU core the solution of an equal number of ducts. However, this parallelization can be fully exploited if the simulation can proceed in parallel from the beginning to the end of the simulation. This means that each core should write on its own variables, instead of just splitting and merging only the solution step of the simulation. However, this technique requires to completely rewrite how the source code is organized in order to be fully exploited.

Another technique to speed up the simulation, that has been applied in this work, can be exploited only for the simulation of the steady state maps. Since it is not necessary to wait for the calculation of the solution of one operating point before the next one, the simulation of the total number of operating points can be

subdivided into n different simulations running on the n physical cores, exploiting the full CPU computation capability (where n is the available number of physical cores of the CPU).

5.5.1 Lumped parameter or mean value IC engine models

In this paragraph it is presented an alternative simulation method of internal combustion engines during transient. It is worth mentioning these models in the framework of this thesis because they are part of the modelling tools that can be exploited to have fast simulation of engines under transient conditions focusing of engine control [54]. The goal of the chapter is to highlight the existence of these models and asses what modelling principle is behind and what results can be obtained and asses how fast they can be with respect to real time.

These models have traditionally been used as tool to develop engine control strategies and design controller architectures. An extensive description can be found in [55]. In particular, these models are called lumped parameter engine models or, more commonly, Mean Value Models (MVM). The name suggests their modelling principles. The engine is modelled as a system of connected 0D elements on which the conservation equation of mass and energy are applied. The equation describing each component are mean value equations and it is not a crank-angle resolve solution. For example, the cylinders are one of these 0D elements and the mass flow $\dot{m}_{cyl}$ elaborated can be assumed to be:

$$\dot{m}_{cyl} = n_{cyl}\,\lambda_v \rho V N/\varepsilon$$

Where n_{cyl} is the number of cylinders, V is the engine displacement, N is the engine speed and ε is the number of revolutions per engine cycle. The volumetric efficiency λ_v has to be assumed or computed by means of 1D models and ρ is the air density used for the calculation of λ_v. In a spark ignition engine, a throttle body is typically present upstream of the cylinders, isolating a volume between the throttle and the cylinders. If the mass flow elaborated by the throttle $\dot{m}_{thr}$ at a given opening percentage is known, the mass and energy balance applied to the intake manifold volume, assuming constant ambient temperature equal to the intake manifold T_m, is:

$$\frac{\partial p_m}{\partial t} = \left(\dot{m}_{thr} - \dot{m}_{cyl}\right)\frac{RT_m}{V_m}$$

Where p_m is the intake manifold pressure, t is time, R is the gas individual constant and V_m is the manifold volume. The mass flow through the throttle valve $\dot{m}_{thr}$ can be calculated from orifice equations for compressible fluid flow [17]. Applying this method to all the systems present in an engine lead to a system of differential equation than con be solved simultaneously and integrated to obtain the solution. Each subsystem size (volume) influences the engine response to the mass flows variations; hence the volume of each section of the intake and exhaust manifold is calculated according the 1D model or real engine volumes. In the MVM model can be included components such as compressors, turbines, wastegates and intercoolers, isolating volumes of the intake and exhaust manifold where an equation, like the one of the intake manifolds is applied. The inertia of the turbocharger is also included, determining the evolution of the turbocharger shaft speed depending on the torque balance on the shaft. The engine performance, such as brake power P_b, can be computed as well, with simplified equations such as:

$$P_b = \eta_g LHV \dot{m}_f$$

The engine global efficiency η_g is assumed or taken from results of a 1D simulation, LHV is the low heating value of the fuel and $\dot{m}_f$ is the fuel mass flow rate, obtained dividing the fresh charge mas s flow rate $\dot{m}_{cyl}$ by the imposed air fuel ratio at which the engine is operating.

A MVM model has been developed in a MATLAB Simulink® environment to investigate the potentiality of this approach. Below are reported the results of a spark ignition turbocharged engine MVM applied to transient

simulation. The simulated operating condition is at fixed engine speed (2500 rpm) and fix throttle and wastegate opening. The simulated time is of 15 seconds of real time. The CPU simulation time was equal to 0.6 seconds, achieving an impressive CPU/real time ratio of 0.04, much faster than real time.

In the Figure 5.15 is shown that the model correctly predicts the mass flow rate of the exhaust being higher than the intake mass flow, with a b-pass mass flow rate through the wastegate due to the partially open position of the valve. Moreover, the mass flow increases as the turbocharger spools up.
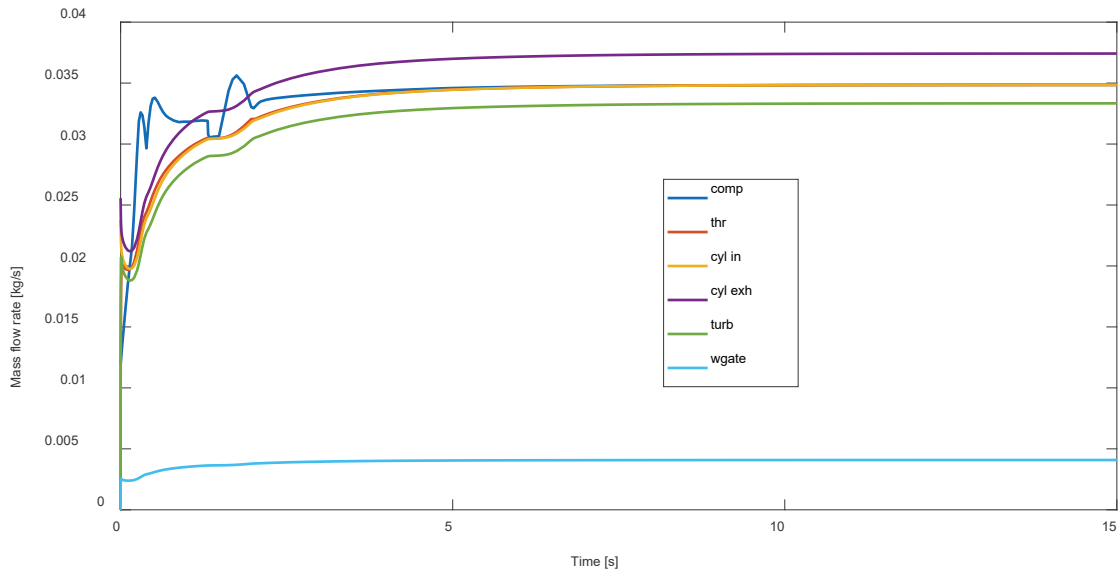

Figure 5.15 – Mass flow rates along the MVM.

In Figure 5.16 instead are reported the predicted pressures in each subsystem, which evolve depending on their respective mass flow balance. The pressure after the throttle is lower due to the partially closed position of the throttle body.
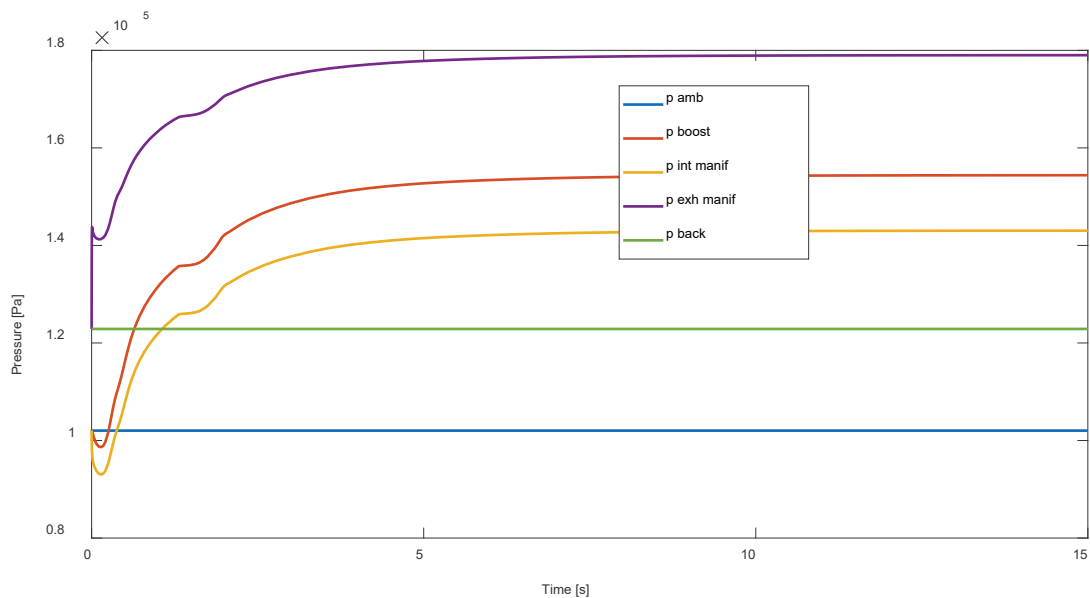

Figure 5.16 – Pressure along the MVM.

The turbocharger speed calculation is reported in Figure 5.17, the evolution correctly reaches an equilibrium once the mass flows reach a steady state and the power balance on the shaft is satisfied (see Figure 5.18).
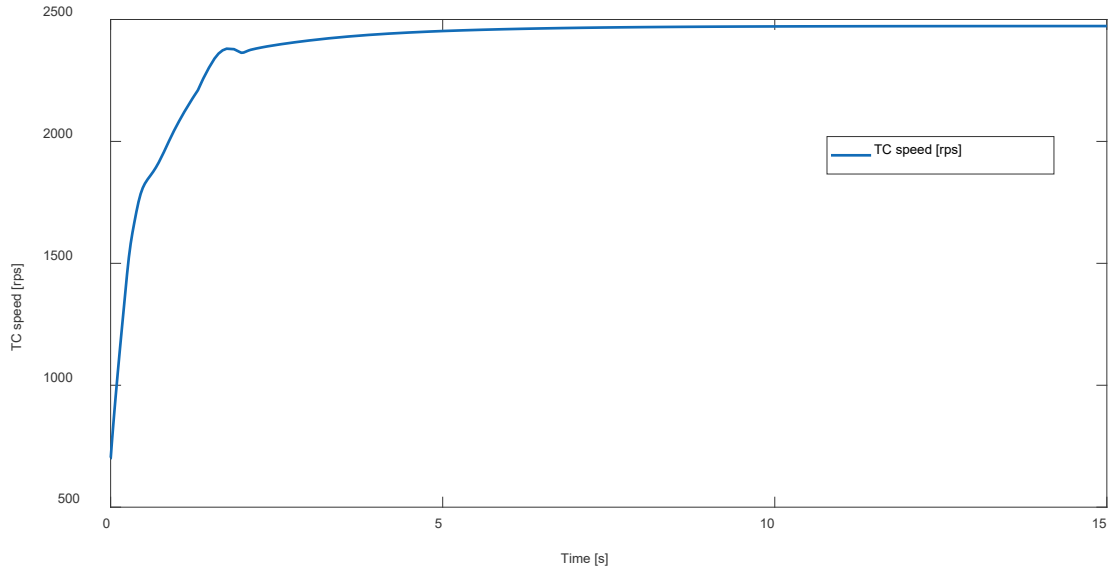
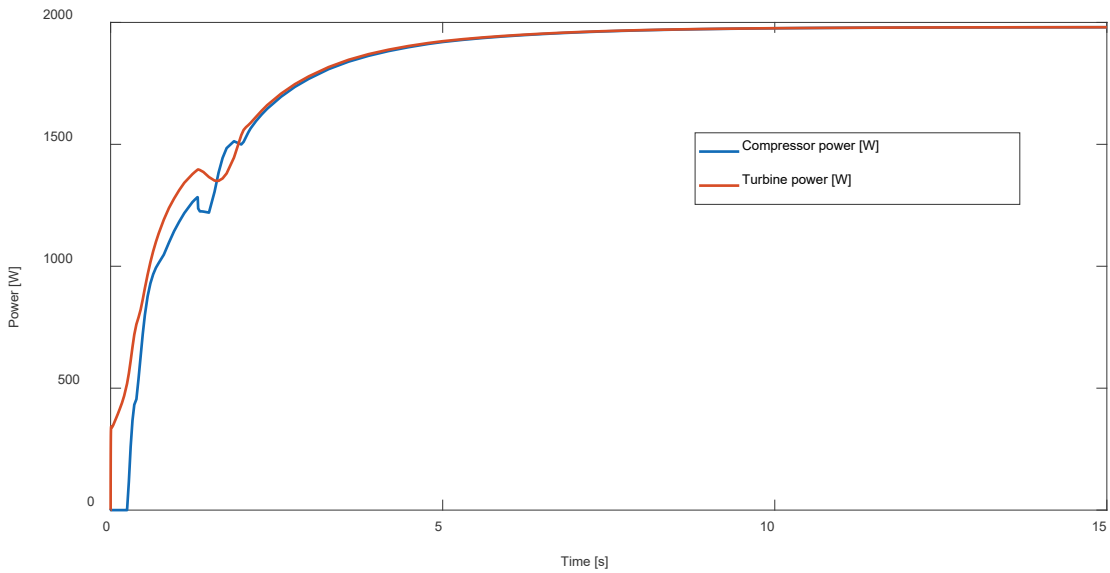Figure 5.17 – Turbocharger speed evolution in the MVM.

Figure 5.18 – Turbine and compressor power matching during the transient computed by the MVM.

The computed engine power during the transient is shown in Figure 5.19, correctly increasing as the mass flow rate elaborated by the engine increases. The fuel consumptions shown in Figure 5.20 consistently increase with the engine power.
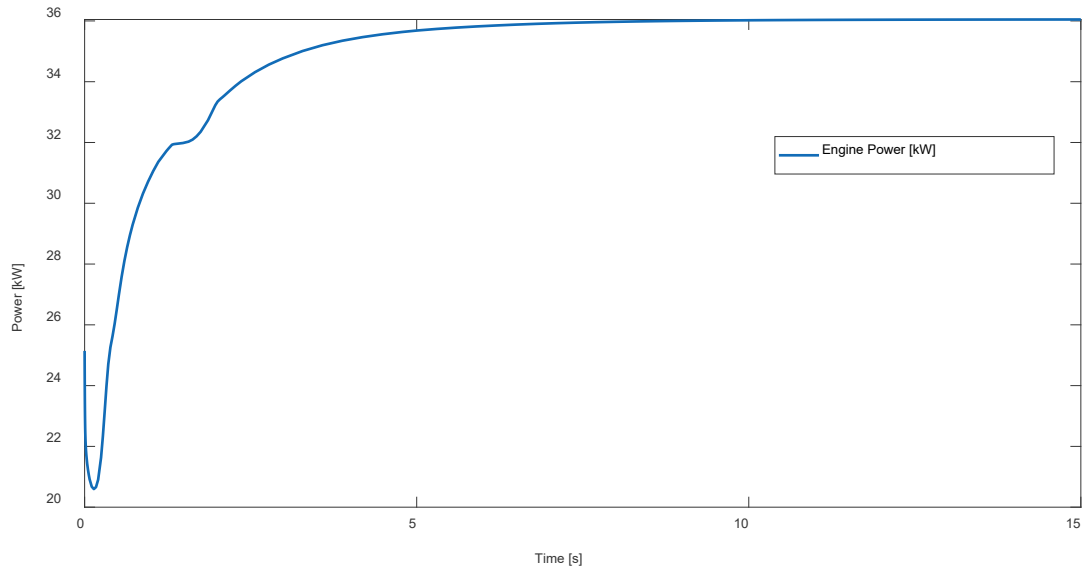
Figure 5.19 – Engine power computed by the MVM.

The engine emissions are not predicted, but by means of a lookup table result from a 1D simulation, could be estimated according to the instantaneous engine speed and torque. Additionally, with the MVM no information is predicted regarding the in-cylinder combustion process such as in cylinder pressure, temperature, or heat release rate.
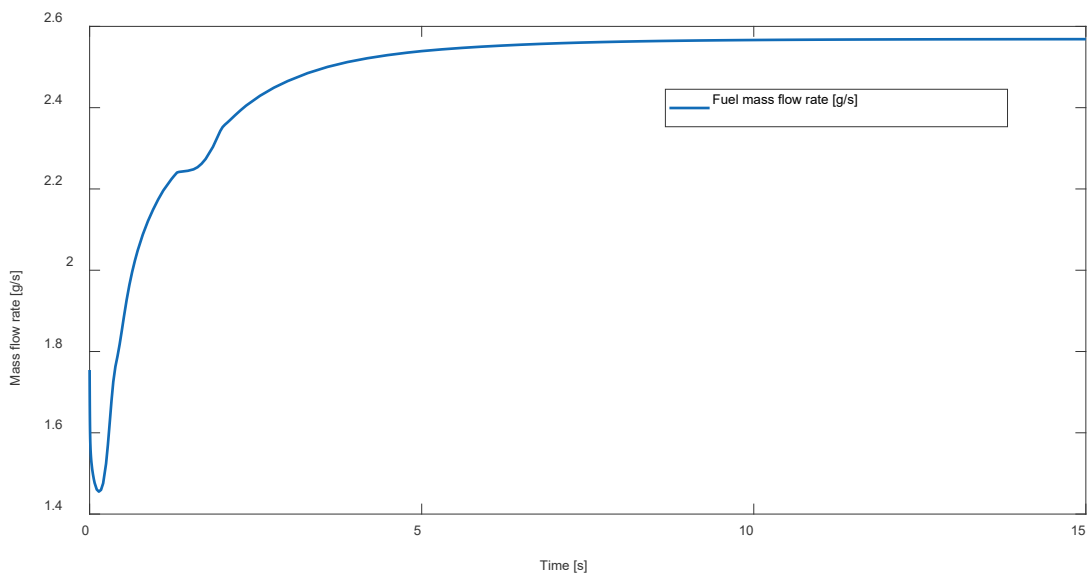
Figure 5.20 – Engine fuel consumption computed by the MVM.

These models allow to predict engine performance in terms of transient response and characteristic times and are very interesting as a potential trade-off between the speed of a map-based simulation and the accuracy of a complete 1D model. For these reasons these models are widely used in the field of the automation and advanced control system engineering, to develop fast and accurate control systems that are tested and calibrated on a control-equivalent model before being applied to the real engine.

6. Driving cycle simulation with the 1D crank angle resolved model

This chapter describes the simulations of different types of driving cycles exploiting the 1D engine models previously discussed. In particular, the results obtained by the simulation of these cycles are compared with experimental data to validate the developed models under engine transient conditions. More specifically, the developed 1D models have been calibrated based on steady state maps and used to simulate transients the same engine in transient conditions, varying continuously the load and the revolution speed. Both the refined and FSM approach have been used for the calculation and the trade-off between accuracy and computational time reduction is discussed.

The transient simulation is conceptually similar to the simulation of a sequence of steady state operating points of the duration of the whole driving cycle. This means that the engine model runs across the mapped points, interpolating the operating parameters from the mapped information, i.e., spark advance, injection and valve timings and so on. In this framework, it is important to highlight that the starting point for is the modelling and validation of the 1D engine under steady state conditions, based on the engine map operating points, which was described in previous sections. This characterization allows the virtual engine to run across any point of the speed and load range during an RDE cycle, consistently adapting all the operating parameters from the knowledge of the steady state map.

During transients the engine speed is imposed and changed every thermodynamic cycle according to the experimental data. The target of the other PID controller on the intercooler and on the boost control can either be used asking them a continuously varying target equal to the measured actual value or by interpolation of the available steady state map. The torque of the engine is instead asked to the PID controller acting on the throttle valve or fuel injection (in case of CI engines). This is crucial difference with respect to the transient simulation done exploiting a map-based engine model, which instantly gives the requested torque provided by lookup tables. Instead, using a 1D crank angle resolved model, the torque output physically depends on the calculated mass of fresh charge trapped in the cylinder (volumetric efficiency), which come from the fluid dynamic solution of the 1D flow equations. This allows to have a more physical based model of the engine which tries to follow the torque profile target.

At the light of these considerations, it is possible to evaluate the responsiveness of the engine and develop refined control strategies to improve the driveability and, eventually, the time-to-torque response of the engine. This also allows to not rely on emission look up table but to predict cylinder out-emission considering instantaneous engine conditions instead of steady state behaviour.

6.1 The importance of modelling the star & stop on electrified vehicles

During some of the experimental cycles investigated, the engine start & stop strategy has been adopted, as frequently happens in modern ICE powered vehicles. In this work the same has been developed for the 1D model transient simulation. The importance of the start & stop modelling is crucial for modelling the electrified vehicles since the thermal state of the engine and of the EAT system depends on the ambient conditions and duration of the on-off events. Hence, it is important to correctly simulate these phenomena to develop the ECU logics behind the engine management algorithms that allows to meet the pollutant emission regulations.

From the 1D model point of view the simulation must not be stopped since it is necessary to keep solving the fluid dynamics to compute the thermal transient of the exhaust pipes, even if the gas is not flowing anymore in the ducts. To this purpose it has been developed in the 1D model the possibility of stopping the engine and keeping active all the other components, such as turbochargers, catalysts (heated or not heated) and so on. To turn off the engine, while preserving the current software architecture, the cylinder deactivation is exploited. All the cylinders are deactivated, and the engine speed is set to a default value so that the physical time can advance. This also allows to better control the engine, since a thermodynamic duration at very low

engine speed would last more than some seconds and since the actuation of the engine occurs with the engine cyclicity the results would not be satisfactory. The deactivation of the cylinders consists in keeping the poppet valves closed. During the engine off events the engine friction is also set to zero since the crank shaft is not moving.

Figure 6.1 shows the gas and wall temperature evolution during the RDE cycle that will be simulated in this chapter. It is evident the on/off periods and the consequent cool down and warm up phases of the exhaust pipes. For clarity, at this stage (results of chapter 6) the cylinders wall temperatures are instead constant and will be done only in chapter 7, exploiting the co-simulation framework developed.
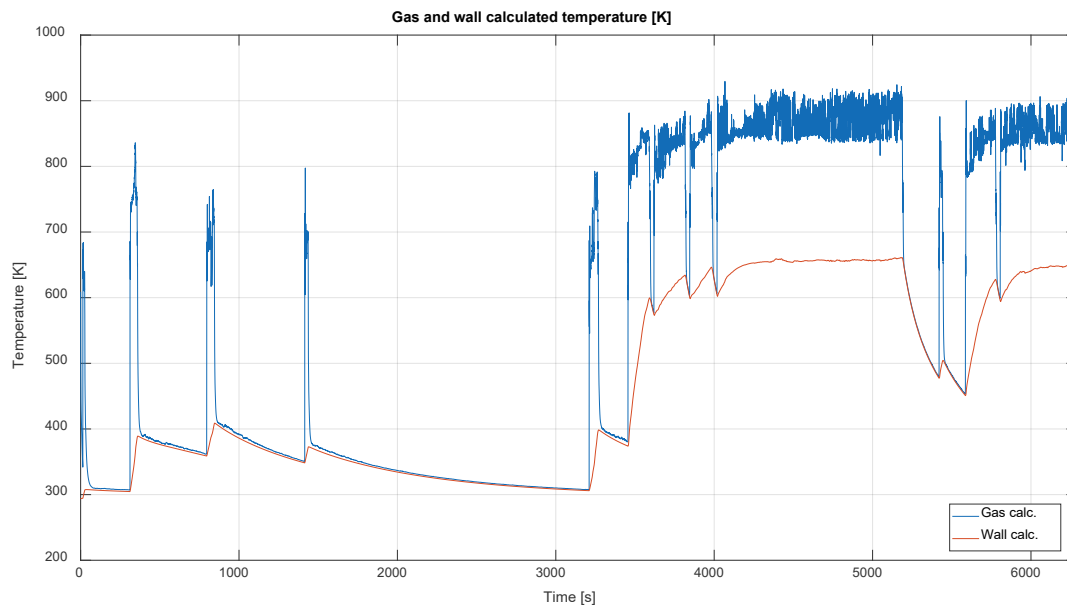

Figure 6.1 - Calculated gas and duct wall temperature in the exhaust manifold upstream of the turbine outside of the head, during the simulation of the RDE cycle of the 3-cylinder engine.

An additional contribution has involved the modification of the numerical solution of the compressor boundary condition. When the real engine is turned off, the cylinders stop breathing the air, but a mass of high-pressure air remains between the compressor and the cylinders. Due to the pressure difference between the intake manifold and the ambient, the trapped air reverses its flow though the compressor and exits from the intake of the engine. This was not supposed to happen in the numerical solver which was developed to simulate a running engine. Hence, the compressor boundary condition has been modified to allow backflow when the engine is stopped. The compressor boundary condition is hence temporarily solved as a normal junction between two ducts, to allow a flow reversal.

The turbine boundary condition did not require any modification, because the pressure difference spontaneously empties the exhaust manifold, by expanding the gas through the turbine or through the wastegate valve.

In Figure 6.2 it is presented an example of the modified behaviour of the boundary condition when the engine stops. The 6-cylinder diesel engine is simulated at fixed engine speed (1750 rpm) and fixed load for 20 seconds, then the engine is turned off. As highlighted by Figure 6.2, the mass flow reverses, and the pressure drops to ambient conditions.
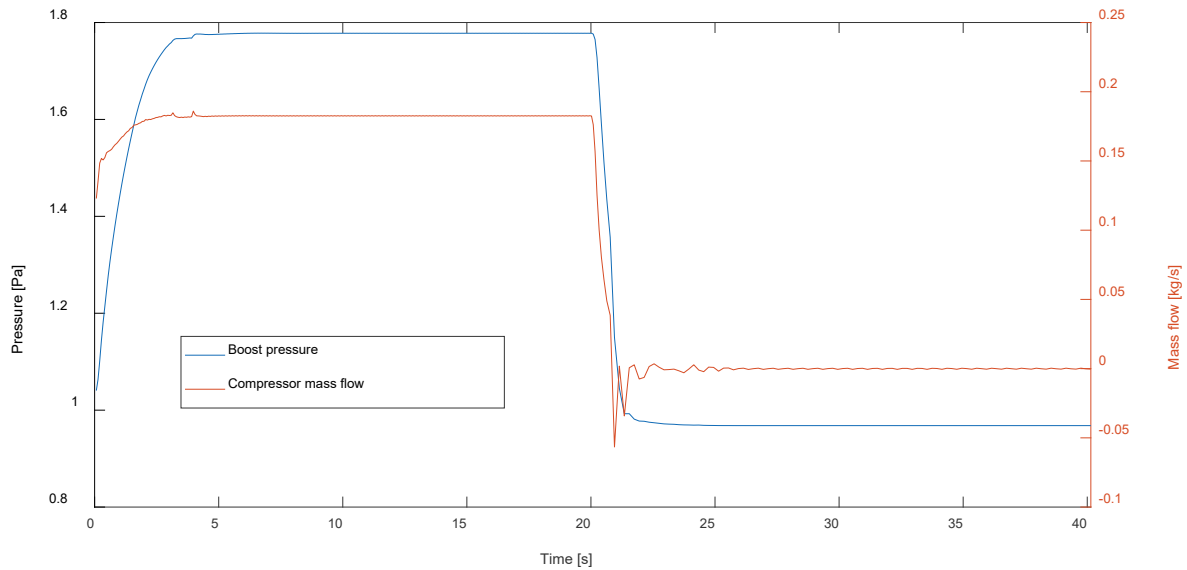
Figure 6.2 – Compressor reverse mass flow and intake manifold emptying when engine stops.

The start & stop events also influence the simulation time, since the gas velocity becomes zero in the whole domain, the time step size increases and the CPU/real time ratio decreases.

6.2 Gasdyn RDE cycle simulations via Simulink® control

To allow the simulation of the RDE cycle, mimicking the control from the ECU, the Gasdyn code needed to be properly interfaced with a controller to allow the real time control of engine parameters. To this purpose it has been developed a co-simulation framework to allow the interactivity between the Simulink® environment (used for control purpose) and the Gasdyn code based on S-functions. In Figure 6.3 it is shown the strategy adopted by the 1D code to simulate a single thermodynamic cycle with all the inputs and outputs that are needed in the co-simulation framework. The experimental data used as inputs (engine speed, engine brake torque, lambda) and to validate the simulation results have been provided by UPV as a result of an intensive simulation campaign carried out the test engine.

The flow diagram of Figure 6.3 highlights how the engine model is a "black box" which is following the input received and gives the quantities required as output. The engine speed and requested engine torque are stored in tables as function of time and sent as input to the engine model, which internally adjusts the operating conditions. The engine speed is directly imposed, while the engine torque depends on the load control. In this case the load is controlled by an internal PID controller, which regulates the throttle valve opening position while monitoring the resulting engine torque. Further important engine parameters to be controlled during the RDE cycles are the air-fuel ratio (lambda), the boost pressure to be achieved by the turbocharger and the intercooler effect. These three quantities continuously vary during the test cycle.

In particular, the lambda value is imposed by acting on the amount of fuel injected. The target required boost pressure and intercooler temperature are targeted by the internal PID controllers: the first acts on the wastegate position, while the second acts on the intercooler wall temperature, to achieve the target outlet gas temperature.

Regarding the engine start & stop events, the off-on signal is sent to the engine according to the experimental engine speed value. A threshold of 700 rpm is used to turn on or off the engine and the strategy is implemented in Simulink® with a user defined MATLAB function.
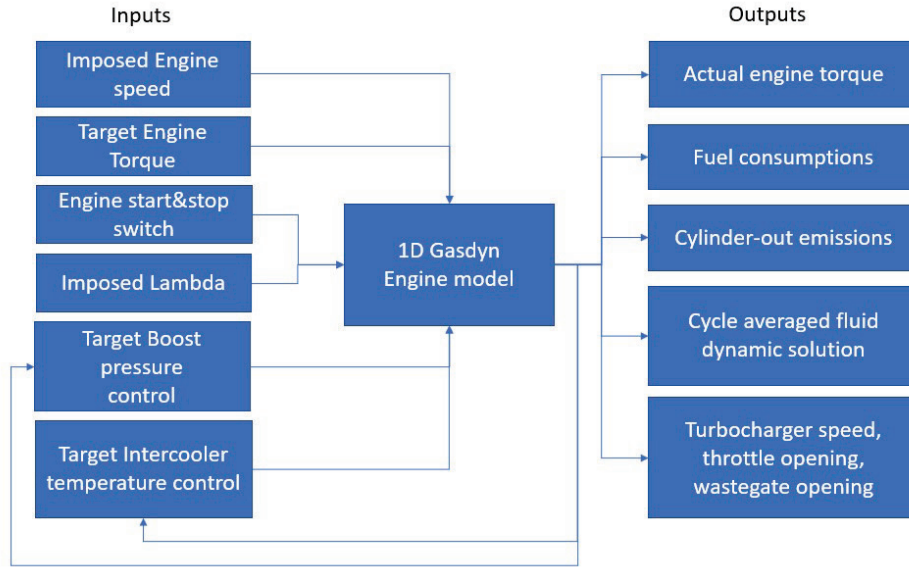
Figure 6.3 – Simplified schematic of the RDE simulation set up (3-cylinder engine).

The experimental cumulative of fuel consumption and emissions have been derived from the instantaneous timeseries which inevitably introduces some uncertainties It is important to remark that the experimental data of all the instantaneous emissions were provided as "dry" concentrations. On the other hand, the experimental, cumulative emission curve of each pollutant emission was not directly available. Hence, the experimental cumulative quantities have been derived by computing the exhaust mass flow rate as the sum of the measured air and fuel mass flow rates, then transforming the $[ppm]$ dry concentrations into mass fractions (multiplying by the specific gas molar mass and dividing by the exhaust flow molar mass) and finally integrating, to achieve the cumulated curve.

$$M_i^{t+dt}[g] = M_i^t[g] + \frac{(ppm_i^t + ppm_i^{t+dt})[10^{-6}]}{2}\left[\frac{mol_i}{mol_{tot}}\right]\frac{(\dot{m}_{exh}^t + \dot{m}_{exh}^{t+dt})}{2}\left[\frac{kg}{s}\right]10^3\left[\frac{g}{kg}\right]\frac{MM_i[g_i/mol_i]}{MM_{exh}[g_{tot}/mol_{tot}]}dt[s]$$

where MM_i indicates the i_{th} specie molar mass and MM_{exh} exhaust molar mass assumed to be 28.9 g/mol. The exhaust mass flow rate is calculated as the sum of the air and fuel consumption mass flow rates. It must be highlighted that this indirect procedure to get the quasi-experimental cumulative quantities does not provide the absolute mass of pollutants emitted, because it is calculated with "dry" concentrations and a "wet" exhaust mass flow. However, it gives a useful indication of the general trend and represented the only viable option based on the experimental data. The only data experimentally available was the instantaneous dry concentration emissions. This indirect procedure might also lead to some differences between experimental and calculated data. On the other hand, this is not an issue for the cumulative fuel consumption presented. Since the engine often runs in rich conditions, it would have been possible to better estimate the molar mass of the exhaust gases, which depends on the air-fuel ratio [56], for both the experimental and calculated cumulative.

6.3 RDE cycle simulation with the 3-cylinder Otto engine

The simulation of the RED cycle has been performed on the 3-cylinder 1D engine model and the results have been compared to the experimental data of the driving cycle provided by UPV. The instrumented engine has been run on a test bench. The engine speed and load of the engine has been controlled to emulate a driving cycle. Figure 6.4 shows the cloud of predicted operating points during the whole RDE test cycle reported on the engine map, to highlight the most frequent areas of operation. It is possible to notice that the engine operates always below 3000 rpm, mostly around 2000 rpm in a range of loads between 0 and 20 bar.

Figures 6.4 and 6.5 show the comparison between predicted and experimental instantaneous quantities, highlighting that the model can accurately follow the required target brake torque profiles. This allows to perform a fair comparison between the experimental and computed data, since the engine speed and load of the engine is the same in time. When the engine torque required shows a sudden increase, the engine model correctly reacts, increasing the throttle opening and the brake torque output. Since the engine control is dynamic and performed by standard single input-single output (SISO) PID controllers, the achievement of the exact value of brake torque at the same experimental times is not guaranteed (see Figure 6.6).

As shown in Figure 6.7, the lambda value imposed from experimental data indicates that the engine works mainly and very frequently in rich conditions. This is consistent with the lambda values observed during the steady state map simulation of this engine (chapter 3 and 4). During the engine off period, the lambda value would be a Non-Computable Data (NCD), since by definition it cannot be determined when the engine is off. Both the experimental and computed lambda values in output, once the engine is off, are the latest valid measured or calculated numerical values.

Moreover, the calculated instantaneous fuel consumption (shown in Figure 6.8) is in good agreement with the measured data. Thanks to the correct description of the fluid dynamic behaviour of the engine, the accurate prediction of the breathed air mass flow rates allows to correctly match the exhaust gas mass flow rate as shown in Figure 6.9. The correct prediction of the gas mass flow rate is also a consequence of the good model response to the instantaneous value of required boost pressure equal to the experimentally measured one, which is reported in Figure 6.9. To achieve this result the internal PID has been used to dynamically control the wastegate position with a continuously varying target value.

The computed turbocharger speed during the RDE cycle is reported in Figure 6.10, together with the throttle valve position. For these two quantities the corresponding experimental measurements were not available for a direct comparison. However, it can be seen how model predicts the slowdown of the turbocharger. The turbo shaft speed decreases when the engine is turned off, however it is limited to a non-zero quantity for reasons related to the numerical solution. Moreover, when the engine is turned on, the turbocharger speed depends on the current boost pressure and engine speed requested along the RDE cycle. Finally, the calculated throttle opening position shows that the engine works most of the time at partial load, with a small throttle opening, as can also be guessed by the load-rpm map of Figure 6.4.

In terms of gaseous emissions prediction, Figure 6.11 and 6.12 show the comparisons between measured and predicted engine-out concentrations of CO_2, CO, NO_x, and unburned hydrocarbons. Overall, the prediction shows a good agreement, with a slight overestimation of CO, and consequent underestimation of CO_2, in some regions of the RDE cycle, in line with the model accuracy resulting from the analysis of the steady-state operation of the engine. As expected, CO_2, CO, and NO_x exhibit a notable sensitivity to engine operating parameters, such as lambda and engine load.

The total unburned hydrocarbon emissions (THC) reported in Figure 6.12 shows the major difference with respect to experimental data. The experimental data clearly show some spikes of THC emissions when the engine is turned on and off, probably due to some misfire events occurring in the cranking phase, when the engine is started and turned off, which are not considered by the computational model.

In general, when the engine is turned off, the model responds correctly, showing zero engine speed and torque and zero cylinder-out emissions, fuel consumption and air mass flow rate. Moreover, the boost pressure drops to ambient conditions and the turbocharger slows down.

Finally, the predicted results in terms of cumulated values are reported in Figures 6.12 and 6.13, focused on fuel consumption, CO_2, CO, NO_x and THC. Overall, the comparison with the experimental data can be considered satisfactory. The figures highlight a slightly lower predicted CO while fuel consumptions and CO_2 show a good agreement. The highest discrepancy is found in the NO_x prediction, where the positive and

negative errors found during the steady state validation have led to a difference (still around 10%) with a compensation effect. Overall, the agreement between cumulated experimental and predicted quantities is fairly good. Some discrepancies can be explained by the inevitable inaccuracy of the simulation model and the uncertainties of the cumulated experimental trends. In fact, the cumulated "experimental" curves have been derived by an indirect method from the instantaneous measured values, as explained in the previous paragraph, with possible errors.

The computational burden of these simulations (a single one) was a total CPU time of 20 hours (for the simulation of a complete RDE cycle), with a CPU/real time ratio around 11. It must be kept in mind that the 1D domain discretization used was the most refined one, with the largest cell count and lowest time step. The machine used was equipped with an Intel® Xeon® CPU 3.70GHz and the simulation was carried out on a single core. At the light of this consideration, it becomes evident the importance of a fast simulation method (FSM) to significantly reduce the computation time, without a significant loss of accuracy.
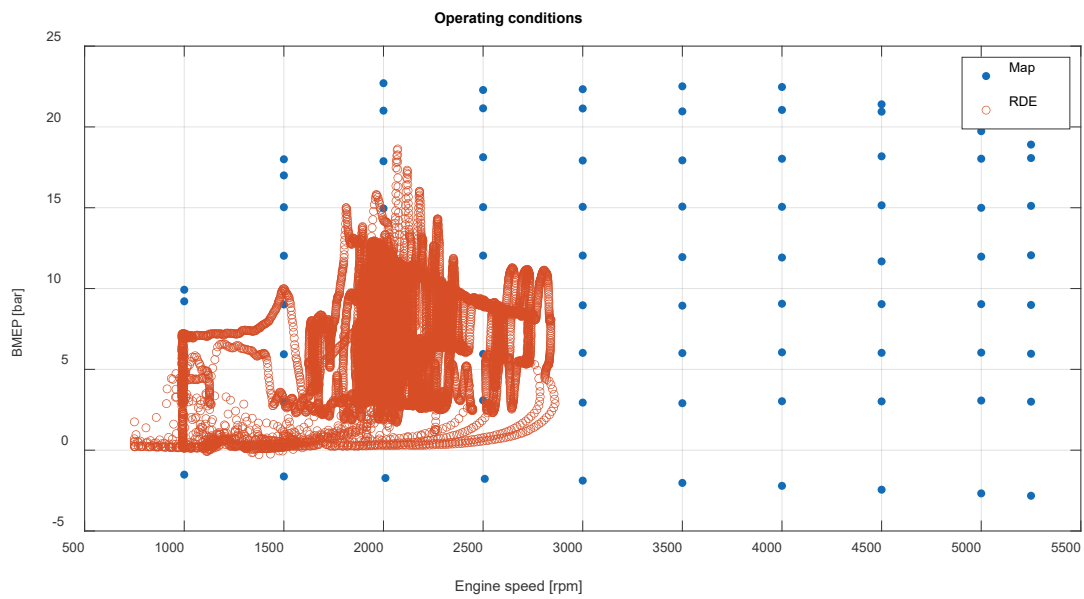

Figure 6.4 - Distribution of the computed operating points on the engine map during the RDE cycle.
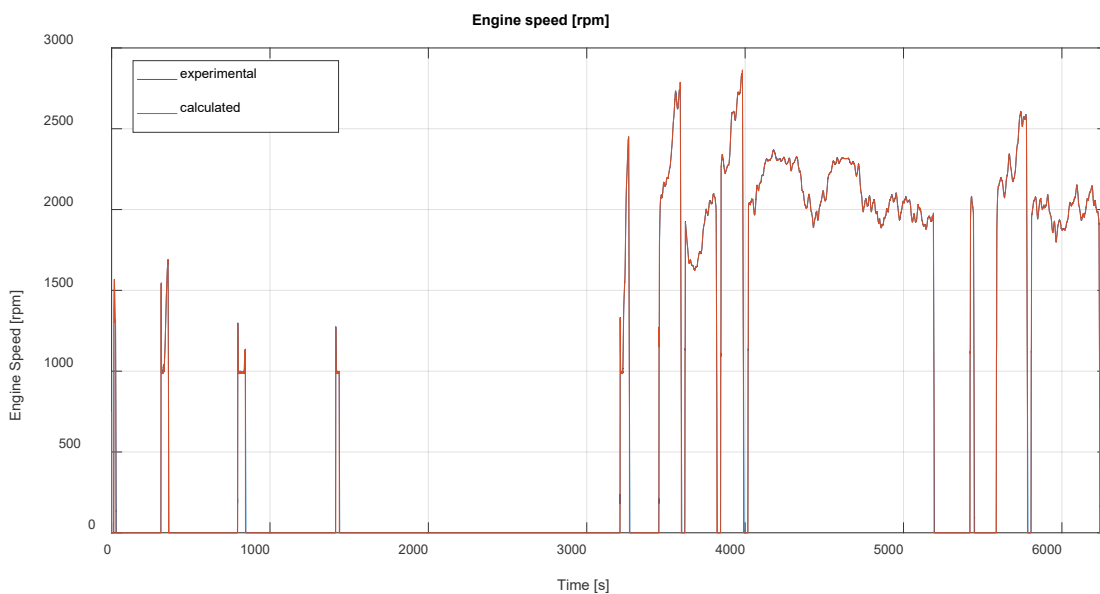

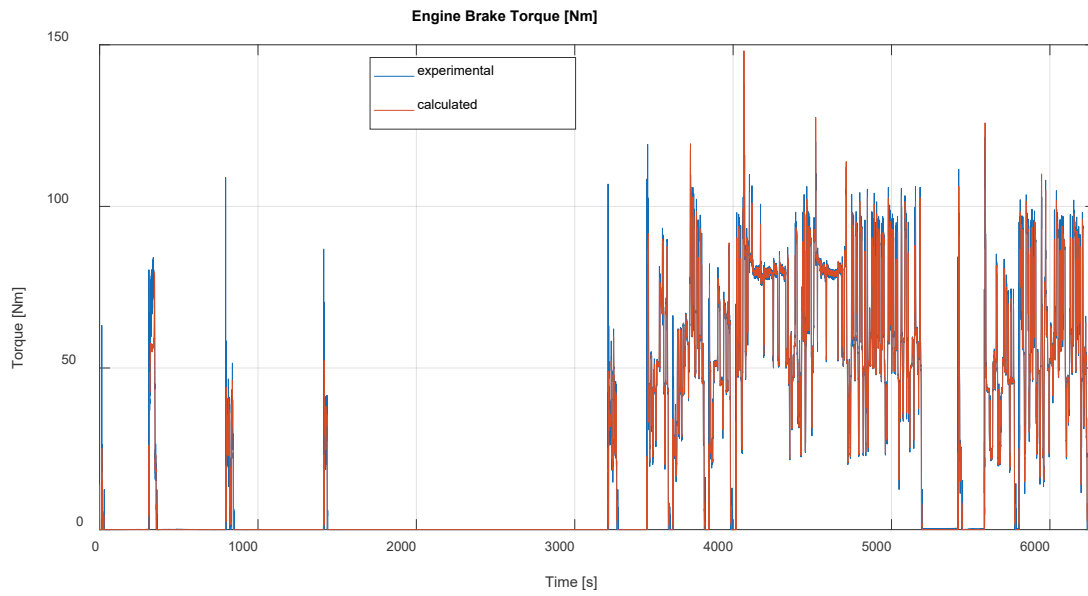Figure 6.5 – Engine speed comparison during the RDE cycle.

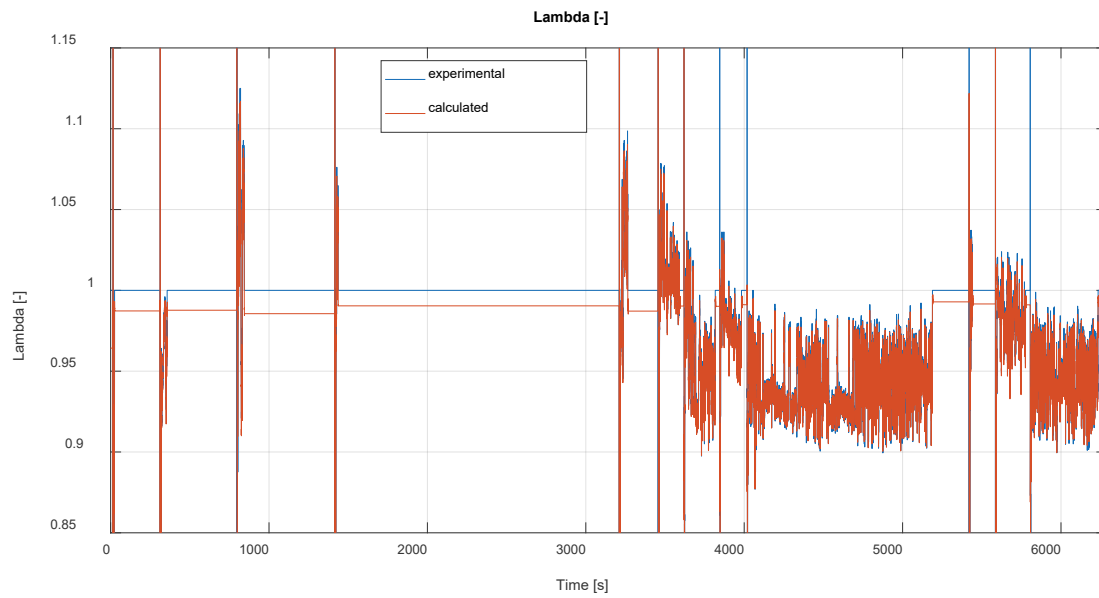Figure 6.6 – Engine brake torque comparison during the RDE cycle.

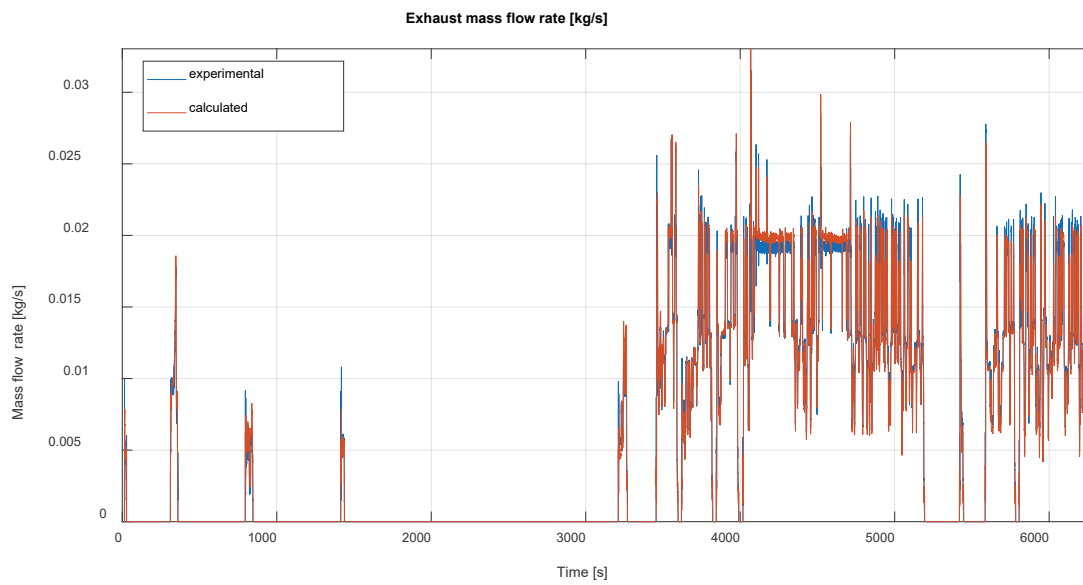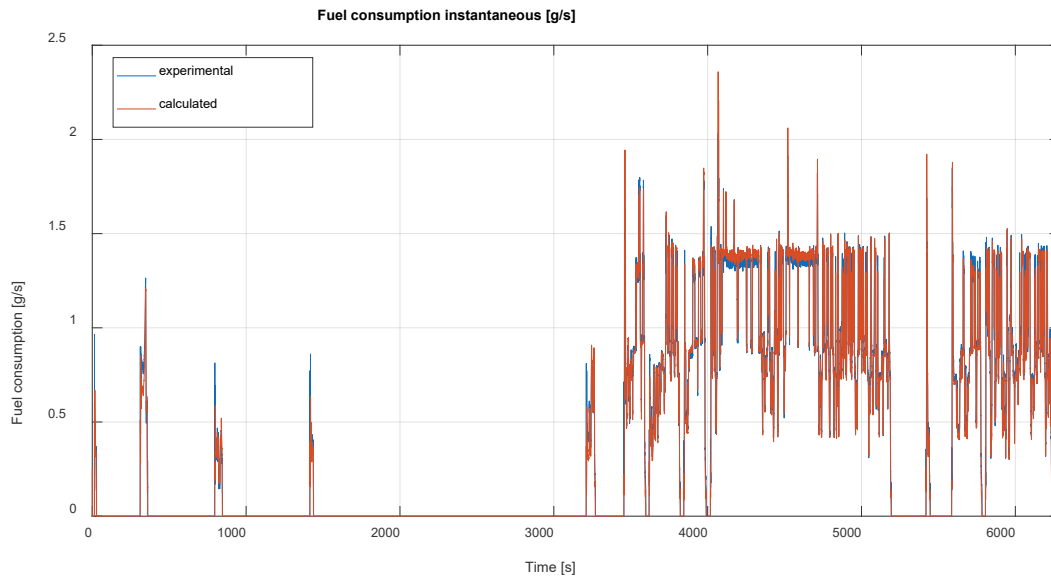Figure 6.7 – Instantaneous lambda comparison during the RDE cycle.

Figure 6.8 – Instantaneous fuel consumption (top) and exhaust gas mass flow rate (bottom) comparison during the RDE cycle.
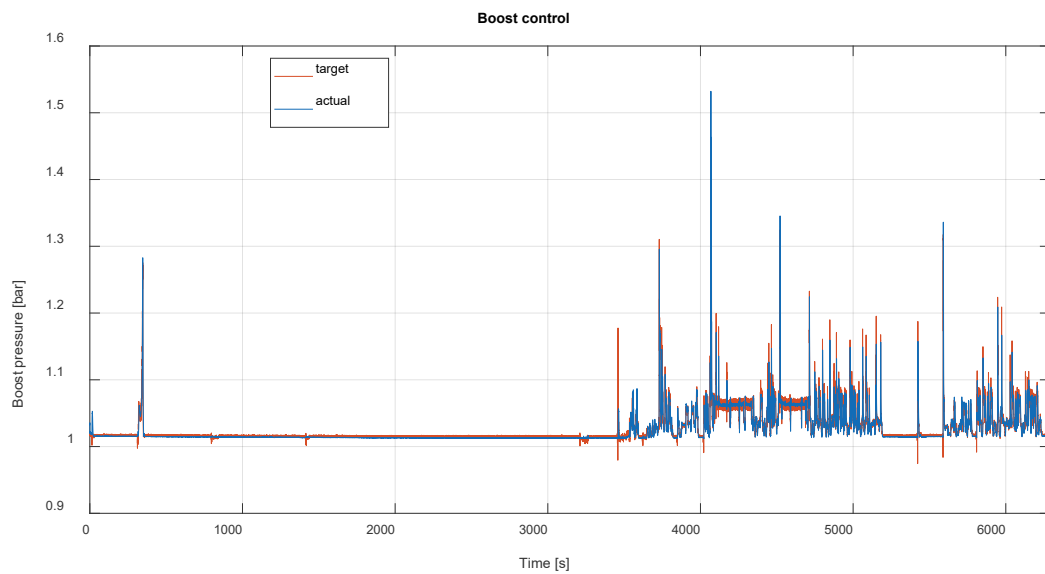

Figure 6.9 – Boost pressure comparison during the RDE cycle.
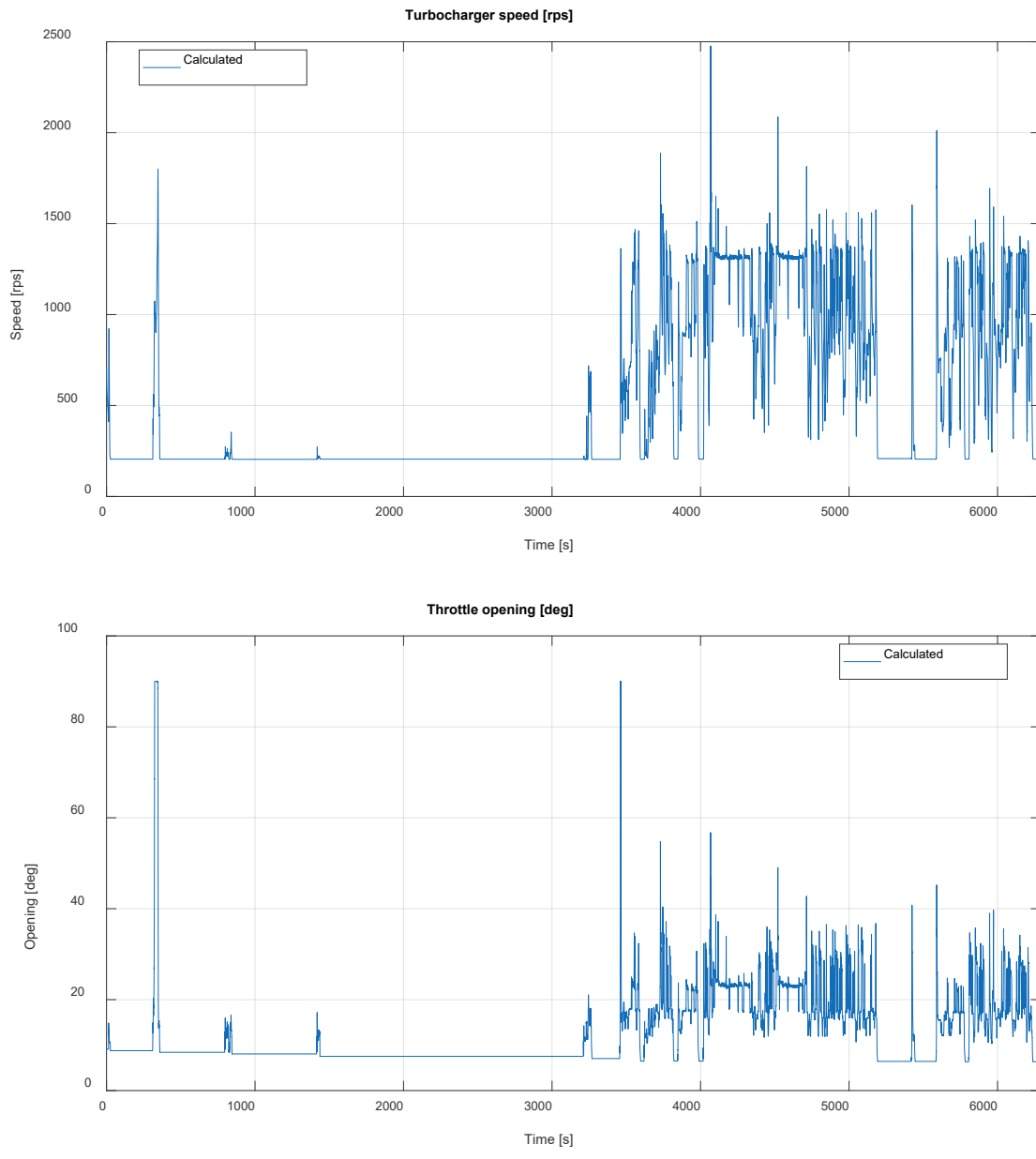
Figure 6.10 – Calculated turbocharger speed (top) and throttle opening (bottom) during the RDE cycle.

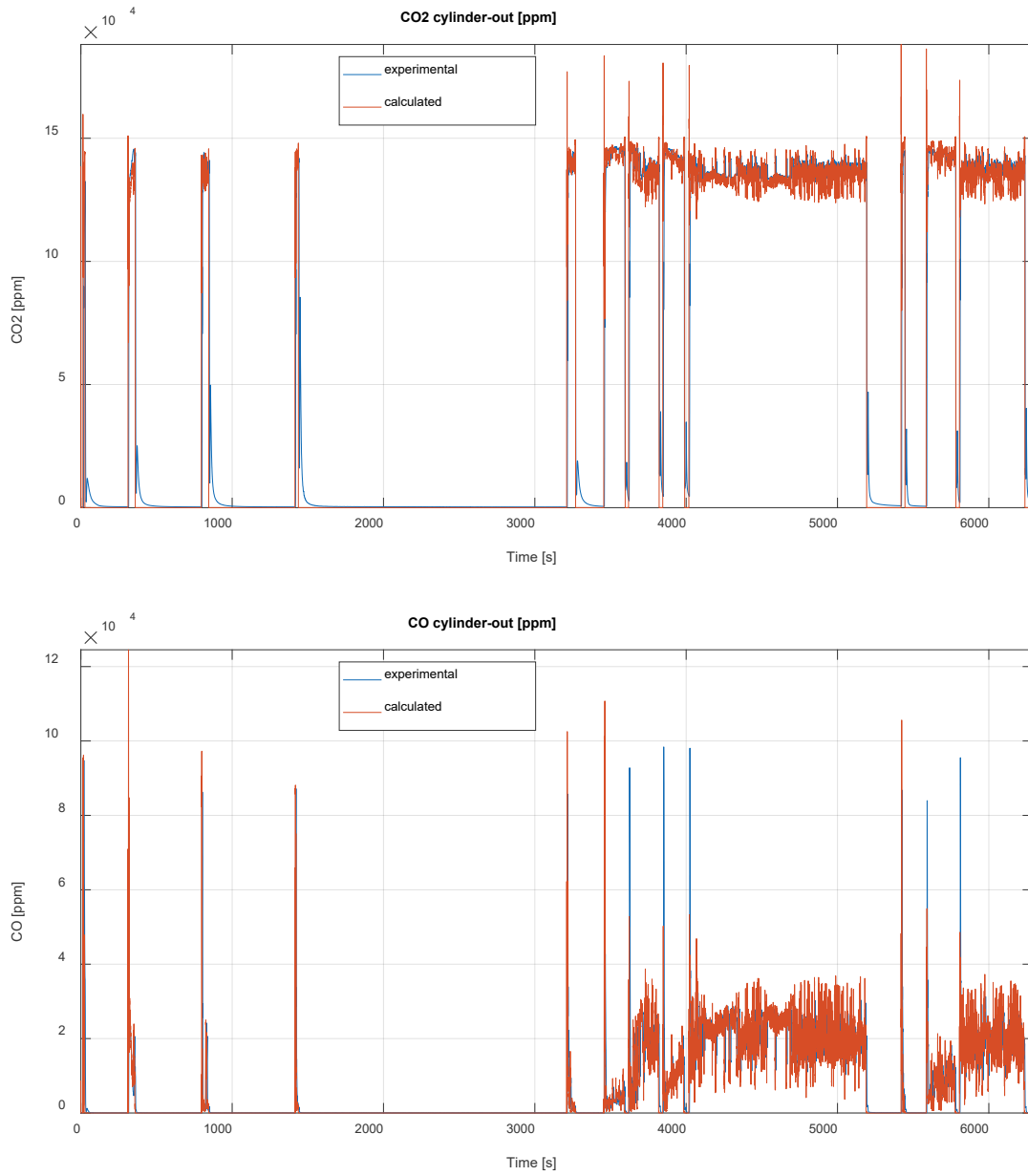Figure 6.11 – Instantaneous cylinder-out CO$_2$ (top) and CO emission (bottom) comparison during the RDE cycle.
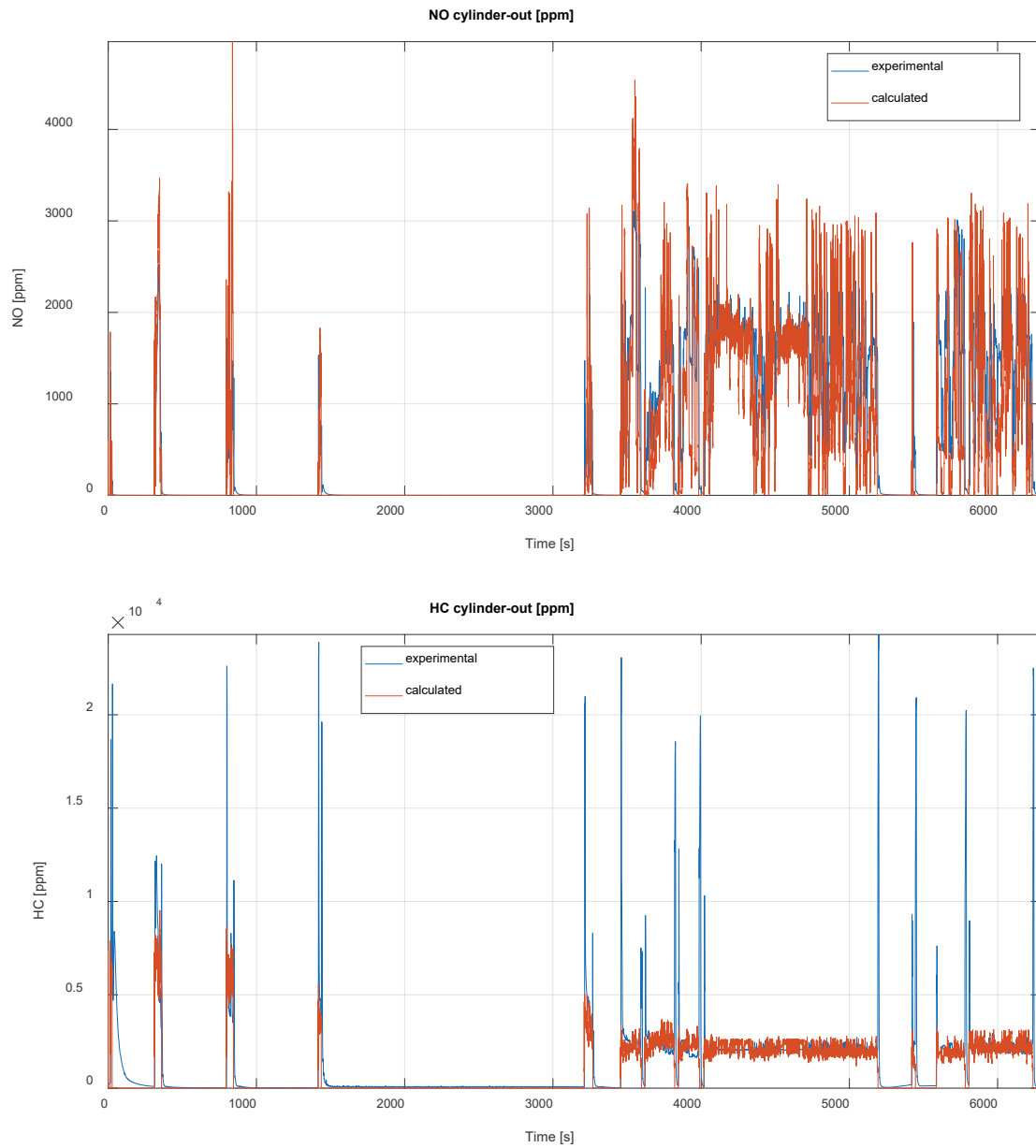
Figure 6.12 – Instantaneous cylinder-out NO$_x$ (top) and THC (C) emission (bottom) comparison during the RDE cycle.
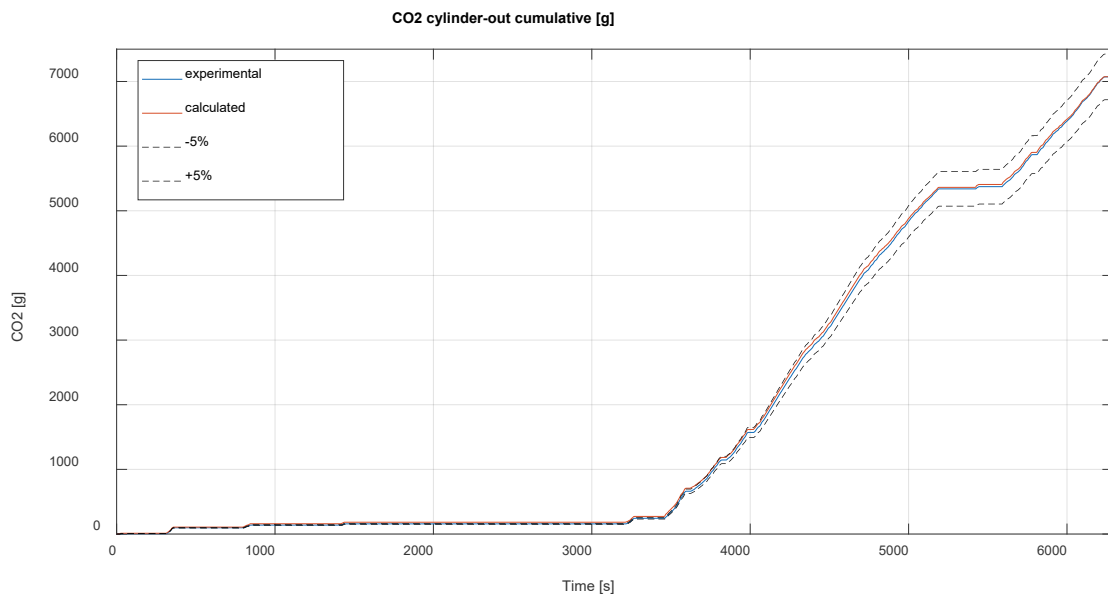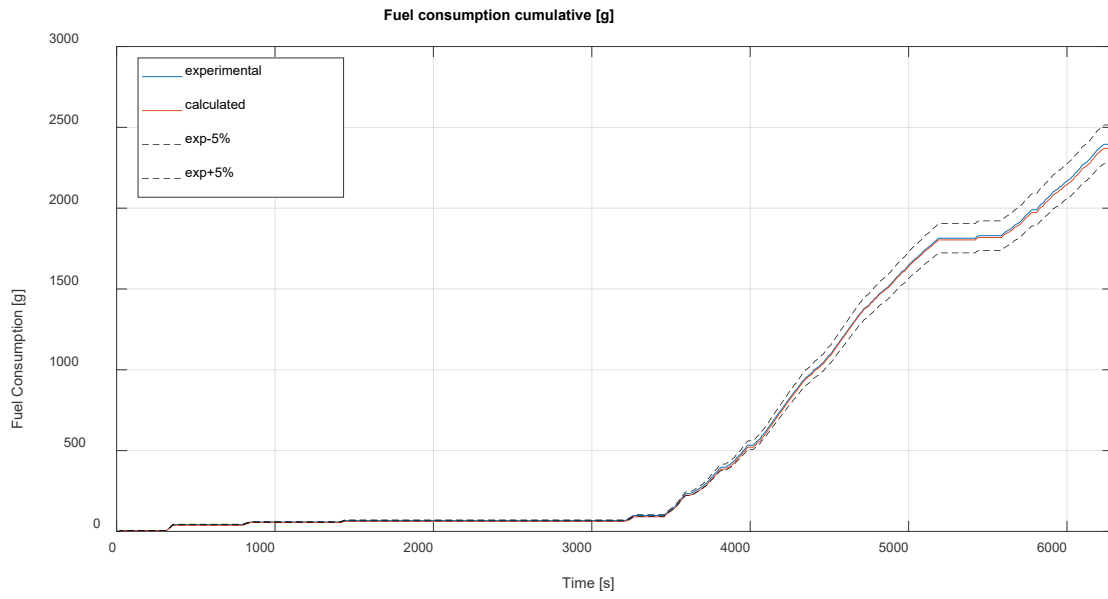
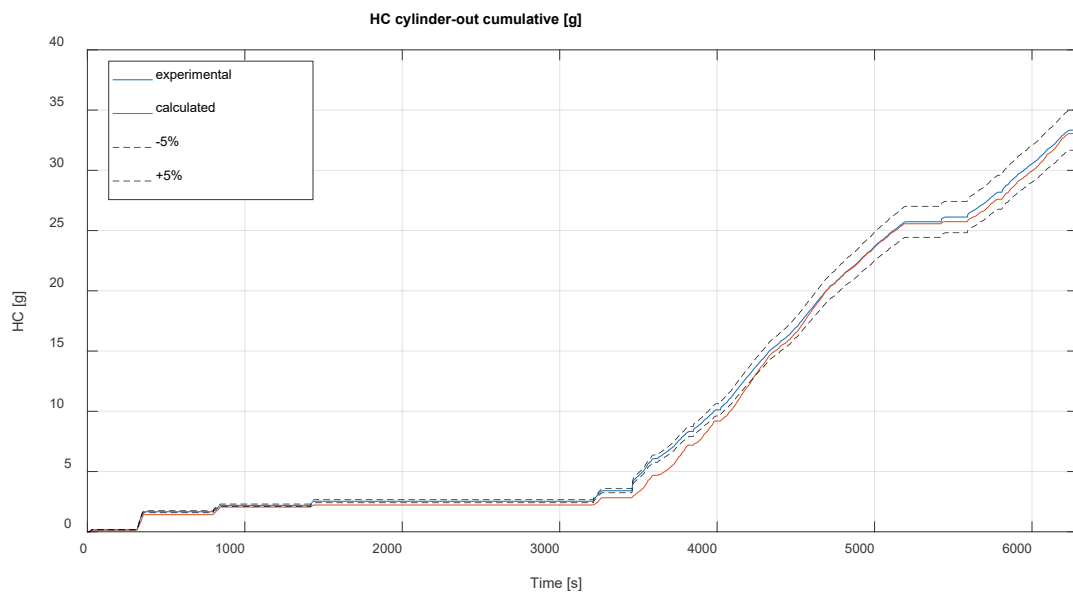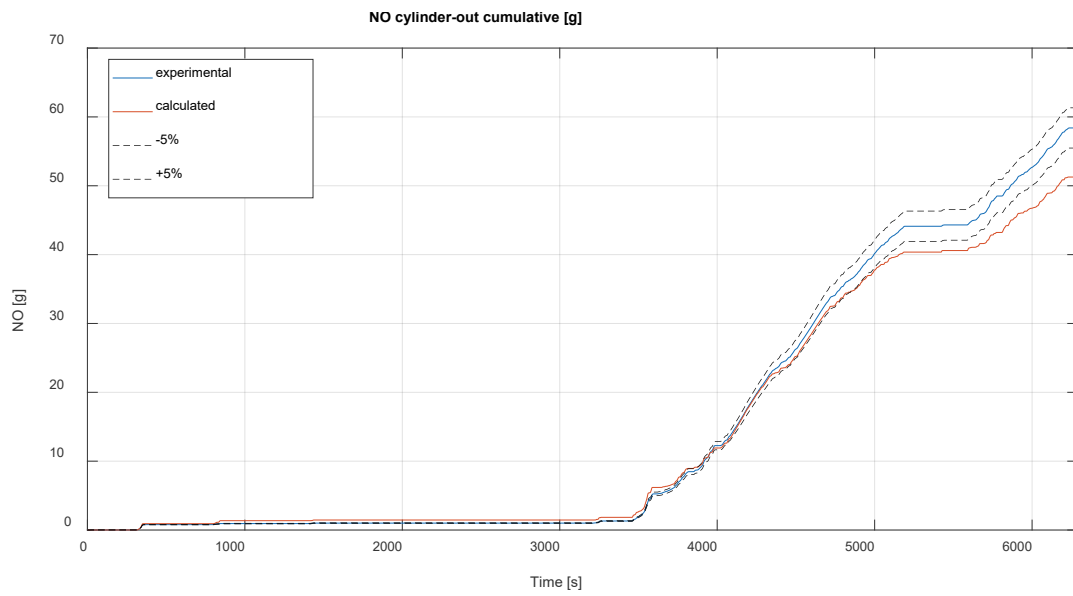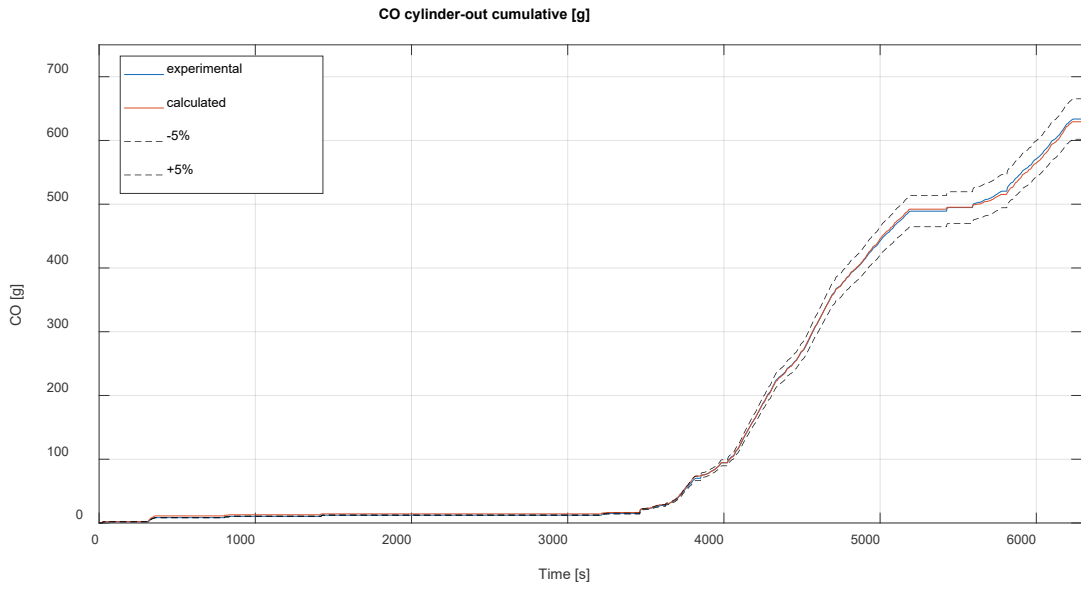Figure 6.13 – Cumulative fuel consumption (top) and CO_2 (bottom) comparison during the RDE cycle.

Figure 6.14– Cumulative CO (top), NOₓ (middle) and THC(C) (bottom) comparison during the RDE cycle.

6.4 RDE cycle simulation with the Fast Simulation Method

As declared in previous chapters, one of the goals of this work is to reduce the computational effort, hence the CPU time, required to carry out the simulation of long driving cycles. In the chapter regarding the steady state map simulation the FSM already showed his potential, and in this section, it will be applied to the same RDE cycle simulation obtained with the refined approach.

The real time duration of the RDE cycle is 6200 seconds long (about 1h and 45 minutes), so the complete cycle simulation with the refined 1D engine model is quite demanding in terms of CPU time. Moreover, since the 1D model is crank angle resolved, the prediction of combustion process in each cylinder, of unsteady flows in pipe systems and of turbocharger matching are themself a demanding task. Initially the accurate solver with refined mesh (around 1 cm in each pipe) has been applied to verify the best results achievable and to consider them as a numerical reference point. Secondly, the same simulations have been repeated using the Fast Simulation Method (FSM) described in the dedicated previous chapter, with coarse meshes (around 10 cm in each pipe), to evaluate the CPU time saved and the reduction of the CPU/real time ratio.

Figure 6.15 shows that a strong reduction has been achieved, with a CPU/real time dropping from 11.5 to 1.8. The results achieved confirm the accuracy of the FSM solver, which decreased the computational time by 80%, while keeping high accuracy, comparable to the one achieved by the refined solver.

Figure 6.16 highlights that the instantaneous quantities calculated during the RDE cycle by the accurate and FSM solvers are nearly not distinguishable: in particular, the instantaneous mass flow rate shows a maximum difference is in the range of 1-2%, whereas some discrepancy can be noted for the instantaneous NO_x at medium/high load (in the range of 8%)

Finally, Figure 6.17 shows marginal difference in the predicted mass of cumulative fuel consumption, CO_2, NO_x and CO during an RDE cycle, which do not change significantly passing from the accurate to the fast solver (between 1 and 8 % depending on the pollutant).

In general, the advantage of this fast approach is evident: it allows to run any RDE cycle with the virtual engine to investigate the influence of several parameters on the virtual engine in terms of performance, efficiency and emissions. It gives the opportunity to explore different viable technical solutions, such as: Miller cycle, advanced combustion modes, variable valve actuation, cylinder deactivation and so on.
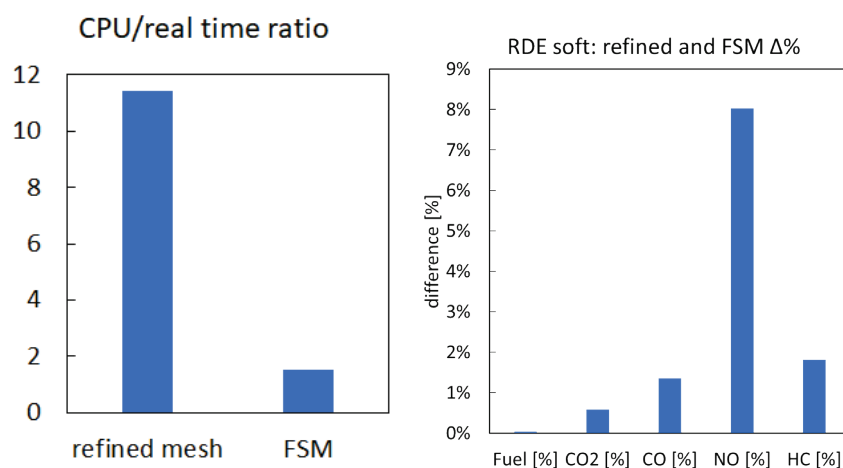
Figure 6.15 – CPU/real time ratios for the accurate and FSM solvers (left from 11.5 to 1.8)
and corresponding percentage difference of cumulated emissions during the RDE cycle (right).

Exhaust mass flow rate [kg/s]
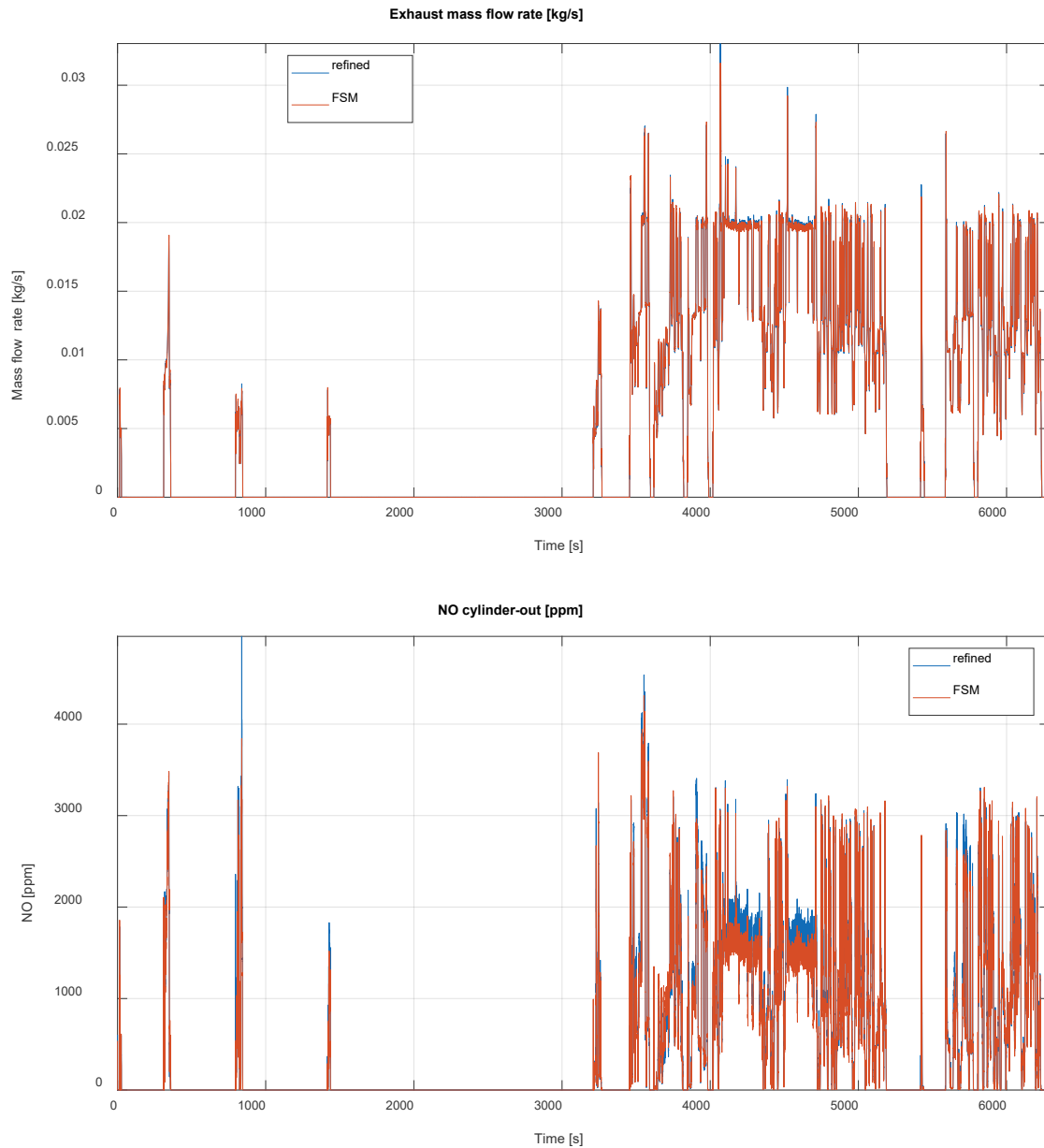
NO cylinder-out [ppm]

Figure 6.16 – Predicted instantaneous exhaust mass flow rates (top) and cylinder-out NO_x emissions (bottom), comparison between the refined and FSM numerical solvers.
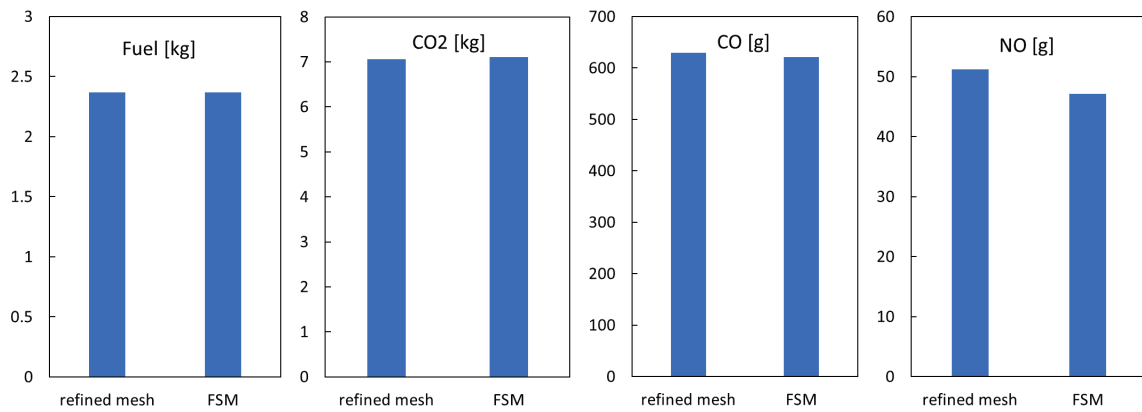
Figure 6.17 – Predicted cumulative quantities during RDE cycle: mass of fuel, CO_2, NO_x and CO, comparison between refined and FSM numerical solvers.

6.4 WHTC cycle simulation with the 6-cylinder Diesel engine

The 1D model of the FPT 6.7 litres, 6-cylinder Diesel engine which has been as previously validated over the entire engine map under steady state operating conditions, is now used to predict the performances and emissions during transient conditions. Recalling the steady state study, it can be said that a general satisfactory agreement was achieved in the case of the steady operating points of the engine map, which is the initial fundamental requirement to achieve a reliable simulation of any driving cycle.

In particular, in this section it will be studied a WHTC (World Harmonized Transient Cycle) cycle that has been carried out by FPT, considering a reference architecture of a hybrid mid-size urban bus. In particular, the proposed WHTC cycle lasts for 1800 seconds (30 minutes) and experimental data are available during the whole cycle for validating the results of the simulations.

In a similar way to the previous activity on the 3-cylinder SI engine model, three PID controllers were used for this 6-cylinder CI engine model: one to control the torque, acting in this case on the injected fuel mass per cylinder per cycle; one to control the compressor boost pressure, acting on the wastegate opening, and a last one to control the temperature downstream of the intercooler, acting on the intercooler temperature. Since no experimental target for boost pressure and intercooler temperature was available, the 1D model resorted to the mapped target data of the steady state maps.

The WHTC test cycle is characterized by frequent accelerations/decelerations, without intervals of engine stop during the 1800 seconds of duration (see Figure 6.18). The results of the simulations have been compared to the experimental data provided by FPT. The data available that have been compared are the following: engine speed and torque, instantaneous and cumulative fuel consumption and emissions of CO_2 and NO_x. Once again, the experimental cumulative have been derived from the instantaneous trends like in previous RDE cycle.

Figure 6.18 shows the comparison of engine speed and torque during the cycle during the WHTC cycle, highlighting the experimental and calculated trends. The experimental trend shows that, when the brake torque becomes negative, hence when the engine works as a brake, the difference between measured and simulated torque increases. This is probably due to an additional mechanism that the real engine uses to increase the braking capability that has not been included in the model. This is a common feature in heavy duty engines, which rely on specific devices to increase the braking without stressing the mechanical brakes. However, neither the presence nor the type of these devices is currently known and included in the simulation. The air mass flow rate predicted by the 1D model is in good agreement with the measured data, with differences when local peaks occur due to strong accelerations and in the last part of the cycle.

In Figure 6.19 are presented all the operating points (BMEP vs. engine speed) covered during the WHTC over imposed to the steady state engine map. This picture gives a clear representation of the most used load-speed points and of the most frequent engine brake conditions.

Figure 6.20 shows the comparison of the instantaneous injected fuel per cycle during the WHTC cycle, showing a good match between measured and calculated data. Higher discrepancies can be seen in the second part of the cycle; however, the same torque is reached, and the difference is most probably due to a different engine calibration and friction level with respect to the mapped data.

The resulting cumulative fuel consumption highlights an acceptable agreement, with a total error bounded between +/-5%, as shown in Figure 6.21. This difference is consistent with the accuracy achieved in the definition of the steady state map. Overall, we can state that the instantaneous measured and calculated fuel injection during the WHTC cycle shows a good agreement.

The comparison of exhaust gas mass flow rate reported in Figure 6.22 highlights the fluid dynamic predictivity of the 1D model, confirming the reliability of the steady state validation process. A higher discrepancy is

shown towards the final part of the cycle. However, it must be highlighted that in this case the instantaneous measurement of the actual boost pressure was not available. Hence, in this simulation the 1D model has used the information of boost pressure mapped during the steady state activity, so that the target boost pressure is chosen according to the current engine speed and load during the simulation.

Figure 6.23 report the comparisons of carbon dioxide and nitric oxide emissions. The instantaneous measured and calculated CO_2 emissions during the WHTC cycle are in good agreement and consistent with the observed differences in the fuel consumption trend. Even though the cumulative predicted fuel is slightly larger than the experimental value, the predicted cumulative CO_2 is lower than the experimental value. This might be due to a multitude of factors, starting from experimental errors to discrepancy in mass flows and CO_2 concentration is the exhaust gases. Regarding the NO_x emissions, larger differences arise in the instantaneous comparison and of course these are reflected in the cumulative curve (see Figure 6.24). The final error is limited to about 5% at the end of the cycle. However, this difference can be explained also with the uncertainty on the fuel used during the transient simulation, which was not known, and it was assumed to be the same of the steady state maps. A better calibration of the emission sub-models could be pursued however the focus of this work is on the application of the FSM to reduce the computational effort to perform this calibration refinement faster.
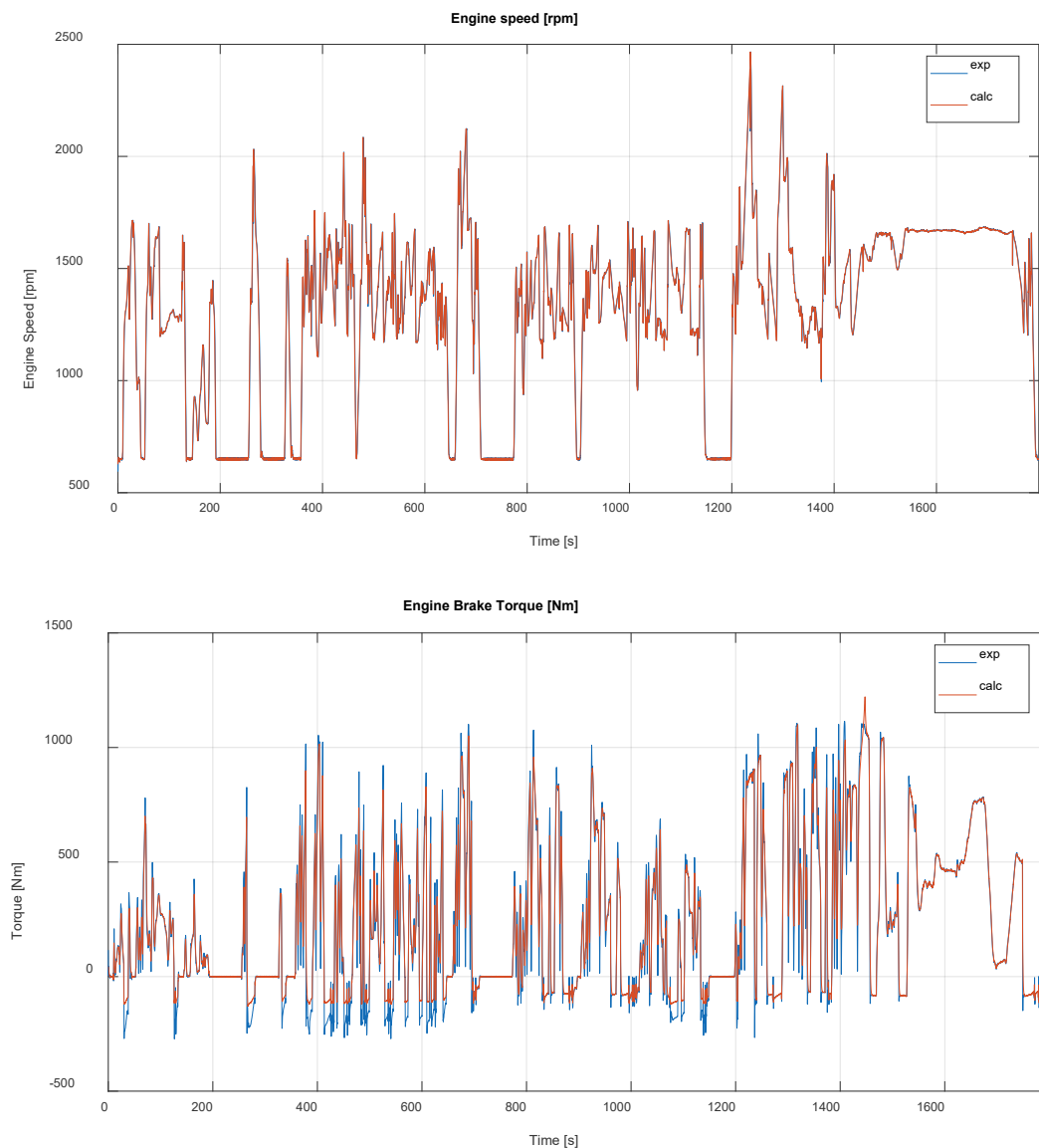
Figure 6.18 – Engine speed (top) and brake torque (bottom) comparison during the WHTC cycle.
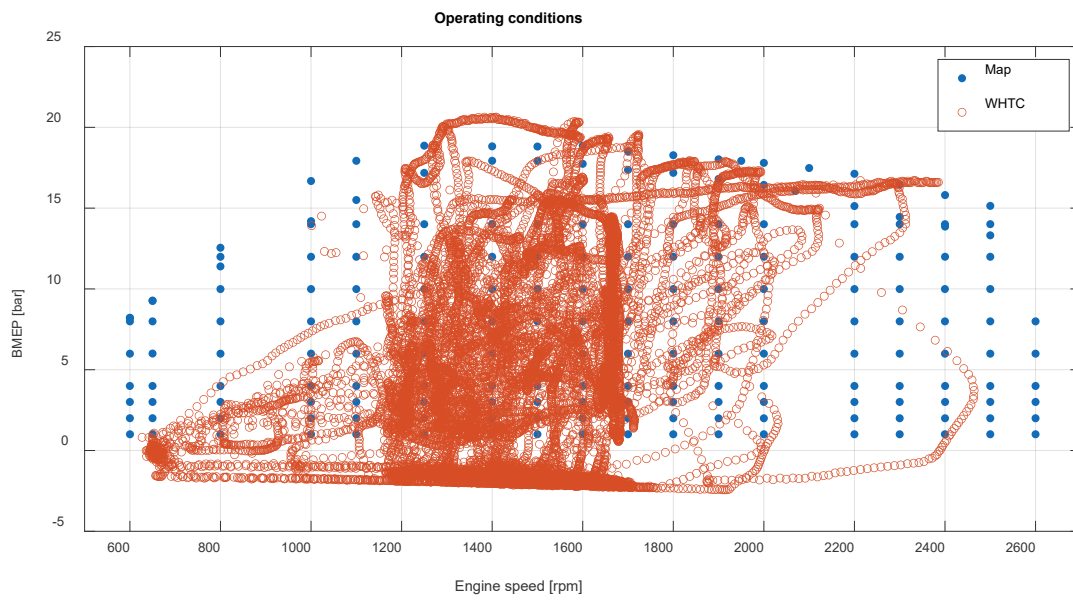
Figure 6.19 - Distribution of the computed operating points on the engine map during the RDE cycle.
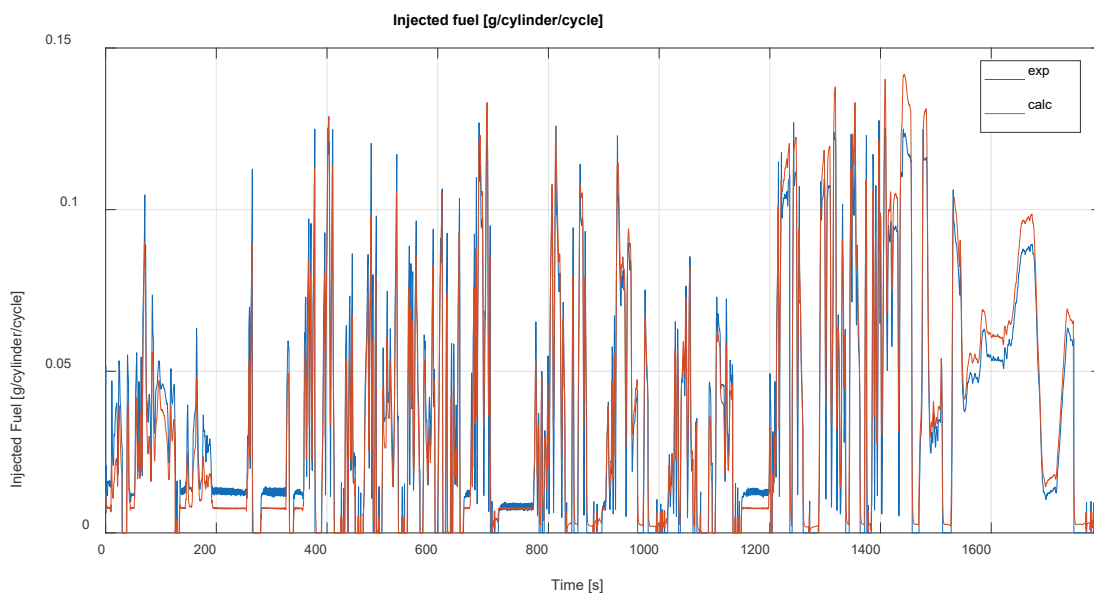
Figure 6.20 – Instantaneous fuel consumption comparison during the WHTC cycle
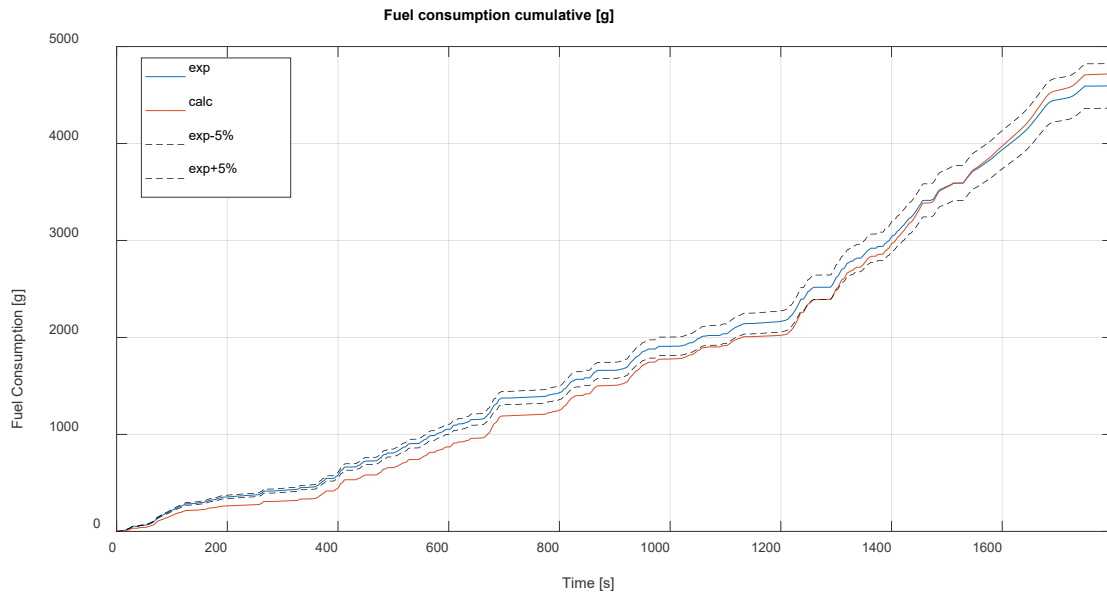
Figure 6.21 – Cumulative (bottom) fuel consumption comparison during the WHTC cycle.
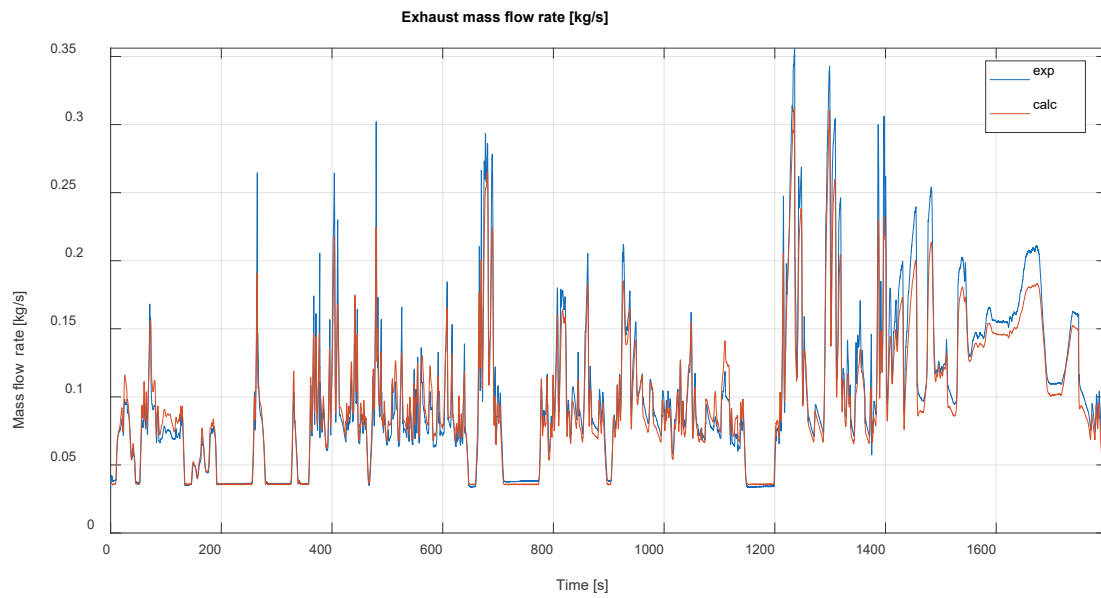
Figure 6.22 – Comparison of the instantaneous exhaust gas mass flow rate during the WHTC cycle.
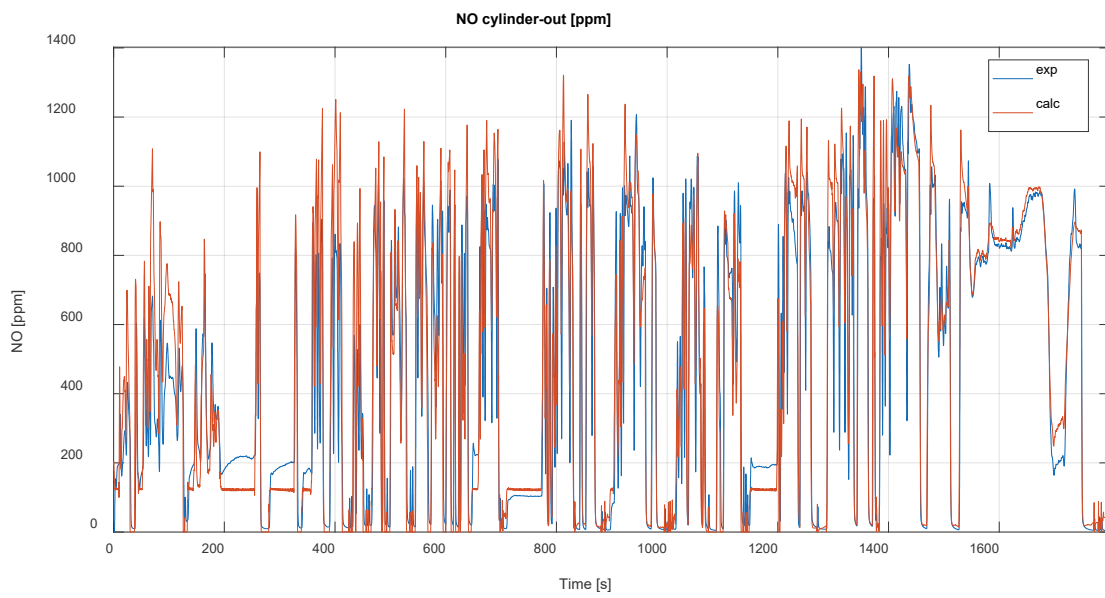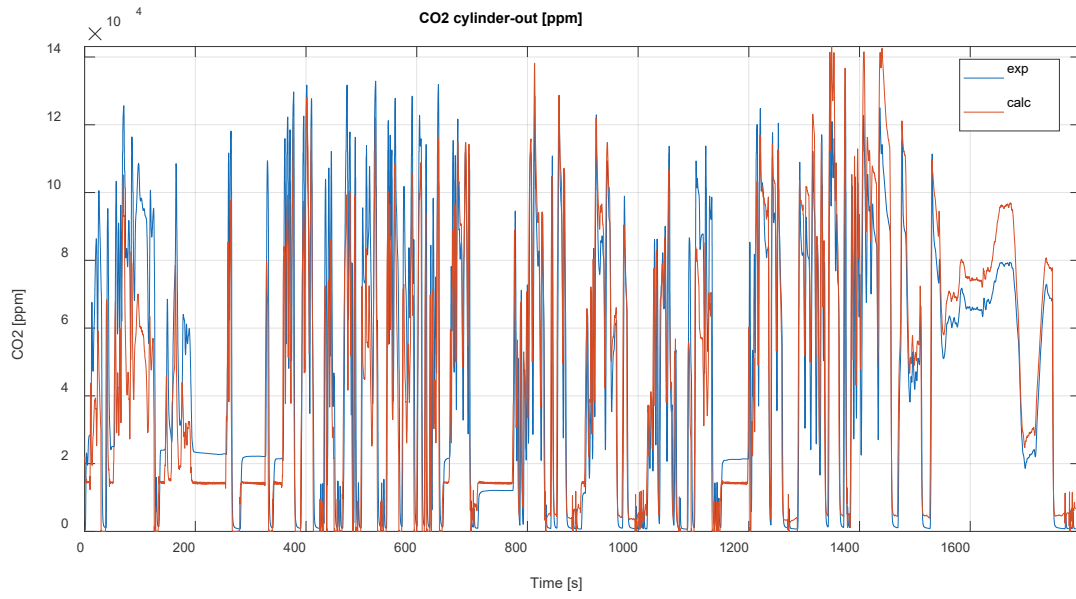
Figure 6.23 – Comparison of the instantaneous cylinder-out CO_2 (top) and NO_x (bottom) during the WHTC cycle.
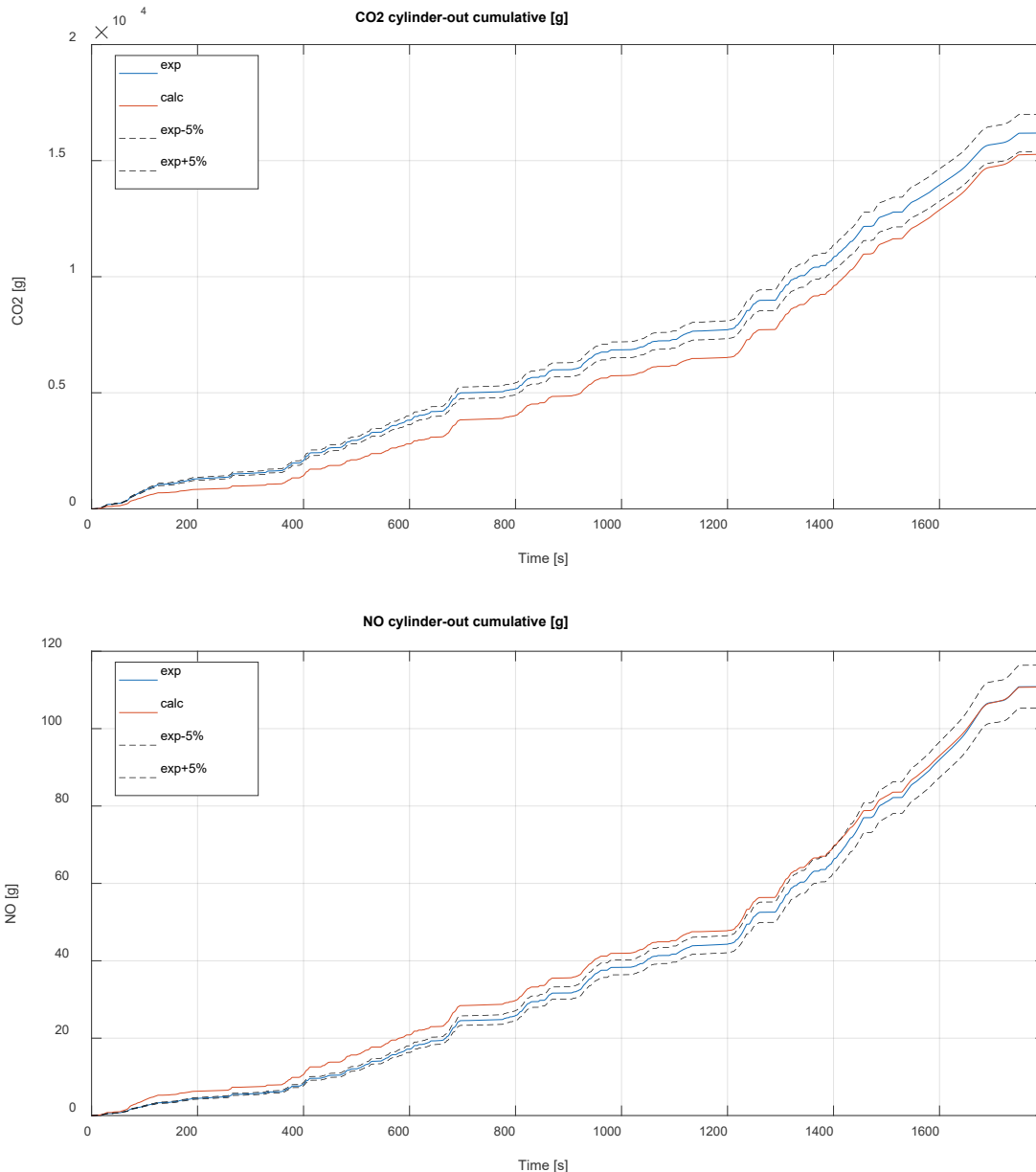
Figure 6.24 – Comparison of the cumulative cylinder-out CO_2 (top) and NO_x (bottom) during the WHTC cycle.

6.5 WHTC cycle simulation with the Fast Simulation Method

In this chapter the FSM is applied to the same WHTC cycle simulation that has been simulated with a refined 1D model. At this point, the 1D FSM model described in the previous chapters has been applied, but the whole methodology is the same of the refined simulation. In Figure 6.25 the instantaneous brake torque comparison between the refined and FSM model is presented: the FSM model behaves very well, following the requested torque similarly to what the refined model does. The same engine speed of the previously presented cycle is imposed.

To confirm the predictive capability of the FSM approach, in Figure 6.25 the comparison of the predicted exhaust mass flow rate is presented: the FSM shows a very similar fluid dynamic solution to the refined model.

Eventually, the in-cylinder process is analysed. The instantaneous cylinder-out NO_x prediction of the FSM model is compared with the refined model results in Figure 6.26, where a very good agreement is obtained, even if the NOx prediction is very sensitive to maximum gas temperature during combustion occurring during

the higher load conditions. However, this is expected by the similarity in the mass flow rates elaborated by the engine.

With Figure 6.27 it is reported a comparison of the cumulative emissions between the refined and FSM simulations. It is presented the cumulative percentage difference at the end of the simulation. The difference is always lower than 2%. In the Figure 6.27 it is also reported the comparison in absolute values.

Once determined that the accuracy of the FSM model is comparable to the refined model, it is evaluated the reduction of CPU/real time (see Figure 6.28). With the FSM model the simulation of the whole cycle took 2 hours, whereas the refined model required 48 hours. The reduction is close to 90%. This allows to use the FSM model for the prediction of many driving cycles and configurations in a shorter time.
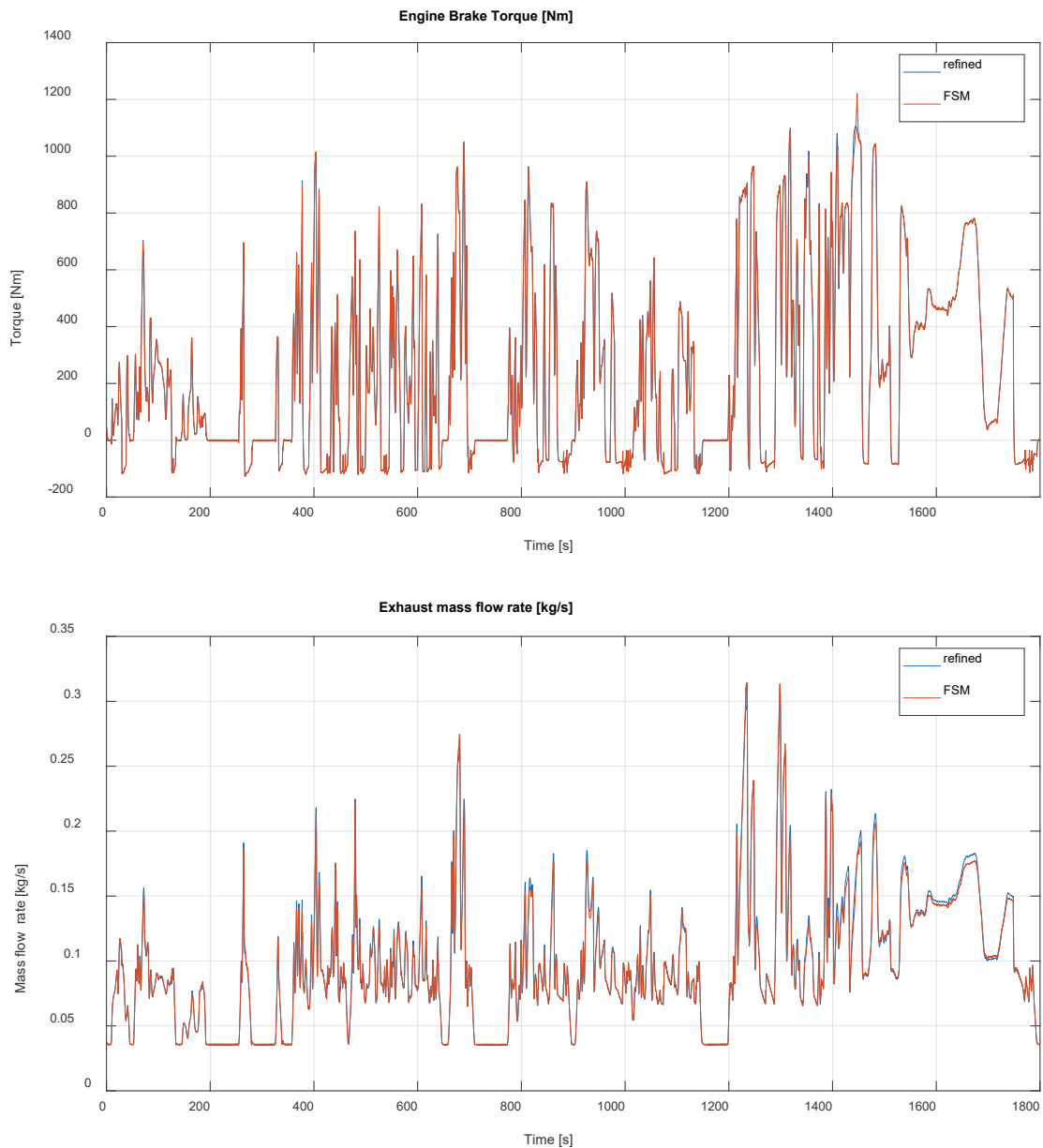
Figure 6.25 – Engine torque (top) and exhaust mass flow rate (bottom) comparison, between the refined and FSM model during the WHTC cycle.

Figure 6.26 – Comparison between refined and FSM instantaneous cylinder-out NO$_x$ emissions.
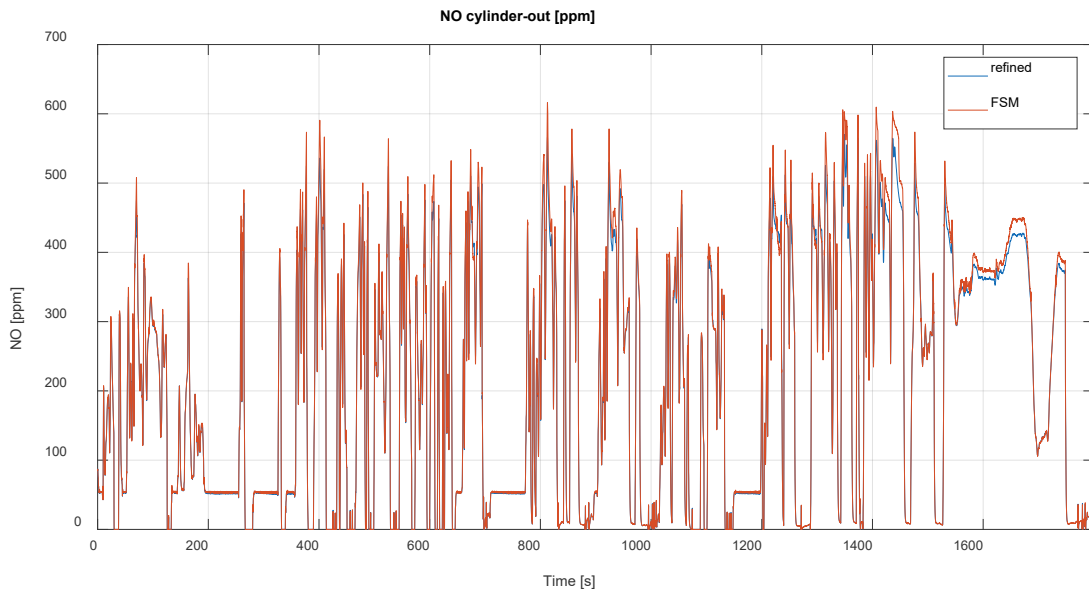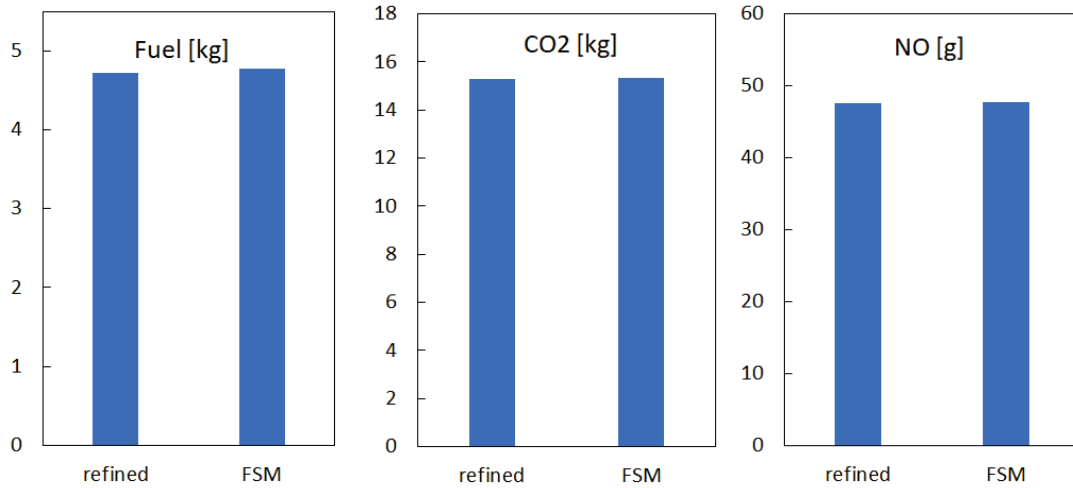

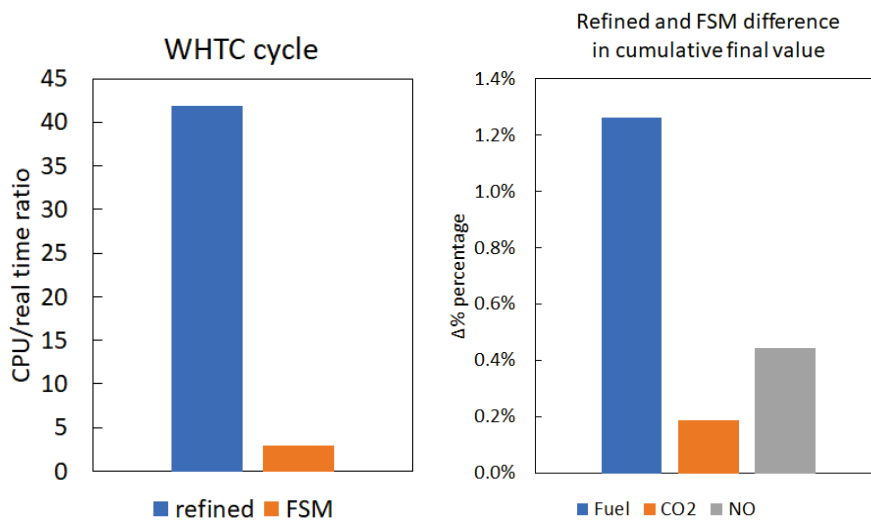Figure 6.27 – Comparisons of the refined and FSM pollutants prediction, final cumulative value.

Figure 6.28 – CPU/real time comparison between refined and FSM model (left), and cumulative percentage difference (right).

7. Co-Simulation framework for coupled PHEV model RDE cycle simulation

One of the goals of this thesis work and of the EU project "VISION-xEV" was to obtain a full integrated simulation model of a modern PHEV to simulate RDE cycles. It has been developed a flexible co-simulation methodology to perform the simulation of a modern hybrid electric vehicle. In a typical PHEV model, there are multiple components, and each element is represented by a sub-model. For example, the vehicle dynamics, IC engine, electric motor, battery, inverter, energy management, thermal management, turbocharger thermal management are all simulated by specific sub-models. Each sub-model relies on inputs which are provided when the model runs isolated. These inputs are usually assumed as data but are often the result of another model. For example, the thermal management input, heat power, is the heat rejected by the IC engine, turbocharger, battery and HVAC, which can be calculated by the respective models.

These sub-models are usually developed by different institutions and companies and might rely on very different informatic structures, because they are not developed in a single common environment. Usually, these sub-models are not linked, meaning that an iterative simulation loop is performed, where one model is run and only after the simulation the results are used to run the second model which requires those inputs; frequently the result of this second model must be sent back to the previous one, so that the first model is run again. This requires multiple simulations, to pass the results back and forth between models. Additionally, every change of configuration needs an additional iteration to verify the compatibility with the other models. All this process represents a time consuming, inefficient, and inaccurate simulation framework.

A fully integrated simulation environment with the real time exchange of inputs and outputs would help to resolve these issues. The seamless exchange of data between models allows to connect the sub-models and immediately evaluate the impact on achieving the performance or emission targets. Moreover, any change of configuration allows to simply substitute one model with its variation.

In the virtual integrated simulation framework, each sub-model is seen as a "black box": only the required inputs and configured outputs are accessible. This allows to interact with the sub-models within an external environment. This approach does not require to merge the sub-models in a unique development environment, but only provides a common ground to communicate. The platform in which this interaction occurs is identified as the "host". The host platform oversees the signal routing and manages the overall simulation, sending input signals and retrieving the outputs. The only common feature that the host and the sub-models must share is the communication protocol called FMI/FMU, which stands for Functional Mock-Up Interface [57]. The logo of this interface procedure is presented in Figure 7.1. The two hosts that have been used in this thesis are AVL Model.CONNECT and MATLAB Simulink®. The Simulink® environment also allows the use of S-functions, which is another communication protocol developed by MATLAB, sharing all the features of FMUs.

Another important characteristic of this "black box" methodology is that the execution of the models can be shared without sharing the models themselves. For example, a Simulink® model can be exported as an FMU module, that can be used in a co-simulation process in Simulink® without seeing the actual model inside the platform, provided that the eventual licenses for the model execution are provided.

Eventually, the communication interface FMI is an open-source protocol which guarantees inter-connectivity between models which comply with the standard, and each sub-model creator can verify its compatibility individually. In addition, many hosts platforms can be developed, all compatible with the FMI communication protocol.

Figure 7.1 – FMI/FMU logo.

7.1 Gasdyn co-simulation

This chapter describes the co-simulation environment developed to allow the interaction with any Gasdyn 1D engine model from outside of its native environment, i.e., the Gasdyn Graphical User Interface (GUI). It is now presented how the general Gasdyn co-simulation model is obtained. The co-simulation of the 1D engine model is achieved thanks to the actuation "on the fly" of a series of internal variables, while the simulation is running. The same applies to the co-simulation outputs. The specific elements developed to perform this task are the "co-simulators".

These co-simulation components must be inserted in the 1D schematic from the Gasdyn graphical interface (GUI). The co-simulators can be divided into input and output elements: the first are used to actuate the 1D engine model, while the second are dedicated to extract information about the operating conditions of the engine and its components. The 1D model must be configured in the GUI, by inserting the co-simulation ports and connecting them to the target element, assigning a name and selecting the associated actuation variable.

For example, by connecting a co-simulation input to a cylinder it is possible to actuate the engine speed, spark advance, or engine start&stop. Once the 1D model is configured, the model can be exported by a dedicated internal tool and an "FMU" file is obtained. This file can be finally imported into a host platform.

The 1D model coupling is cyclic, this means that every input or output signal is calculated and imposed at every thermodynamic cycle. The actuation and extraction steps are determined by the duration of the thermodynamic cycle, which is physically determined by the engine speed: i.e., it is not possible to change the engine speed while the thermodynamic cycle is under progress, but only at the end of the ongoing cycle, updating the control variables for the next one.

It is important to highlight that the 1D engine model is based on a crank-angle resolved solver, as explained in the previous chapters. Many actuation possibilities have been introduced, covering the whole range of inputs available in the typical "standalone" Gasdyn 1D engine model, to provide the maximum versatility. A generic list of actuation and output parameters is reported in the Figures 7.2 below for both SI and CI engine types.

Usually much less signals are needed for the investigated co-simulations described in this thesis. However, with the aim of generalizing the methodology as much as possible and in view of its interface with an engine ECU model, more actuation options have been introduced.

	Input singals	units			Output singals	units
1	Engine speed	rpm		1	Engine torque	Nm
2	Engine requested torque	Nm		2	Engine speed	rpm
3	Throttle valve opening	%		3	Fuel consumption	g/s
4	Injected fuel	kg/cylinder/cycle		4	Peak cylinder pressure	bar
5	Spark advance	deg aTDC		5	Lambda	-
6	Injection pressure	MPa		6	NOx	-
7	Number of injections	-		7	CO	-
8	Start of Injection1	deg bTDC		8	C3H6	-
9	Start of Injection2	deg bTDC		9	C3H8	-
10	Start of Injection3	deg bTDC		10	O2	-
11	Start of Injection4	deg bTDC		11	CO2	-
12	Injection fraction1	-		12	H2O	-
13	Injection fraction2	-		13	H2	-
14	Injection fraction3	-		14	Soot - PM	g/h
15	Injection fraction4	-		15	Piston heat flux	W
16	Compression Ratio	-		16	Liner heat flux	W
17	Cylinder1 deactivation	-		17	Cylinder head heat flux	W
18	Cylinder2 deactivation	-		18	Boost pressure	bar
19	Cylinder3 deactivation	-		19	TC shaft speed	rps
20	Cylinder head temperature	K		20	Compressor inlet mfr	kg/s
21	Cylinder liner temperature	K		21	Compressor inlet Temperature	K
22	Cylinder piston temperature	K		22	Compressor inlet pressure	bar
23	Intake Valve Opening	deg		23	Compressor outlet mfr	kg/s
24	Intake valve profile	-		24	Compressor outlet Temperature	K
25	Exhaust Valve Opening	deg		25	Compressor outlet pressure	bar
26	Exhaust valve profile	-		26	Intake manifold mfr	kg/s
27	WG opening	%		27	Intake manifold Temperature	K
28	Intercooler wall temperature	K		28	Intake manifold pressure	bar
29	Back pressure	bar		29	Turbine inlet mfr	kg/s
30	Ambient pressure	bar		30	Turbine inlet Temperature	K
31	Ambient temperature	K		31	Turbine inlet pressure	bar
32	Engine start/stop	-		32	Turbine outlet mfr	kg/s
33	Turbine inlet duct wall tempperature	K		33	Turbine outlet Temperature	K
34	Turbine outlet duct wall tempperature	K		34	Turbine outlet pressure	bar
35	Compressor inlet duct wall tempperature	K				
36	Compressor outlet duct wall tempperature	K				
37	Electric motor speed	rpm				
38	Electric motor power	W				
39	Duct wall temperature	K				
40	PID target value	-				

Figure 7.2 - General list of input and output signals for SI (left) and CI (right) engines.

Figure 7.3 below shows the typical set-up of the 1D engine model for co-simulations. In the graphical schematic the co-simulator elements (circles) are highlighted; each of them allows to modify the desired selected parameters. Each co-simulator has a user-defined name, which allows to identify the ports from each other in the host platform, when the coupling is performed.
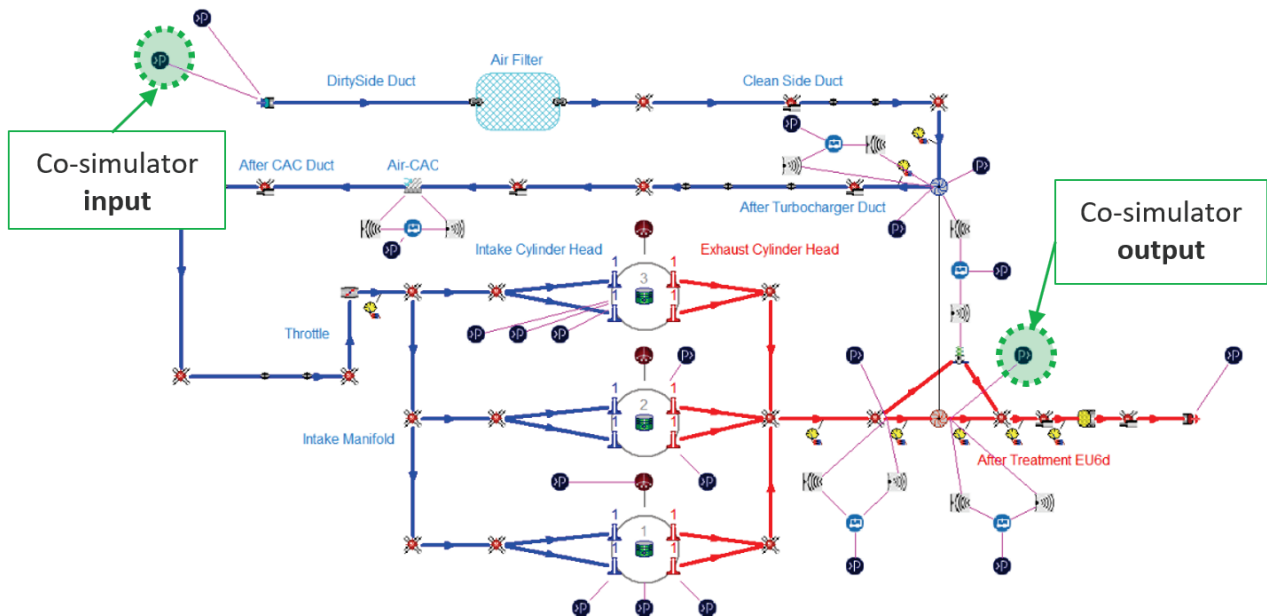

Figure 7.3 - 1D RSA 3-cyl. engine model configured with co-simulator elements.

7.2 Synchronization of the co-simulation

Many sub-models can be involved in a co-simulation model. Each sub-model could have a different numerical solution. The models could potentially advance in time at very different time scales, but when considering a co-simulation this is not possible. So, the host platform manages the input and output routing, but each model decides how often, or with which frequency, listen for inputs and give outputs, hence the host must wait for the slowest model to be up to date, before signalling the other models to continue. The important thing is that the physical time is always the same for all sub-models in the co-simulation environment.

7.3 Type of signals that can be exchanged in co-simulation

The reader has probably noted that the list of signals that is possible to give o retrieve from the 1D engine model consists of single real values. It is possible to group different signals under a single 'bus' but it was not possible to exchange arrays of data.

7.4 Co-simulation via MATLAB S-function interface

This paragraph describes the first methodology developed to allow the co-simulation with any Gasdyn 1D engine model: the S-function block under MATLAB Simulink® environment (see Figure 7.4 below). The implemented S-function is linked to the installed Gasdyn solvers and libraries on the PC and can be imported and executed as any other block of the Simulink® library. To use this block, the input files of the 1D engine schematic (in co-simulation configuration) must be compiled using the Gasdyn interface (GUI), then the S-function must be set to point to the desired inputs. Once the Simulink® 'Gasdyn S-function' has been configured, the desired signals arriving from other model blocks or from experimental data can be connected to the S-function ports. The configured output signals are continuously computed and can be used by external models, while the co-simulation is running. This co-simulation configuration is exploited for the prediction of RDE cycles, as discussed in the next sections.
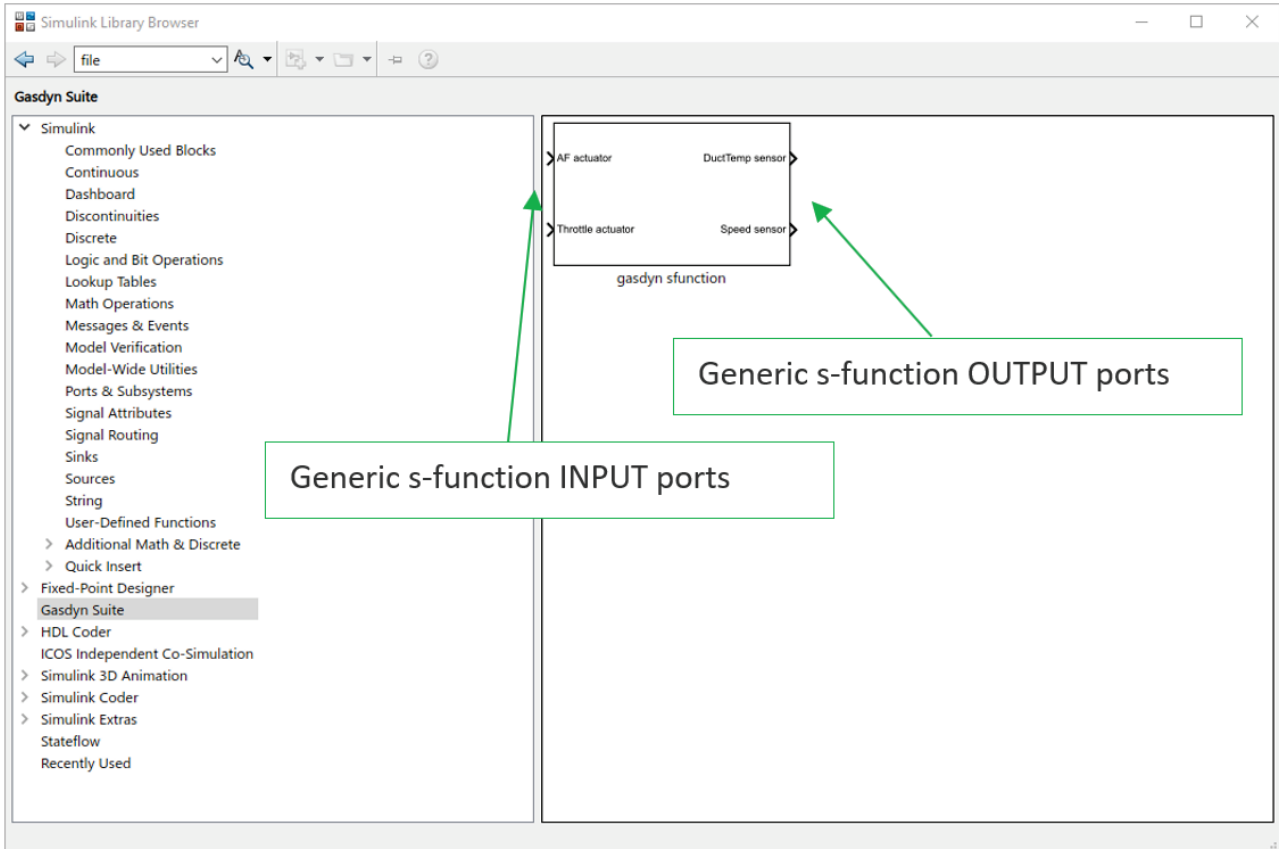

Figure 7.4 - Gasdyn S-function block for co-simulation in MATLAB Simulink® environment.

7.5 Co-simulation via FMU interface

This paragraph describes the second methodology developed to interact with a generic Gasdyn 1D engine model by means of any FMU or FMI compliant host platform, hence through the FMU file format (fmu file extension). FMI and FMU are synonyms; it is important to highlight that the FMU/FMI is a standard communication and execution protocol defined to ensure that all .fmu files created, compliant with this standard, can exchange information in a generic co-simulation framework. The FMU file of a Gasdyn 1D engine model can be created by the Gasdyn GUI by clicking on 'export FMI', see Figure 7.5. This automatic procedure implemented creates a file of the corresponding configured engine model with the extension '.fmu', which can be imported and used in any co-simulation platform which is FMU compatible. Moreover, the FMU 1D engine model can be also imported in the Simulink® environment through the Simulink® 'import FMU' block.
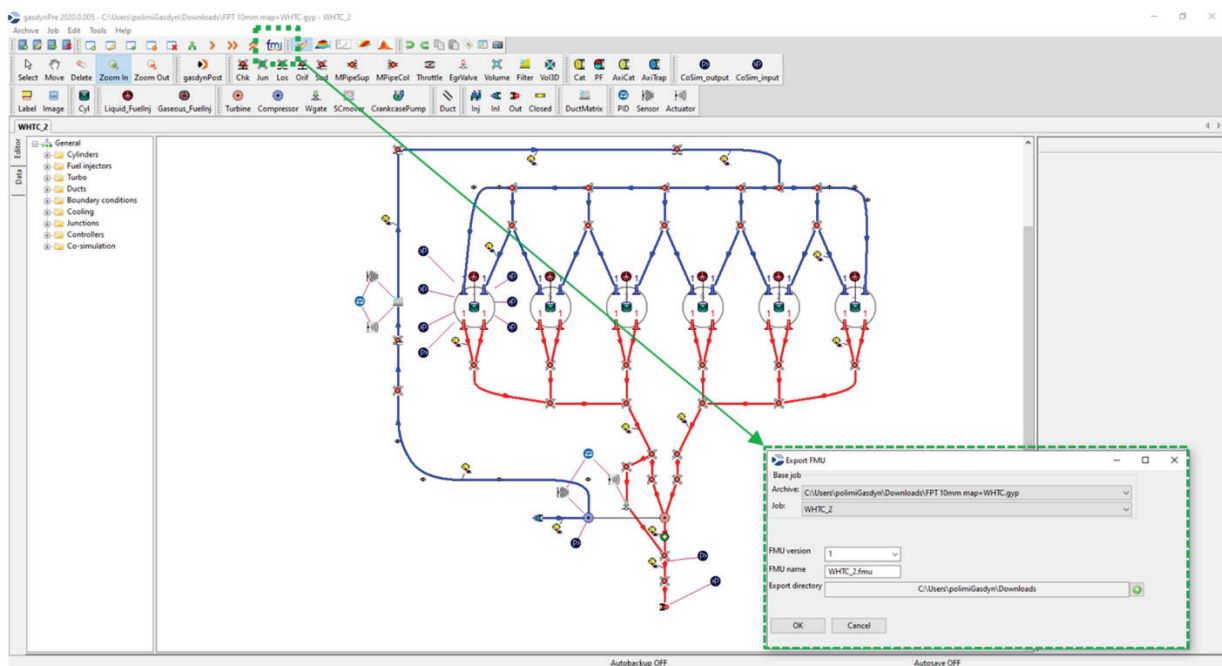

Figure 7.5 - 1D FPT 6-cyl. engine model configured for co-simulation and creation of the corresponding FMU file.

7.6 Coupling with the thermal ICE model

In this chapter it is described the coupling achieved with the thermal model of the engine developed by UPV (Universitat Politècnica de Valencia). During RDE cycles, the engine can be continuously started at different thermal levels and, during prolonged engine-off periods, the engine can cool down at ambient temperature, so that at successive restart it is not warmed-up anymore. This coupling aims at modeling the effect of the engine thermal state on its 1D simulated performances. The goal is also to improve the fidelity of the simulation, to better represent the real engine.

From the 1D engine model point of view, the engine block thermal state can impact mainly through two effects:

1) First, the surface wall temperatures of the combustion chamber, discretized as liner, head and piston, are not constant during the simulation and are different between each other. The evolution of these surface temperatures in time depends on the heat released by the combustion process and on the heat rejected to the cooling system. Without a model that can predict these temperatures according to the actual engine operating conditions, the 1D model can only use constant (hot or cold) surface temperatures during the whole RDE simulation, which is not realistic.

2) Secondly, it is well known that the engine lubricating oil can have a very different viscosity according to its temperature [57]. Indeed, for different climates, different oil types are prescribed for the same engine. A cold and more viscous engine oil does not flow smoothly and increases the friction between the lubricated parts inside the engine crankcase. This resistance to the motion of the engine parts results in an increase of engine load, to achieve the same net performance of a warm engine with warm oil inside the crankcase. The expected effect of this increased resistance is the raise of the fuel consumption. This coupling aims at filling this first simulation gap, and its main impact is expected on the cylinder-out emissions, since it affects the pollutant formation during and after combustion.

The UPV thermal model resolves the thermal calculation of the engine components and of the cooling system, including the simulation of the oil and water circuits. For a detailed description of this sub-model the reader is invited to have a look at [58] The connection between the 1D engine model and the thermal model occurs in the cylinders, where heat is transferred from the working fluid to the solid components of the engine. On one hand, the heat rejected by the 1D model depends on the metal temperatures of the piston, line and head. On the other hand, the cooling performance of the UPV model depends on the actual heat rejected by the 1D model. With a co-simulation it is possible to feed the thermal model with the actual heat calculated from the 1D model and, vice versa, feed the 1D model with the metal temperatures calculated by the UPV model. Hence, the coupling between the 1D and UPV model aims to affect both calculations with the predicted input from the other model.

To realize this co-simulation, a co-simulator input connected to the 1D solver variables identifying the combustion chamber temperatures, has been implemented. To transfer the heat power to the UPV model, a co-simulator output calculating the respective heat rejected to the head, liner and piston has been implemented.

Additionally, it has been found that the engine oil temperature influences the overall engine friction. A simple model proposed by [57] has been implemented to account for this. The friction is increased by an amount which depends on the current engine oil temperature, which is calculated by the UPV model. To consider this effect in the 1D engine calculation, a dedicated sub-model has been implemented. The computed engine friction is increased by a factor that depends on the ratio between the engine oil viscosity at current temperature and the viscosity at a hot reference conditions, usually 90°C. The simple equation in Figure 7.6 has been adopted:
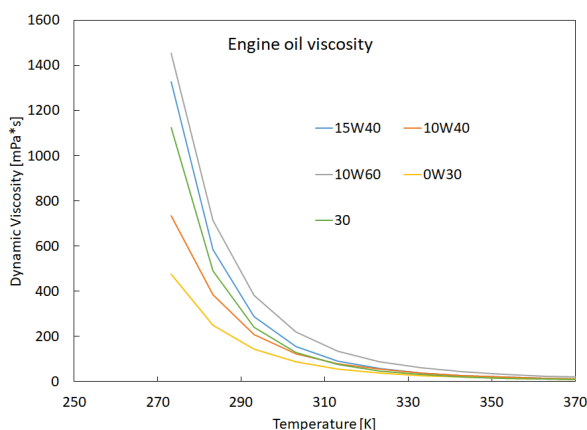
$$fmep = fmep_{ref} * \left(\frac{\mu}{\mu_{ref}} \right)^n$$

Where:

$fmep_{ref}$ = FMEP at reference (hot) conditions
μ = oil viscosity at current oil temperature
μ_{ref} = oil viscosity at reference (hot) conditions
n = calibration coefficient

Figure 7.6 – Engine oil viscosity trend and model equation.

The term $fmep_{ref}$ is the engine friction used during steady state simulation, which was derived as the difference between the experimental BMEP and IMEP. The IMEP has been derived from the indicated cycle. The typical value of n is 0.15 ÷ 0.19 for small gasoline engines and 0.21 ÷ 0.35 for large heavy duty diesel engines. There are several types of engine oil, each one with its own viscosity characteristics. Many of them

have been implemented in the database of the Gasdyn code, however for this particular use case the "SAE15W40" oil has been selected (see Figure 7.6).

The coupling between the Gasdyn 1D engine model and the UPV thermal model is configured as follows. At every thermodynamic cycle, the 1D engine model computes the heat power loss [W] due to the wall heat flux in the combustion chamber of each cylinder. As anticipated, this heat loss depends on the temperature and surface area of the cylinder head, the liner and the piston. These values are transferred to the UPV model, together with the current engine speed (this last data is needed by the UPV model).

The 1D engine model receives back, from UPV model, the calculated engine oil temperature and the temperature of the metallic surfaces of the combustion chamber (liner, piston and head). The cooling system model is made of two separate model, one for the liquid circuit (hydraulic) and one for the metal thermal transient. With Figure 7.7 the models' interactions are presented. A more detailed description of the hydraulic and thermal model developed by UPV can be found in [58].
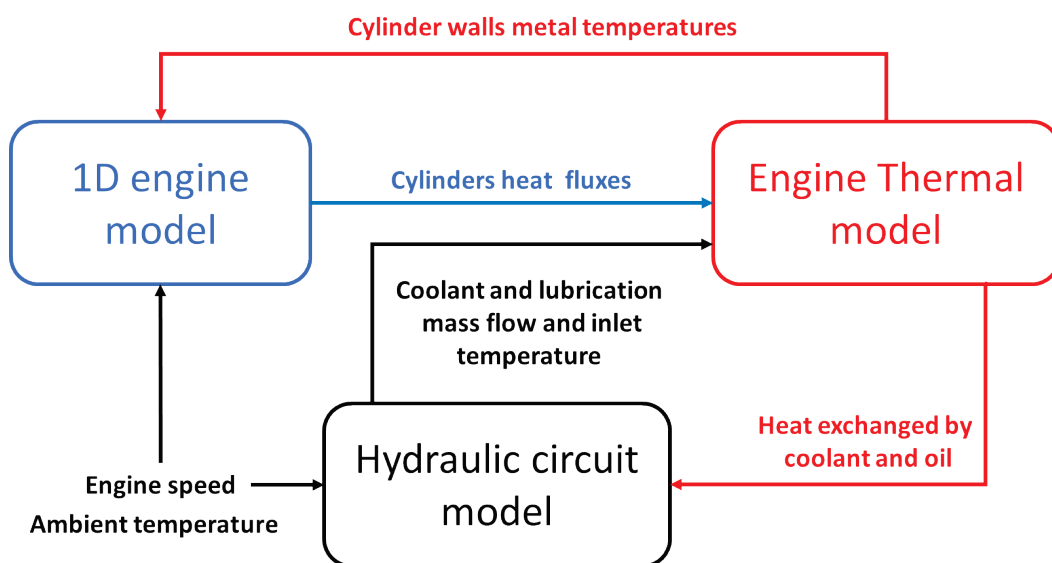
Figure 7.7 – Integration of ICE thermal model, 1D engine model and hydraulic model.

The coupling strategy has been demonstrated on the same RDE cycle previously presented. The comparison between the cumulative fuel consumptions shows a small difference, as reported in Figure 7.8. This is due to the following main effects: first, the additional friction of the engine is not that high and secondly, as soon as the engine warms up a little, the effect becomes small, as shown in the graph of engine oil viscosity as a function of temperature (see Figure 7.6). The final difference in the cumulated fuel consumption is approximately 1%, even if at the start of the RDE cycle it was clearly greater.

Figure 7.8 – Comparison of the predicted cumulative fuel consumption,
between the standalone and the coupled simulations during the RDE.

To highlight the effect of an increased friction due to a lower engine oil temperature, on the basis of the coupling occu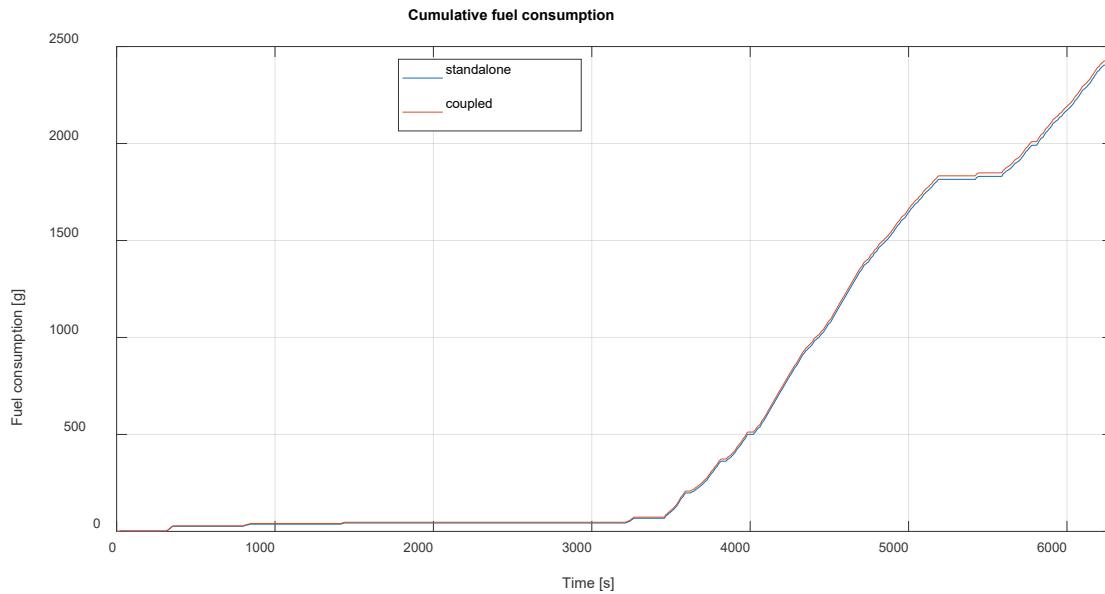rring between the UPV engine thermal model and the 1D engine model, the average friction mean effective pressure (FMEP) during standalone and coupled simulations is reported in Figure 7.9. It is evident that the friction is different mainly at the beginning of the RDE cycle, since the oil is cold at the start. Then the difference becomes smaller and smaller as the simulation progresses and the oil heats up, until the two FMEPs coincide in warm conditions.
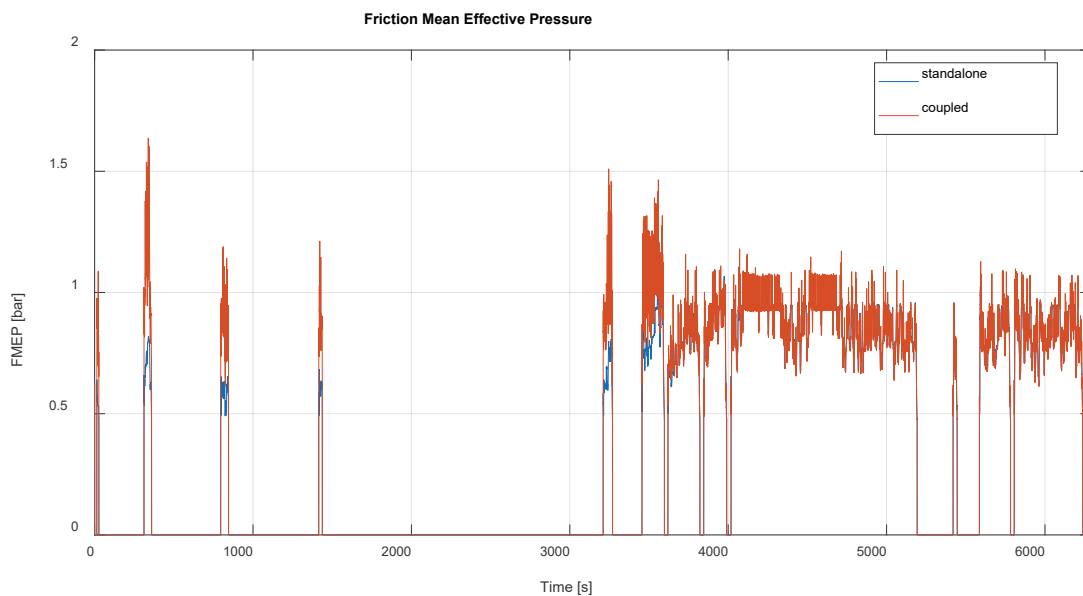
Figure 7.9 – Predicted FMEP comparison between the standalone and coupled simulations during the RDE cycle.

The time series of the rejected thermal powers during the RDE cycle is also shown in Figure 7.10. It is evident how the thermal power depends on the operating conditions of the engine, mainly engine load and speed. However, no heat is rejected when the engine is turned off, as there is no combustion, and the engine oil temperature drops.

The time series of the wall temperature of the combustion chamber surfaces, calculated by the UPV model according to the real-time heat thermal power rejected by the 1D engine model, is reported in Figure 7.11. As confirmed by the trend of the engine oil temperature, the surface temperatures of the combustion chamber also drops when the engine is off.

Figure 7.12 below remarks the evolution of the engine oil temperature calculated by the UPV model, due to the heat transfer through the surfaces of the combustion chamber (in the 1D engine model), highlighting the interaction between the two models.
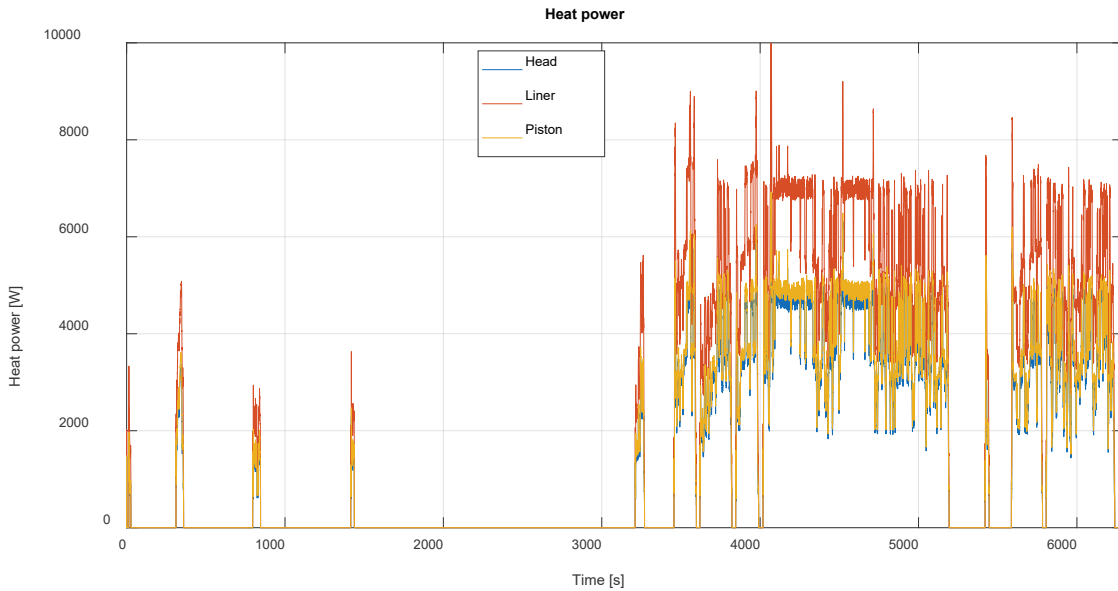

Figure 7.10 - Combustion chamber surface temperatures calculated by the UPV model and provided to the 1D engine model.
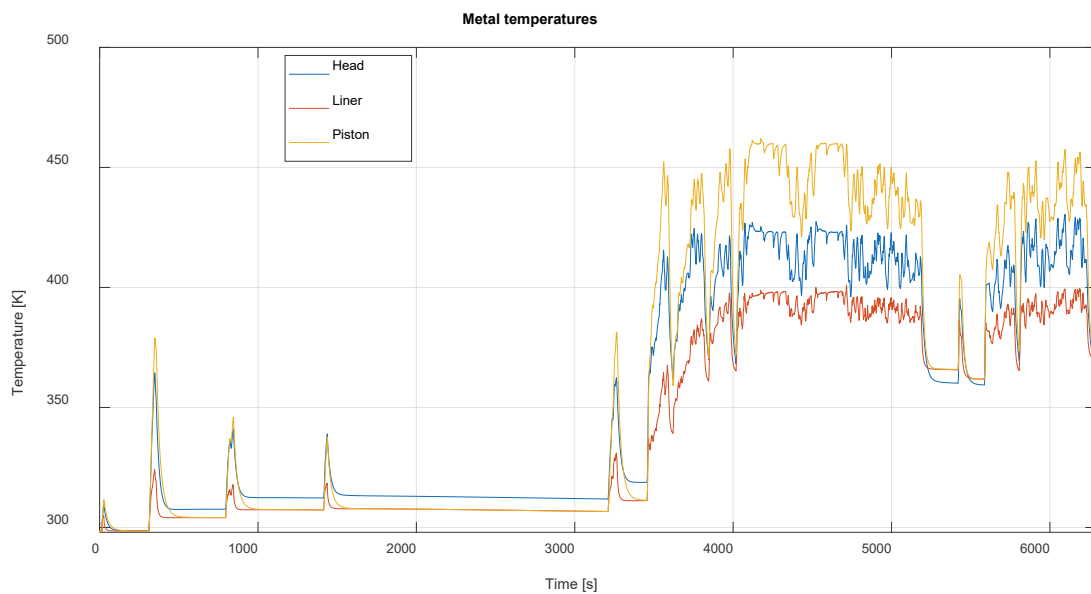

Figure 7.11 - Heat powers rejected through the combustion chamber surfaces, calculated by the 1D engine model, provided to UPV engine thermal model.
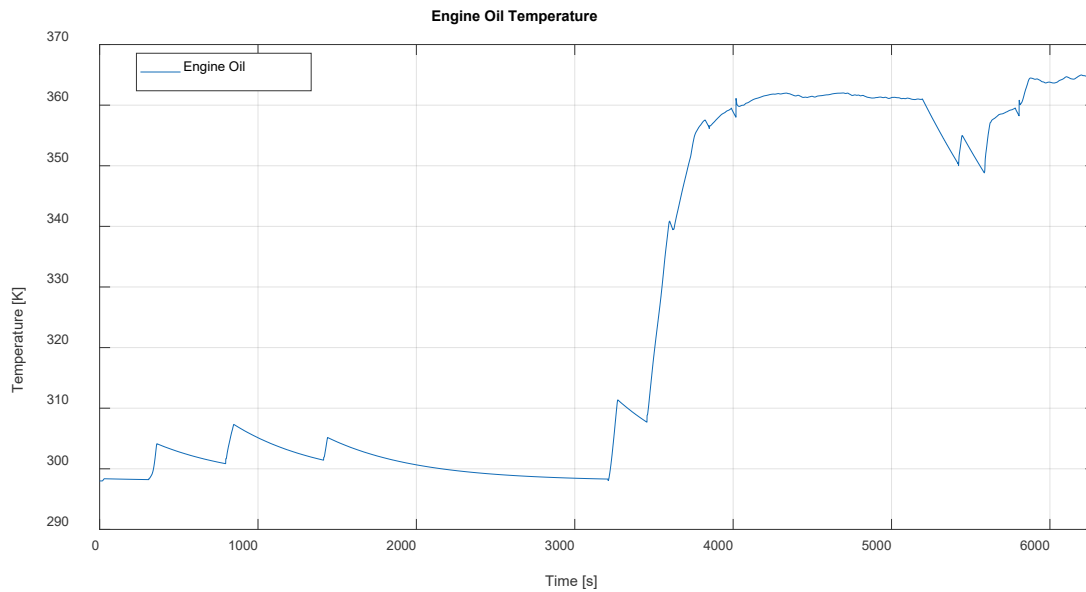
Figure 7.12 - Engine oil temperature calculated by UPV model and transferred to the engine 1D model for friction correction.

With regard to the predicted pollutant emissions, it is possible to observe how the predicted cylinder-out emissions have changed thanks to the coupled approach. The cylinder-out predicted concentrations in [*ppm*], shown in Figure 7.13, of the instantaneous HC during the RDE cycle show a significant difference, especially at the beginning of the cycle, when the surfaces of the combustion chamber are cold, and the emission of hydrocarbons is larger. The difference with the uncoupled simulation gets smaller and smaller as the engine warms up, however it settles at a slightly different average value. This is because the final hot temperature of the combustion chamber surface is different from that used for the standalone simulations. The instantaneous NO_x trend comparison is presented in Figure 14 and shows a smaller difference: the coupled simulation, due to the lower temperature of the combustion chamber, reaches lower maximum temperatures thus producing slightly lower NO_x. The same consideration on the steady state wall temperature difference is valid for the NO_x.

Figure 7.13 – Hydrocarbon pollutant emission comparison with the standalone and coupled simulations during the RDE cycle.

110

NOx cylinder-out

Figure 7.14 – NOₓ pollutant emission comparison with the standalone and coupled simulations during the RDE cycle.
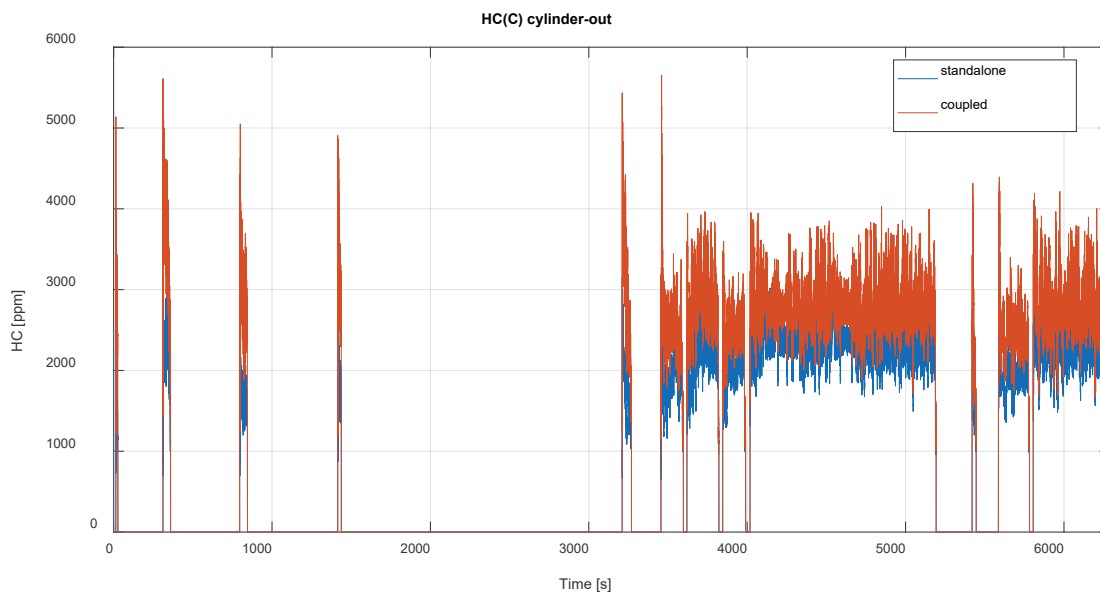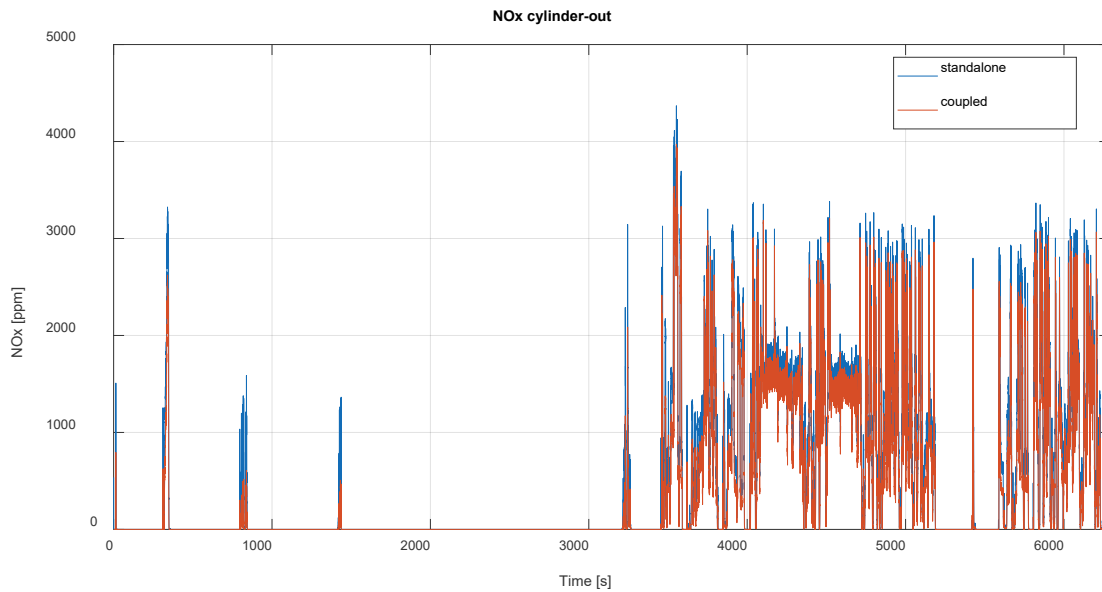
7.7 Coupling with the Exhaust After Treatment system model

In this section it is described the coupling strategy developed to interconnect the 1D engine model and the exhaust after treatment (EAT) system model. This development has been carried out in collaboration with AUTh (Aristotle University Thessaloniki), which provided the EAT model, developed in their own simulation tool [59]. The activity has the goal of coupling the models in a direct way, so that the tailpipe emissions can be evaluated within a co-simulation framework which includes the engine and exhaust after-treatment models running simultaneously. During RDE cycles, it is mandatory to evaluate the thermal state of the after-treatment device, since it influences its conversion efficiency. For this reason, it is important to accurately predict the gas mass flow rate and the gas temperature provided by the engine. To perform the coupling, the cylinder-out emissions of each combustion are transferred as the inlet composition of the EAT model, along with the cycle-averaged mass flow rate and temperature of the exhaust gas at the outlet of the turbine. To realize this coupling, specific co-simulators have been implemented in the 1D model. The coupling schematic is presented in Figure 7.15 below.
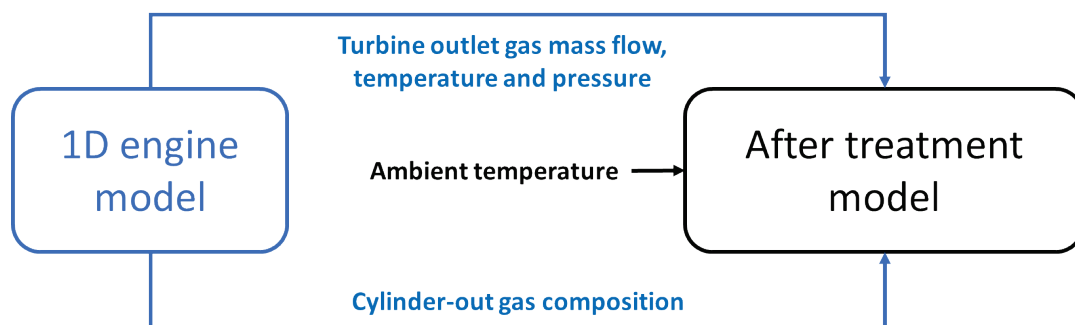
Figure 7.15 – Integration of the 1D engine model and the exhaust after treatment model.

The coupling is demonstrated on the same RDE cycle previously presented in chapter 6. By means of the coupling between the 1D engine model and the exhaust gas after-treatment model (AUTh was in charge for that), it is possible to evaluate the real-time conversion of pollutants and thermal evolution of the EAT. The instant exhaust emissions are reported in Figures 7.16 and 7.17, demonstrating that the EAT can convert pollutants, reducing oxidizing CO, while the CO2 steadily increases (Figure 7.17). A complete oxidation of CO

is not achieved, due to lack of oxygen in the gas stream, dictated by the rich lambda operating conditions of the engine, as indicated by experimental data.
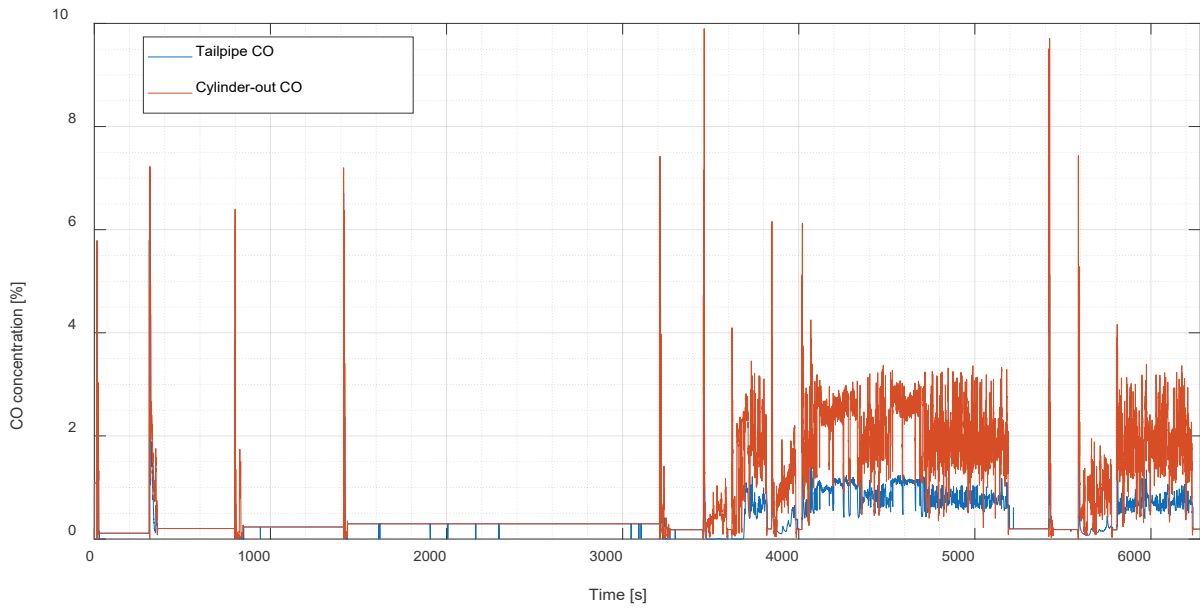
Figure 7.16 - Conversion of CO through the EAT model.
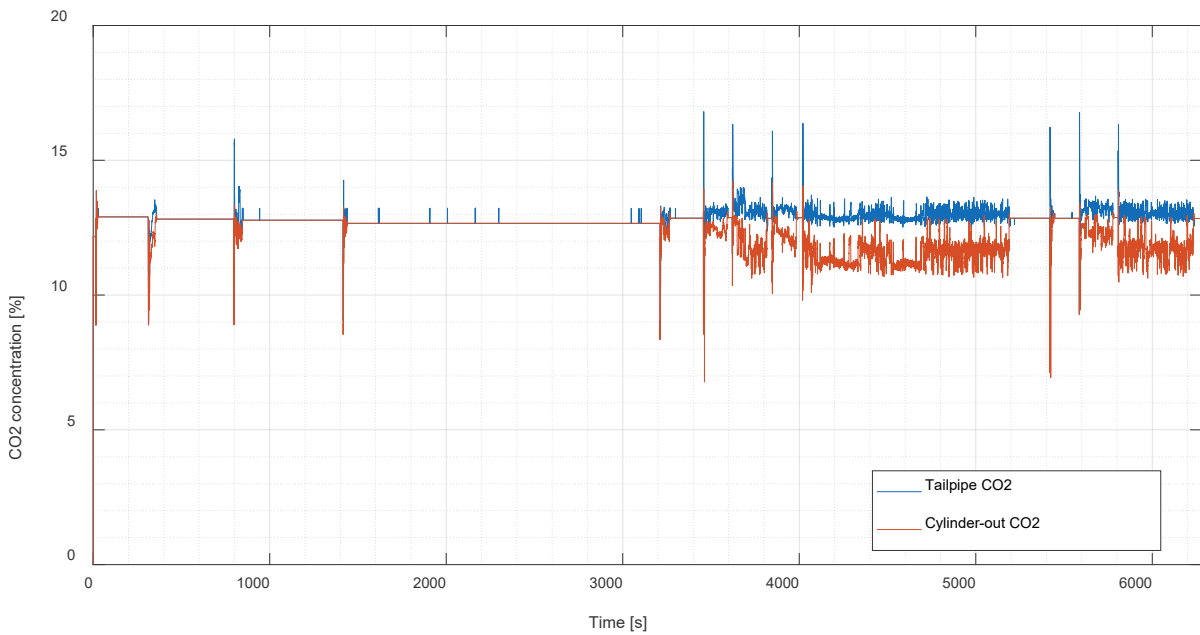
Figure 7.17 – Tailpipe and cylinder-out predicted CO2.

The calculated backpressure and the temperature of the after-treatment system are also reported in Figure 7.18. These results demonstrate that the model coupling is carried out correctly: the EAT conversion process depends on the inputs from the 1D model, with the two models connected in real time. Particularly interesting is the possibility of predicting the shutdown times of the catalytic converter, which depend on the mass flow rate, the temperature and the composition of the gas stream supplied by the 1D engine model. The predicted back pressure reported in Figure 7.18 shows a good sensitivity to the exhaust mass flow rate, increasing as expected when the mass flow rate increases.
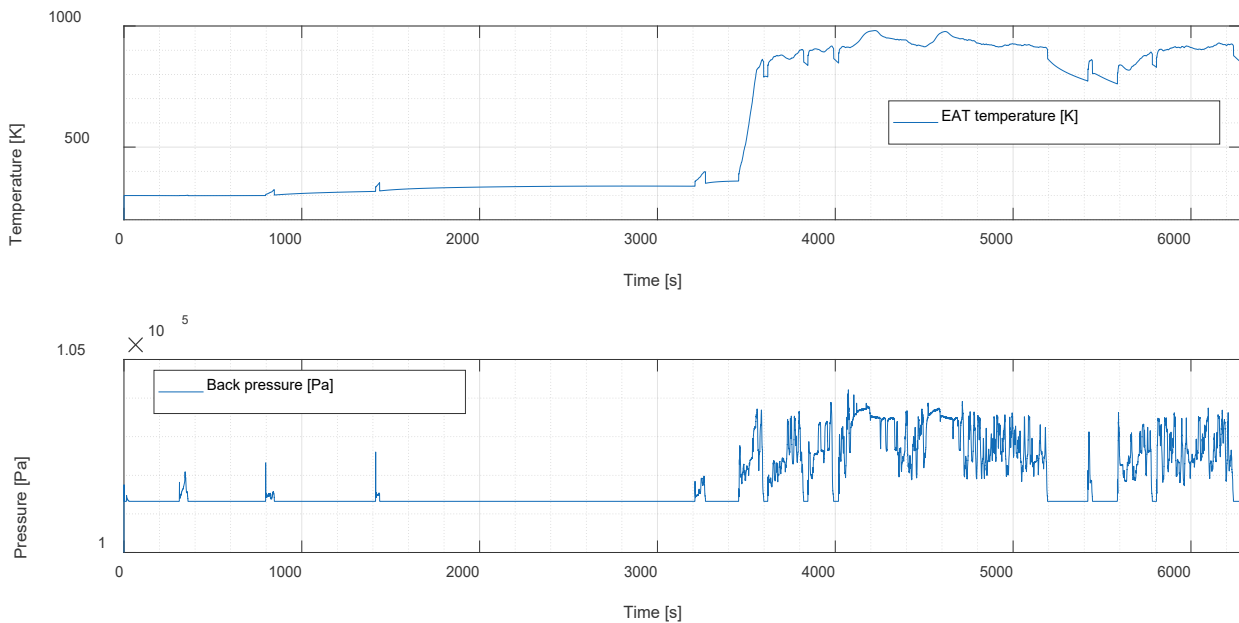
Figure 7.18 – EAT light-off (top) and back-pressure (bottom) predictions of the coupled model.

7.8 Coupling with the turbocharger thermal model

In this section the connection between the 1D engine model and the turbocharger thermal model is described. This activity has been carried out in collaboration with TUB (Technical University Berlin) [60,62], in charge for the development of this sub-model and indicated the coupling strategy with the 1D model to be followed.

During RDE cycles, the turbocharger continuously varies its working temperature, starting from ambient conditions and warming-up, due to the hot exhaust gases flowing from the cylinders. To preserve their mechanical integrity, turbochargers are always lubricated and cooled when the engine is running. The lubrication also serves as a vector of heat dissipation, to avoid an excessive thermal stress of the turbocharging group. Additionally, there is a contribution of heat conduction between the compressor wheel/casing and the turbine wheel/casing, which is responsible of a considerable heat flux whose direction depends on the operating temperatures of the compressor and the turbine. This represents a heat source for the gas flowing through the turbocharger, which must be considered. Hence, the thermal state of the turbocharger affects the gas temperature at the outlet of the turbine and the compressor [63].

The 1D engine model relies on a 0D description of the turbocharger, based on the characteristic maps for the turbine and compressor provided by the manufacturer. These maps are usually obtained experimentally, under steady state of both fluid dynamic and thermal conditions. Hence, the measured maps represent the performance of the turbomachinery at the temperature at which the turbocharger was running during the measurements. However, as anticipated before, the performances (characteristic maps) of the turbocharger depend on the turbine/compressor thermal state.

To consider this effect in a co-simulation framework, the following procedure is adopted. The general idea is to remove the heat transfer contribution from the 1D model by using adiabatic maps in the compressor and turbine boundary condition solution. These adiabatic maps are obtained from the manufacturer maps by a corrective adiabatization process performed by TUB [61]. Then the thermal effects are reintroduced into the 1D engine model, by means of suitable source terms in the energy conservation equation (heat transfer) of the ducts prior and after the compressor and the turbine. The adiabatic maps of the compressor and turbine, obtained by TUB, have been treated to allow their use in a 1D code, mainly extending their range by interpolations and extrapolations performed over the manufacturer maps. Looking at Figures 7.19, it is

113

evident the difference between the compressor characteristic curves obtained in adiabatic conditions and those measured in presence of heat transfer. The compressor pressure ratio is similar. Instead, the efficiency of the compressor at low mass flow rates and low speed is much higher removing the heat transfer contribution. This is because, at low mass flow rates and speed of the machine, the heat transfer from the turbine is strongly affecting the compressor outlet gas temperature, due to the higher 'residence time' available for heat transfer to occur. The figures also suggest that, at higher rotational speed and mass flows elaborated, the increase of heat transfer coefficient is not enough to impact on the outlet gas temperature. The 'adiabatic' curves show the compressor is fluid dynamically efficient even at low speed, indicating a lower gas temperature would be reached if the compressor were properly insulated from the turbine.
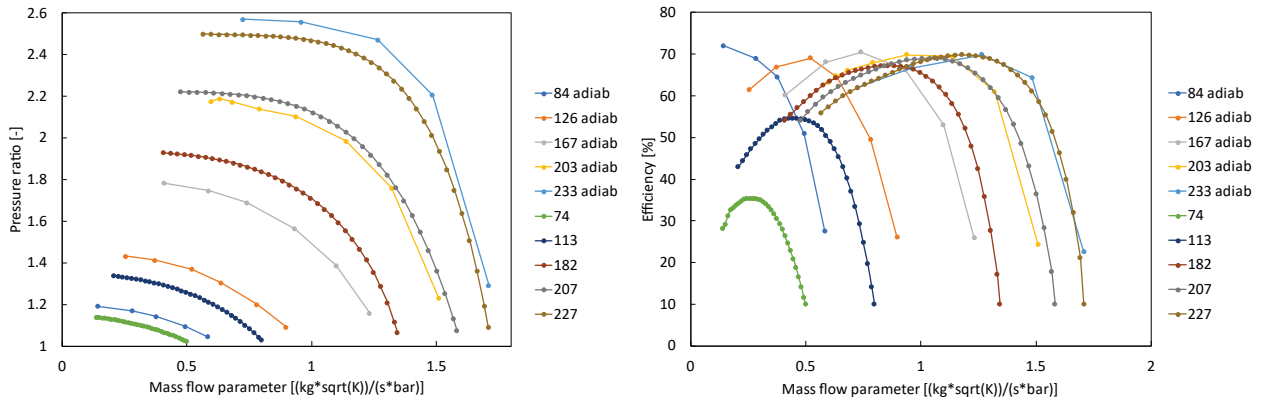
Figure 7.19 – Adiabatic ("adiab") and measured compressor characteristic map comparison.
Curves at similar speed parameter values [*rps/sqrt(K)*].

Therefore, the development of the model coupling focused on how to correct on-the-fly the 1D model in such a way to consider this difference. So, while the simulation proceeds, the 1D engine model computes the cycle averaged turbocharger speed and mass flow rates through the compressor and turbine, and the gas temperatures at the inlet and outlet of both machines. These quantities are transferred to the TUB model, which computes the output gas temperatures, considering the heat transfer occurring in the machines. These corrected gas temperatures are fed back to the 1D engine model, which uses them as a target value for a dedicated internal PID controller. The PID aims at reaching the target gas temperature by acting on the wall temperature of the associated 1D duct, increasing or decreasing the heat transfer source term in the 1D modelling, to impose the actual heat transfer computed by the TUB turbocharger model. The coupling procedure is schematically represented in Figure 7.20 below:
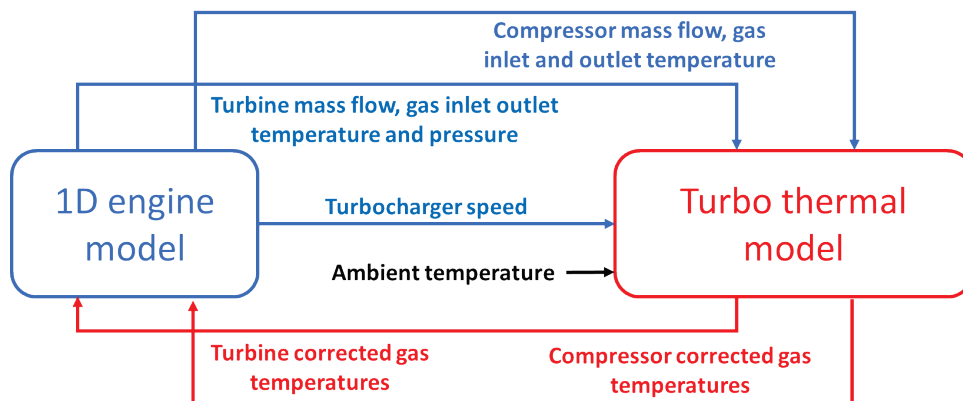
Figure 7.20 – Integration of the 1D engine model and the turbocharger thermal model.

To highlight the coupling effect of the turbocharger thermal model on the IC engine 1D simulation, the predicted gas temperatures of a stand-alone and coupled simulations are compared. Figure 7.21 shows the

turbine outlet gas temperature. The coupling methodology correctly shows a lower turbine outlet temperature during the whole cycle. The difference between the corrected gas temperature and the standalone simulation gets smaller as time increase. This is expected because initially the turbocharger (and turbine housing) is cold, and the turbine outlet temperature is cooled more than the cool down due to the expansion. The coupled model allows to compute the gas temperature at the inlet of the catalyst considering the thermal state of the turbocharger since the outlet temperature of the turbine is what affects the inlet temperature of the catalyst.
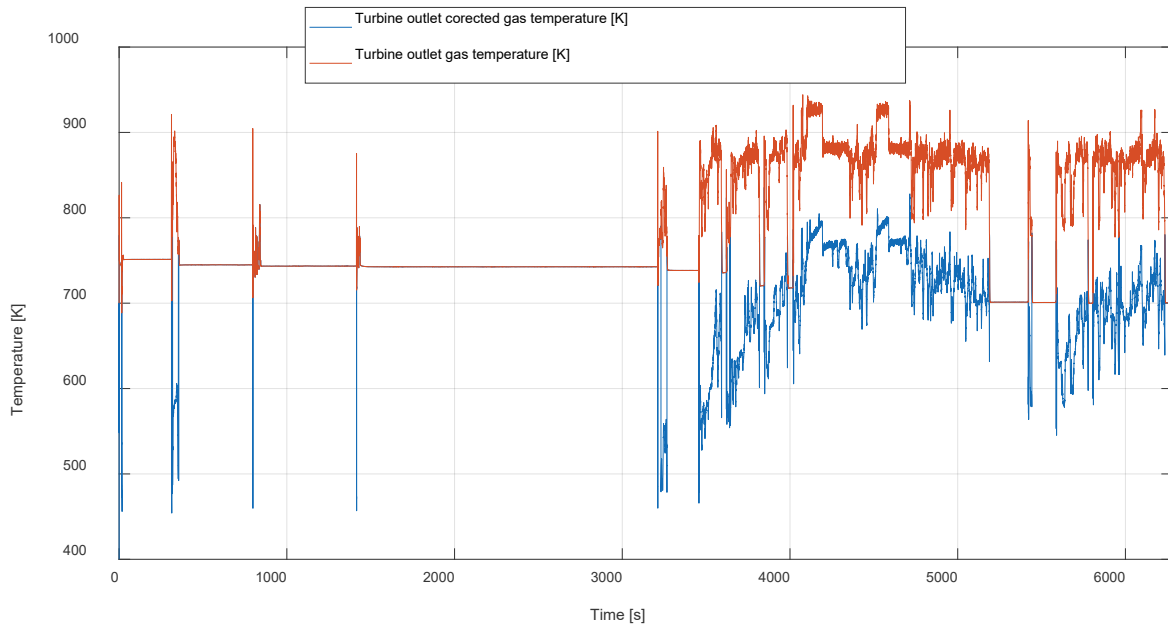
Figure 7.21 - Turbine outlet gas temperature, standalone 1D model (orange) and corrected coupled model (blue).

Figure 7.22 instead shows the compressor outlet temperature. It is evident an increase of the outlet temperature of the compressor, it can be appreciated especially during the last part of the cycle. Once the turbocharger is warm the compressor outlet gas temperature is warmed by the heat transfer from the hot turbine and from the compressor housing that has been warmed up.
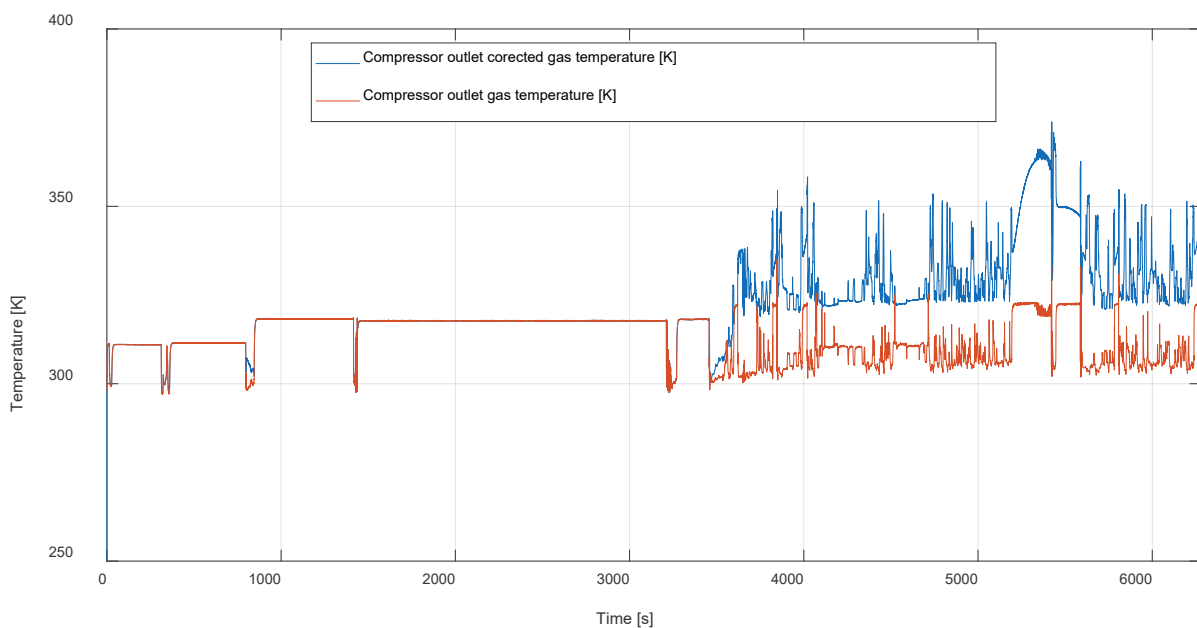
Figure 7.22 - Compressor outlet gas temperature, standalone 1D model (orange) and corrected coupled model (blue).

7.9 Other interconnections - intercoupling

For completeness the other connections among the sub-models not involving the 1D ICE model are now presented. To give an overview of the functional connections, the following Figure 7.23 is proposed, highlighting the co-simulation links of the complete coupled model developed.

The heat power dissipated by the turbocharger is calculated by the TUB turbocharger thermal model and transferred to the UPV cooling system model, which includes it in the thermal power to be dissipated. Vice versa the UPV model sends to the TUB thermal model the mass flow rate and inlet temperatures of the cooling and lubricating fluids.

No signals are exchanged between the thermal model of the engine and the turbocharger with the after-treatment system model.

Figure 7.23 – Overview of the co-simulation framework between ICE-centred sub models.

8. The integrated Plug-in Hybrid Electric Vehicle model

As presented in the previous chapters, the 1D engine model and the other sub-models of the engine components (developed by the partners of the European Union project "VISION-xEV") have been coupled for the simulation of an RDE cycle. However, the vehicle has not been modelled yet, therefore it is now introduced in the overall co-simulation model. Hence, the coupling approach is extended and enhanced, integrating the sub-models into a modern Plug-In Hybrid Electric Vehicle (PHEV) model.

The vehicle model has been provided by AVL partner. The host platform where all the sub-models have been coupled to obtain the full PHEV model is the Model.CONNECT platform [64,65], also provided by AVL. A picture of the initial vehicle model, in which the individual blocks can be identified, is presented in Figure 8.1 below. As a starting point, it already includes some sub-models de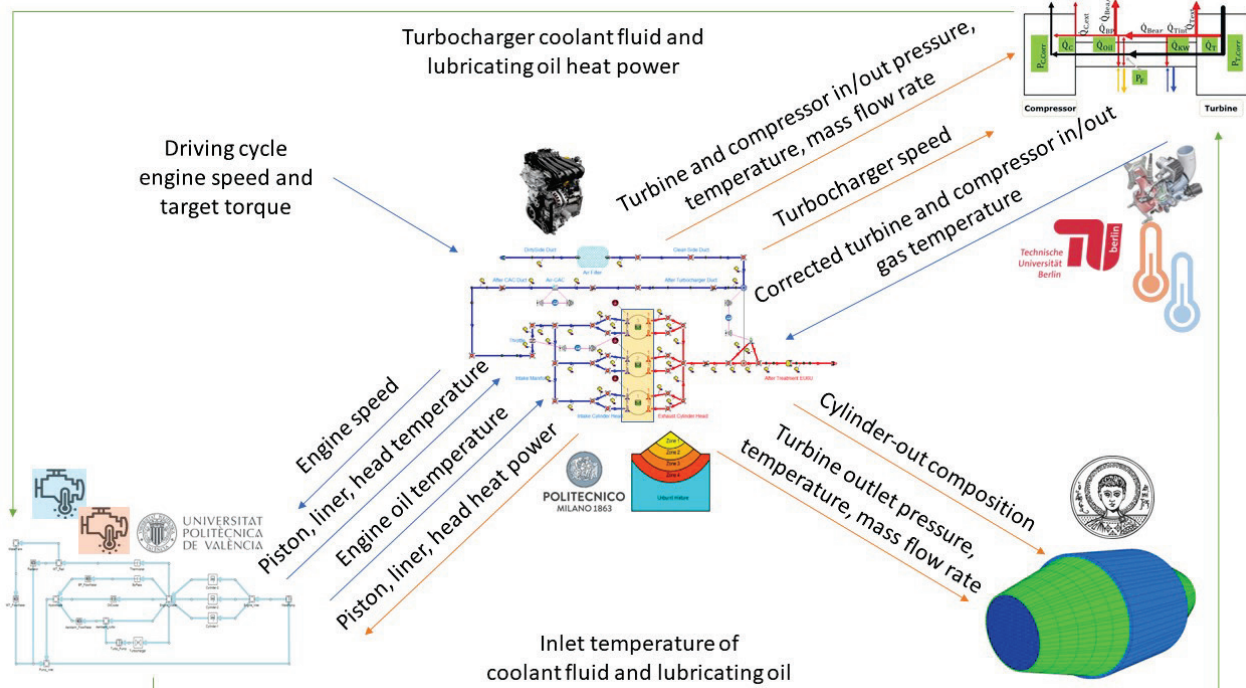veloped by different partners. All the sub models are imported as FMU modules. The vehicle model consists of the following blocks: a driver, a vehicle dynamics element, a battery, an electric motor and an IC engine model. The torque split is also embedded in the vehicle control model, which decides to switch on or off the engine. However, the IC engine model initially used is not a 1D model but a map-based tool, which essentially performs interpolations on look-up tables. In this activity the 1D model and the sub-model previously discussed are introduced in the complete vehicle model, replacing the 1D map-based engine with the complete 1D version of the virtual engine.

Figure 8.1 - Starting Plug-in Hybrid Electric Vehicle model configuration.

The objective of this activity was to connect the detailed models from all partners: PoliMi (1D ICE), UPV (cooling system), AUTh (EAT) and TUB (thermal turbo) to the general vehicle model, by means of the FMU protocol interface. The informatic framework has challenged all the partners involved, but finally the communication issues of the models have been fixed. The first step of the integration process was focused on the addition of the core model of the hybrid vehicle: the 1D engine model. This is the only model connected to almost all the other blocks. Figure 8.2 below highlights the achieved inter-connected model.
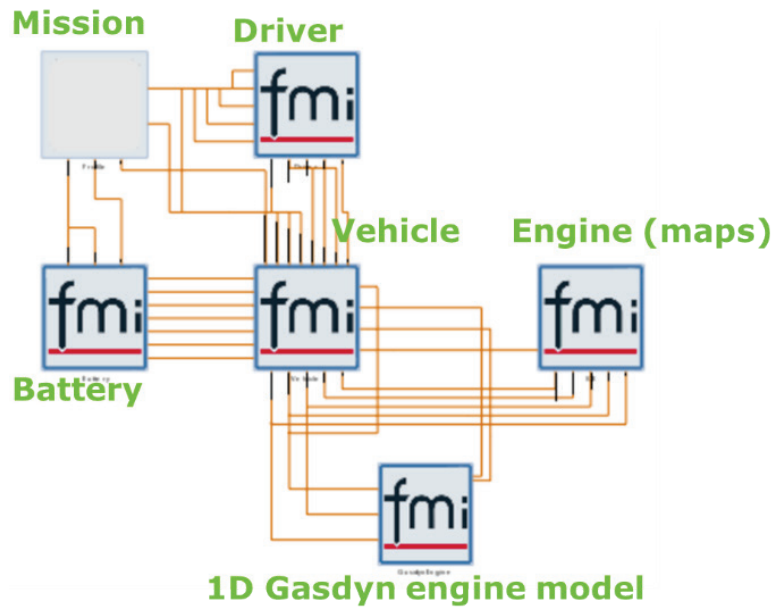
Figure 8.2 - Intermediate coupled HEV configuration (1D ICE integration).

The 1D model used is the FSM model (Fast Simulation Method), to reduce the simulation time. In this model the engine speed is calculated by the vehicle dynamics module, which transmits a torque request to the 1D virtual engine; then, thanks to the torque output from the 1D engine model, it calculates the engine speed evolution. In this feature occurs the main difference between the 1D engine model and the map based one. In fact, the latter instantly satisfies the requested torque, while the 1D model response depends on the fluid dynamics and engine dynamics (throttle opening and boost increase).

It must be mentioned that the map-based engine has not been completely removed, since some operating signals computed by this block are still needed by the vehicle block and cannot be computed by the 1D model. There is no connection between the map-based and the 1D engine models, since the signals provided by the map-based model are not relevant to the 1D engine model simulation. However, the most important coupling, represented by the torque and engine speed interaction that influences the vehicle speed, has been successfully implemented. The engine off signal is used to control the 1D engine status, depending on the control strategy implemented in the complete vehicle model.

Finally, the other sub-models presented in previous chapters have been integrated as well. The final complete, coupled vehicle model is reported in Figure 8.3 below. This modelling platform also allows to simulate different configurations of the same vehicle, for example evaluating the impact of a new after-treatment system, or of a different engine calibration on the emissions during an RDE cycle. It is simply required to replace the corresponding FMU block with the modified one, representing the new system or engine configuration.
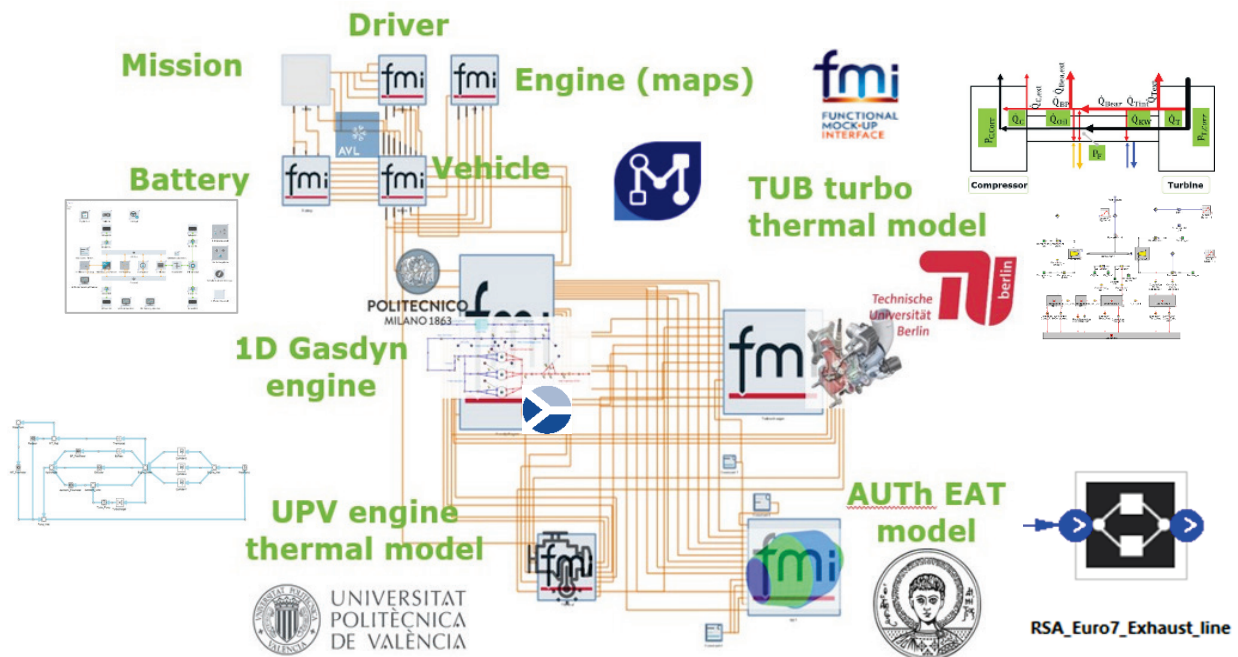
Figure 8.3 - Final coupled models for simulation of PHEV – integration and connection of all partners sub-models.

In conclusion, a simplified schematic regarding the most important signals exchanged in real-time among the four engine sub-models is reported in Figure 8.4. The timing of the variable exchange process is managed by the host platform, Model.CONNECT by AVL, which coordinates the execution of each sub-model. The host platform waits for each model to complete its time step, before communicating the input/output variables needed by the various models.
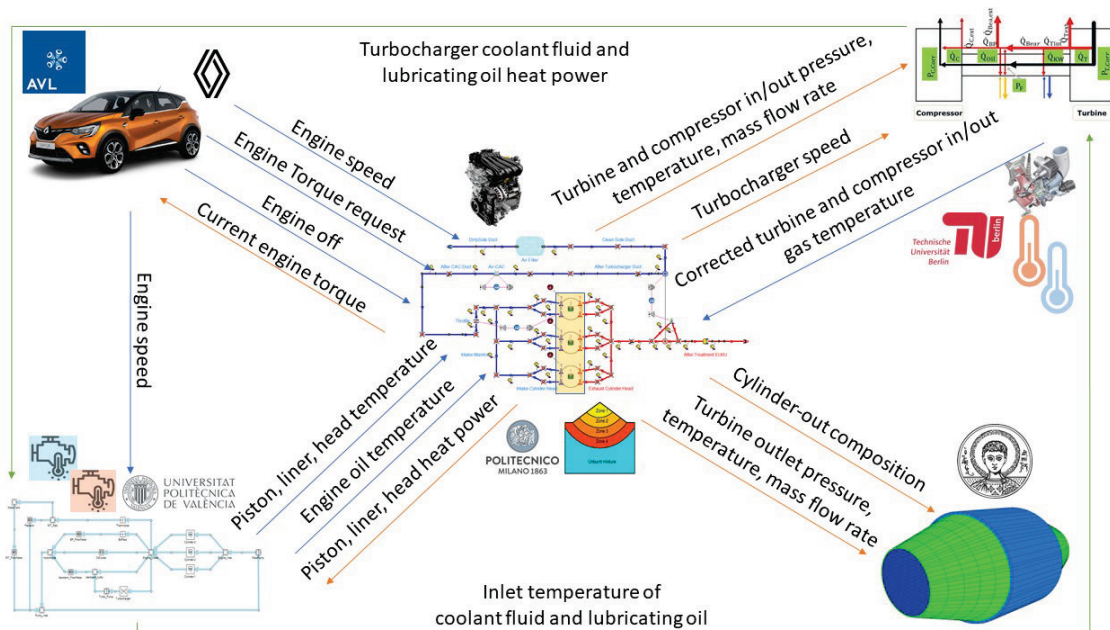

Figure 8.4 – Simplified description of input/output signals exchanged among sub-models.

8.1 Coupled PHEV model RDE simulation

The integrated PHEV model is now applied to the simulation of an RDE cycle (not the same presented previously). In what follows three RDE cycle simulations of a PHEV are presented. Mission profiles have been provided by CNR partner; all cycles start from 20% of initial battery State of Charge (SOC).

In Figure 8.5 the CNR RDE "route_a1", provided by the partner CNR, is shown. As it can be observed, the mission velocity profile is well tracked, and the battery is discharged/charged according to the vehicle decelerations and accelerations. This means that the interaction between the vehicle dynamics and the 1D engine model works properly.

Looking at the three RDE cycles performed in Figure 8.5, 8.7 and 8.10, it can be noticed how the vehicle model follows a strategy focused on maintaining the initial state of charge (SOC) of the battery during the driving cycles.
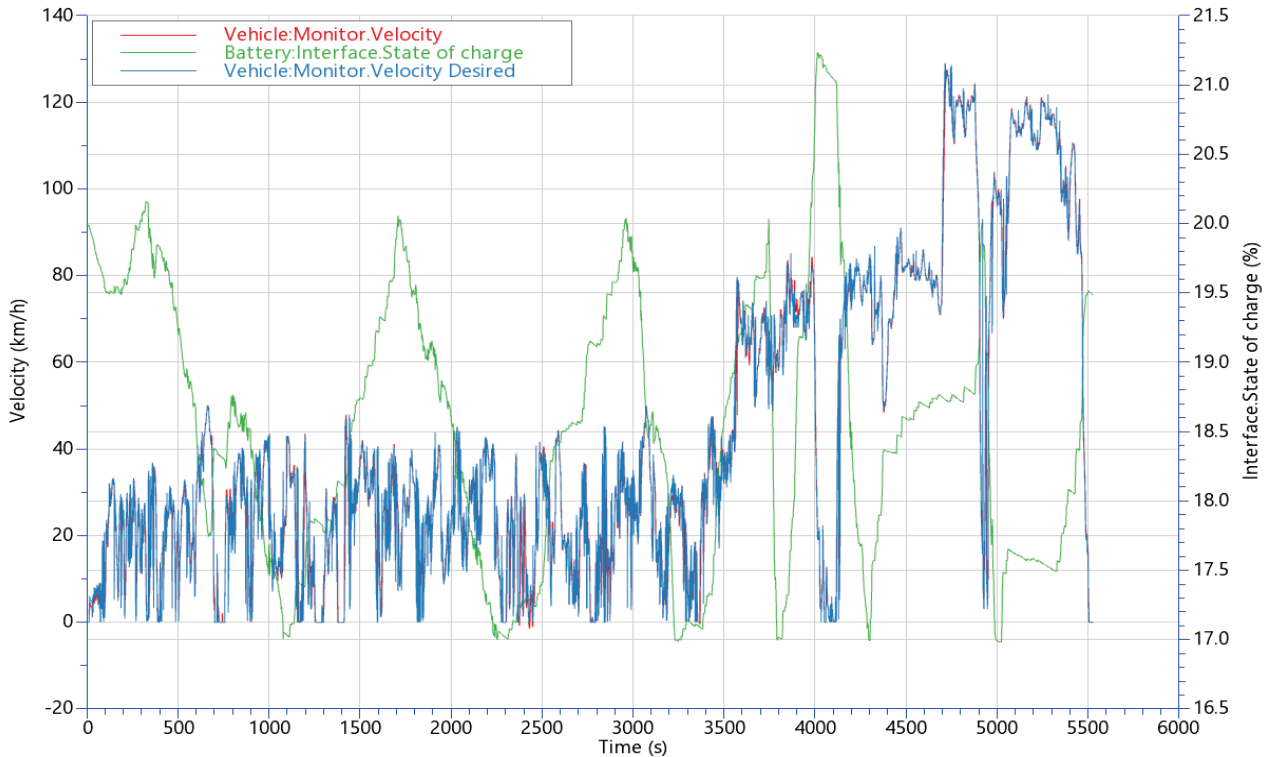

Figure 8.5 - CNR RDE "route_a1" coupled model simulation.

Further calculated quantities can be extracted from the coupled simulation of the CNR RDE "route_a1". Figure 8.6 illustrates some relevant quantities to highlight the model coupling occurring during the RDE cycle. In particular, the thermal power computed by the 1D engine model and transferred through the cylinder walls is used in real-time by the engine thermal model, to compute the lubricating oil temperature and the combustion chamber temperatures, which are then sent back to the 1D engine model.

Moreover, the turbocharger thermal model correctly computes the housing temperatures of the compressor and turbine. Similarly, the exhaust after-treatment module can predict the evolution of the system temperature, thanks to the signals of exhaust mass flow rate and gas temperature coming from the 1D engine model. The battery temperature can also be monitored real-time, showing that it consistently changes when the SOC of the battery changes. In all the RDE time series the engine start & stop effects can be captured. In these simulations the start & stop events are managed on the basis of the strategies implemented in the CRUISE-M vehicle block (control).
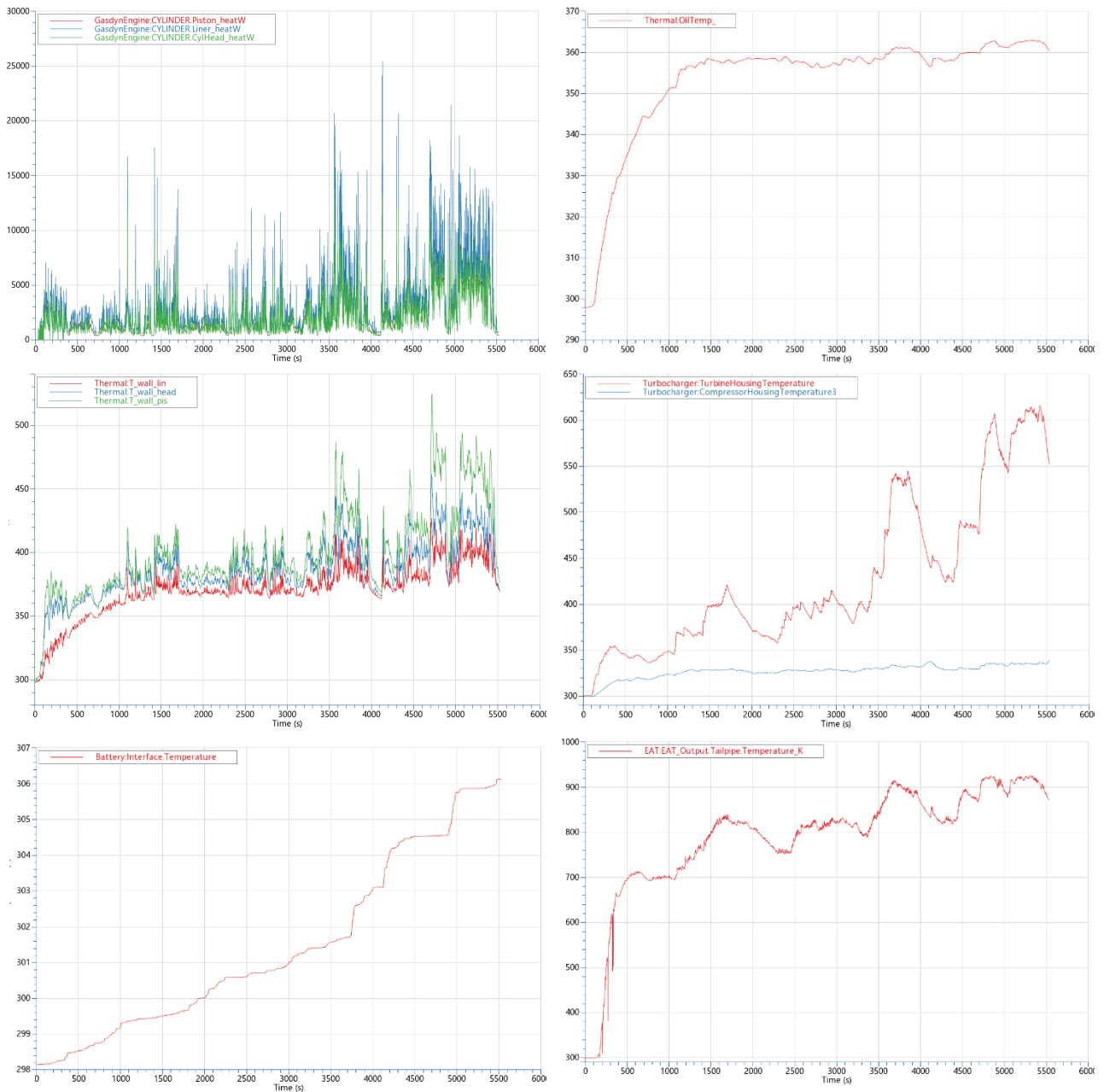
Figure 8.6 - Signals computed and exchanged in real time between sub-models (CNR RDE "route_a1").

Two further RDE test cycles have been simulated, namely CNR RDE "route_a2" and CNR RDE "route_c1". Figures 8.7 and 8.10 respectively show the reliability and applicability of the coupled simulation framework achieved. Using the same initial SOC of the battery, the simulation correctly predicts the vehicle behaviour, according to the characteristics of the different target velocity profiles. This also shows the flexibility of the general modelling tool developed.

As an example of the EAT coupling possibility, the predicted cumulative CO_2 and CO during the CNR RDE "route_a2" cycle, both as cylinder-out and tailpipe emissions, are reported in Figure 8.8, to highlight the conversion occurring in the three-way catalyst. In addition, Figure 8.9 shows the corresponding predicted total emissions of CO_2 and CO (a) and fuel consumption (b) which are in agreement with the values commonly found in the homologation performance of modern PHEV.
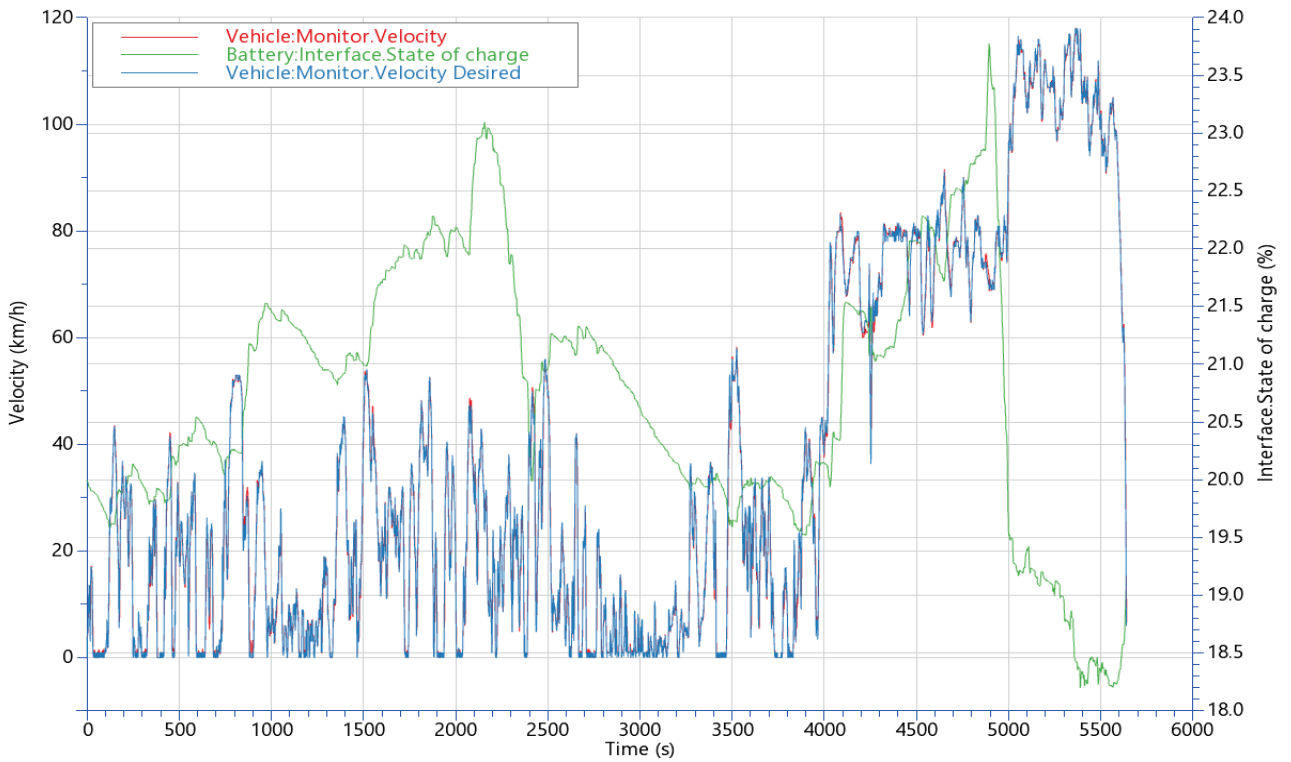
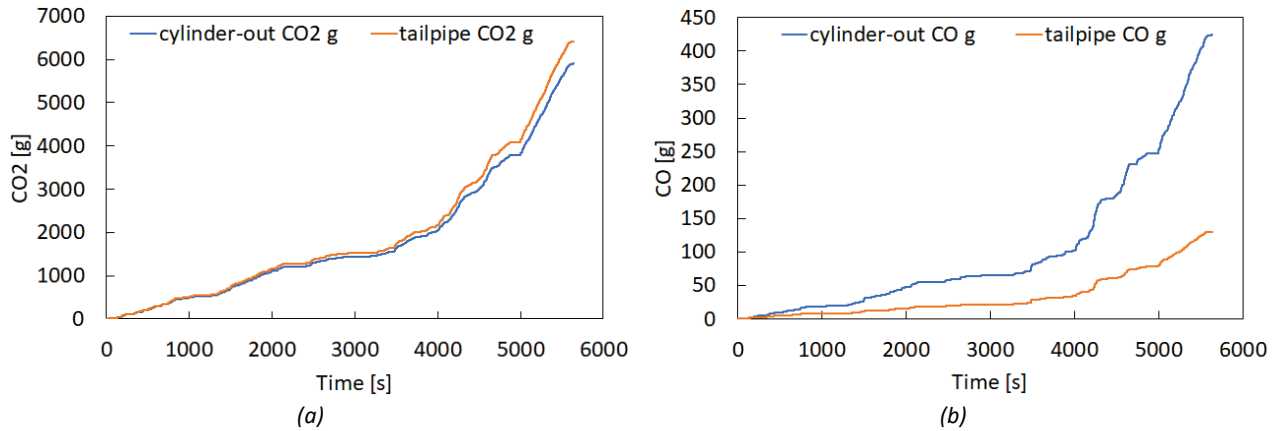Figure 8.7 - CNR RDE "route_a2" coupled model simulation.

(a)   *(b)*

Figure 8.8 – CNR RDE "route_a2" coupled simulation: predicted cumulative CO_2 (a) and CO (b) cylinder-out and tailpipe emission.

Global emissions

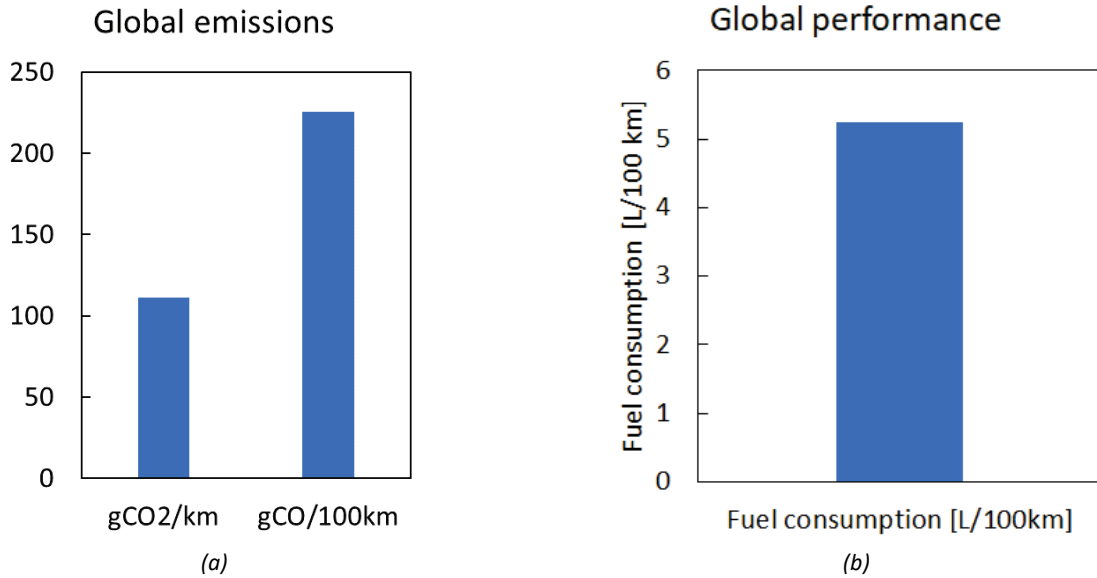

(a)

Global performance

(b)

Figure 8.9 - CNR RDE "route_a2" coupled model: predicted global main emissions (a) and fuel consumption (b).
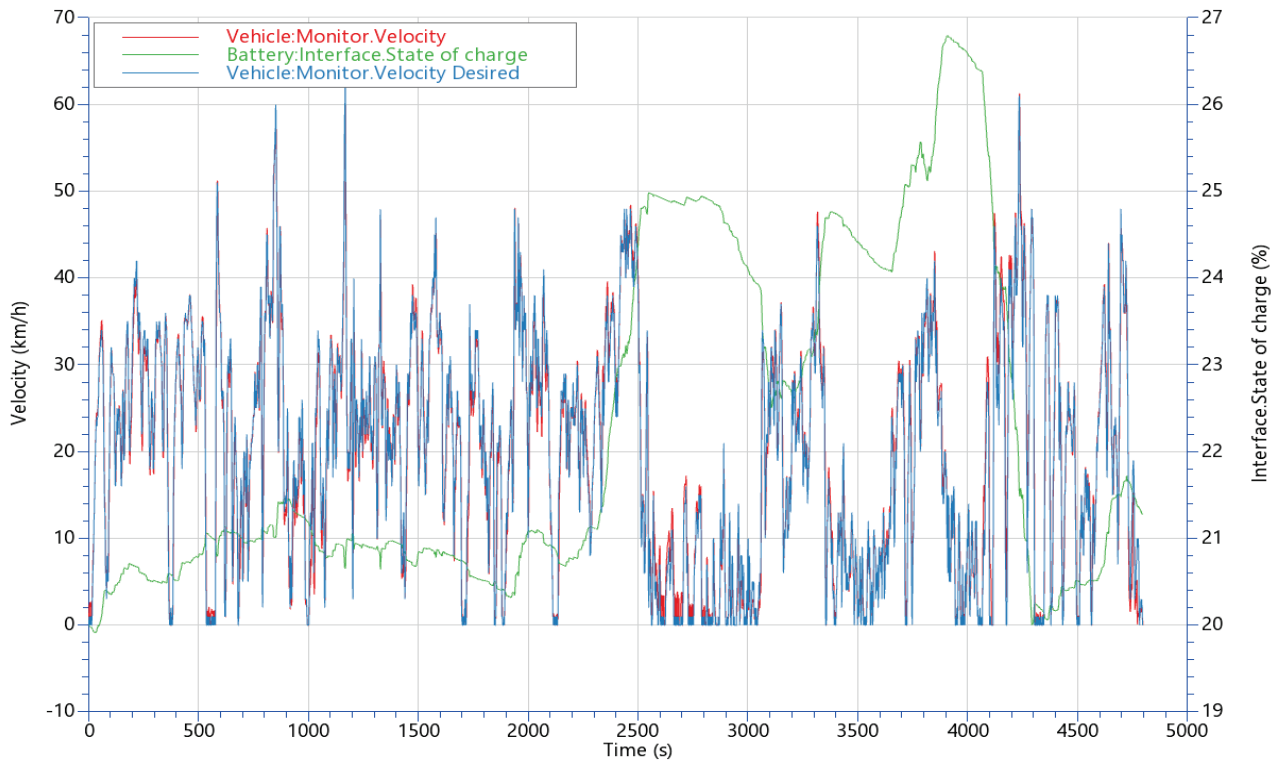

Figure 8.10 - CNR RDE "route_c1" coupled model simulation.

Furthermore, an analysis of the computational effort requested by the simulation of these Real Driving Emission cycles has been carried out. All the simulations have been performed with the FSM (Fast Simulation Model) version of the 1D engine models. Figure 8.11 points out the CPU times and CPU/real time ratios achieved, confirming the results described in previous chapters. However, the CPU/real time ratio, which appears in the range 2.5-3.5, might have increased a bit, due to the additional computational overhead related to the coupled sub-models, which are executed at the same time. This CPU/real time ratio is acceptable, since it allows to run several RDE cycle simulations during the night-time and have the results ready for the morning after. For example, in 8 hours it is possible to simulate two or three RDE cycles of 1.5-hour duration. This would be not possible without the Fast Simulation Method developed, considering the use of a crank-angle resolved, 1D fluid dynamic model.
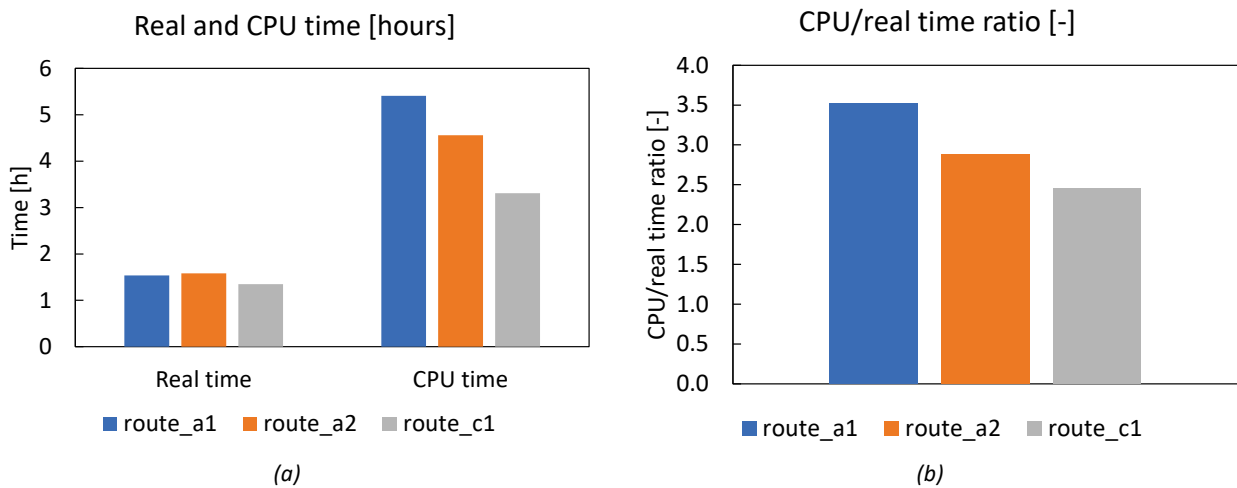
Figure 8.11 - Real and CPU times (a) and CPU/real time ratio (b).

9. Conclusions

In conclusion, in this chapter a summary of the work is presented, the main achievements are highlighted and the possible future developments are discussed.

9.1 Summary

- **Chapter 1** introduces the thesis topic, the 1D modelling of IC engines, and the current specific framework of application. The goal of the thesis is analysed clarifying the aim of the work which is the fast and reliable prediction of engine performance and emission of a modern hybrid vehicle. A review of the literature works in this field is presented, highlighting the differences, advantages and drawback of the approaches proposed in the past and still in use. It is highlighted what limits have constrained the wide application of 1D models in long transient simulations.

- **Chapter 2** is focused on the theoretical formulation of the mathematical model that describes the system object of the simulation activity. The fundamental conservation equations obtained then have to be solved numerically. A selection of numerical techniques, covering all aspects of the fluid dynamic problem, is theoretically presented to assess the simulation tools which have been used to carry out the simulations. The in-cylinder processes are also discussed both for spark ignition and compression ignition engines.

- **Chapter 3** gives an overview of what practically means using the numerical tools previously presented to simulate an engine. Moreover, two engines, under examination across all the thesis, are introduced: the spark ignition 3-cylinder, 1 litre engine and the 6-cylinder, 7 litres, compression ignition engine. The engines architecture and technical specifications are identified. The corresponding digital twin of the engines under study are presented, explaining the process of creating the 1D models from the manufacturer data and translating the 3D geometry in a 1D model.

- **Chapter 4** is dedicated to the steady state validation activity. In this chapter the numerical model results are compared to the results of the experimental campaign carried out by the European project partners, to asses the predictivity and robustness of the mathematical models presented. Several overall engine quantities are compared, from performance to cylinder-out emission. The results have suggested that the virtual engines can represent with good accuracy the real engines.

- **Chapter 5** finally introduces the key tool which deals with one of the goals of the thesis, hence the reduction of the computational effort required. The Fast Simulation Model methodology (FSM) is presented. In particular the different 1D model discretization procedure is described, and the dedicated numerical tool developed is presented, forming a bundled solution to tackle the issue of the computational burden. This methodology is applied to the very same engines presented in previous chapter. The steady state validation activity is repeated, checking that the standard and FSM simulation produce similar results. This is to allow the use of this faster simulation methodology for the driving cycle simulations which are covered in the following chapters.

- **Chapter 6** instead draws the attention to the simulation methodology of the engine under transient conditions. The activity proposed is again a validation of the engine models against experimental data., The objective is to verify that the predictivity achieved under steady state conditions can be obtained also during engine transient simulation. Once again, the standard and fast simulation (FSM) approaches are compared, to ensure consistency of the Fast Simulation Method.

- **Chapter 7** deals with the second goal of the thesis. To achieve a complete vehicle model the 1D engine models are coupled to the European project partner's models. The functional connectivity between the models developed is presented, highlighting the new opportunities in terms of increased physical fidelity of the co-simulation framework and hence results.

- **Chapter 8** eventually reaches the final coupling stage: the complete vehicle model level. The previously developed co-simulation framework is merged into a single integrated simulation network. The fast real time prediction of a hybrid vehicle performances and emissions during a real driving cycle is achieved. The complete coupled simulation model is applied to a few real driving cycles, showing the benefits of the co-simulation framework.

9.2 Main Achievements

In conclusion this thesis work has achieved the integrated modelling of a modern PHEV. The theoretical background covered the main 1D modelling topic: from fluid dynamics to combustion. The state-of-the-art numerical methodologies have been presented, especially the FSM exploited to reach the goals of this thesis. This modelling framework has been applied to the modelling of two engine which have been validated on extensive steady state maps with both refined and coarse mesh. The results have highlighted the model predictivity and the dramatic reduction of CPU/real time ratio. The 1D models have then been applied to the simulation of real-world driving cycles, confirming the good match with experimental data and low computational effort also during transient operation of the same models. In this framework the integration activity has allowed to couple, via FMU interface, the 1D models to external models to simulate the whole PHEV during a driving cycle. The developed co-simulation model has been applied for the simulation of an RDE cycles, showing excellent predictivity of the fully virtual model while maintaining the good low computational effort. The thesis has been strongly linked to the pathway of the "VISION-xEV" EU project, reaching the objectives and targets required by the project.

The main milestones achieved can be summarized as:

- The 1D models of two real engines have been obtained.
- Extensive steady state and transient validation has been performed against experimental data.
- The simulation effort has been reduced by orders of magnitude while preserving accuracy.
- The co-simulation framework has been implemented.
- A fully integrated model of a complete Plug-in Hybrid Electric Vehicle has been simulated.

9.3 Future Developments

The co-simulation framework presented has been possible using a common protocol to communicate signals between models developed in different environments. Moreover, it has been ascertained that the thermal engine plays the central role in this model coupling. It would be convenient to include the sub model into the 1D simulation tool Gasdyn. Embedding in a single model the fluid dynamic model, the turbocharger thermal model, the engine warm up model and the after-treatment model would allow to perform an instantaneous coupling instead of a cyclic coupling, if possible.

A brief exploration activity has been performed in the field of mean value models, which proved to be very fast but currently rely on look up tables It would be nice to increase the predictivity of the MVM.

Eventually the other simulation techniques mentioned in the thesis, such as separating the intake and exhaust solution, can be explored in the future to reach even faster CPU/real time ratio.

Abbreviations

BMEP	Brake Mean Effective Pressure
BSFC	Brake Specific Fuel Consumption
CFD	Computational Fluid Dynamics
CMT	Centro Motores Térmicos
CNR	Consiglio Nazionale delle Ricerche
CO	Carbon monoxide
CO_2	Carbon dioxide
CG	Corberán Gascon
CPU	Central Processing Unit
DTM	Diffusion Term Momentum
EVO	Exhaust Valve Opening
EVC	Exhaust Valve Closing
EOS	Equation of State
FMEP	Friction Mean Effective Pressure
FMU/FMI	Functional Mock-Up Interface
FPT	FPT Motorenforschung AG
FSM	Fast Simulation Method
GUI	Graphical User Interface
IMEP	Indicated Mean Effective Pressure
HC/THC	Thermal/Hydro-Carbon
ICE	Internal Combustion Engine
IVO	Intake Valve Opening
IVC	Intake Valve Closing
MOC	Method of Characteristics
NCD	Non-Computable Data
NO_x	Nitrogen oxides (NO, NO2)
RDE	Real Driving Emission
RPM	Revolutions Per Minute
PHEV	Plug-in Hybrid Electric Vehicle
SAE	Society of Automotive Engineers
SOC	State Of Charge
STL	Standard Triangle Language or Standard Tessellation Language
TUB	Technische Universität Berlin
TVD	Total Variation Diminishing
UPV	Universitat Politècnica de Valencia
WHTC	World Harmonized Transient Cycle (heavy duty vehicles)
WLTP	Worldwide Harmonised Light Vehicle Test Procedure
VGT	Variable Geometry Turbine

References

[1] VISION-xEV European Project website: https://vision-xev.eu/.

[2] Maschmeyer H., Kluin M., Beidl C., *Real Driving Emissions - A Paradigm Change for Development*, MTZ worldwide, 76, 16-21, 2015, https://doi.org/10.1007/s38313-014-1014-y.

[3] Joshi A, *Review of Vehicle Engine Efficiency and Emissions*, SAE International Journal, 2020, https://doi.org/10.4271/2021-01-0575.

[4] Grill M., Keskin M.T., Bargende M., *Virtual rde: Ensuring rde conformity of hybridized powertrains in the early stage of the development process,* VDI Berichte, 2020, pp. 343-354. https://doi.org/10.51202/9783181023730-I-343.

[5] Doulgeris S., Toumasatos Z., Prati MV., Beatrice C., Samaras Z., *Assessment and design of real-world driving cycles targeted to the calibration of vehicles with electrified powertrain*, International Journal of Engine Research, 2021, doi: https://doi.org/10.1177/1468087421103872.

[6] Mamikoglu S., Dahlander P., *Modelling of Hybrid Electric Vehicle Powertrains - Factors That Impact Accuracy of CO_2 Emissions*, SAE Technical Paper, 2019, https://doi.org/10.4271/2019-01-0080.

[7] Martínez F., Arnau F., Piqueras P., Auñon A., *Development of an Integrated Virtual Engine Model to Simulate New Standard Testing Cycles*, SAE Technical Paper, 2018, https://doi.org/10.4271/2018-01-1413.

[8] Onorati A., Ferrari G., Montenegro G., Caraceni A., Pallotti P., *Prediction of S.I. Engine Emissions During an ECE Driving Cycle via Integrated Thermo-Fluid Dynamic Simulation*, SAE Technical Paper, 2004, https://doi.org/10.4271/2004-01-1001.

[9] Di Pierro G., Millo F., Scassa M., and Perazzo A., *An Integrated Methodology for 0D Map-Based Powertrain Modelling Applied to a 48 V Mild-Hybrid Diesel Passenger Car*, SAE Technical Paper, 2018, https://doi.org/10.4271/2018-01-1659.

[10] Stockar S., Canova M., Guezennec Y., Della Torre A., Montenegro G., Onorati A., *Modeling wave action effects in internal combustion engine air path systems: Comparison of numerical and system dynamics approaches*, International Journal of Engine Research, 2013, https://doi.org/10.1177/1468087412455747.

[11] Deppenkemper K., Zyalcin C., Ehrly M., Schoenen M., Bergmann D., Pischinger S., *1D Engine Simulation Approach for Optimizing Engine and Exhaust Aftertreatment Thermal Management for Passenger Car Diesel Engines by Means of Variable Valve Train (VVT) Applications*, SAE Technical Paper, 2018, https://doi.org/10.4271/2018-01-0163.

[12] De Bellis V., Malfi E., Cacciatore D., Aliperti A., Rizzi L., *Fuel Consumption and Pollutant Emission Optimization at Part and Full Load of a High-Performance V12 SI Engine by a 1D Model*, SAE Technical Paper, 2019, https://doi.org/10.4271/2019-24-0080.

[13] Zanelli A., Millo F., Barbolini M., *Driving Cycle and Elasticity Manoeuvres Simulation of a Small SUV Featuring an Electrically Boosted 1.0 L Gasoline Engine*, SAE Technical Paper, 2019, https://doi.org/10.4271/2019-24-0070.

[14] Cerri T., D'Errico G., Montenegro G., Onorati A. et al., *A Novel 1D Co-Simulation Framework for the Prediction of Tailpipe Emissions under Different IC Engine Operating Conditions*, SAE Technical Paper, 2019, https://doi.org/10.4271/2019-24-0147.

[15] Millo, F., Di Lorenzo, G., Servetto, E., Capra, A. et al., *Analysis of the Performance of a Turbocharged S.I. Engine under Transient Operating Conditions by Means of Fast Running Models*, SAE Int. J. Engines, 2013, https://doi.org/10.4271/2013-01-1115.

[16] Ferrari G., D'Errico G., Onorati A, *Internal Combustion Engines*, Esculapio, 2022.

[17] Heywood J.B., *Internal Combustion Engine Fundamentals*, McGraw Hill, USA, 1988.

[18] Blumberg P.N., Lavoie G.A., Tabaczynski R.J., *Phenomenological models for reciprocating internal combustion engines*, PECS, 1979, https://doi.org/10.1016/0360-1285(79)90015-7.

[19] Shapiro A.H., *The Dynamics, and Thermodynamics of Compressible Fluid Flow, Vol I*, John Wiley & Sons, USA, 1953.

[20] Versteeg H.K. and Malalasekera W., *An Introduction to Computational Fluid Dynamics - The Finite Volume Method*, Pearson, 1995.

[21] Benson R.S., *The Thermodynamics and Gas Dynamics of Internal Combustion Engines, Vol I and II*, Clarendon Press, Oxford, 1982.

[22] Winterbone D.E. and Pearson R.J., *Theory of Engine Manifold Design*, Professional Engineering Publishing, London, 2000.

[23] Winterbone D.E. and Pearson R.J., *Design Techniques for Engine Manifolds*, Professional Engineering Publishing, London, 1999.

[24] Onorati A., Montenegro G., *1D and Multi-D Modelling Techniques for IC Engine Simulation*, SAE International, 2020.

[25] Payri F., Boada F., *Modifications to the method of characteristics for the analysis of the gas exchange process in internal combustion engines*, Proc. Inst. Mech. Engr., Vol 200, 1986, https://doi.org/10.1243/PIME_PROC_1986_200_189_02.

[26] Serrano J.R., Arnau F.J., Piqueras P., Onorati A., Montenegro G., *1D gas dynamic modelling of mass conservation in engine duct systems with thermal contact discontinuities*. Math. Comput. Model. 2009, https://doi.org/10.1016/j.mcm.2008.03.015.

[27] Courant R, Friedrichs K, Lewy H, *Über die partiellen Differenzengleichungen der mathematischen Physik*, Math. Ann., 1928, https://doi.org/10.1007/BF01448839.

[28] Harten A., *High Resolution schemes for hyperbolic Conservation Laws*, Journal of Computational Physics, Vol 49, 1983, https://doi.org/10.1016/0021-9991(83)90136-5.

[29] Corberán J.M., Gascón M.LL., *Construction of Seconds Order TVD Schemes for Non-Homogeneous Hyperbolic Conservation Laws*, Journal of Computational Physics, 172, 261-297, 2001, https://doi.org/10.1006/jcph.2001.6823.

[30] Corberán J.M., Gascón M.LL., *TVD Schemes for the Calculation of Flow in Pipe of Variable Cross-Section*, Mathematical Computing Modelling, Vol. 21, No. 3 pp 85-92, 1995, https://doi.org/10.1016/0895-7177(94)00216-B.

[31] Tamborski M., *Simulazione 1D dei flussi non stazionari nei motori a C.I. mediante i metodi numerici CE-SE e GC-TVD*, MScs Thesis, Politecnico di Milano, 2018.

[32] Galindo J., Arnau F.J., Tiseira A., Piqueras P., *Solution of the turbocompressor boundary condition for one-dimensional gas-dynamic codes*, Math. Comp. Mod., Volume 52, Issues 7–8, 2010, https://doi.org/10.1016/j.mcm.2010.05.003.

[33] Hadef J.E., Colin G., Chamaillard Y., Talon V., *Physical-Based Algorithms for Interpolation and Extrapolation of Turbocharger Data Maps*. SAE Int. J. Engines, 2012, https://doi.org/10.4271/2012-01-0434.

[34] Demesoukas S., Caillol C., Higelin P., Boiarciuc A., *Zero-Dimensional Spark Ignition Combustion Modelling - A Comparison of Different Approaches*, SAE Technical Paper, 2013, https://doi.org/10.4271/2013-24-0022.

[35] Woschni G., *A Universally Applicable Equation for the Instantaneous Heat Transfer Coefficient in the Internal Combustion Engine*, SAE Technical Paper, 1967, https://doi.org/10.4271/670931.

[36] Ghojel J, *Review of the development and applications of the Wiebe function: A tribute to the contribution of Ivan Wiebe to engine research*, International Journal of Engine Research, 2010, https://doi.org/10.1243/14680874JER06510.

[37] Zimont V.L., *Gas premixed combustion at high turbulence. Turbulent flame closure combustion model*, Experimental Thermal and Fluid Science, 2000, https://doi.org/10.1016/S0894-1777(99)00069-2.

[38] Broatch A., Novella R., Garcia T., Gómez-Soriano P., *Investigation of the effects of turbulence modeling on the prediction of compression-ignition combustion unsteadiness*, International Journal of Engine Research, 2021, https://doi.org/10.1177/1468087421990478.

[39] Poulos, S. and Heywood, J., *The Effect of Chamber Geometry on Spark-Ignition Engine Combustion*, SAE Technical Paper, 1983, https://doi.org/10.4271/830334.

[40] Zhou, Q., Lucchini, T., D'Errico, G., and Hardy, G., *Validation of Diesel Combustion Models with Turbulence Chemistry Interaction and Detailed Kinetics*, SAE Technical Paper 2019-24-0088, 2019, https://doi.org/10.4271/2019-24-0088.

[41] Tamborski M, D'Errico G, Lucchini T, Onorati A. *Detailed prediction of HRR and NOx emissions in CI engines via a novel thermodynamic model with constant equivalence ratio zones*, International Journal of Engine Research, 2022, https://doi.org/10.1177/14680874221128645

[42] Lucchini T., D'Errico G., Onorati A., Frassoldati A., *Modeling Non-Premixed Combustion Using Tabulated Kinetics and Different Flame Structure Assumptions,* SAE Int. J. Engines, 2017, https://doi.org/10.4271/2017-01-0556.

[43] D'Errico G., Ferrari G., Onorati A., Cerri T., *Modeling the pollutant emissions from a S.I. engine*, SAE Technical Paper, 2002, https://doi.org/10.4271/2002-01-0006.

[44] Miller R., Davis G., Lavoie G., Newman C., *A Super-Extended Zeldovich Mechanism for Nox Modeling and Engine Calibration*, SAE Technical Paper, 1998, https://doi.org/10.4271/980781.

[45] Lavoie G.A., Heywood J.B., Keck J.C., *Experimental and Theoretical Study of Nitric Oxide Formation in Internal Combustion Engines*, Combustion Science and Technology, 1970, https://doi.org/10.1080/00102206908952211.

[46] Erickson W.D. and Probhu R.K., *Rapid Computation of Equilibrium Composition: An Application to Hydrocarbon Combustion*, AIChE Journal, vol. 32 no. 7, 1986. https://doi.org/10.1002/aic.690320704.

[47] Schramm J., Sorenson S.C., *A model for hydrocarbon emissions from SI engines*, SAE Technical Paper, 1990, https://doi.org/10.4271/902169.

[48] Montenegro G., Onorati A., Cerri T., Della Torre A., *A Quasi-3D Model for the Simulation of the Unsteady Flows in I.C. Engine Pipe Systems,* SAE Technical Paper, 2012, https://doi.org/10.4271/2012-01-0675.

[49] Montenegro G., Della Torre A., Onorati A., Fairbrother R., *A Nonlinear Quasi-3D Approach for the Modelling of Mufflers with Perforated Elements and Sound-Absorbing Material*, Adv. Acoust. Vib, 2013, https://doi.org/10.1155/2013/546120.

[50] Della Torre A., Montenegro G., Cerri T., Onorati A., *A 1D/Quasi-3D Coupled Model for the Simulation of I.C. Engines: Development and Application of an Automatic Cell-Network Generator*, SAE Int. J. Engines, 2017, https://doi.org/10.4271/2017-01-0514.

[51] Ballerini A., *1D Thermo-Fluid Dynamic Simulation of Hydrogen Internal Combustion Engines: Implementation of new models in Gasdyn*, MScs Thesis, Politecnico di Milano, 2021.

[52] Bizzini A., *Fast Simulation Numerical Methods for 1D fluid-dynamics: Improvement and Applications on Renault-Nissan Turbocharged Internal Combustion Engine*, MScs Thesis, Politecnico di Milano, 2021.

[53] Ierardi C., *Il metodo 3D Cell per la modellazione termo-fluidodinamica 1D dei motori a combustione interna*, MScs, Politecnico di Milano, 2019.

[54] Isermann R., *Engine Modelling and Control*, Springer, 2014.

[55] Guzzella L, Onder C., *Introduction to Modeling and Control of Internal Combustion Engine Systems*, 2004, Springer.

[56] Test Procedure for the Measurement of Gaseous Exhaust Emissions from Small Utility Engines, J1088_201303.

[57] https://fmi-standard.org/.

[58] Shayler P., Leong D., Murphy M., *Contributions to Engine Friction During Cold, Low Speed Running and the Dependence on Oil Viscosity*, SAE Technical Paper, 2005, https://doi.org/10.4271/2005-01-1654.

[59] Broatch A., Olmeda P., Plá B., Dreif A., Onorati A., Marinoni A., *Numerical assessment of integrated thermal management systems in electrified powertrains*, Applied Thermal Engineering, 2022, https://doi.org/10.1016/j.applthermaleng.2022.119822.

[60] Papetti, V., Dimopoulos Eggenschwiler, P., Emmanouil, V., and Koltsakis, G., *Analysis of TWC Characteristics in a Euro6 Gasoline Light Duty Vehicle,* SAE Technical Paper 2019-24-0162, 2019, https://doi.org/10.4271/2019-24-0162.

[61] Kazemi Bakhshmand, S.; Luu, L.T.; Biet, C., *Experimental Energy and Exergy Analysis of an Automotive Turbocharger Using a Novel Power-Based Approach*, Energies 2021, 14, 6572. https://doi.org/10.3390/en14206572.

[62] Lim, S., Kazemi Bakhshmand, S., Biet, C., and Mihaescu, M., *Experimental and Numerical Investigation of a Turbocharger Turbine Using Exergy Analysis at Non-Adiabatic Conditions*, SAE Technical Paper 2020-01-2225, 2020, https://doi.org/10.4271/2020-01-2225.

[63] Marelli, S., Marmorato, G., Capobianco, M., and Rinaldi, A., *Heat Transfer Effects on Performance Map of a Turbocharger Compressor for Automotive Application*, SAE Technical Paper 2015-01-1287, 2015, https://doi.org/10.4271/2015-01-1287.

[64] Rahman, R., Biswas, A., Lindquist, C., Khandaker, M. et al., *Co-Simulation Methodology for PHEV Thermal System Development*, SAE Int. J. Adv. & Curr. Prac. in Mobility, 2020, https://doi.org/10.4271/2020-01-1392.

[65] Kalantzis, N., Fletcher, T., Ahmedov, A., Yuan, R. et al., *Co-Simulation Methods for Holistic Vehicle Design: A Comparison*, SAE Technical Paper 2020-01-1017, 2020, https://doi.org/10.4271/2020-01-1017.

Publications

It is reported below the list of publications achieved during the Ph.D. The published works have been a joint effort with the other members of the ICE group at Politecnico di Milano and with the involved partners of the European Project "VISION-xEV".

[1] Marinoni A., Onorati A., Manca Di Villahermosa G., Langridge S., *Real Driving Cycle Simulation of a Hybrid Bus by means of a Co-Simulation Tool for the Prediction of Performance and Emissions,* MDPI Energies, 2023, https://doi.org/10.3390/en16124736.

[2] Marinoni A., Onorati A., Montenegro G., et al., *RDE cycle simulation by 0D/1D models to investigate IC engine performance and cylinder-out emissions*, International Journal of Engine Research. 2022, https://doi.org/10.1177/14680874221141936.

[3] Broatch A., Olmeda P., Plá B., Dreif A., Onorati A., Marinoni A., *Numerical assessment of integrated thermal management systems in electrified powertrains*, Applied Thermal Engineering, 2022, https://doi.org/10.1016/j.applthermaleng.2022.119822.

[4] Montenegro G., Onorati A., D'Errico G., Cerri T. et al., *Prediction of Driving Cycles by Means of a Co-Simulation Framework for the Evaluation of IC Engine Tailpipe Emissions*, SAE Technical Paper, 2020, https://doi.org/10.4271/2020-37-0011.

[5] Marinoni A., Tamborski M., Cerri T., Montenegro G., D'Errico G., Onorati, A., Piatti E., Pisoni E.E., *0D/1D Thermo-Fluid Dynamic Modelling Tools for the Simulation of Driving Cycles and the Optimization of IC Engine Performances and Emissions*, MDPI Appl. Sci., 2021, https://doi.org/10.3390/app11178125.

[6] Ballerini A., Cerri T., Onorati A. and Marinoni A., *Advances in 1D thermo-fluid dynamic simulation of S.I. hydrogen fuelled engine*, 2022, IOP Conference Proceedings, https://doi.org/10.1088/1742-6596/2385/1/012055.

[7] Montenegro G., Tamborski M., Della Torre A., Onorati A. et al., *Development and Application of a Quasi-3D Model for the Simulation of Radial Compressors of Turbochargers for Internal Combustion Engines*, SAE Technical Paper, 2019, https://doi.org/10.4271/2019-24-0187.

[8] Montenegro G., Tamborski M., Marinoni A., Della Torre A., Onorati A., Marelli S., *A quasi-3D approach for the modelling of an automotive turbocharger's compressor.* AIP Conference Proceedings, 2019, https://doi.org/10.1063/1.5138846.

Acknowledgments

Ad maiora!

amarino